9950 - 514

RE-ENTRY SYSTEMS DIVISION

PHILADELPHIA, PENNSYLVANIA

(NASA-CR-164161) GENERIC AEROCAPTURE ATMOSPHERIC ENTRY STUDY, VOLUME 1 Final Report (General Electric Co.) 241 p HC A11/MF A01 CSCL 22A

N81-21098

Unclas
G3/13 42001

GENERAL ELECTRIC

DOCUMENT 80SDR2226
24 OCTOBER 1980

GENERIC AEROCAPTURE ATMOSPHERIC ENTRY STUDY

FINAL REPORT

* VOLUME I *

CONTRACT NO. 955689

"This work was performed for the Jet Propulsion Laboratory, California Institute of Technology sponsored by the National Aeronautics and Space Administration under Contract NAS7-100."

RE-ENTRY SYSTEMS DIVISION
3198 Chestnut St., Philadelphia, PA 19101

GENERAL ELECTRIC

NOMENCLATURE

A	Reference (base) area - square meters
A_F	Flap area (2 flaps), square meters
A_{yw}, A_{zw}	Acceleration along wind axes (X_W along velocity vector, Y_w, Z_w rotate with body)
ACTHR	RCS roll acceleration, rad/sec
API	Autopilot integrator signal
AXBR	Reference drag in guidance law
AXW	Acceleration along X wind axis (drag), meters per sec^2
A/C	Aerocapture
A/M	Aeromaneuver
AU	Astronomical Unit
AZB	Acceleration along Z_B (body) axis (= $-A_N$), meters per sec^2
AZBM	= -AZB limited to a minimum value
CDEL	= CDELR * QB - Roll acceleration per degree flap deflection
CDELR	Coefficient of roll acceleration due to flap deflection
CDIST	Coefficient which, when multiplied by dynamic pressure, yields roll disturbance acceleration.
c.g., X_{CG}	Center of Gravity
CM	Center of Mass
CP	Carbon Phenolic
c.p., X_{CP}	Center of Pressure
CRDB	Cross-range, deadband, meters
CRNG	Cross-range distance, km
C_2	Lateral distance between CG and CP

C_3	Vertical CG displacement
C_A	Axial force coefficient
C_D	Drag coefficient
C_L	Lift coefficient
C_N	Normal force coefficient
C_{N_P}	Flap panel normal force coefficient
C_X	X body force coefficient ($= -C_A$)
C_h	Flap hinge moment coefficient
C_{ℓ_O}	Coefficient of roll torque due to roll asymmetries
C_{ℓ_β}	Coefficient of roll torque due to β
C_{ℓ_δ}	Coefficient of roll torque due to flap deflection
C_m	Coefficient of pitching moment
C_{m_α}	Coefficient of pitching moment due to α
C_{mq}, C_{nr}	Pitch and yaw damping coefficients
C_{no}	Coefficient of yaw torque due to yaw asymmetries
C_{n_β}	Coefficient of yaw moment due to β
C_{n_δ}	Coefficient of yaw torque due to yaw nose deflection
C_{y_β}	Coefficient of side force due to β
C_{y_δ}	Coefficient of side force due to yaw nose deflection
C_{z_α}	Coefficient of normal force due to α
D	Drag Force
D_B	Vehicle Base Diameter, m
DELR	$= \delta_\ell$ - Roll flap deflection, degrees
DELRC	Commanded roll flap deflection
DIST	Roll disturbance acceleration, rad/sec^2

$DIST_N$	Roll disturbance acceleration during constant drag portion of aerocapture trajectory
DSN	Deep Space Network
DRNG	Down range distance, km
ETR	Actuating signal for control jets
ESM	Elastomeric Shield Material
ERG1	Attitude error, rad
ERG1D	Attitude error, deg
ER1R	Roll rate error signal, rad/sec
FLRL	Actuator slew rate limit in first order model
FPA	Air relative flight path angle, deg.
G_E, g_E	Earth's gravitational acceleration (9.8 m/sec^2)
GMO	Air relative path angle at entry
G_{zv}	Component of gravity along Z_V axis (velocity axis, X_V along velocity vector, Y_V horizontal)
GN&C	Guidance, Navigation and Control
h	Heat transfer coefficient, $\dot{q}_H / (H_R - hw)$
hw	Enthalpy of gas evaluated at wall temperature, J/KG
H	Altitude, ft.
H_R	Recovery enthalpy, J/KG
HM	Altitude, meters
IA	Gyro input axis
IMP	Control impulse, N-m-sec
IUS	Inertial Upper Stage
I_{xx}, I_{yy}, I_{zz}	Roll, pitch and yaw moments of inertia
I_P	Pitch moment of inertia
I_R	Roll moment of inertia

I_{sp}	Specific impulse, sec
K	Constant in roll control logic
K_A	Flap actuator constant
K1, K2, K3	Roll control gains
KBPS	Thousands Bits Per Second
L	Lift force
LIM1, ..., LIM5	Roll control limits
L_A	Apex length of vehicle, meters
L_{cr}	Roll control lever arm, meters
L_c	Pitch/yaw control lever arm, meters
MM	Multi-Mission
MMRC	Moving mass roll control
MU	Gyro mass unbalance
M_c	Roll control torque, N-m
M_H	Flap hinge moment
M_D	Roll disturbance torque
M	Mach Number
M_m	Mass of movable mass (kg)
MSR	Mars Sample Return
P	Local pressure
p, q, r	Roll, pitch and yaw angular rates
P_A	Flap actuator power
PROP	Autopilot proportional signal
PWC	Pulse width command signal
QB = $\bar{Q}$	Dynamic pressure, N/m^2
QB_N	Dynamic pressure on constant drag portion of trajectory

$\dot{q}$	Local heat transfer rate, w/cm^2
PN	Phenolic Nylon
P	Propulsion tank pressure, psia
P_S	Stagnation Pressure, atm.
QB, Q	Dynamic pressure, kn/m^2
QB_N	Dynamic pressure during constant drag phase of aerocapture trajectory
RCS	Raction Control System
RCIMP	Roll control impulse, rad/sec
R_B	Base radius, meters
Re_θ	Reynolds Number based on local properties and momentum thickness
Re_∞	Free Stream Reynolds Number
RHO, RDLN	Atmosphere density
RG1	Bank angle, rad
RG1D	Bank angle, deg.
RG1R	Roll rate, rad/sec
RG1RD	Roll rate, deg/sec
RG1RL	Limited bank angle rate signal
RG1DD	Roll control acceleration, rad/sec^2
RG1DL	Roll rate limit
RG1C	Bank angle command
RKRAT	Constant in roll control logic (= K)
R_I	Intermediate radius of vehicle, meters
RTG	Radioisotope Thermal Generator
R_B	Base radius, meters
R_N	Nose radius, meters

SAM	Silicone Ablator Material
SF	Scale factor
SM	Single Mission
SRA	Spin reference axis
STS	Space Transportation System
T, t	Time, sec
TDIST	Average thruster acceleration for PWM RCS Roll Control in rad/sec2
TPS	Thermal Protection System
T_H	Aerodynamic torque on movable nose
T_c	Pitch/yaw control torque
V	Inertial velocity, m/s
V_∞	Hyperbolic flyby or freestream velocity, m/s
VA	Air relative velocity, m/sec
V_{EXIT}	Exit velocity, m/sec
VM	Inertial velocity, m/s
VAM	Air relative velocity, m/s
VM200	Exit velocity at 200 km altitude, m/s
VMEX	Exit velocity at 250 km altitude, m/s
V_F	Volume of fuel tank, m^3
V_O	Volume of oxidizer tank, m^3
W	Weight of vehicle, kg
W_M	Weight of MMRC movable mass, kg
W_{TP}	Total propellant weight, kg
W_F	Weight of fuel, kg
W_O	Weight of oxidizer, kg
W_T	Tank weight, kg.
W_{TF}	Weight of fuel tank, kg

W_{TO}	Weight of oxidizer tank, kg
X	Axial distance, m
Y	Radial distance, m
Y_M	Position of movable mass, m
$\dot{Y}_M$	Rate of movable mass, m/s
α	Angle of attack
α_T	Trim angle of attack
δo	Shock stand off distance
δ_N	Nose bend angle, deg
δ_F	Flap deflection angle, deg
δ_e, $\dot{\delta}_e$	Flap angle and angular rate
β	Angle of sideslip
β_T	Trim angle of sideslip
$\gamma(0)$	Air relative flight path angle at entry
γ_1	Bank angle (=RG1)
ρ	Material or gas density, kg/m^3
θ	Cone angle
ωRL	Rate loop crossover frequency
ΔCR, ΔDR	Crossrange and downrange deviations from nominal, km
$\Delta VM200$, $\Delta VMEX$	Deviations from nominal of VM200 and VMEX

Subscripts

e	Denotes local conditions
t	Denotes at transition to turbulent flow
∞	Denotes freestream conditions
S	Denotes stagnation point
ac	Denotes aerodynamic center location
FB or fb	Distance from base

ABSTRACT

This report presents the results of an atmospheric entry study to define a generic Aerocapture vehicle capable of missions to Mars, Saturn, and Uranus. A single external geometry has been developed and, along with several control concepts, has been evaluated through atmospheric entry simulations.

Aerocapture is a system design concept that uses an aerodynamically controlled atmospheric entry to provide the necessary velocity depletion to capture payloads into planetary orbit.

Selected design concepts are presented that are capable of providing the control accuracy required while providing thermal protection for the mission payload.

The system design concepts consist of the following elements:

(1) An extendable biconic aerodynamic configuration with lift to drag ratio between 1.0 and 2.0 thus allowing control of aerodynamic drag by vehicle roll control (i.e., rolling the lift vector relative to the local vertical).

(2) Roll control system concepts to control aerodynamic lift and disturbance torques to allow orbit insertion within the required accuracy.

(3) Aeroshell design concepts capable of meeting dynamic pressure loads during Aerocapture, and

(4) Entry thermal protection system design concepts capable of meeting thermodynamic loads during Aerocapture.

TABLE OF CONTENTS

VOLUME I

SECTION		PAGE
	NOMENCLATURE	i
	ABSTRACT	viii
I	INTRODUCTION AND SUMMARY	I-1
	A. Introduction	I-1
	B. Summary	I-2
	C. Conclusion	I-7
II	SYSTEM REQUIREMENTS	II-1
	A. Mission Definition	II-1
	B. Design and Performance Requirements	II-1
III	AERODYNAMIC CONFIGURATION	III-1
	A. Aerodynamic Configuration Screening Approach	III-1
	B. Generic Aerocapture Vehicle Configuration Selection	III-4
	C. Summary	III-9
IV	THERMAL PROTECTION SUBSYSTEM	IV-1
	A. Aerothermodynamic Design Approach	IV-1
	B. Convective Heat Transfer Design Techniques	IV-2
	C. Radiative Heat Transfer	IV-5
	D. Ablative Mass Loss	IV-8
	E. Material Thermal Response	IV-10
	F. Heat Protection Material Selection	IV-11
	G. Summary	IV-18
V	CONTROL SYSTEMS	V-1
	A. Introduction	V-1
	B. Results and Conclusions-Control System Evaluations	V-3
	C. Analysis and Simulation Results	V-6
	D Trajectory Studies	V-26
VI	VEHICLE DESIGN	VI-1
	A. Approach	VI-1
	B. Generic Vehicle Design	VI-2
	C. Saturn Orbiter Dual Probe Aeroshell Design	VI-3
	D. Mars Sample Return Aeroshell Design	VI-8
	E. Uranus Mission Aeroshell Design	VI-9
	F. Vehicle Design Summary	VI-9
VII	CONCLUSIONS	VII-1
VIII	NEW TECHNOLOGY AND RECOMMENDATIONS	VIII-1
IX	REFERENCES	IX-1

TABLE OF CONTENTS
(continued)

LIST OF ILLUSTRATIONS

LIST OF TABLES

VOLUME II

APPENDIX A SO2P TRAJECTORIES

APPENDIX B MSR TRAJECTORIES

APPENDIX C URANUS TRAJECTORIES

I. INTRODUCTION AND SUMMARY

A. INTRODUCTION

Aerocapture is a system design technique that utilizes aerodynamic drag to obtain the velocity depletion necessary to obtain a closed planetary orbit from a hyperbolic flyby trajectory. It is accomplished through an aerodynamically controlled atmospheric entry during which vehicle L/D is varied to maintain a constant drag. When the required velocity depletion is calculated, the vehicle pulls full lift up and exits the atmosphere. The Aerocapture concept has been analytically demonstrated, at JPL, to provide a significant increase in the quantity of "in orbit" payload for planetary missions.

Generic Aerocapture indicates the utilization of a common aerodynamic configuration for missions to any of several planets. This report describes the results of a generic Aerocapture atmospheric entry study performed by General Electric Re-entry Systems Division under contract to the Jet Propulsion Laboratory of the California Institute of Technology.

The primary objective was to develop conceptual designs of atmospheric entry systems with moderate to high L/D ratios to establish feasibility of aerocapture for missions to Mars, Saturn, and Uranus. Saturn aerocapture will be accomplished by using the atmosphere of Titan to provide the required velocity depletion. To a large extent, the study is based on the experience gained and the results obtained from a previous study, "Mars Aerocapture Vehicle Definition."

The overall study output consists of design concepts of vehicle configurations, structure, thermal protection and controls for the Mars Sample Return (MSR), Saturn Orbiter Dual Probe (SO2P) and Uranus Orbiter Probe (UOP) missions. The design concepts are based on trajectory analyses supplied by JPL and refined at GE-RSD through added simulation of a 'real' control system response. The control implementation utilized the JPL recommended entry trajectory guidance and control approach (i.e., analytic drag control entry guidance and modulated lift vector roll control). In accordance with the scope of the study, the designs were selected to show mission feasibility based on state of the art concepts. System optimization from an analytic or hardware standpoint was not performed.

Emphasis was placed on selection of the aerodynamic configuration; definition of the aerodynamic loads; sizing of the aeroshell structure; selection and distribution of thermal protection materials on the structure; definition of control system concepts; and aerocapture performance verification through flight control simulations.

B. SUMMARY

1. Approach - Based on the results presented in the Mars Aerocapture Vehicle Definition Study Final Report, Ref. I-1, a biconic configuration baseline was selected at the study outset. The basic approach was then to evolve a specific biconic configuration with the required aerodynamics and packaging capability for all three missions; assess its trajectory accuracy over a range of entry conditions and for several control schemes for the baseline SO2P mission; extend the trajectory assessments to the MSR and Uranus missions; and then, based on the environments developed from these trajectories, develop aeroshell and control system design concepts along with system mass properties.

2. Results

a) Aerodynamic Configuration - The two configurations selected in the previous study, Mars Aerocapture Mission, along with two others, were evaluated for the generic Aerocapture mission (Figure III-2 and Table III-2). All configurations had an L/D greater than 1.0 and a C_D greater than 0.4. Configuration 7-6, scaled down to a length of 6.3 meters to meet STS-IUS/SEPS requirements, was initially selected. This configuration provided the maximum payload packaging volume, tended to minimize the nose bend required to trim the vehicle and provided some degree of longitudinal and directional stability. Using the S02P mission as baseline, payload packaging studies at JPL indicated a satisfactory payload arrangement within the aeroshell (Figure VI- 9). Evaluation of the packaging density of this arrangement led to the conclusion that the other three configurations were not suitable for the S02P mission without significant changes to the payload as conceived by JPL.

The payload for the MSR mission is essentially larger than the S02P payload. An additional 3.3 meter long space is available in the STS payload bay since only the IUS is required for this mission. A 3.3 meter conic frustum extension was added to the S02P baseline configuration to accommodate the additional payload (Figure III-3). As conceived, the full 9.6 meter MSR aeroshell is used for aerocapture, and subsequently, the forward 6.3 meter (basic) aeroshell is used to aeromaneuver the Lander to the surface of Mars.

The aerodynamic characteristics, Table III-3 and Figure III-7, of the basic (S02P, Uranus and Mars aeromaneuver) and stretched (Mars aerocapture) aeroshells were calculated for control system simulations and calculation of the thermal environment. In addition, the local pressure distributions over the generic aerocapture vehicle have been predicted at the selected trim angle of attack and provided for use in the structural analysis task.

b) Control System - The roll control system requirements are to provide the required bank-reverse-bank roll control logic and torque (thereby controlling vehicle L/D to maintain a constant drag), and to control roll disturbance torques. The required roll control system accuracy is $\pm$ 25 m/sec variation in exit velocity over the range of entry path angles for Aerocapture. In the initial study, Ref. I-1, a simple dual thrust level, bang-bang system was selected to show mission feasibility. As an extension to this, several other types of control were investigated for the generic Aerocapture system. They included an improved reaction control system using pulse width thrust modulation and two types of aerodynamic control: flaps and a moving mass roll contro . The SO2P Aerocapture vehicle was used as a baseline for these studies. As indicated in Section V of Ref. I-1, most of the required RCS fuel is used o control the roll disturbance caused by a lateral offset between center-of-pressure and center-of-mass (C_2). A mass properties analysis was performed for the SO2P vehicle and results indicated that C_2 could be controlled to 0.6 cm. This offset, along with the aerodynamic characteristics from Section I'I and the mass properties from Section VI were used for the roll control system evaluations.

The results, indicated in Table V-1, show that for the SO2P mission, an RCS system has the highest mass. It should be noted that the system must have a 3-axis RCS for exoatmospheric control and that only 4.5 kg of fuel is required for roll command control. Therefore, the aerodynamic trim control systems (i.e., disturbance torque control only) are the systems to be compared. The significant increase in mass to achieve roll command control is due to the magnitude of the required accelerations. It should also be noted that the RCS pulse system mass represents a theoretical minimum number and the actual system weight may be somewhat higher. The roll control numbers to be compared are:

RCS (PWM)	57.8 kg	
Flaps (trim)	108.5 kg	Includes 4.5 kg for roll commands
MMRC (trim)	65.5 kg	

With a maximum difference of approximately 40 kg, ultimate selection must be based on a more detailed evaluation of payload mass distribution, and aerodynamic complexity of flaps and expendables management. For example, if C_2 increased from 0.6 to 1.6 cm, the mass of the RCS and MMRC (with similar travel) will increase to more than double its value, while the flap mass increase can be minimized by increasing flap deflection. In addition, use of an MMRC roll control on a generic vehicle could impose severe payload packaging constraints.

Entry trajectories were run using the flap roll control system to determine exit velocity accuracy and path angle corridor. The results, presented in Section V, are summarized below:

Mission	Path Angle (deg.)	Exit Accuracy (m/sec)
SO2P (8 km/sec)	23.0 to 33.0	0 to 41
SO2P (13 km/sec)	23.5 to 29.0	-13 to +7
MSR	14.5 to 16.5	- 4 to +5
Uranus	8.0 to 12.0	0 to 40

Trajectory results also provided aerothermodynamic loads and flap hinge moments for determination of the aeroshell and flap design concepts.

The atmospheres used for the trajectory studies were:

SO2P (Titan)	Titan Thin Atmosphere
Mars	Viking 75 Project Mars Engineering Model, M-75-125-3, NASA Langley Viking Project Office
Uranus	Model 212, May 20, 1980 Orton and Appleby To be published - Icarus

c) Thermal Protection System - The TPS material selection is driven by the requirement to minimize the local TPS weight while choosing from contemporary materials. Heat transfer has been calculated for all missions and is summarized in Figure IV-16. As indicated, heat transfer along the windward meridian varies.

from approximately 100 w/cm^2 (MSR) to 2500 w/cm^2 (Uranus). This heat transfer can be as much as a factor of five lower on a side ray and a factor of ten lower on the leeward side. As such, several materials are used on each vehicle. The heat transfer, as indicated in Table IV-1 is a combination of convective and radiative. TPS material selection is based on peak heat transfer and material thickness is based on both heating load and heating time. Carbon phenolic (a high performance ablator) was chosen for the Uranus and SO2P (13 km/sec) peak heat rates while ESM (a low density ablator) performs satisfactorily for SO2P (8 km/sec) and Mars. Lower density ESM, AM and Nomex felt are used on the cooler sections of the vehicles. See Tables V-2 through 6.

d) Structure and Aeroshell - The selected "structure" was again a honeycomb sandwich as in Ref. I-1. Structure thickness and mass have been calculated for all missions and are presented in Figures VI- through and Tables VI - through . The structure sizing was based on launch loads and the distributed dynamic pressure encountered during atmospheric entry. Based on the TPS solutions derived in Section IV, the TPS "maps" of the SO2P, MSR and Uranus missions are indicated in Figures VI

The resulting aeroshell masses, including structure and TPS, are:

SO2P (8 km/sec)	472 kg
SO2P (13 km/sec)	919 kg
MSR	50[illegible] kg
Uranus	987 kg

3. Conclusion - Generic Aerocapture aeroshell and control system design concepts have been developed to allow further evaluation of the mission design concepts. A set of allowable launch masses for a specific mission concept is presented in Table I-1, along with aeroshell and control masses developed in this study.

As indicated the SO2P (8 km/sec), MSR and Uranus missions show positive mass margins. The SO2P (13 km/sec) has a negative margin of 120 kg. Further mission evaluations are required to either decrease entry velocity or change the required payload capability. Also, utilization of new heatshield materials such as PD218 (See Section IV), will significantly decrease the aeroshell mass.

The required exit velocity accuracy of 25 m/sec can be achieved for all missions using either a flap, MMRC or RCS control system.

In general, it is concluded that a generic Aerocapture configuration can be utilized for the studied missions.

The variation in dynamic pressure over the range of mission does not require a large change in structural mass (70 kg, Table VI-18). As a result, identical structures appear feasible for SO2P, Uranus and the Mars Aeromaneuver missions. However, the range of peak heating does cause a large change in TPS mass (670 kg). Therefore, it is recommended that the TPS be designed for the specific mission environments.

Table I-1 Generic Aerocapture Mass Comparisons

Mission	Launch Capability (kg)	Payload (kg)	Allowable Aerocapture System Mass (kg)	Estimated* Aerocapture System Mass (kg)
SO2P (8 km/sec)	2660 (SEEGA)	1500	1160	570
SO2P (13 km/sec)	2400 (SEEGA)	1500	900	1020
MSP	5000	4000	1000	600
Uranus	2400 (10 year mission)	1250	1150	[illegible]
	1800 (7 year mission)		550	

* Includes 100 kg for flaps

II. SYSTEM REQUIREMENTS

A. MISSION DEFINITION

The Generic Aerocapture Atmospheric Entry Study developed Aerocapture system design concepts for three missions : SO.P at entry velocities of 8 and 13 km/sec; MSR at an entry velocity of 5849 km/sec and Uranus at an entry velocity of 30 km/sec. Flight path angles are determined in the study to identify the Aerocapture limits for SO2P and Uranus. The atmospheres used for the entry trajectories are listed in Secti n I. Initial trajectories were supplied by JPL, then further refined at GE-RS using developed vehicle aerodynamics and mass properties and control s stem characteristics. For purposes of this study, an accepted and proven entry trajectory guidance and control approach was used as recommended by JP . The technique is analytic drag control entry guidance and modulated lift vector ro.l control - a completely autonomous method.

B. DESIGN AND PERFORMANCE REQUIREMENTS

Table II-1 presents a summary of the des n and performance requirement for the generic Aerocapture vehicle.

Table II-1

System Design and Performance Requirements

Envelope	
SO2P, Uranus	4.3m diameter, 6.3m length
MSR	4.3m diameter, 9.6m length
Launch Mass	
SO2P	2660 kg (8 km/sec), 2400 kg (13 km/sec)
MSR	5000 kg
Uranus	2400 kg (10 year mission), 1800 kg (7 year mission)
Payload	
SO2P	1500 kg
MSR	4000 kg
Uranus	1250 kg
L/D	1.0 to 2.0
C_D	0.4 to 1.0
Launch Load	6 g axial
	3 g lateral
Control Accuracy	$\pm$ 25 m/sec on ex t velocity

III. AERODYNAMIC CONFIGURATION

A. AERODYNAMIC CONFIGURATION SCREENING APPROACH

The configuration selected for the generic aerocapture vehicle is capable of packaging the required payload, fits within the length and width constraints of the Space Shuttle payload bay, provides a lift to drag ratio between 1 and 2, and a drag coefficient between 0.4 and 1.0. The specific packaging requirements, hypersonic entry performance requirements and aerodynamic characteristic criteria employed in the configuration screening process are outlined in Table III-1.

Several classes of configurations exist that meet the hypersonic performance requirements. These include axisymmetric and elliptical cross section cones, biconics and arbitrary cross section bodies. Generally, the sphere cones are too long to meet the Space Shuttle payload bay length constraint and package the required payloads. The existing aribtrary bodies have been designed with other mission requirements in mind (e.g., subsonic landing capability or higher L/D), and thus, they are geometrically more complex than necessary for this aerocapture/aeromaneuver vehicle. Evaluation of the aerodynamics of elliptical and arbitrary cross section vehicles is more complex than for the axisymmetric vehicles. Elliptical and arbitrary cross section vehicles were not considered because axisymmetric vehicles met the aerodynamic requirements and provide a greater payload volume. The class of configurations that lends itself to the packaging constraints most readily is an axisymmetric biconic with $\Theta_{NOSE} > \Theta_{FRUSTUM}$. These biconics can be trimmed at an angle of attack, simultaneously producing both lift and drag forces to provide maneuvering capability. Trimming can be accomplished by a variety of techniques including c.g. offset, bent nose, aft frustum slice or flaps.

Perhaps the least complex concept is that of a fixed bent nose, which provides a nearly fixed trim angle of attack and the bank to turn steering approach. This concept has been evaluated in detail in several DOD programs and successfully demonstrated in earth entry flight tests. It was thoroughly evaluated for the aerocapture mission and presents a feasible, well characterized, solution. The aerodynamic screening and design procedure employed for this class of maneuvering entry vehicle includes:

- Select a basic body external geometry that accommodates the specified payloads and meets the launch vehicle (shuttle payload bay) constraints.
- Determine variation of basic body C_D, L/D, and aerodynamic center location (X_{AC}, Y_{AC}) with angle of attack and select a trim angle of attack to meet L/D and C_D requirements
- Identify the required basic body center of gravity location to provide adequate yaw stability margin at the trim angle of attack, to minimize yaw angle (β_T) excursions.
- Determine the control surface deflection (nose or flap) required to trim the vehicle (δ) with the selected c.g. location.
- Evaluate pitch stability at the trim angle of attack to determine if adequate pitch stability exists to minimize angle-of-attack excursions.
- Iterate c.g. location, trim angle, control concept, and guidance scheme to obtain acceptable yaw and pitch stability, as required.
- Evaluate lift vector control concepts.

1. <u>Aerodynamic Prediction Techniques and Validation</u> - The GE 3D Flow Field (3DFF) capability has been used to provide accurate and rapid estimates of the aerodynamic characteristics of candidate maneuvering aerocapture vehicle configurations. These techniques have been employed to generate the full set of aerodynamic coefficients for use in the mission/trajectory simulations for the selected configurations. The 3DFF system consists of two primary codes; a 3D Inviscid Code (3IFF) (Ref. III-1) and a 3D Viscous Code (3VFF) (Ref. III-2). The inviscid technique is used to estimate surface pressures and shock shape

for various body geometries, including biconic, triconic and elliptical shapes; asymmetric noses; bent nose bodies and aft slices. The 3VFF design code considers flow features such as mass addition from the thermal protection system, asymmetric boundary layer transition in the pitch and yaw planes, and real gas characteristics. The effects of angle of attack on local property variations, streamline spreading and changes in boundary layer profile derivatives at the wall are included in the code. The induced pressure resulting from the viscous flow is calculated, and the resulting aerodynamic coefficients are computed. These consist of the inviscid flow contributions for forces and moments and the viscous contributions caused by induced pressure and skin friction. It was also used to predict the aerothermodynamic environment of the entry configurations. The aerodynamic data generated using these codes have been verified by extensive ground and flight testing of maneuvering biconic entry vehicles.

2. Vehicle Aerodynamic Coefficient Data Bank - Maneuvering entry vehicle design studies have generated a large aerodynamic coefficient analytical and experimental data bank for conic and biconic bodies with various control surfaces. This data bank covers a range of aft frustum angles, θ_F, from 4 to 8 deg; forward nose angles θ_N, of 8 to 16 deg; nose radius-to break radius ratios, R_N/R_I, of 0.2 to 0.5; break radius-to-base radius ratios R_I/R_B, of 0.2 to 1.0; Mach Numbers 2 to 20; and angles of attack of 0.5 to 21 degrees in air.

The extent of the existing biconic data bank is illustrated in Figure III-1 and compared to the L/D and C_D range specified for the generic aerocapture vehicle. Significant increases in C_D of this biconic family result from slight (2-5 degrees) increases in angle of attack. This effect has been evaluated for the selected concepts. Although some separated flow is expected on the leeward side, the pressures there are quite low; therefore, it is anticipated that the windward pressures dominate and no significant shift in C_D or C_L occurs with separation onset at the higher angles of attack.

The AFFDL/MDAC hypersonic arbitrary body computer program HABP, Reference III-3, has been employed to determine the aerodynamic characteristics of the selected configuration at very high angles of attack (>20 degrees). The HABP results compare quite well with the flow field results in the intermediate angle of attack range where both techniques were used.

B. GENERIC AEROCAPTURE VEHICLE CONFIGURATION SELECTION

Initially a goal was established to utilize a common aerodynamic configuration for the SO2P, MSR, and Uranus missions. A conical frustum extension could be added to the MSR Aeromaneuvering configuration to accommodate the MSR Aerocapture portion of the mission.

The configurations selected in the previous study for Mars Aerocapture Mission feasibility, identified in Figure III-2 as 7-6 and 5-7 (Reference I-1) were considered as major candidates for the generic aerocapture mission. Two additional configurations were evaluated. One configuration, 7-10, exhibited characteristics geometrically in between those two previously selected and a new configuration, identified as 4-4, appeared to provide adequate payload packaging volume with reduced surface area, Figure III-2.

Selected aerodynamic characteristics of these candidate basic body configurations are summarized in Table III-2. To maintain payload packaging flexibility of this generic aerocapture vehicle concept, the configuration that maximizes the payload volume, can package the larger spherical payload at the required aerocapture vehicle c.g. location, and has the further aft c.g. location requirement is the more desirable. These characteristics are also summarized in Table III-2. Configuration 7-6 was again selected as representing the most attractive configuration, given the general missions requirements, Figure III-3. For the MSR Aerocapture mission, a conic frustum extension was added to accommodate the additional payload, Figure III-3. This vehicle is identified in Table III-2 as configuration 7-12.

1. Aerodynamic Characteristics of Selected Generic Aerocapture Vehicle

The aerodynamic characteristics screened to this point are for zero nose bend (since nose bend is usually a second order effect on C_L, C_D, L/D and the required X_{CG}) and a flight medium of air. Calculations have been made for the selected configuration using the 3IFF code to determine the effect of nose bend angle on the axial center of pressure location in the pitch plane and thus determine the nose bend angle required to meet the desired trim angle of attack. These results were originally reported in Reference 1-1 and are presented here in Figure III-4 for completeness, for the freestream conditions typical of initial pull-up in Mars in a flight medium of CO_2. Note that an axial c.g. location of 0.738 L_{apex} with a nose bend angle of 7 degrees results in a trim angle of 20 degrees while maintaining a very adequate (by standard design practice) yaw stability margin of 2.8 percent. Axial and normal force coefficient variations with nose bend angle and angle of attack are illustrated in Figure III-5. Longitudinal stability characteristics for the configuration with a selected nose bend angle of 7 degrees are illustrated in Figure III-6. This configuration provides a pitch stability margin, $\frac{X_{cg}}{L_A} - \frac{X_{ac}}{L_A} = \frac{dC_{Mcg}}{dC_N}$ at the 20 degree trim angle of -0.084 (stable). The force coefficients and moment coefficient derivatives due to pitch and yaw are provided for use in the 3DOF and 6DOF trajectory and control simulations in Table III-3.

For the purpose of this feasibility study, the inviscid aerodynamic characteristics are assumed to be independent of gas composition, an assumption that will be evaluated in the next phase of the program. The inviscid axial force coefficient does not include a contribution due to the vehicle base. The axial force increment identified as $\Delta CA_{viscous}$ consists of increments due to skin friction and induced pressure. For turbulent flow, the skin friction contribution is the dominant contribution, providing 91 percent of $\Delta CA_{viscous}$ for the MSR case. Turbulent flow is to be exp :ted due to the magnitude of the freestream Reynolds Number at pull up, 9×10^{6} based on vehicle length. The total axial force coefficient includes an esti ıte of the base drag increment. The skin friction contribution to $\Delta CA_{viscous}$ i expected to vary with both gas composition and vehicle size, but due to the s ze of the inviscid term will have less than a 10 percent effect on the tota axial force coefficient. These effects have been neglected in this feasibilit study.

An unsteady flow field code exists, Refere ce III-4, to predict the dynamic damping coefficients $C_{mq} + C_{m\dot{\alpha}}$ and $C_{Nq} + C_{N\dot{\alpha}}$ o sphere cone and biconic vehicles. For this feasibility study, however, it is re mmended that a representative value of -0.2/radian be used for both coefficients the 6DOF simulations.

The local pressure distributions over the eneric aerocapture vehicle have been predicted at the selected trim angle of tack and provided for use in the structural analysis task.

2. Aerodynamic Characteristics of MSR Vel cle

Inviscid aerodynamic computations have be made for the Mars Sample Return vehicle employing both the GE 3IFF and the HA codes in CO_2. Solutions were obtained on 3IFF for angles of attack of 10 a 15°, and on HARB for angles of attack up to 25°. At 20° angle of attack, 3I would not produce a solution due to development of local subsonic flow regions in the body shock regime. Axial and normal force coefficients, lift to drag ratio, and axial center of pressure location variation with angle of attack are illustrated in Figure III-7. The axial force coefficient includes an estimate o the base drag and an increment due to skin friction and induced pressure in CO_2, scaled from results of the previous study.

3. Generic Aerocapture Configurations Applicability as Aeromaneuver Vehicle - The aeromaneuver portion of the MSR mission at Mars consists of a controlled lifting entry from close Mars orbit where the aerodynamic characteristics of the generic aerocapture vehicle at lower freestream Mach Numbers must be defined. An examination of the basic body characteristics at $M_\infty = 4$ in air, Reference I-1, indicates an aft movement of the pitch center of pressure ($\alpha = 0.5°$) from the $M_\infty = 20$ case. Using this as an indication of otential yaw center of pressure movement, we would expect this configuration t experience a gain in yaw stability at the lower Mach Numbers. Base dra would also be increasing, thus contributing to a general reduction of L/D.

Predicted axial center of pressure location for the aeromaneuver vehicle is expected to vary somewhat with freestream Mach Number. For a fixed center of gravity location, this results in a predictabl small trim angle of attack variation. This effect is usually greater for the aeromaneuver portion then the aerocapture because of the larger freestream M ch Number range. In additicn, some uncertainty exists in the predicted vehic e aerodynamic characteristics. Typical flight experience has demonstrated a 3 aerodynamic coefficient axial an normal force prediction accuracy of ±10 percen , given the angle of attack. The impact of these uncertainties, along with the eed for real time measurement of L/D, should be addressed in future studies.

4. Generic Aerocapture Vehicle Flap Chara teristics

For purposes of this feasibility analysis, split windward flaps are considered as one technique for providing roll control for the 7 degree bend nose configurations. In order to provide data for estimation of flap actuation requirements, preliminary estimates of hing mo ents generated by the differential flap deflection have been made.

Basic data for this analysis were obtained from wind tunnel data for flaps mounted on a similar forebody. The hinge mome it requirement, C_h, sensitivity to c.g. offset was evaluated for two conditions: 1) for a basic roll moment coefficient, C_{1_δ} capability of 0.002, i.e., th flaps are initially deflected at an angle such that as the flaps are differe tially deflected $\pm$ 1 degree the change in C_1 due to δ_F is 0.00020; (this was a complished at δ_F = 7.0); and 2) for the flaps initially trailing at a δ_F =) or a C_{1_δ} = 0.00009.

Hinge moment coefficients, C_h, are determi ed from the panel load, CN_P, using the following equation:

$$C_h = CN_P \frac{A_F}{A_B} \frac{1}{L_A}$$

where:

A_F - Flap area

A_B - Reference area = ve icle base area

1 - distance from flap eading edge to flap center of pressure (used . 5 L_{FLAP})

L_A - reference length (v hicle aft frustum apex length)

NOTE: A_F/A_B = 0.182

Total Flap Chord = 0.326 D

Total Flap Span = 0.436 D

These hinge moments for an angle of attack of '0 degrees are shown in Figure III-8. Also presented are the maximum flap deflection angles required to provide the necessary roll torque. As would be expected, the large lateral c.g. offsets cause large hinge moments to control torque.

These data and analyses have been used to provide information for the initial feasibility studies for roll control of a bent nose vehicle. Additional analyses would be performed to optimize the roll control scheme. Items to be considered would be nose bend angle, flap geometry, body slice geometry, and possible use of split flaps (located off of the windward ray).

C. SUMMARY

Potential maneuvering vehicle basic body candidates have been screened for the generic aerocapture missions considering the packaging constraints and the desired aerodynamic performance characteristics. A single configuration was selected for the SO2P and Uranus Aerocapture, and MSR aeromaneuver vehicle applications with a conical frustum addition to perform the MSR aerocapture application. These were selected based on meeting the aerodynamic characteristics requirements, ease of packaging the given payloads in the vehicles and the vehicles in the Space Shuttle payload bay, minimizing the nose bend required to trim the vehicle, minimizing the vehicle surface area where possible and providing some degree of longitudinal and directional static stability. Configurations selected are summarized in Figure III-3 with the aerodynamic coefficients summarized in Table III-3 and Figure III-7.

Dominant flow regimes for the aerocapture vehicles is continuum flow with turbulent flow present over most of the vehicle at pull up.

Aerodynamic characteristics defined have considered the inviscid, skin friction and induced pressure effects, although only the inviscid effects are of first order.

Table III-1 Configuration Screening Criteria

Packaging Requirements	Fit within shuttle payload bay MSR Vehicle must package a lander and orbiter SO2P and Uranus Vehicles will package an orbiter and probe(s)
Performance Requirements	$1.0 < L/D < 2.0$ $0.4 < C_D < 1.0$ Both aerocapture and aeromaneuver vehicles are fixed trim
Aerodynamic Criteria	Minimize center of pressure variations with M_∞ Select basic bodies with $X_{CP_{\alpha_T}} \geq X_{CP_{\alpha = 0.5^\circ}}$ Eliminate all basic bodies with $X_{AC} < X_{CP}$ to speed screening.

TABLE III - 2

GENERIC AEROCAPTURE BASIC BODY CONFIGURATIONS

CONFIGURATION NUMBER	θ deg.	θ deg.	R_N/R_I	R_I/R_B	L/D	$C_{D_{TOTAL}}$	R_B (m)	L_A (m)	R_N (m)	$\frac{X_{CP}}{L_A}$ @0.5°	DIAMETER OF PACKAGABLE SPHERE AT REQ'D c.g.(m)
4-4	4	16	0.17	0.76	1.17	0.486	1.09	15.6	0.15	0.760	1.47
5-7	5	10	0.31	0.50	1.65	0.470	0.81	9.25	0.12	0.700	1.07
7-6	7	13	0.20	0.745	1.25	0.432	1.315	10.71	0.196	0.744	1.80
7-10	7	12	0.33	0.50	1.40	0.440	1.08	8.62	0.661	0.712	1.47
[illegible]	[illegible]	[illegible]	0.20	0.57	[illegible]	0.432	1.72	14.00	0.196	[illegible]	

$\alpha = 21°$

$M_\infty = 20$

$\delta_N = 0°$

AIR DATA BANK

Table III-3 Generic Aerocapture Veh cle Aerodynamics Summary

Configuration [illegible]-6

$\alpha = 20^\circ$, $M_\infty = 30$, $Rey_\infty = 3.5 \times 10^5/m$

Force Coefficients CO_2

Flow State	$C_{A_{inv}}$ $P_B = P_\infty$	$\Delta C_{A_{viscous}}$	$C_{A_{total}}$	$C_{N_{inv}}$	$C_{N_{total}}$	Pitch X_{CP}/L_A	C_D	C_L	L/D
Laminar	0.245	0.0158	0.262	0.692	0.690	0.736	0.482	0.559	1.16
Turbulent	0.245	0.0621	0.308	0.692	0.682	0.736	0.522	0.536	1.03

Moment Derivatives

C_{m_α}	C_{n_β}	C_{ℓ_β}	C_{Y_β}	$\frac{\partial C_{m_{C}}}{\partial C_N}$
-2.58^{-3}	$+8.84^{-4}$	-2.43^{-4}	-3.20^{-2}	-8.4^{-2}

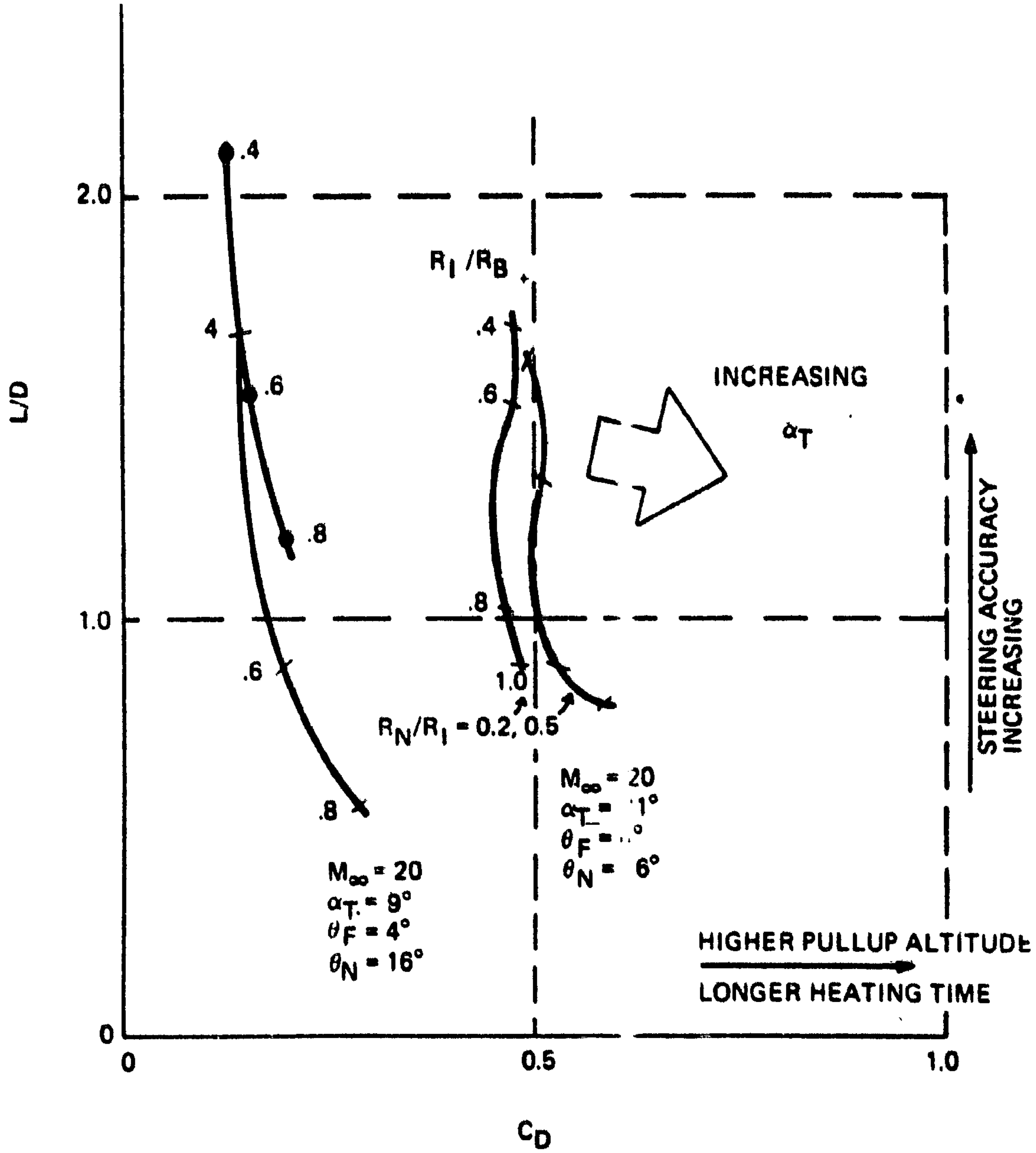

Figure III-1 Existing Bi onic Data Base

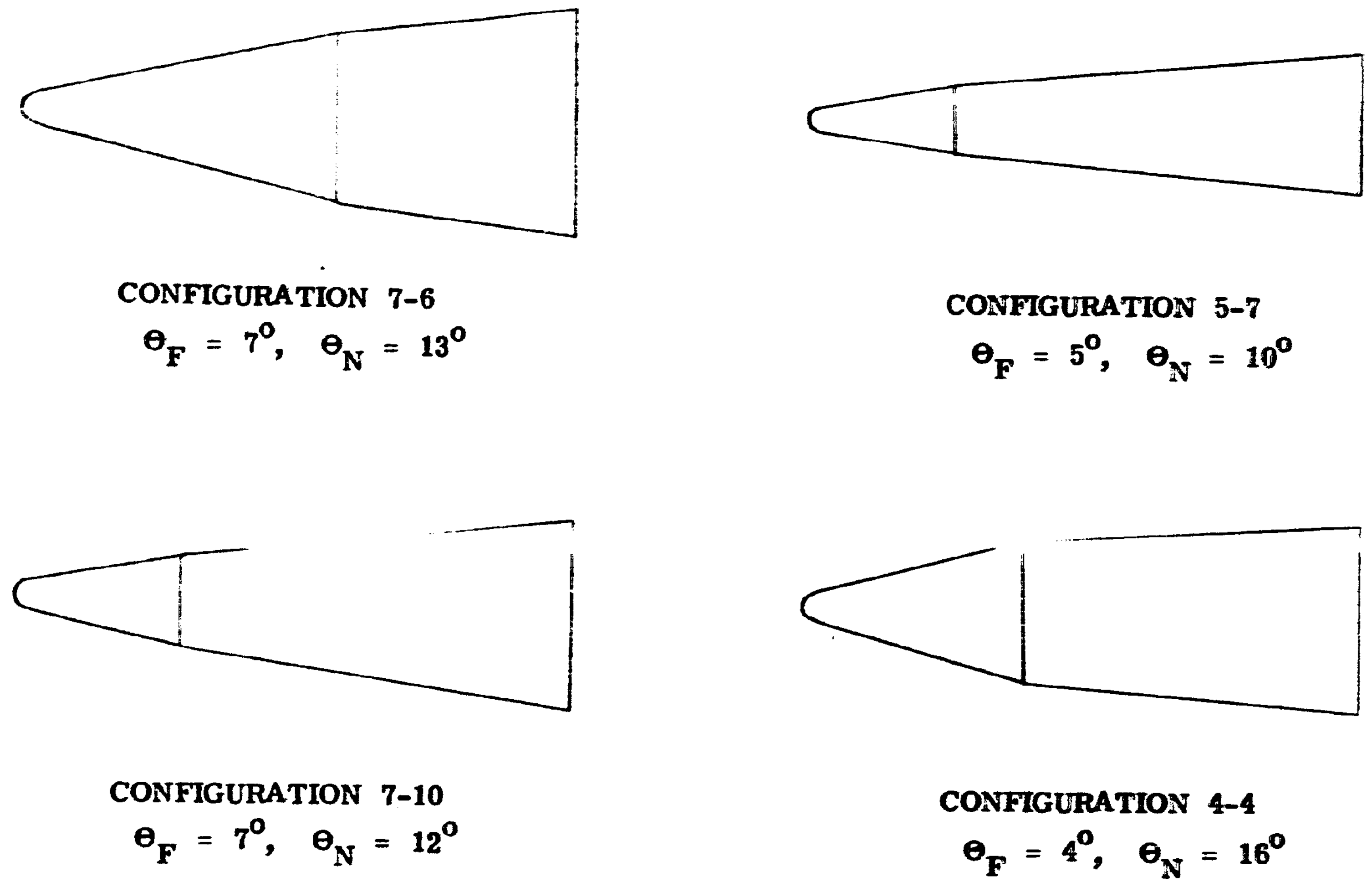

Figure III-2 Basic Body Configuration Candidates

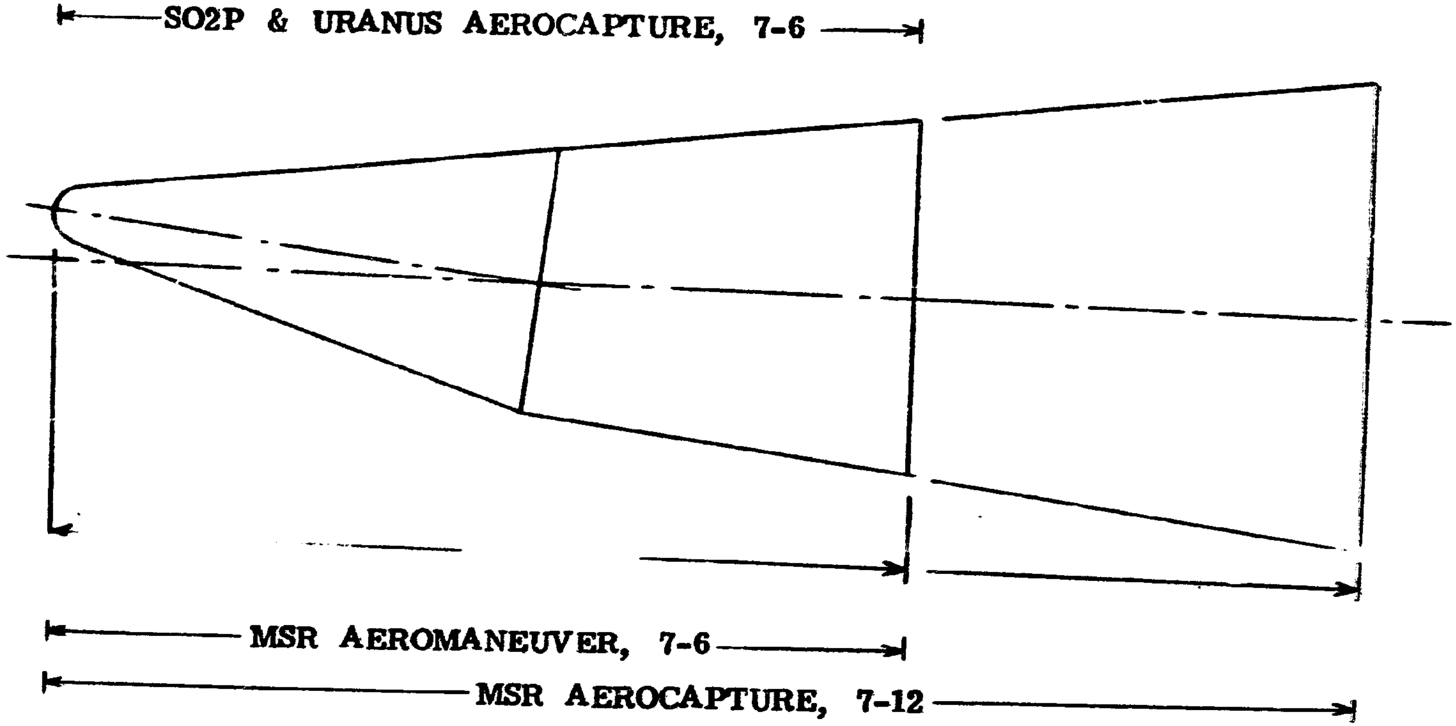

CONFIGURATION	L	θ_F	θ_N	R_N/R_I	R_I/R_B	R_B	L_A	R_I	R_N
7-6	6.3	7^o	13^o	0.2	.745	1.32	10.71	.98	.2
7-12	9.6	7^o	13^o	0.2	.570	1.72	14.01	.98	.2

Figure III-3 Generic Aerocapture Configurations Selected

- NOSE BEND ANGLE OF 7° IS SELECTED TO PROVIDE A TRIMMED ANGLE OF ATTACK OF 20° AT M_∞ = 30 FOR X_{CG}/L_A = .738
- YAW CENTER OF PRESSURE MOVES TO X/L_A = 7.66 for δ_N = 7° PROVIDING 2.8% YAW STABILITY MARGIN

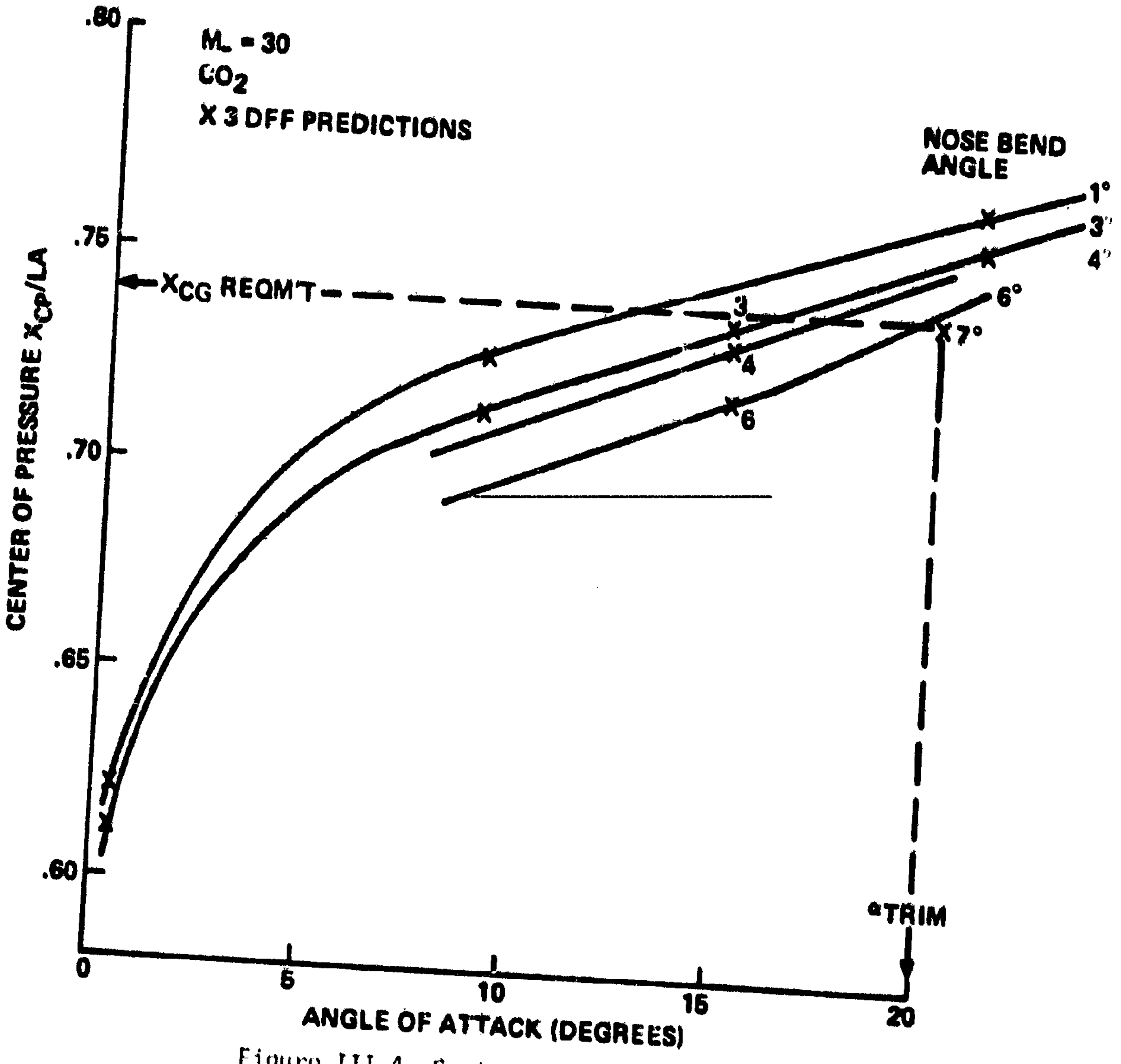

Figure III-4 Center of Pressure Locations for Generic Aerocapture Vehicle

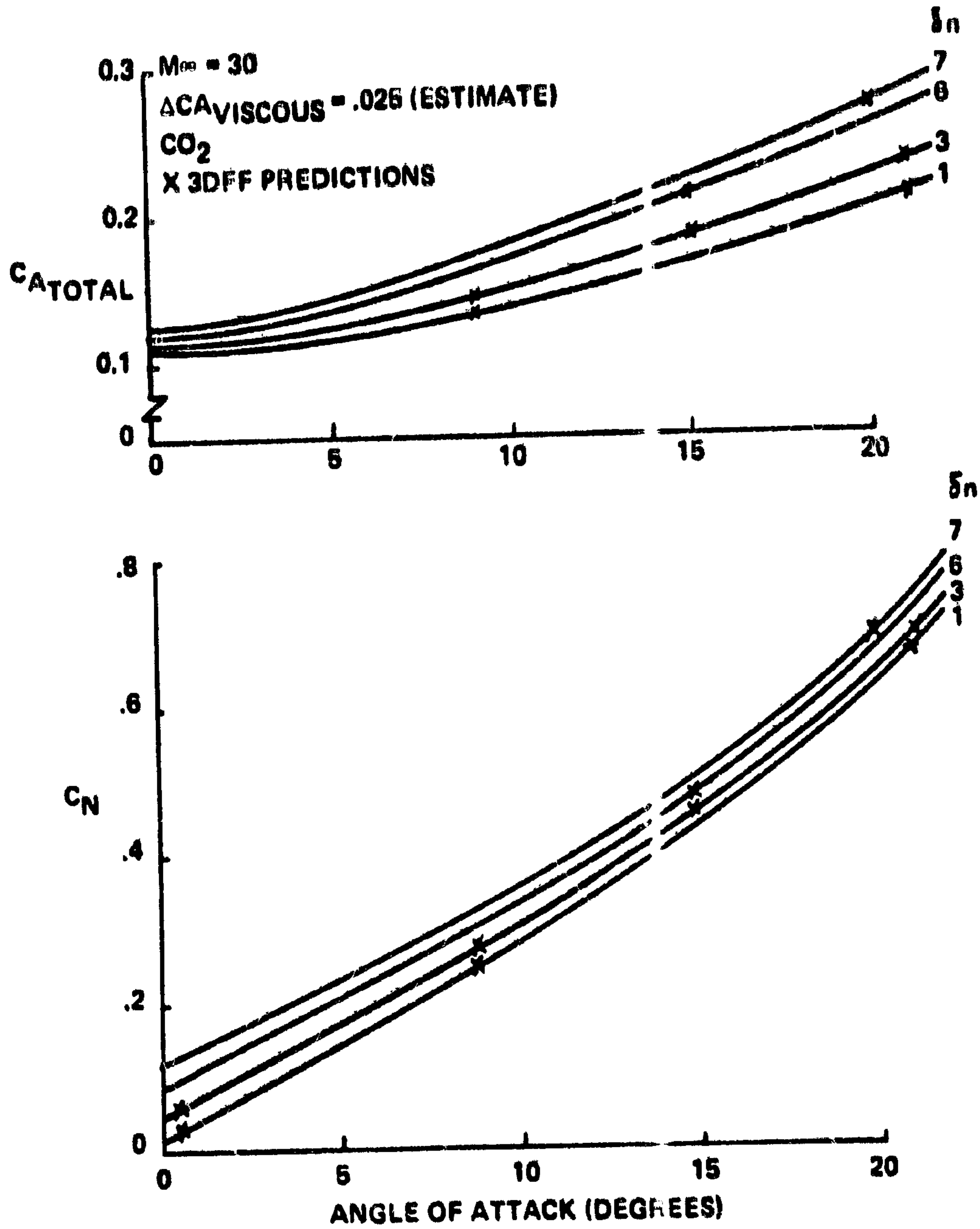

Figure III-5 Effect of Nose Bend Angl on Axial and Normal Force Coefficients of Generic Aer capture Vehicle

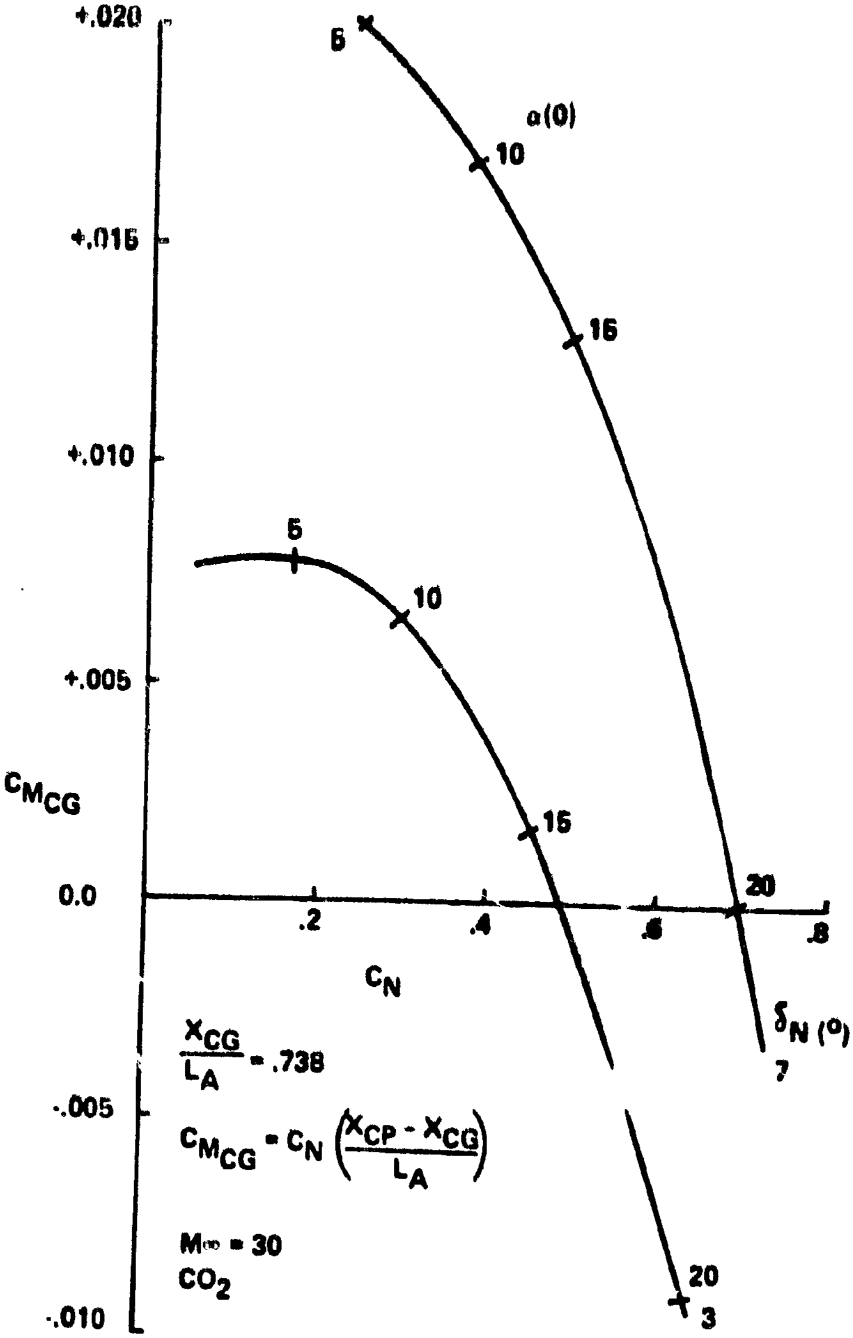

Figure III-6 Longitudinal Stabi ity Characteristics of Generic Aerocaptur Vehicle

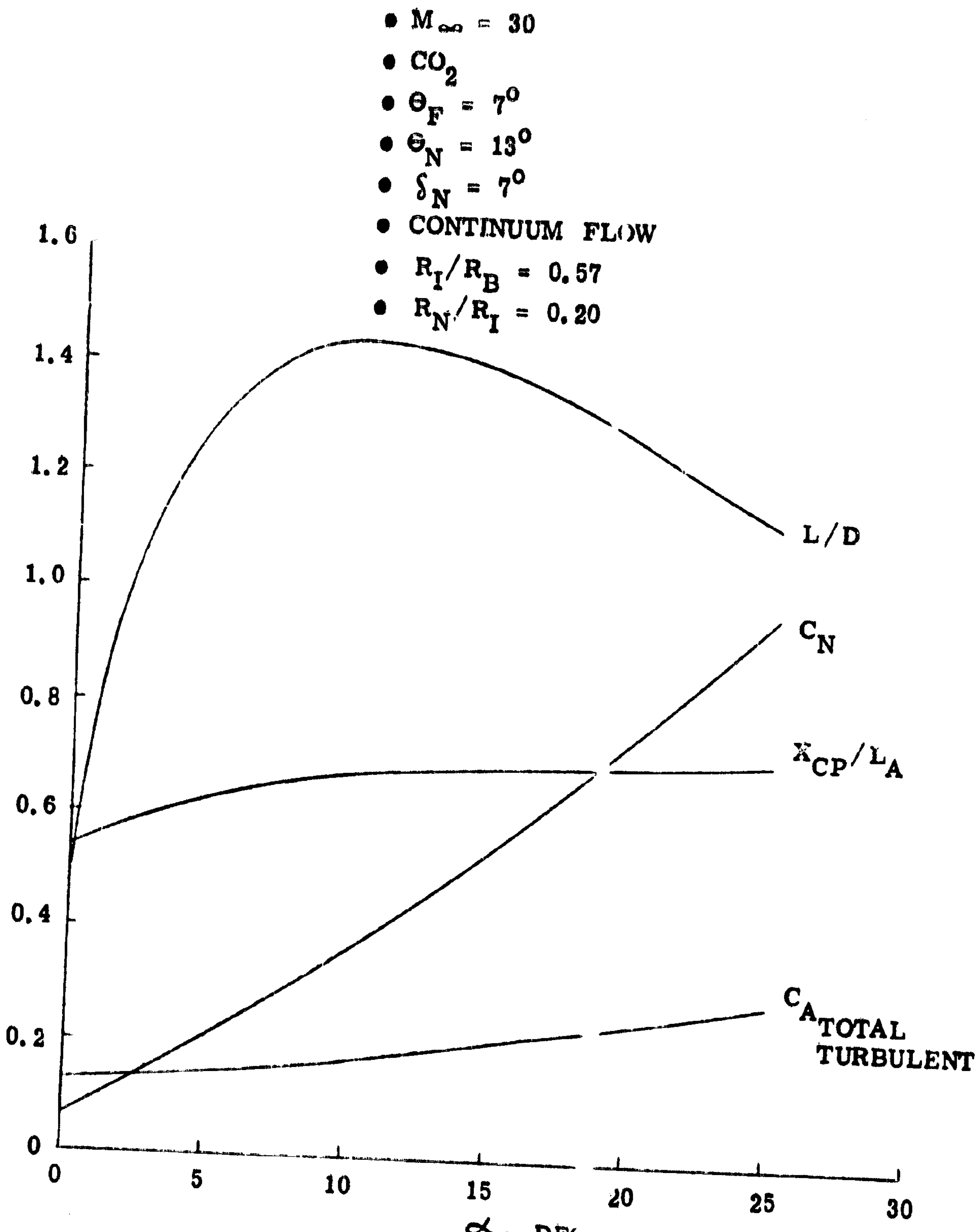

Figure III-7 Aerodynamic Characteristics of Mars Sample Return Vehicle

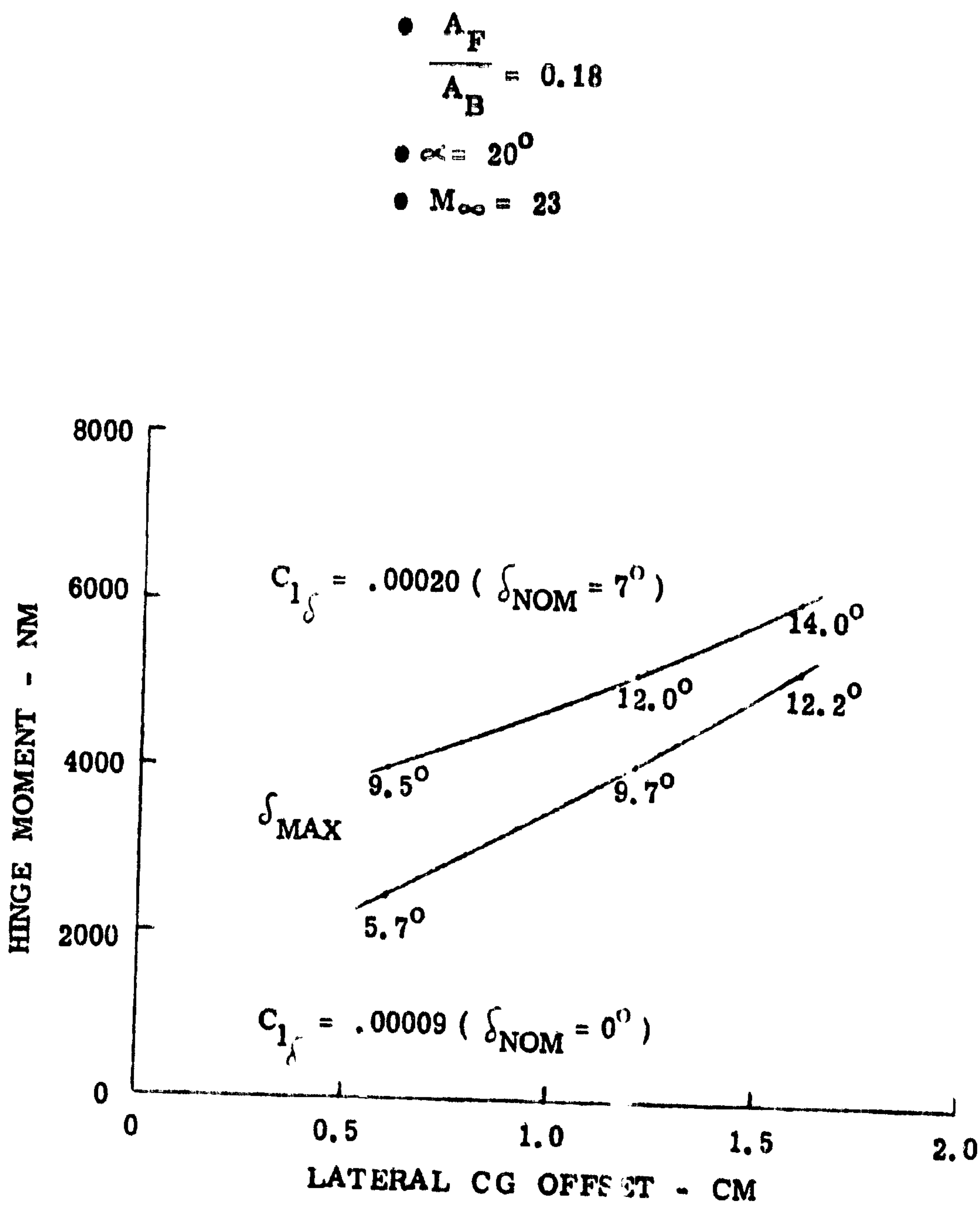

Figure III-8 Sensitivity of Hinge Moment to Center of Gravity Offset

IV. THERMAL PROTECTION SUBSYSTEM

A. AEROTHERMODYNAMIC DESIGN APPROACH

State-of-the-art minimum mass Thermal Prot ction Systems, TPS, that meet all atmospheric entry requirements have been selec ed for the Generic Aerocapture missions. Since the mass of the TPS and its s pporting substructure is a major portion of the aerocapture vehicle, selection f a minimum-mass TPS concept greatly enhances the potential science return enefits of the aerocapture missi n concept.

Reference entry trajectories supplied by J L were used for initial screening of acceptable entry corridors. Employing the redicted aerodynamic characteristics of the selected Generic Aerocapture con igurations, entry trajectories were computed and control simulations conducte as a part of this study. A number of reference heating parameters were simultaneously computed employing engineering correlations for eventual use in sizing the thermal protection systems. Results from the selective calculations of the 3D inviscid and viscous flow field codes were used to establish the shock shape, local pressure, local Reynolds number, and local laminar turbulent f'ow, which results in a significant increase in local heat transfer rates, was based on available flight test transition data correlations analytically scaled to the Aerocapture vehicle geometry. The thermal protection material thi kness was sized to limit the maximum bondline/structure temperature to 600 (590K), a contemporary design practice based on bond strength degradation. ypically, during the period of maximum entry loads, the bond and structure a at room temperature and reach their peaks during the long soak out after th heating period is over and the structural loads are minimal. TPS requiremen were evaluated considering both the shallow and steep ends of the trajectory d a nominal initial temperature of 100°F (310K).

B. CONVECTIVE HEAT TRANSFER DESIGN TECHNIQUES

The convective heating rate distributions to the aerocapture vehicle have been calculated by means of the GE 3D Viscous Boundary Layer Code, 3VFFF (Ref. III-2). This program calculates the Lees/Eckert Reference Enthalpy and Vaglio-Laurin laminar, transitional and turbulent heating rate distributions, as well as skin friction and viscous drag over sphere-cone and biconic configurations at angle of attack. The code uses integral boundary layer techniques, including entropy swallowing effects, along boundary layer edge loci computed on the basis of the local pressure gradient. The inviscid flow field pressure and shock shape are obtained from data generated by the GE 3D Flow Field Program (Ref. III-1), 3IFF.

Comparison of the 3VFF heating predictions with wind tunnel data in air is shown in Figure IV-1 for a representative biconic geometry for $M_\infty = 12.0$. Vaglio-Laurin local heating distributions were used in these predictions and in all aerocapture vehicle frustum heat protection analyses. The good agreement shown in this figure is typical and thus verifies the prediction techniques for the biconic class of configurations that will be used as baseline in this study. Local convective heat transfer distributions have been computed at conditions representative of peak heating in CO_2 and are illustrated in Figures IV-2 and IV-3.

1. <u>Atmosphere Models</u> - Atmospheric density and speed of sound variations with altitude were provided by JPL and are present in Figures IV-4 and IV-5 for the various planets.

2. <u>Reference Laminar Stagnation Point Heat Transfer</u> - The Reference laminar stagnation point heat transfer rate in CO_2 at the stagnation point of a hemi-shperical nose can be approximated by:

$$\dot{q}_s = 1.156 \times 10^{-5} (H_R - h_w) \sqrt{\frac{P_S}{R_N}} \left[\frac{W}{cm^2}\right]$$

where: P_S in Atm.

R_N in m

H_R, h_w in J/KG

This approach was selected after comparing the available hypersonic ground test data in CO_2 to theoretical and semi-empirical approaches suggested by various investigators, Ref. IV-1, and to our 3D viscous flow field solutions in 100% CO_2 employing Lees' solution, Figure IV-6. Estimates of the laminar stagnation point heat transfer in CH_4 were also computed with the above expression.

The reference laminar stagnation point heat transfer rate in 89% H_2 - 11% He (by volume) can be approximated by:

$$\dot{q}_s = 3.50 \times 10^{-6} (H_R - h_w) \sqrt{\frac{P_S}{R_N}}$$

This approach was selected for consistency with the CO_2 results and after examining results presented by Moss for Jovian entry, Ref. IV-2, Figure IV-7

3. Reference Maximum Turbulent Heat Transfer Rate - For the range of planetary entry conditions considered, transition to turbulent flow will occur prior to peak heating as far forward as $X/R_N = 3$, except for the shallow Titan entries where it occurs after peak laminar heating (Figure IV-21). Vehicle shape, angle of attack, and free stream density and velocity are the first order parameters affecting magnitude of the turbulent heat transfer rates. Gas composition is expected to be a second order effect for CO_2 and CH_4.

The reference turbulent heat transfer rate in CO_2 is taken as the maximum value of the turbulent heat transfer rate occurring on a hemispherical nose at zero angle of attack. It can be shown that this maximum occurs at about 33° off the stagnation point, assuming a modified Newtonian pressure distribution and can be cast in terms of the free stream conditions, Ref. IV-3, as:

$$\dot{q}_T R_N^{0.2} = 1.943 \times 10^{-7} \rho_\infty^{0.8} V$$

The constant has been increased for air by a factor of 1.24 to bring the estimate into line with air results from the 3VFF code. Estimates of the reference turbulent heat rate in CH_4 were also computed with the expression above.

The reference turbulent heat transfer rate to a hemisphere in 89% H_2 - 11% He is approximated by:

$$\dot{q}_T R_N 0.2 = 6.15 \times 10^{-8} \rho_\infty^{0.8} V$$

The constant in this equation was selected after examination of the non-blowing turbulent heat transfer results presented by Moss for Jovian entry, Refs. IV-4 to IV-6.

4. Turbulent Leeward - Turbulent leeward heating data in air for spherically blunted cones at angle of attack has been reviewed by Nestler, Ref. IV-7. He concluded that leeward turbulent heating levels are less than zero angle of attack values and are relatively independent of freestream Reynolds Number, approaching a $\frac{h}{h_{\alpha = 0}} = .3$ for α/θ_c values greater than about 2. Typical α/θ_c values of this study range from about 3 to 4 for the aft cone. This value of $\frac{h}{h_{\alpha = 0}} = .3$ was used throughout this study, independent of gas composition and angle of attack. This is considered a reasonable approach at this stage of evaluation, since the leeward heat protection weight is much less than the windward.

C. RADIATIVE HEAT TRANSFER

The Pioneer Venus and Galileo Programs have provided recent impetus for the development of full viscous shock layer solutions for the radiative heat flux distribution on sphere cones, Ref. IV-8 and IV-2, as well as more approximate techniques, Refs. IV-9 and IV-10. Design studies have previously been completed using these techniques in both CO_2 and H_2 - He mixtures and reported in Refs. IV-5, IV-11, and IV-12. For this initial assessment of radiative heat transfer rates experienced by the Generic Aerocapture vehicle, engineering correlations consistent with results produced by these more comprehensive codes have been employed to establish approximate radiative heating levels.

1. <u>Stagnation Point Radiative Heat Transfer</u> - The radiative heat transfer calculations in CO_2 are based on the non-adiabatic shock layer results of Page and Woodward, Ref. IV-13, which is an extension to the Venus atmosphere of a theory previously applied to earth entry, Ref. IV-14. In order to facilitate design calculations, the radiative heating levels given in Ref. IV-13 as Table 1 in terms of re-entry velocity, stagnation to reference pressure ratio, and shock layer standoff distance have been correlated, Ref. IV-15, by separating the results into three velocity regimes. The equation defining this correlation is:

$$\dot{q}_{R_{NA_0}} = \lambda \ (p)^{1.16} \left[\frac{V_\infty}{10^4}\right]^{\sigma} \delta o^{0.56} \quad (W/Cm^2)$$

where:

$\sigma = 19.2, \lambda = 6.2(10^5), V_\infty \leq 7000$ m/sec

$\sigma = 4.1, \lambda = 2(10^2), \quad 7000 \leq V_\infty \leq 10{,}000$ m/sec

$\sigma = 9.12, \lambda = 2(10^2), \quad 10{,}000 \leq V_\infty \leq 13{,}000$ m/sec

p = local pressure in atmospheres

δo = shock standoff distance in centimeters

Although the usually accepted value of the exponent of adiabatic shock standoff distance is 0.6, a value of 0.56 appeared to give a slightly better comparison with the results of Page and Woodward. Figure IV-8 is a plot of the radiative heat flux calculated using the correlation equation vs. the values given in Ref. IV-13. The radiative rates of Page and Woodward were used since they are the most recent complete parametric results available, and because the results of previous analyses, such as those of Wolf and Spiegel, Ref. IV-16, were no in a form suitable for ease of computation, or did not include the important CO (+4) contribution to the heating rates in a carbon dioxide atmosphere.

Since the published Page and Woodward radiative heating rates are for a non-adiabatic shock layer, no correction factor was necessary to account for non-isothermal effects. This correlation of the Page and Woodward results has been applied to several Pioneer Venus design cases and compares favorably, Figure IV-9, to the more complete calculations reported by Brewer, Ref. IV-12, employing the computational technique developed by Falanga and Olstad, Ref. IV-9.

Also of concern is the effect of shock layer cooling on the convective heating. Figure IV-10 presents a plot of the stagnation point convective heating results of Page and Woodward compared to the stagnation point rates predicted by the methods of Zoby, Ref. IV-17, Marvin and Deiwert, Ref. IV-18. Note that the Page and Woodward results are for 90%, CO_2, 10% N_2, while the other theories are for 100% CO_2. Also, the Marvin and Deiwert results are calculated using their simplified equation (Equation 11, Ref. IV-18). No significant difference due to shock layer cooling is indicated by the results of Figure IV-10.

The radiative heat transfer calculations in He - H_2 mixtures are based on a correlation of the Project Galileo stagnation point results reported by Brewer, Brant, and Fogaroli, Refs. IV-10 and IV-11. The Galileo results were generated based on the viscous shock layer solutions of Moss, Ref. IV-2, for the radiative flux distribution along the surfaces of large angle sphere cones and hyperboloids and the tabulated matrix of precalculated RAD/EQUAL code results of Nicolet, Refs. IV-19 and IV-20. The correlations of the Project Galileo results is modeled after that suggested by Stickford and Menard, Ref. IV-21, for a 61% H2 - 36% He - 3% N_e mixture and takes the form, Figure IV-11, of:

$$\dot{q}_{R_{A_0}} = \lambda \rho_\infty^{1.23} \left(\frac{V_\infty}{10^4}\right)^\sigma \delta_o^{0.56}$$

Based on the results presented in Ref. IV-10, he radiative heating can be expected to be a factor of two higher for the eavy atmosphere (78% H_2) and bout half the nominal value for the light atmospher (100% H_2).

Hypersonic radiative heat transfer results in CH_4 are not yet available, and generation of them was beyond the scope of thi study. For purposes of esti ating the radiative ~~heat transfer~~ transfer from radiating CH_4 the CO_2 correlation was empl yed. Preliminary results of computations in radiati g CH_4-N_2 mixtures, Ref. IV-3?, indicate this to be a reasonably conservative pproach.

2. Shock Stand Off Distance - The shock s and off distance around the ntry probe is obtained from an exac General Electr c flow field calculation in 100% CO_2. This calculation technique has been well validated in air, e.g., see Ref. IV-22. The full shock shape employed is show in Figure IV-12. The stagna on point adiabatic shock stand off distance is c pared in Figure IV-13 to Serb n, Ref. IV-23, and Li-Geiger, Ref. IV-24, relatio ships for predicting the sho stand off distance in air. The flow field res lt favors the Li-Geiger rela on-ship. Ridyard and Storer demonstrated in Ref. IV-25 that for values of $\rho_2/\rho_1 > 20$ the Li-Geiger relationship is preferred over Serbin. In addition, Serbin, Ref.

IV-23, and Storer, Ref. IV-26, have recognized that the shock stand off distance can be correlated for various gases with a single parameter, ρ_2/ρ_∞, the density ratio across the shock. Therefore, the agreement of the air and CO_2 results is not surprising. This correlation was used to estimate the shock stand off distance in the CH_4 and H_2-He mixtures.

3. Radiative Heating over the Skirt - For purposes of this study, the radiative heating over the conical section of the vehicle has been estimated from a review of the sphere cone distributions reported in Figure 5 of Ref. IV-10 for H_2 - He mixtures and in Figure 8 of Ref. IV-12 for CO_2. Employing a tangent cone approach, the equivalent cone angle of our forward frustum is 40° at α = 20°. This results in the radiative heat flux dropping to about 20% of the stagnation point value at $X/R_N > 2$.

D. ABLATIVE MASS LOSS

Several specific materials, representing general classes of ablators, were evaluated for generic aerocapture mission applications. For the milder heating experienced by the MSR and some areas of the SO2P, thermally efficient, shape stable charring ablators are attractive. These ablators include ESM 1004X-NS, ESM 1004AP and SAM. The ESM's are of the foamed silicone elastomer family which have a tailorable density. The 1004X-NS and 1004AP have densitiies of 240 and 580 kg/m^3 and are shape stable to heat flux levels of 85 and 90 W/cm^2. SAM, a derivative of Silica RSI, is expected to be shape stable at heat fluxes up to 85 W/cm^2.

For those areas of the vehicle and those missions that receive heat transfer rates above 90 W/cm^2, higher performance ablators that experience char surface recession by melting, vaporization, sublimation, or mechanical scrubbing must be considered. In the heat flux range of approximately 90 to 565 W/cm^2, ESM 1004 LPS

(ρ_V = 880 kg/m^3) will probably provide the lightest weight heat protection option. Performance of this material, in an air environment has been described in Ref. IV-27. Char melting commences at a heat transfer rate of about 90 W/cm^2 and proceeds at higher melt rates as the heat transfer rate is increased. The variation of char mass loss rate with incident heat flux in air is illustrated in Figure IV-14, taken from Ref. IV-27, and is incorporated in REKAP. The mass loss rate is not expected to be affected by the atmospheric gas composition.

As the heat flux increases into the range of 565 to 1130 W/cm^2, materials like phenolic nylon (ρ_V = 1200 Kg/m^3) may be attractive. This material has an attractive thermal conductivity and is nearly shape stable for low values of aerodynamic shear ($\leq$48 N/m^2), Ref. IV-28. For shear levels above 48 N/m^2, the char fails mechanically and is swept away, thus forcing the use of a material like carbon phenolic. Flight and ground test char removal data were evaluated in Ref. IV-28. For aerodynamic shear levels above 48 N/m^2, a correlation of char removal data was made of the form $Q^* = \frac{\dot{q}_{chw}}{\dot{\rho}_{surface}} = f\,(H_R - h_w)$. For values greater than 27.8 MJ/kg (V_E = 7.5 km/sec) $Q^* \rightarrow$ 31.2 MJ/kg. This value has been employed to generate material tradeoffs in this study.

For application in the higher heat flux areas, $\dot{q}$ > 1130 W/cm^2, materials of the carbon phenolic family (ρ_V = 1450 kg/m^3) are usually attractive. The recent activity on the Pioneer Venus and Galileo programs and the many Earth entry scientific and strategic programs have provided a large bank of both analytical and test results. Ablation material surface reactions with the dissociated boundary layer have been modeled for several carbon atmosphere combinations. Carbon ablation in CO_2 was evaluated for the Pioneer Venus program, Ref. IV-2. It was shown that the difference between performance in CO_2 and air is small in the sublimation region and in the diffusion controlled regime the mass loss is about 60% greater in CO_2, Figure IV-15. Carbon ablation in H_2 - He mixtures was evaluated for the Galileo program, Ref. IV-10. In this case, a much greater difference was observed between the air and H_2 - He results, Figure IV-15. Sublimation is seen to commence earlier in the H_2 - He mixture than in air or CO_2 and the wall gas enthalpy, the primary term that controls the carbon surface recession (higher h_w resulting in lower mass loss rates), is seen to be considerably higher for the H_2 - He mixture. Carbon mass loss rates in dissociated CH_4 were unavailable at initiation of this study, and have been recently generated. These results are illustrated in Figure IV-15 for a local pressure of one atmosphere, and have been employed in this study to generate carbon phenolic thermal response and mass loss results.

E. MATERIAL THERMAL RESPONSE

Having determined the heating rates, heating times and time integrated heating loads using the techniques discussed above, TP trade studies have been conducted through use of design correlations derived from the results of the GE Reaction Kinetics Ablation Program (REKAP). The REKAP ablation analysis technique (Ref. IV-29) was developed to provide predictions of the surface recession, degradation and thermal penetration for a variety of materials over a wide range of flight conditions and environments. The program includes the decomposition of a plastic material and the flow of pyrolysis gases through a porous char, the effect of mass addition on aerodynamic heat transfer, surface recession caused by melting and/or vaporization, and the oxidation and vaporization of graphitic type materials. This code has made possible the analysis of numerous materials including the silicone and epoxy elastomers (e g., ESM), carbon phenolic, the family of graphites and carbon-carbon composites, teflon, silica phenolic, phenolic nylon, boron nitrides, quartz, and other silica-based glassy materials like RSI and SAM. The REKAP computer code has been used successfully on a number of ground and flight test programs.

The TPS design rationale for the aerocapture vehicles involves specification of bond and structure thicknesses and maximum allowable temperatures in both bond and structure. In the preliminary vehicle design phase, the heatshield materials have been sized and bonded with 25.4 mm of an RTV silicone elastomer to the structure. The peak bond temperature is limited to 590K with the structure soaking out to a temperature of nearly 590K at a time when loads are low. The TPS is normally selected by review of the heating rates for the range of trajectories considered and usually sized by the larger heating loads of the shallow path angle trajectory.

F. HEAT PROTECTION MATERIAL SELECTION

1. General Considerations - Heat protection material selection is driven by the requirement to minimize the total TPS weight while choosing from contemporary materials. Other materials may become available prior to hardware implementation of the aerocapture vehicle. It has been found that a meaningful parameter to indicate potential range of a materials application is the peak heat transfer rate expected. The variation of the peak heat transfer rate on the aerocapture vehicle forecone on the windward meridian across the entry corridors for the MSR, SO2P and Uranus entry vehicles is illustrated in Figure IV-16. The peak heat transfer rate also varies significantly over the aerocapture vehicle, Figures IV-17 and IV-18, being as much as a factor of five lower than the windward meridian on the side ray location and as much as a factor of ten lower on the leeward side.

2. MSR Thermal Protection Selections - The MSR configuration evaluated is a scaled down version of the Mars Single Mission Aerocapture Vehicle selected in the previous study, Ref. I-1, with a conical skirt extension added to the aft frustum, Figure III-3, for a total length of 1.6M. Reference heat transfer, freestream Reynolds Number, and dynamic pressure were computed during the guidance and control studies and are summarized in Table IV-1.

Following the boundary layer transition onset criteria logic outlined in Ref. I-1, an Earth entry flight derived Re_θ criteria, Ref. IV-30, has been applied to the MSR vehicle. To simplify this study, the local Re_θ boundary layer trip criteria has been translated back to a freestream Reynolds Number. It was determined that for the MSR vehicle, the freestream Reynolds Number that would result in turbulent flow covering most of the windward side of the vehicle would be a 2.2×10^5/meter. A review of the values of Rey_∞ at $\left[\dot{q}_T R_N^{0.2}\right]_{max}$, Table IV-1, indicates that transition to turbulent flow will have occurred prior to the peak of $\dot{q}_T R_N^{0.2}$. Employing techniques described in Section IV-B, heat transfer rate time histories for a representative forward cone body point on the windward meridian (X/R_N = 12.5) have been generated for the range of entry path angles and are illustrated in Figure IV-19. Heat transfer rate distribution over the vehicle at the time of peak heating is illustrated for the steep path angle in Figure IV-17. The general heat protection material selection criteria have been superimposed on this Figure. The parameters that drive the sizing of the heat protection materials are the time integrated heat flux and the heating time. It is seen from Table IV-1 that these parameters are maximum for the shallow path angle entry case. The TPS materials selected from consideration of the peak heat flux values of the steep trajectory, Figure IV-17, have been sized for the time integrated heat flux and heating times experienced during the shallow trajectory. These heat loads and heat protection material requirements are summarized in Table IV-2.

The ablative materials selected are consistent with those selected as minimum weight candidates for the previous Mars Aerocapture Vehicle Definition Study, Ref. I-1, since the peak heat transfer rates, heat loads and heating times are quite similar.

The MSR vehicle requires a thermal protection material on the aeromaneuver vehicle that can function in a reusable mode. It must function during the aerocapture maneuver and then subsequently during the entry maneuver. Low density ablators such as ESM and SAM are expected to be reusable with some small loss of thermal efficiency because of the charring experienced during the aerocapture maneuver. It was found in the previous study that due to the milder entry conditions of the out-of-orbit entry, the heat load was a factor of 5 less and the heating time a factor of 6 less than the aerocapture maneuver. Thus, it is expected that use of the precharred ablator material for aeromaneuver will result in a peak bondline temperature of much less than 590K.

3. <u>SO2P Thermal Protection Selection</u> - The SO2P configuration evaluated is a scaled down version of the Mars Single Mission Aerocapture Vehicle selected in the previous study with a total length of 6.3M. Reference heat transfer, free-stream Reynolds Number, and dynamic pressure were computed during the guidance and control studies and are summarized in Table IV-1.

Following the boundary layer transition criteria logic described earlier for the MSR vehicle, a review of the values of Rey_∞ at $\left[\dot{q}_T R_N^{0.2}\right]_{max}$, Table IV-1 indicates that transition to turbulent flow will occur generally before peak turbulent heating for the steep trajectories and after peak turbulent heating would have occurred for the shallow trajectories. Convective heat transfer rate time histories for a representative forward cone body point on the windward meridian (X/R_N = 12.5) have been generated for the range of entry path angles and are illustrated in Figures IV-20 and 21. Convective heat transfer rate distribution over the vehicle at the time of peak heating is illustrated for the steep path angle cases in Figure IV-18 for an entry velocity of 13 km/sec.

Radiative heat transfer to the stagnation point area in the Methane environment has been estimated, Figure IV-22, employing the CO_2 atmosphere results described in Section IV-C, since results for CH_4 are currently not available. It is seen that for the shallow trajectory, which sizes the heat protection system, the radiative heat flux at the stagnation point, is estimated to be only 17% as large as the convective heat flux for V_E = 13 km/sec. For the purposes of sizing the heat protection system in this study, the total radiative plus convective heat load has been assumed to be 1.25 times as large as the convective heat load. For the slower trajectories at V_E = 8 km/sec, the radiative heating is assumed to be negligible.

The TPS materials selected from consideration of the peak heat flux values of the steep (V_E = 13 km/sec) trajectory, Figure IV-18, have been sized for the shallow trajectory. These heat loads and heat protection material requirements are summarized in Table IV-3.

The materials selected for the high speed entry have also been sized for the low speed, V_E = 8 km/sec, entry. However, consideration of the peak heat transfer rates experienced during the slow speed entry indicates that low density charring ablators could be used over the entire SO2P vehicle and offer a lighter weight heat protection system. The materials selected as providing the lightest weight locally while meeting the constraint of performing adequately for the peak heat fluxes expected for the steep trajectories are identified with their thickness requirement in Table IV-4.

Several tradeoff studies were conducted in arriving at these final selections. Employing the char mass loss models described in Section IV-D, char recession histories were generated for ESM, phenolic nylon, and carbon phenolic for the windward meridian location at $X/R_N = 12.5$, Figure IV-23. It is seen that the ESM experiences nearly 6.8 cm of recession, phenolic nylon about 3 cm, and carbon phenolic a negligible amount in the methane environment. The shape stability of the carbon phenolic is highly desirable, although as currently constructed it is not as good an insulator as ESM or PN.

The thermal response of carbon phenolic when exposed to a typical methane heating environment on the windward meridian of the forward cone has been predicted with REKAP for both 8 and 13 km/sec entries. The predicted surface temperature reached a maximum value of a little over 2200K. This was not sufficient to initiate sublimation, as would be expected from the results shown in Figure IV-15. The carbon phenolic thickness vs. maximum bondline temperature occurring at soak out are illustrated in Figure IV-24. These data were factored into our carbon phenolic thickness requirement data bank for air, and a design correlation for use in heated methane generated for this study.

Carbon phenolic, although attractive as a heat protection material for short periods of intense heating (Figure IV-16 summarizes some contemporary applications) is not a very weight efficient insulator. This can be confirmed from a review of the thermal properties in Table IV-5 and a comparison of the carbon phenolic and low density ablator weights summarized for the 8 km/sec entry of SO2P in Figure IV-25. An experimental development material, PD 218, Ref. IV-31, is a low density carbon foam with excellent thermal properties and adequate structural properties for this application. Thermal response calculations were performed on a carbon phenolic PD 218 composite. The carbon phenolic outer layer is employed to help suppress the surface temperature response and minimize the char mass loss. The PD 218 is employed as a light weight insulator to meet the bondline temperature requirements. The computations indicate that a combination of 5 mm of carbon phenolic plus 4 cm of PD 218 (a combined weight of 13.7 kg/m^2) can replace 3.6 cm of carbon phenolic (51.3 kg m^2). This concept provides the potential for significant weight reduction for the V_E = 13 km/sec SO2P Titan entries.

4. Uranus Thermal Protection Selection - The Uranus aerocapture configuration evaluated is the scaled down version of the Mars Single Mission Aerocapture Vehicle selected in the previous study, Ref. 1, with a total length of 6.3 m. Reference heat transfer, freestream Reynolds Number, and dynamic pressure were computed during the guidance and control studies and are summarized in Table IV-1.

Following the boundary layer transition criteria logic described earlier for the MSR vehicle, a review of the values of Rey at $\left[q_T R_N 0.2\right]_{max}$, Table IV-1, indicates that transition to turbulent flow will always occur before peak turbulent heating.

Convective heat transfer rate time histories for the stagnation point and a representative forward cone windward location where turbulent flow predominates have been generated for the 12° entry path angle case for the nominal atmosphere. Convective heat transfer rate distributions over the vehicle at the time of peak heating is illustrated for the 12° entry case in Figure IV-26.

Radiative heat transfer to the stagnation point area in the 89% H_2 - 11% He mixture have been estimated employing an engineering correlation of Galileo results described in Section IV-C. The convective heat transfer rate dominates the TPS response, Figure IV-27. The stagnation point convective heat transfer rate peaks at 3728 Btu/ft^{2}sec (4213 w/cm^2), the adiabatic non-blowing radiative heat transfer rate at the stagnation point peaks at about 780 Btu/ft^{2}sec (880 w/cm^2), the turbulent heat transfer rate at X/R_N = 12.5 peaks at 2406 Btu/ft^{2}sec (2719 w/cm^2) with the radiative decreasing to about 20% of the stagnation point values at that station. Based on these comparisons, the radiative heating has been considered negligible for this study, although in subsequent design studies it must be included.

With peak heat transfer rates over most of the vehicle being high enough that carbon mass loss will be significant, the first TPS evaluated was all carbon phenolic over all sides of the vehicle. The required nominal ablator thicknesses are summarized in Table IV-6. Some weight reduction might be possible by use of a carbon phenolic - PD 218 composite, where the carbon phenolic thickness is sufficient to cover the expected char mass loss with margin and the PD 218 is used to provide a lighter weight insulation layer.

5. Control Surface Heat Protection

Split windward flaps are being considered as one of the control options, Section V. Typically, these flaps introduce significant flow field perturbations and experience heating rates well above the local approach conditions. The flaps are expected to be deflected at about 5 with a differential deflection from that point of ±5°. This creates an effective total impact angle to the flow of from 27 to 37°. The forecone has an effective impact angle of 40°.

For the purposes of this study, the heat protection requirements for the flaps is assumed to be equivalent to the requirement on the forecone. For SO2P, if the heating to the flaps is a factor of two higher, the flap thermal protection requirements will increase by 30%. If the heating increases by an order of magnitude, the thermal protection requirement will increase by 180%.

G. SUMMARY

Thermal protection materials have been selected and sized for a generic aerocapture vehicle for entry at Mars, Titan and Uranus in the entry corridors defined in the trajectory and control simulation studies described in Sectio V. Hypersonic convective and radiative heat transfer to these vehicles was estimated based on a combination of 3D inviscid and viscous flow field solutions generated for the aerocapture vehicle and engineering correlations developed from the numerous complete convective and radiative heat transfer evaluations conducted in CO_2 and H_2-He mixtures for the Pioneer Venus and Galileo programs.

A summary is presented in Table IV-1 of the peak and time integrated convective and radiative heat transfer rates, the peak dynamic pressure, the freestream Reynolds Number at peak turbulent heating and the heating times computed. I' was concluded that generally transition to turbulent flow is expected to occur prior to peak heating except for the shallow path angle entries into Titan, Figures IV-19, IV-20, and IV-21.

The thermal protection material selection nd sizing is driven by the peak and time integrated heat transfer rates exper nced and the heating times, summarized in Figure IV-16. It is seen that . propriate contemporary mater ls are available ranging from low density ablato for MSR and low speed Titan entry to high performance ablators for Uranus nd high speed Titan entry.

However, the long heating times associated with use of the high performance ablators fall outside the demonstrated capability of current entry vehicle applications and thus need to be experimentally demonstrated.

Thermochemical response of graphitic heatshields in CO_2 and H_2-He mixtures was available from the previous studies; response in a CH_4 mixture was not available, so was generated during this study.

Sizing of the thermal protection system was accomplished by employing design correlations derived from the results of GE RELAP. The nominal thermal protection material requirements for the generic aerocapture vehicle in the several mission applications are summarized in Tables IV-2, IV-3, IV-4, and IV-6. Comparisons between the thermal protection material weight required of representative windward meridian locations are presented in Figure IV-28. For the low speed Mars and Titan entries, low density, near shape stable ablators offer attractive solutions. Low density ablators were selected over a metallic reradiative type or an RSI approach due to the limited reuse required, simplicity of design, the fabrication and applications data base existing and cost. For the 13 km/sec Titan entry in CH_4, carbon phenolic is predicted to be shape stable since there is no oxidation experienced and the peak surface temperature expected is well below the sublimation temperature. A developmental material, PD 218 (a low density carbon foam), used as an insulative layer is shown to reduce the local TPS weight requirement by a factor of 3. For Uranus entry, a high performance ablator such as carbon phenolic is required and experiences some mass loss due to sublimation.

Table [illegible] Summary of Reference Heating Parameters

PLANET	$m/C_D A$ kg/m²	$m/C_L A$ kg/m²	V_E km/sec	γ_E deg.	G_{REF} (g's)	q_{MAX} [illegible]	P_e @ $\dot q_{MAX}$ [illegible]	$\dot q \sqrt{P_e}$ MAX (W/cm²)	$\int \dot q \sqrt{P_e}\, dt$ (W-sec/cm²)	$\dot q^2$ MAX [illegible]	$\int \dot q^2\, dt$ (W-sec/cm²)	$\dot q P_e^3$ MAX (W/cm²)	$\int \dot q P_e^3\, dt$ (W-sec/cm²)	t_{PULSE} (sec)
MARS	977	771	5.36	14.5	1.5	14.5	8E5	76	10300	106	13000	6200	7.2E5	260
				15.5		15.2	8.5E5	82.5	9900	118	12700	6700	7.2E5	250
				16.5		22.0	11.9E5	99	9900	155	12000	9700	7.2E5	270
TITAN	513	546	8.0	23	3.0	15.0	2E5	110	28000	125	27000	5800	13.2E5	420
				28		15.4	2.5E5	145	24200	165	26000	8880	13.3E5	370
				33		22.5	3.8E5	176	22000	228	24700	13000	13.2E5	245
			[illegible]	23	4.0	20.[illegible]	[illegible]	200	47000	180	44500	9300	21.5E5	460
				28		20.5	2.5E5	365	40000	265	42000	14300	21.2E5	310
				33		34.5	5.0E5	[illegible]	35000	440	39500	24700	[illegible]	270
			11.0	23.5		15.9	1.7E5	425	88000	360	81000	15800	97.3E5	420
				26.0		26.5	[illegible]	480	80000	440	76000	30000	77.3E5	350
				29.5		29.0	[illegible]	585	76500	600	76000	29200	53.5E5	290
URANUS	596	527	30.0	8	15.[illegible]	89	5.0E5	1610	1.7E5	1390	1.24E6	1.9E6	15.8E6	200
				12	14.[illegible]	[illegible]	4.3E5	[illegible]	1.5E5	1706	1.18E6	2.4E6	16.0E6	165
				8	[illegible]	133	6.4E5	1776	1.5E5	1746	1.17E6	2.7E6	15.5E6	175
				[illegible]	[illegible]	[illegible]	[illegible]	[illegible]	1.37E5	2184	1.14E6	3.1E6	15.8E6	145

Table IV-2

MSR Thermal Protection System Requirements Summary

Ma.s Entry

V_E = 5859 m/sec

Vehicle Station X/R_N	Peripheral Location (deg.)	$\int \dot{q}_c dt$ ($w \cdot sec/cm^2$)	Flow-State Lam.	Flow-State Turb	Material Selected	Thick. (cm)	Unit Weight (kg/m^2)
2	0	2.30^{+4}	X		ESM1004AP	1.24	7.2
5		2.28^{+4}	X	X		1.24	7.2
18		4.4^{+3}	X	X		0.91	5.3
35.6		1.78^{+4}	X	X		1.19	6.8
49.4		1.24^{+4}	X	X		1.12	6.4
2	90	3.74^{+3}	X	X	SAM	1.83	2.3
5		5.72^{+3}	X	X		1.88	2.4
18		3.33^{+3}	X	X		1.83	2.3
35.6		1.36^{+3}	X	X		1.75	2.2
49.4		1.49^{+3}	X	X		1.75	2.2
5.5	180	1.72^{+3}	X	X	SAM	1.75	2.2
18.5		1.0^{+3}	X	X	Nomex Felt	1.93	1.6
35.6		407	X	X		1.88	1.6
2	90		X	X	ESM1004AP	0.89	5.1
5.5		5.72^{+3}	X	X		0.97	5.6
35.6		1.36^{+3}	X	X		0.71	4.1
49.4		1.49^{+3}	X	X		0.71	4.1

Table IV-3

S02P Thermal Protection System Requirements Summary

Titan Entry

V_E = 13 km/sec

Vehicle Station X/R_N	Peripheral Location (deg.)	$\int \dot{q}_c dt$ (w·sec/cm^2)	Flow - State LAM	Flow - State Turb	Material Selected	Thick. (cm)	Unit Weight (kg/m^2)
2	0	1.97^{+5}	X		Carbon Phenolic	4.45	64.2
5		1.23^{+5}	X			4.06	58.8
18		1.98^{+4}	X			1.85	26.9
31		5.84^{+4}	X			2.92	42.5
5.5	90	4.04^{+4}	X			2.46	35.6
18.5		2.05^{+4}	X			1.88	27.3
31		1.00^{+4}	X			1.45	21.0
5.5	180	1.21^{+4}	X		ESM1004AP	1.40	8.1
25		3.24^{+3}	X		ESM1004X	1.99	4.74
5.5	90	1.04^{+4}	X		ESM1004AP	1.73	10.0
18.5		2.05^{+4}	X	X		1.55	8.9
31		1.00^{+4}	X	X		1.35	7.8

Table IV-4

SO2P Thermal Protection System Requirements Summary

Titan Entry

$V_E = 8$ km/sec

Vehicle Station X/R_N	Peripheral Location (deg.)	$\int \dot{q}_c dt$ $(w \cdot sec/cm^2)$	Flow Lam	State Tur	Material Selected	Thick. (cm)	Unit Weight (kg/m^2)
0	0	5.54^{+4}	X		ESM1004LPS	3.23	28.3
5	↓	4.43^{+4}	X	X		2.77	24.4
18	↓	7.66^{+3}	X	X	ESM1004AP	1.33	7.5
31	↓	2.23^{+4}	X	X	↓	1.55	9.0
5.5	90	1.34^{+4}	X	X	ESM1004X	2.79	6.7
18.5	↓	7.09^{+3}	X	X	↓	2.39	5.7
31	↓	3.42^{+3}	X	X	↓	1.98	4.8
5.5	180	4.02^{+3}	X	X	ESM1004X	2.08	5.0
25	↓	1.09^{+3}	X	X	SAM	1.98	2.5
5.5	90	1.34^{+4}	X	X	ESM1004LPS	2.0	17.6
18.5	↓	7.09^{+3}	X		ESM1004AP	1.27	7.3
31	↓	3.42^{+3}	X		↓	1.12	6.4

Table IV-5

Comparison of Candidate Thermal Protection Materials

Thermophysical Properties

Material	Density kg/m^3	Thermal Conductivity $W/m°K$	Specific Heat (cal/gm K)
Carbon Phenolic	1450	6.4×10^{-1}	0.28
Phenolic Nylon	1200	2.3×10^{-1}	0.41
ESM 1004LPS	880	1.8×10^{-1}	0.31
ESM 1004AP	580	1.48×10^{-1}	0.31
ESM 1004X	240	9.6×10^{-2}	0.36
PD 218*	160	9.3×10^{-2}	0.21
SAM	130	3.1×10^{-2}	0.23
Nomex Felt	83	4.3×10^{-2}	0.49

* A DEVELOPMENTAL MATERIAL

Table IV-6

Thermal Protection System Requirements Summary

Uranus Entry

V_E = 30 km/sec

Vehicle Station X/R_N	Peripheral Location (deg.)	$\int \dot{q}_{c}\,dt$ $(w\cdot sec/cm^2)$	Flow - State Lam	Turb	Material Selected	Thick. (cm)	Unit Weight (kg/m^2)
0	0	5.75^{+5}	X		Carbon Phenolic	4.83	69.8
2		3.32^{+5}	X			3.81	55.2
5		2.2^{+5}	X	X		3.3	47.8
18		4.36^{+4}	X	X		1.65	23.9
31		1.25^{+4}	X	X		2.49	36.1
5.5	90	6.0^{+4}	X	X		1.85	26.9
18.5		3.4^{+4}	X	X		1.52	22.0
31		1.62^{+4}	X	X		1.19	17.3
5.5	180	1.63^{+4}	X	X		1.19	17.3
25		4.9^{+3}	X	X		1.02	14.6

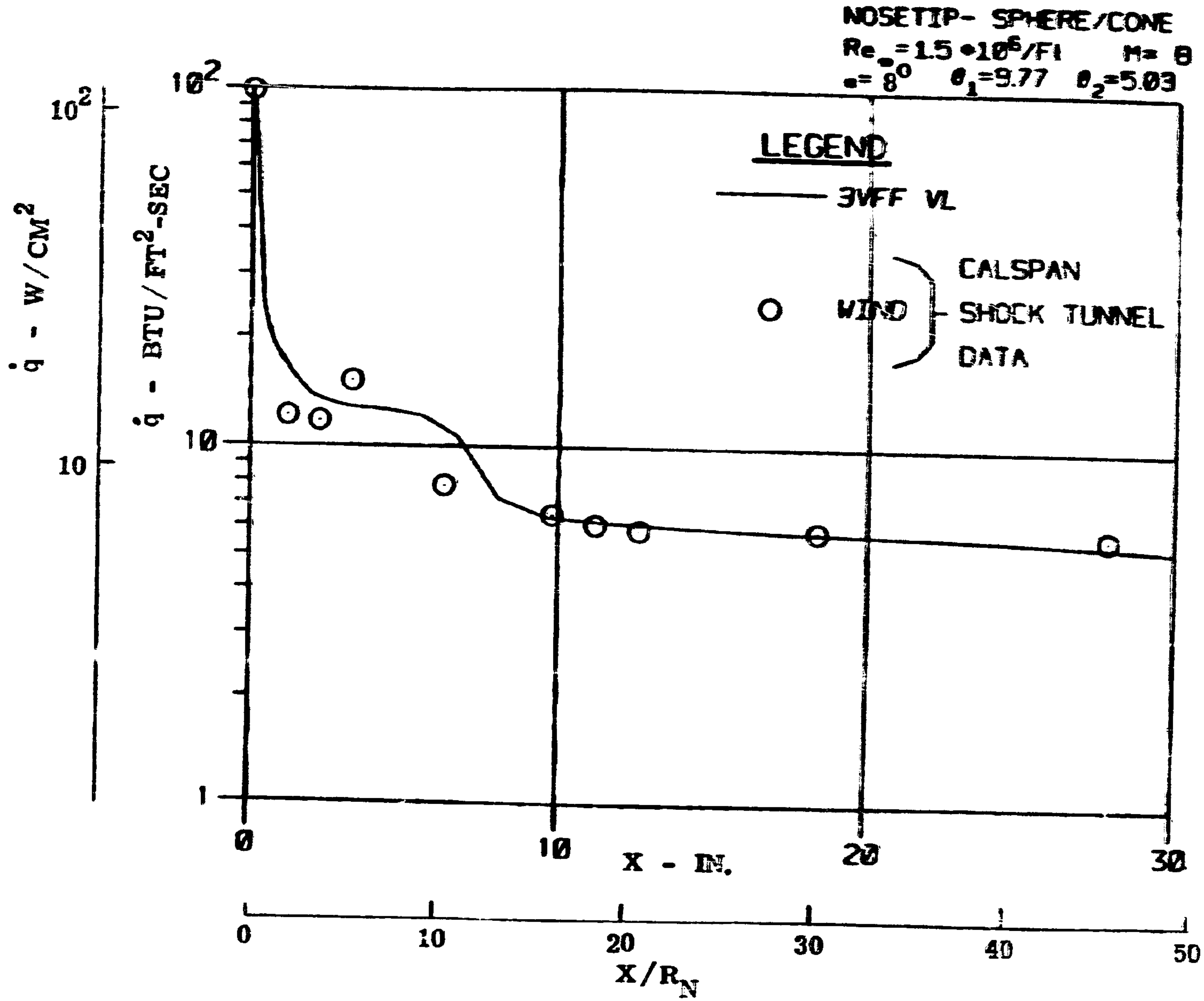

Figure IV-1 Comparison of Predicted to Measured Local Heat Transfer Rate On A Biconic Configuration in Laminar Flow

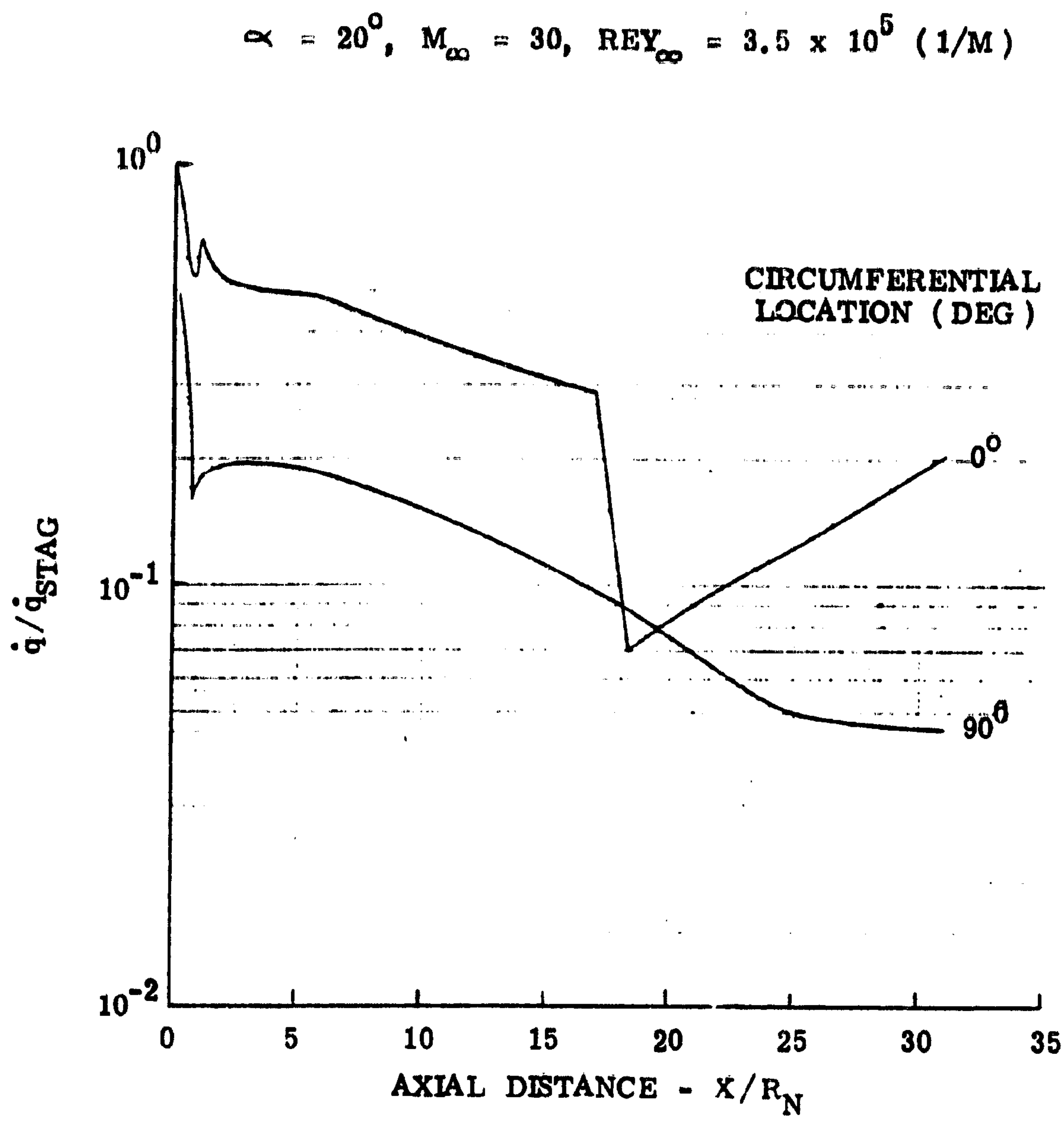

Figure IV-2 Laminar Heat Transf r Distribution on Generic Aerocaptur Vehicle in CO_2

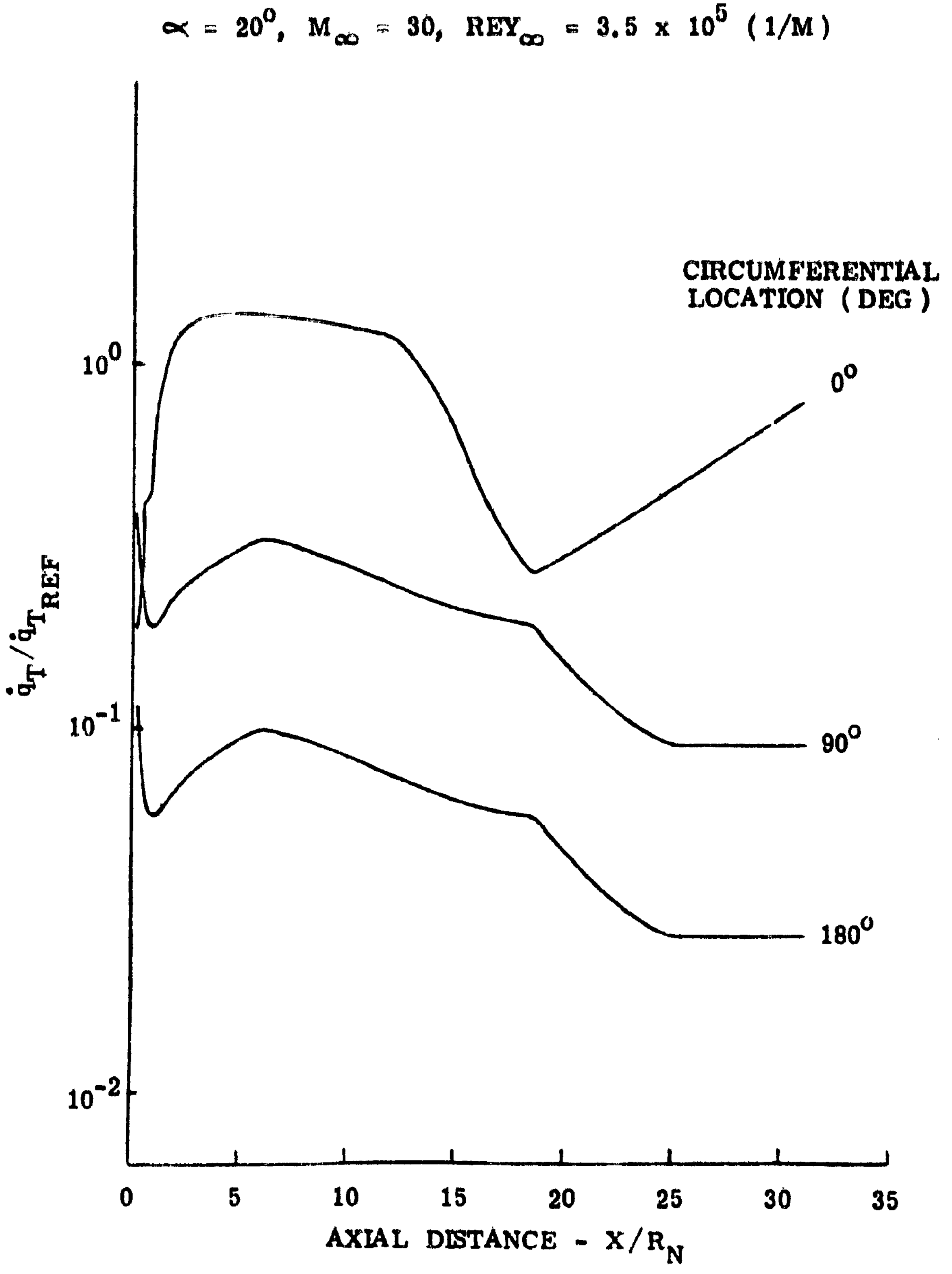

Figure IV-3 Turbulent Heat Transfer Distribution on Generic Aerocapture Vehicle in CO_2

• MODEL 212 MAY 20, 1980
ORTON & APPLEBY
TO BE PUBLISHED - ICARUS

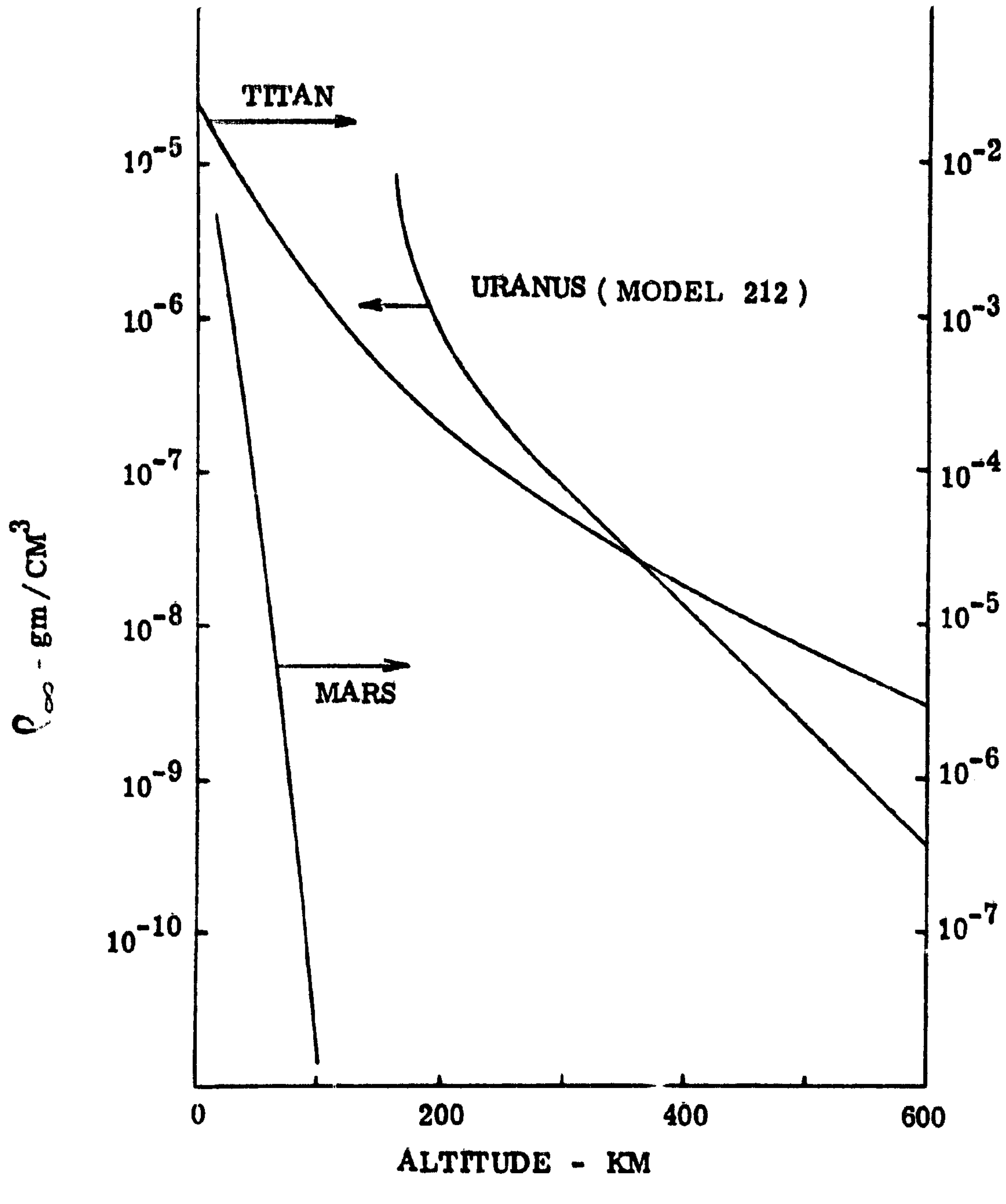

Figure IV-4 Atmosphere Models for Generic Aerocapture

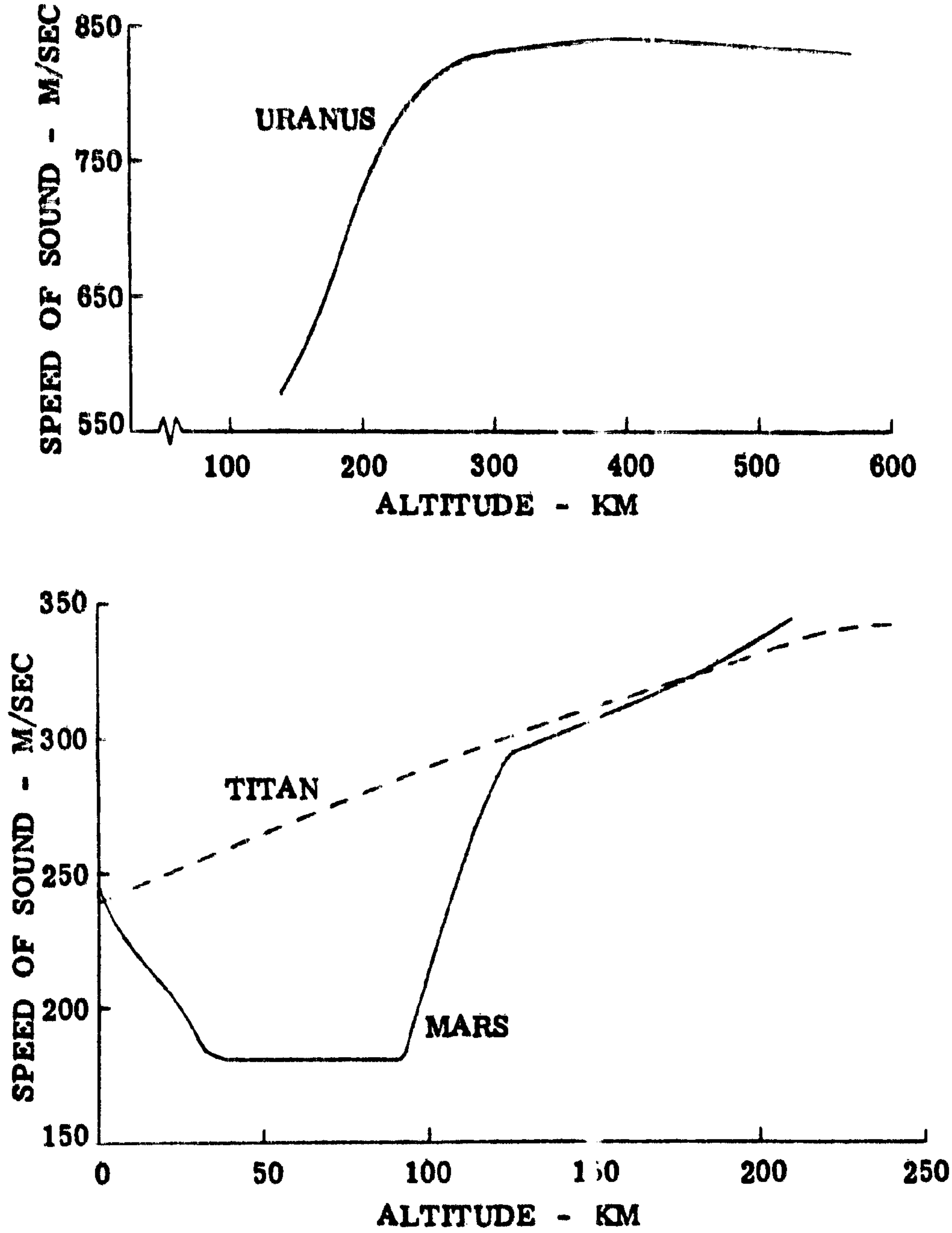

Figure IV-5 Atmosphere Models for Generic Aerocapture - Speed of Sound Variation

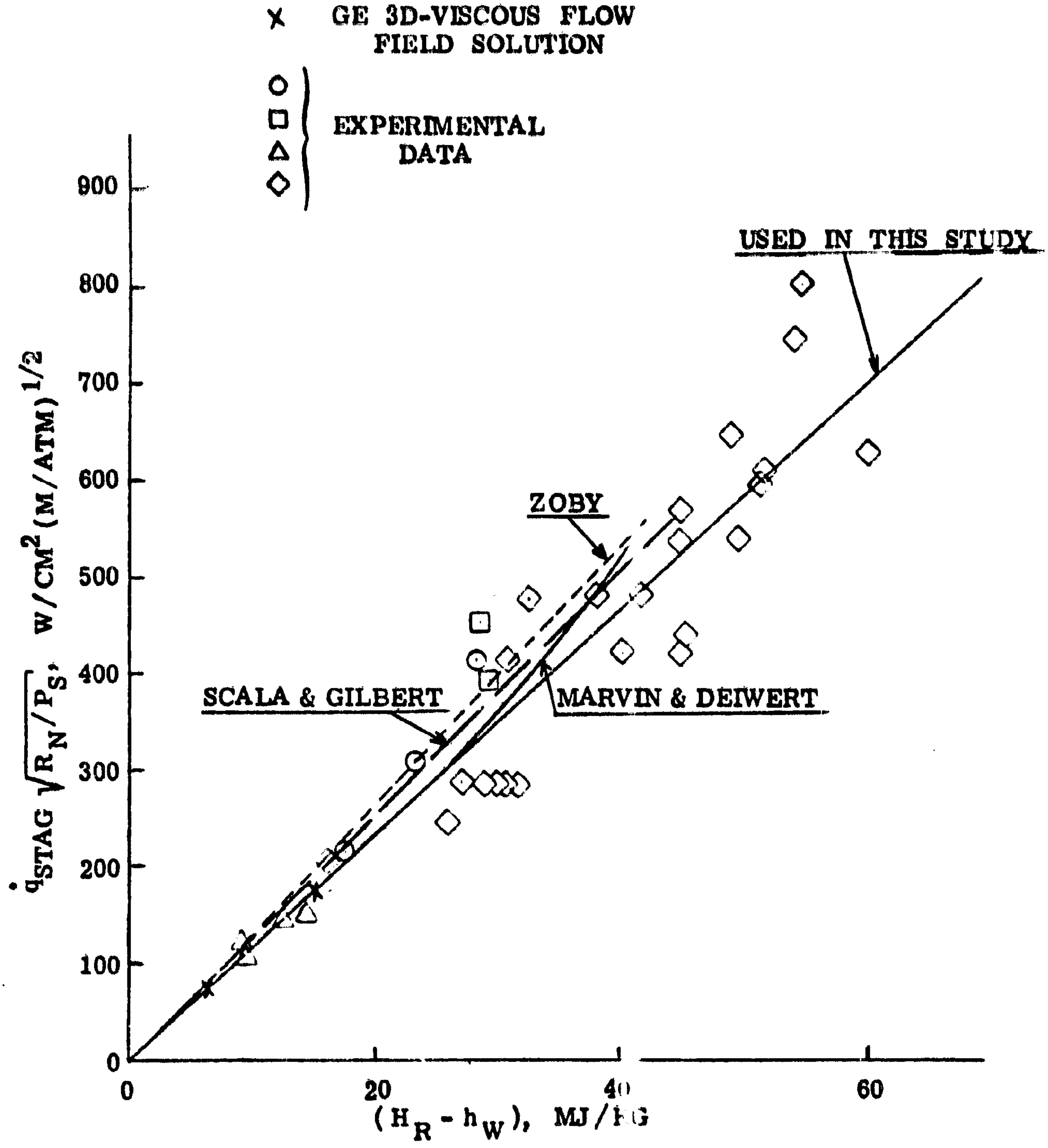

Figure IV-6 Comparison of Available Theories with Experimental Data for Hypersonic Heat Transfer in 100% CO_2

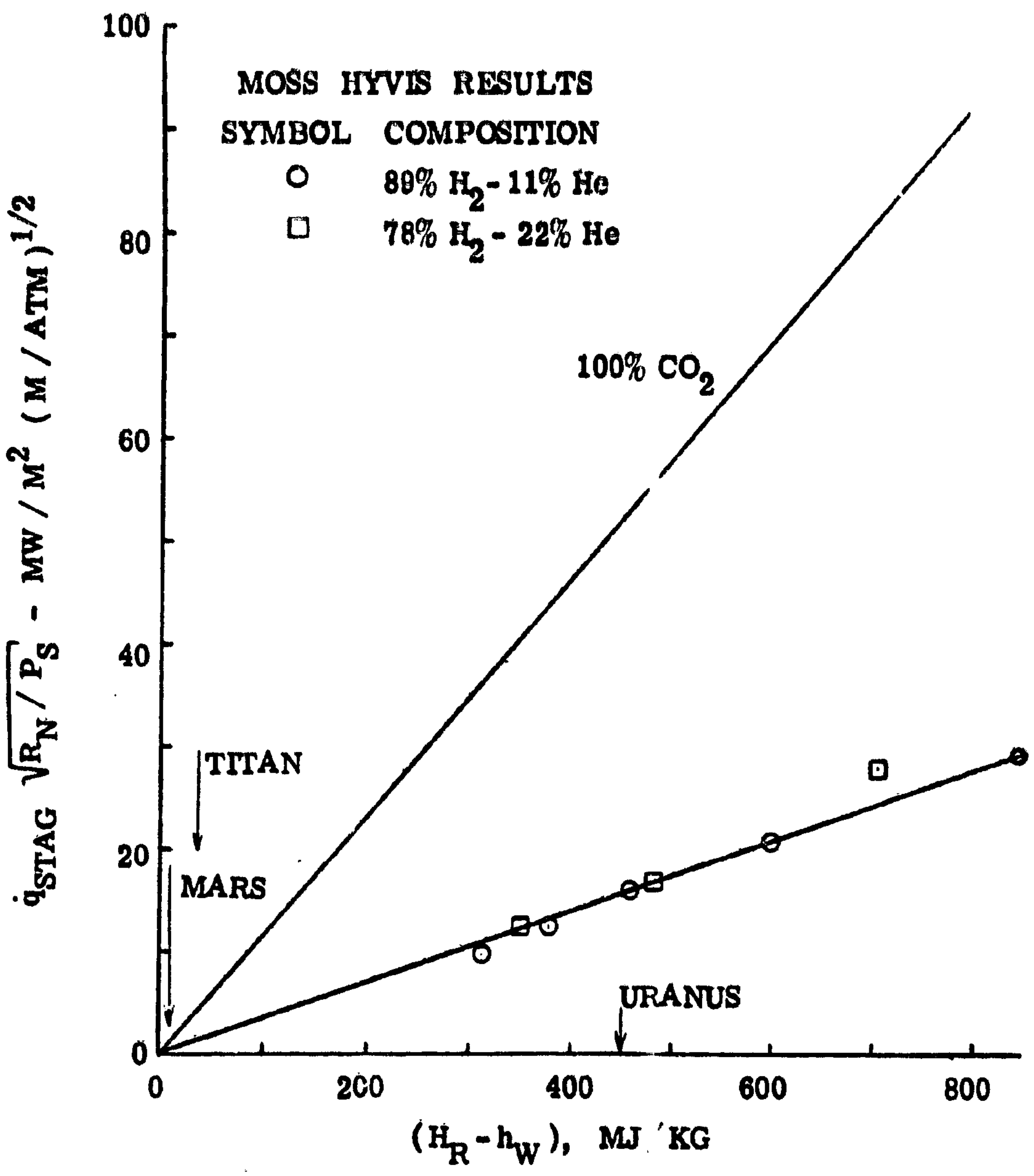

Figure IV-7 Correlation of Hypersonic Heat Transfer Results in H_2 - He Mixtures and Comparison to CO_2

$$\dot{q}_R = \lambda\,(P/P_S)^{1.16}\,(V_\infty/10^4)^{\sigma}\,\delta_S^{.56}$$

$$0.0 < (V_\infty/10^4) < 0.7,\ \sigma = 19.2,\ \lambda = 4.28 \times 10^4$$

$$0.7 \le (V_\infty/10^4) \le 1.0,\ \sigma = 4.1,\ \lambda = 2 \times 10^2$$

$$1.0 < (V_\infty/10^4) \le 1.3,\ \sigma = 9.12,\ \lambda = 2 \times 10^2$$

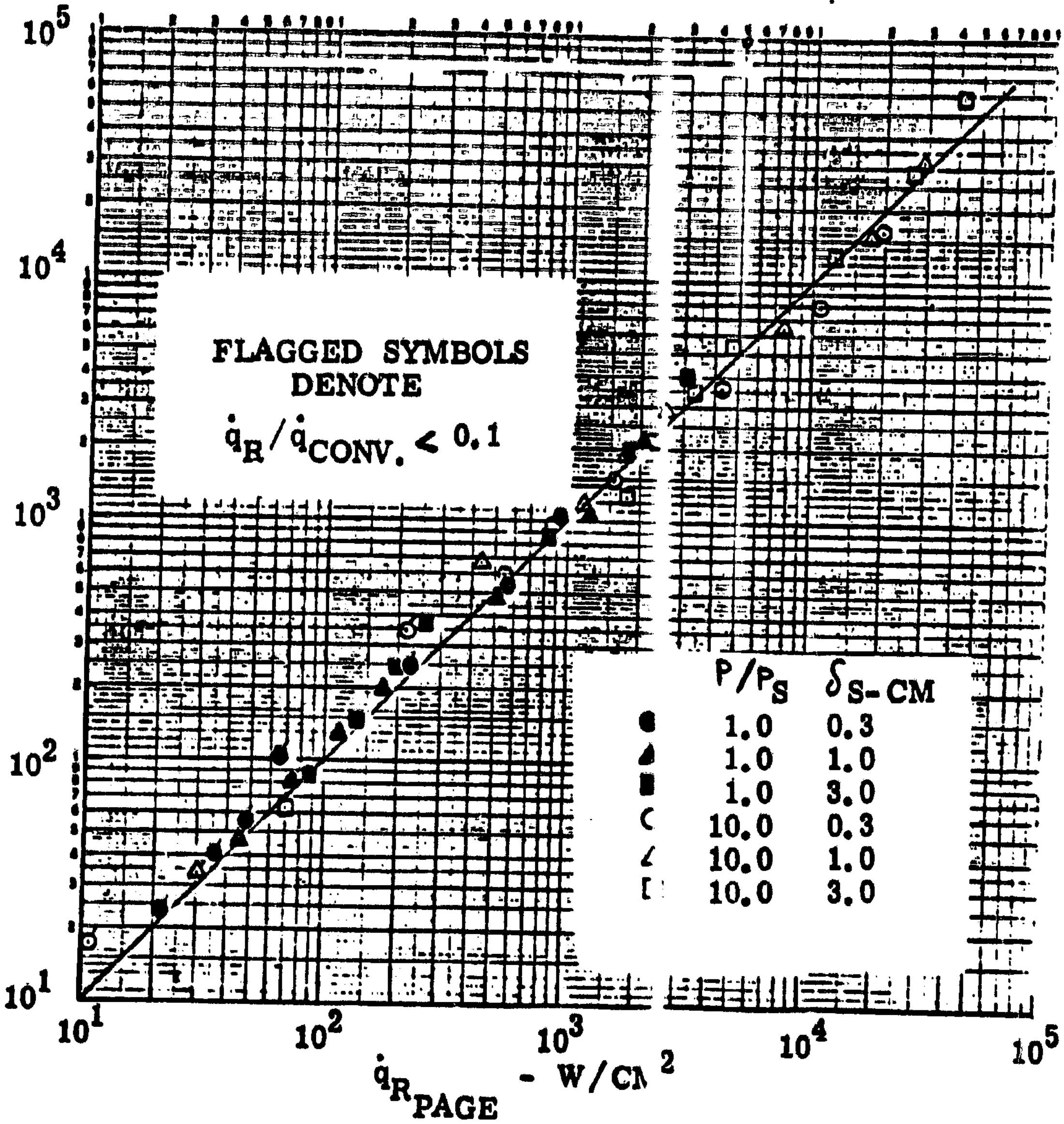

Figure IV-8 Correlation of Hypersonic R iative Heat Transfer Results in ½

• STAGNATION POINT

• $\gamma = 32.4^0$

——— ANALYTICAL, Ref.

— — — ENGINEERING CORRELATION

FIGURE IV-8

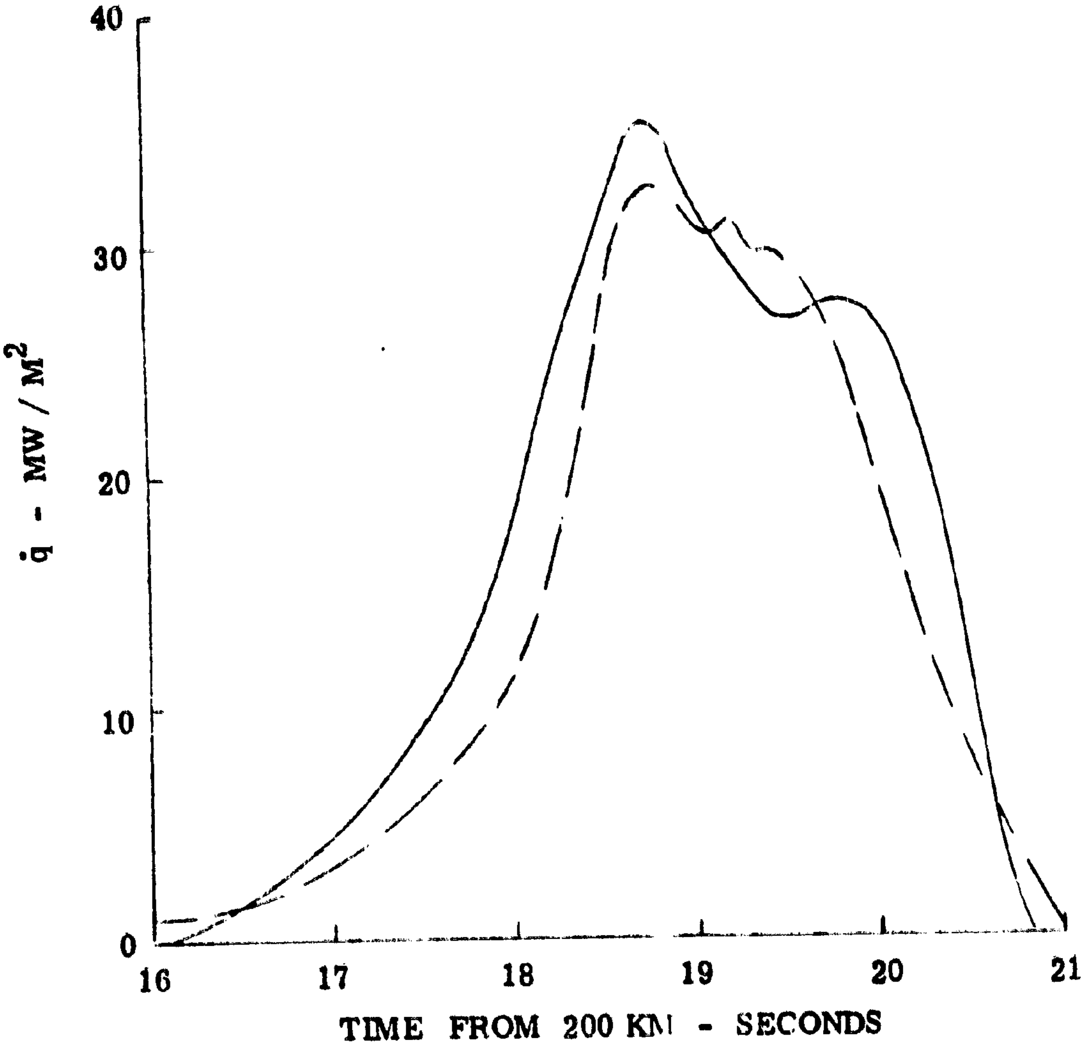

Figure IV-9 Radiative Heat Transfer Rate

Pioneer Venus Large Probe

• δ_0 = 1 CM

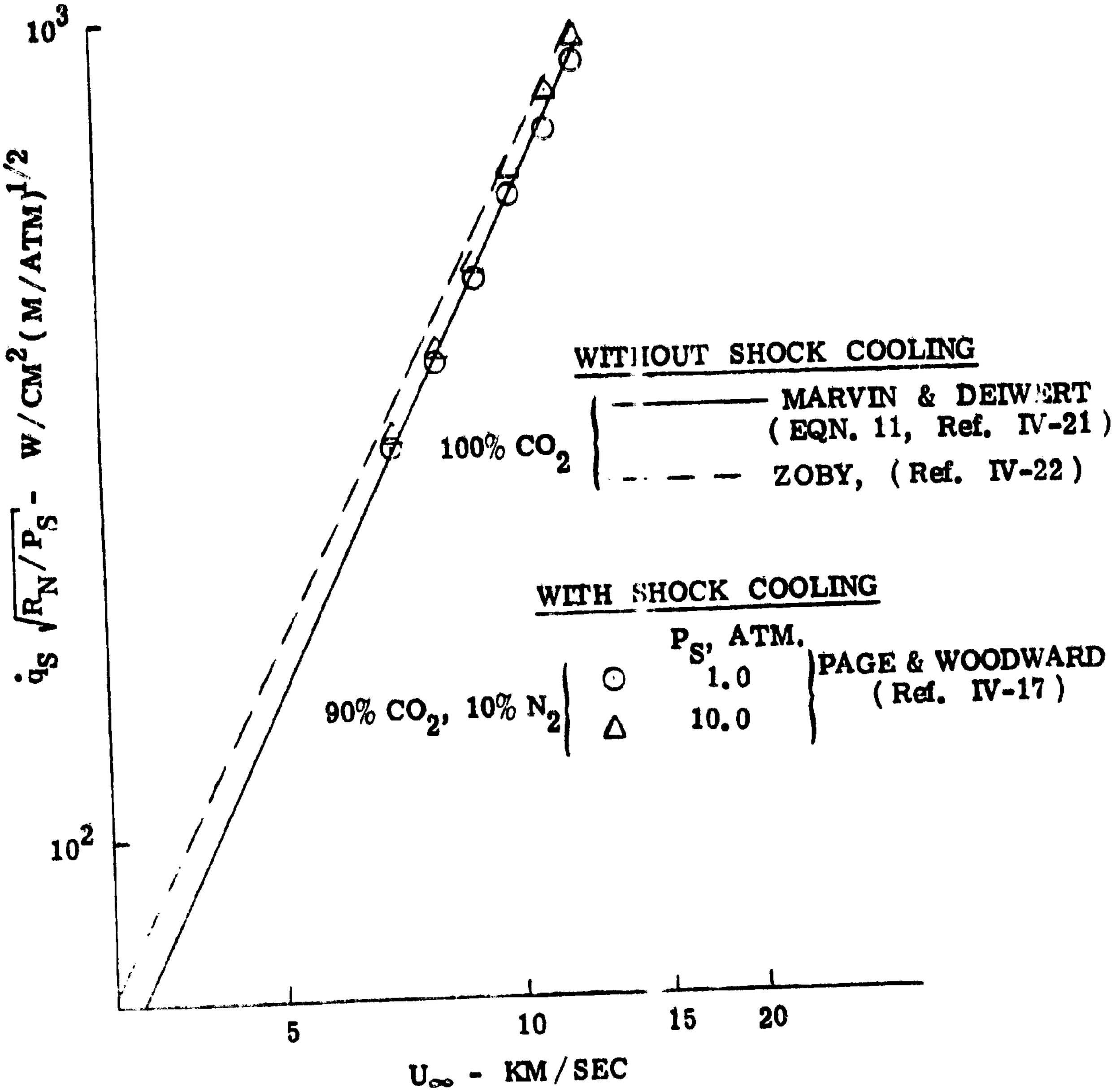

Figure IV-10 Effect of Shock Cooling on Stagnation Point Convective Heating in CO_2

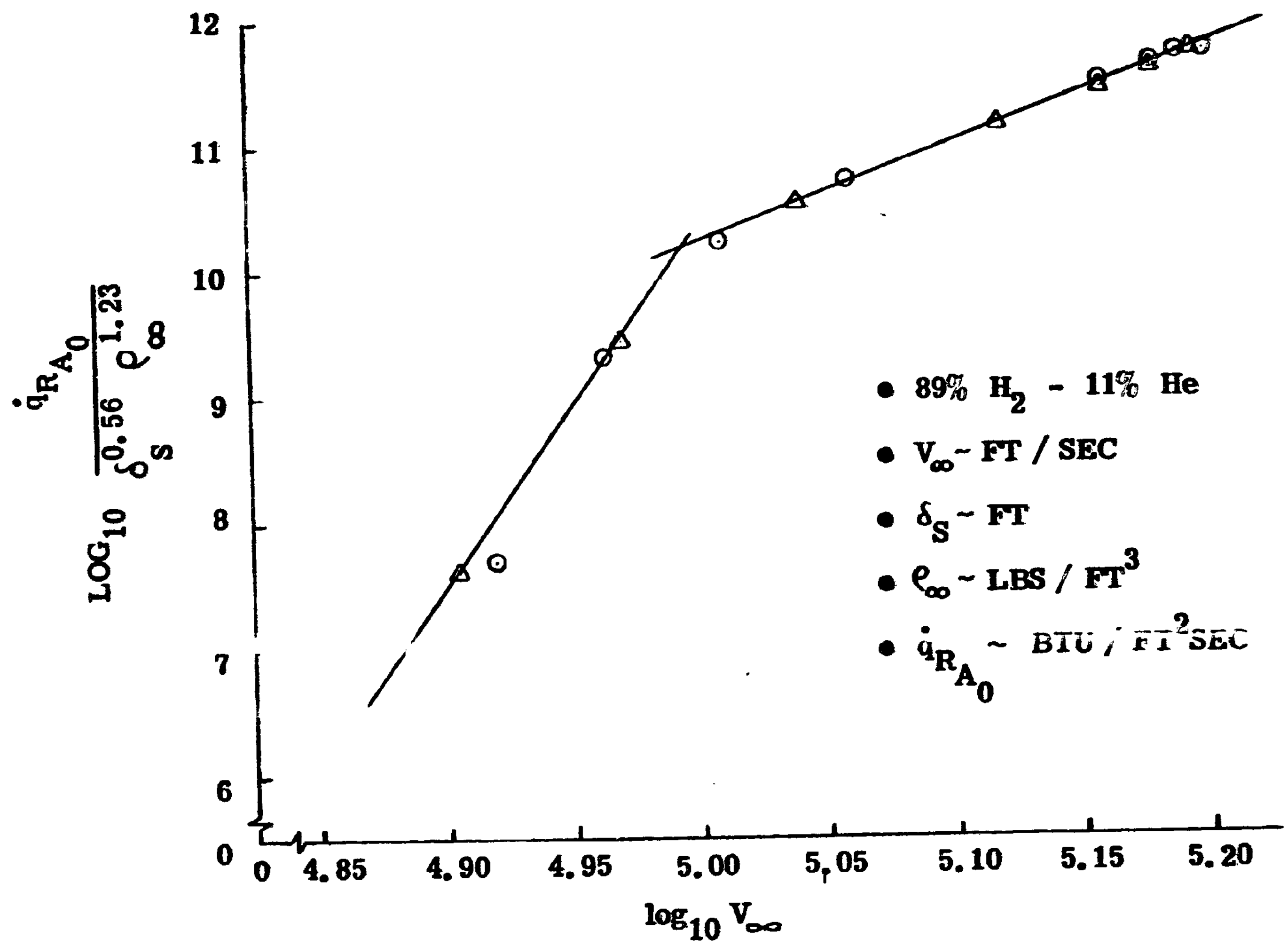

Figure IV-11 Variation of Stagnation Point Radiative Heating Parameter with Velocity for 89% H_2 - 11% He

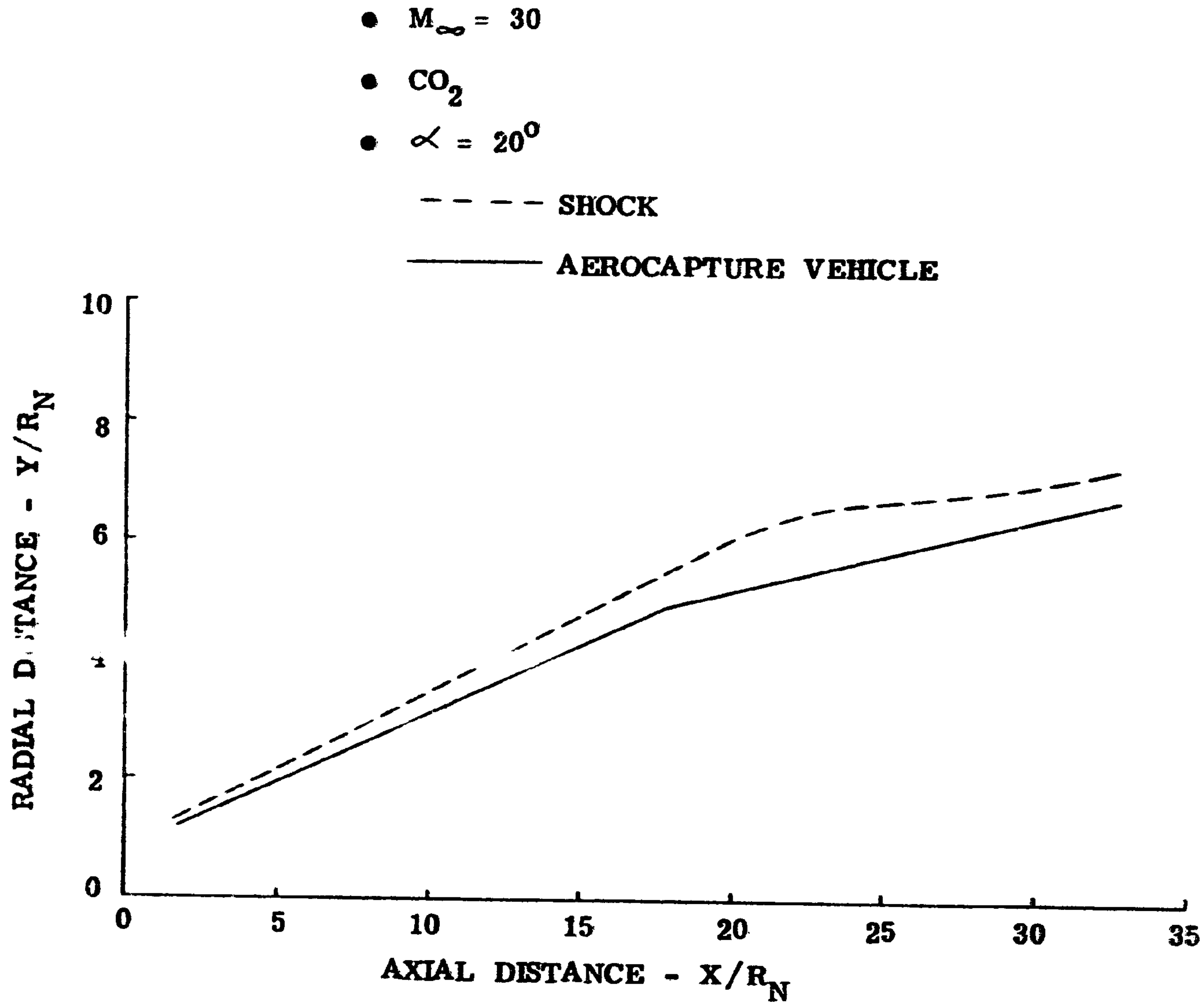

Figure IV-12 Generic Aerocapture Vehicle Shock Shape

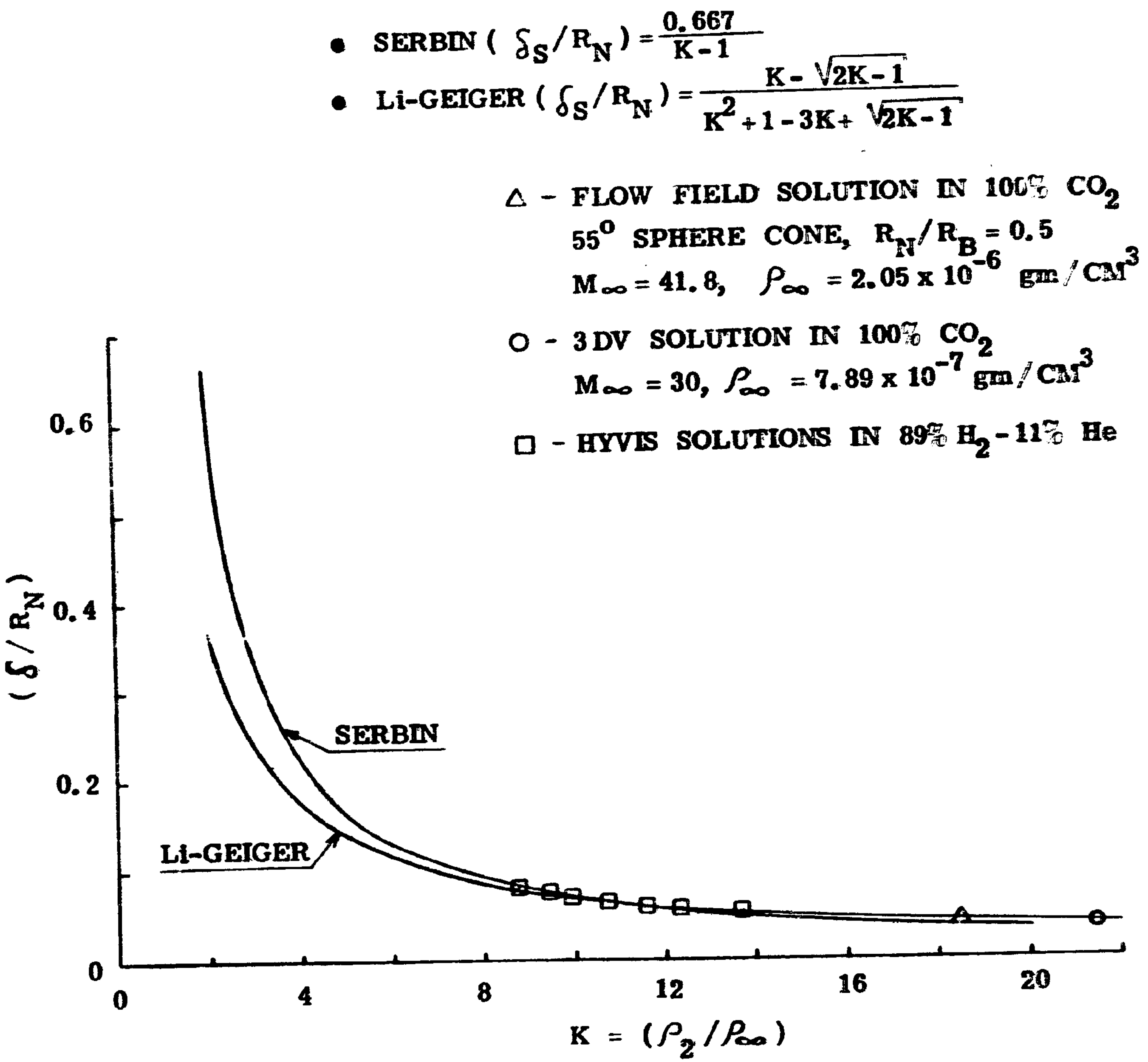

Figure IV-13 Stagnation Point Adiabatic Shock Stand Off Distance

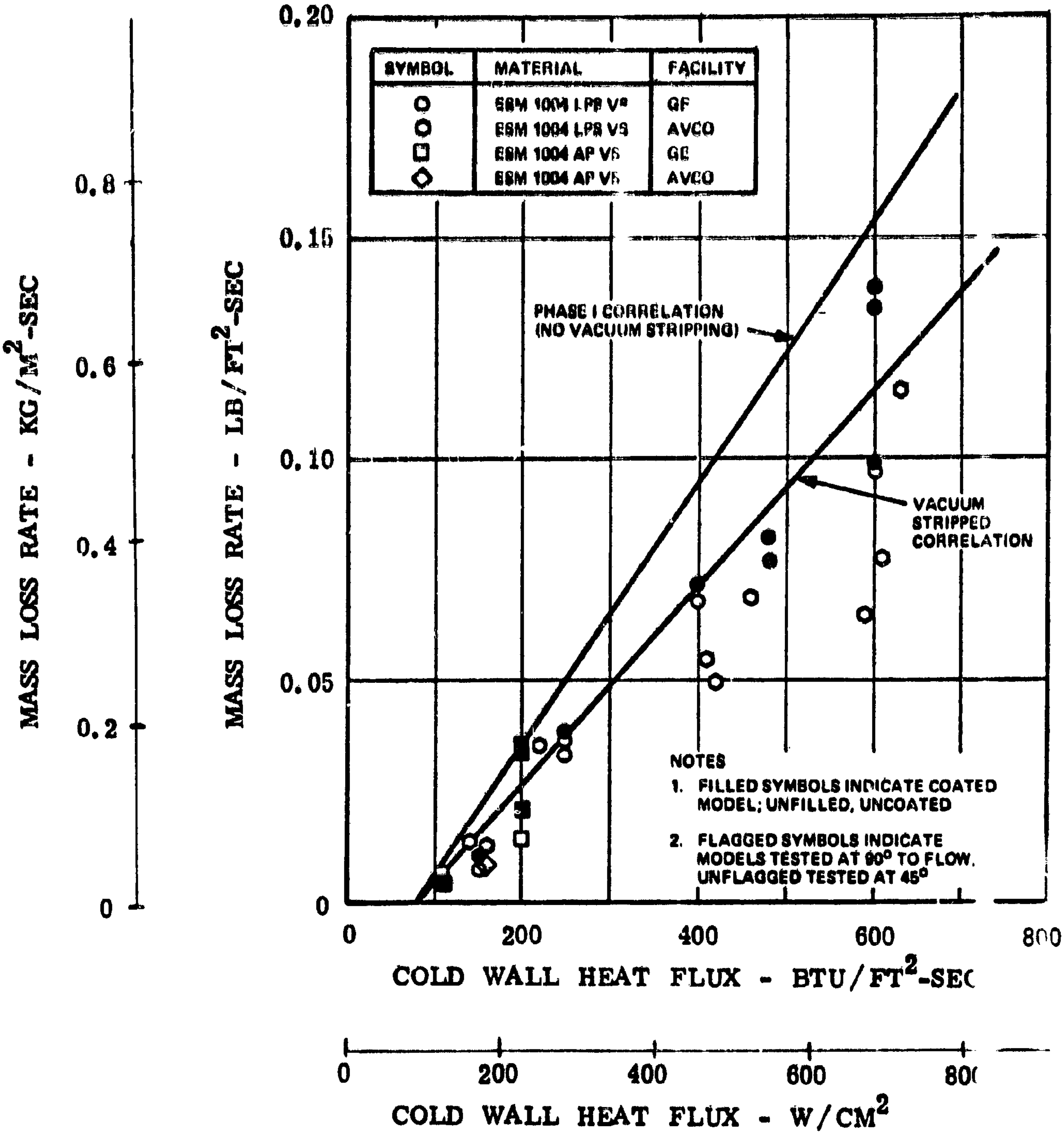

Figure IV-14 ESM1004AP and ESM1004LPS Mass Loss Rates

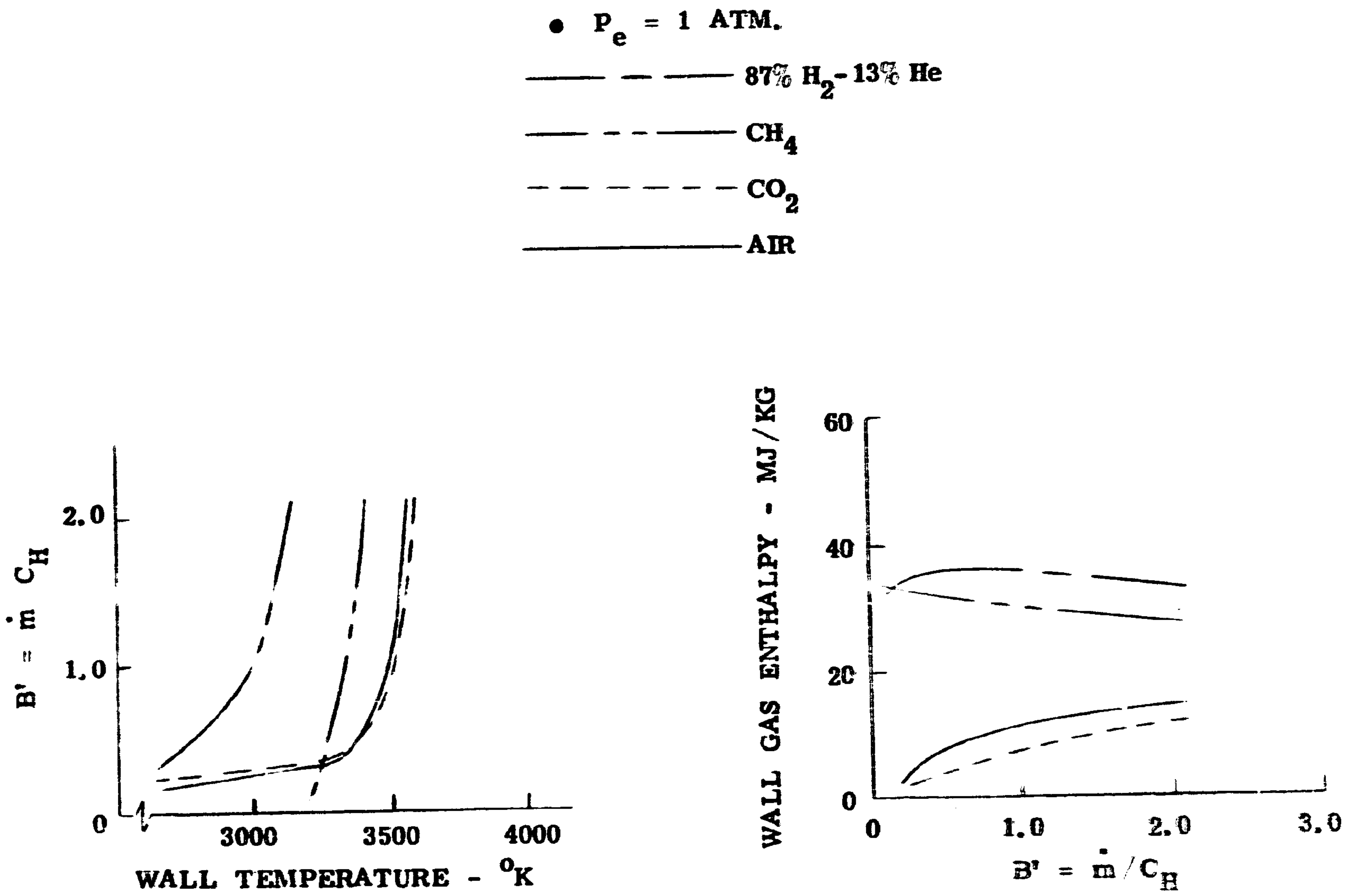

Figure IV-15 Atmospheric Composition Has Large Effect on Carbon Ablative Performance

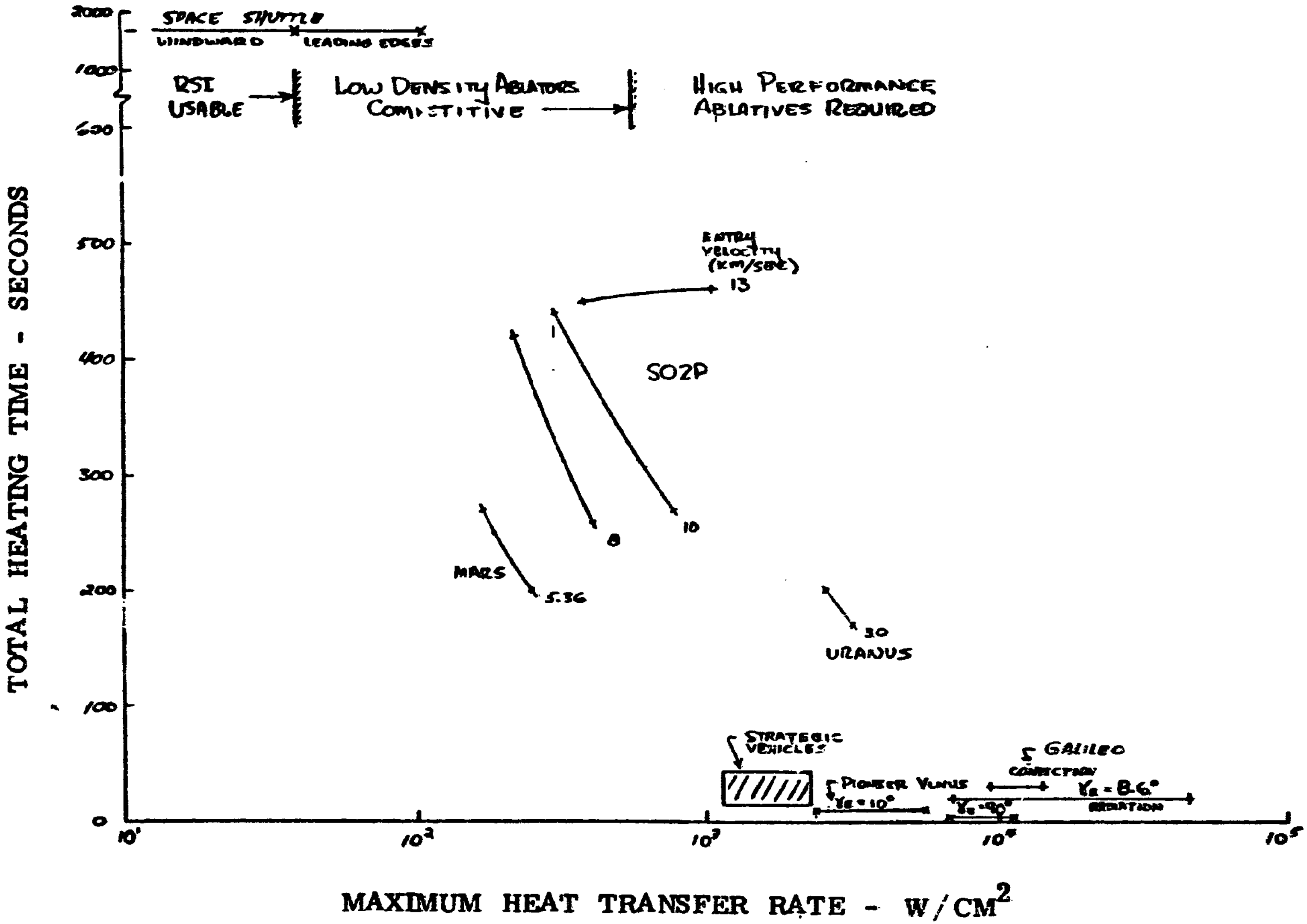

Figure IV-16 Comparison of Peak Heating Rates and Heating Times Expected for Generic Aerocapture to Current Entry Vehicles - Windward Forecone Location -

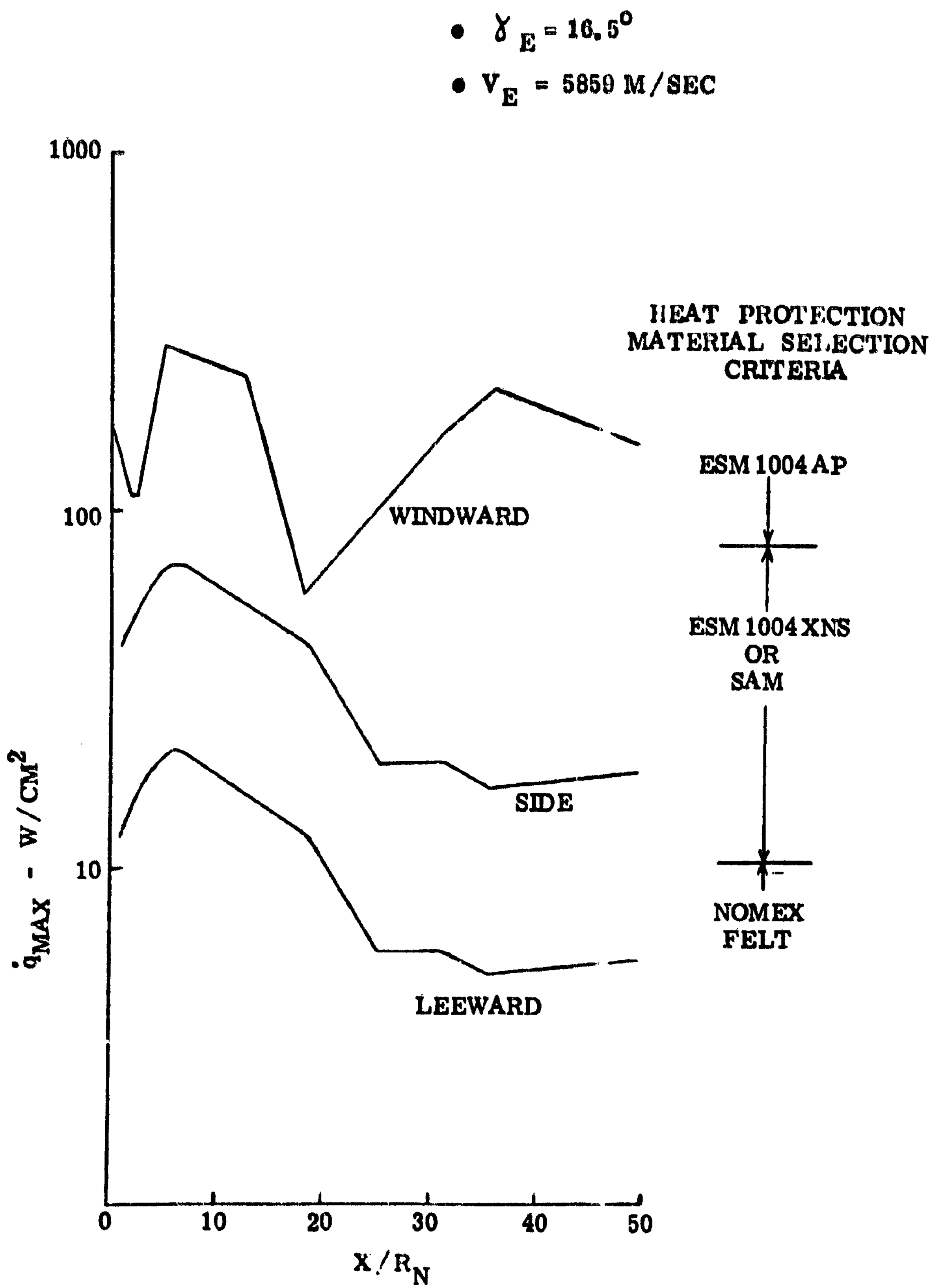

Figure IV-17 Peak Heat Transfer Rates for MSR Vehicle

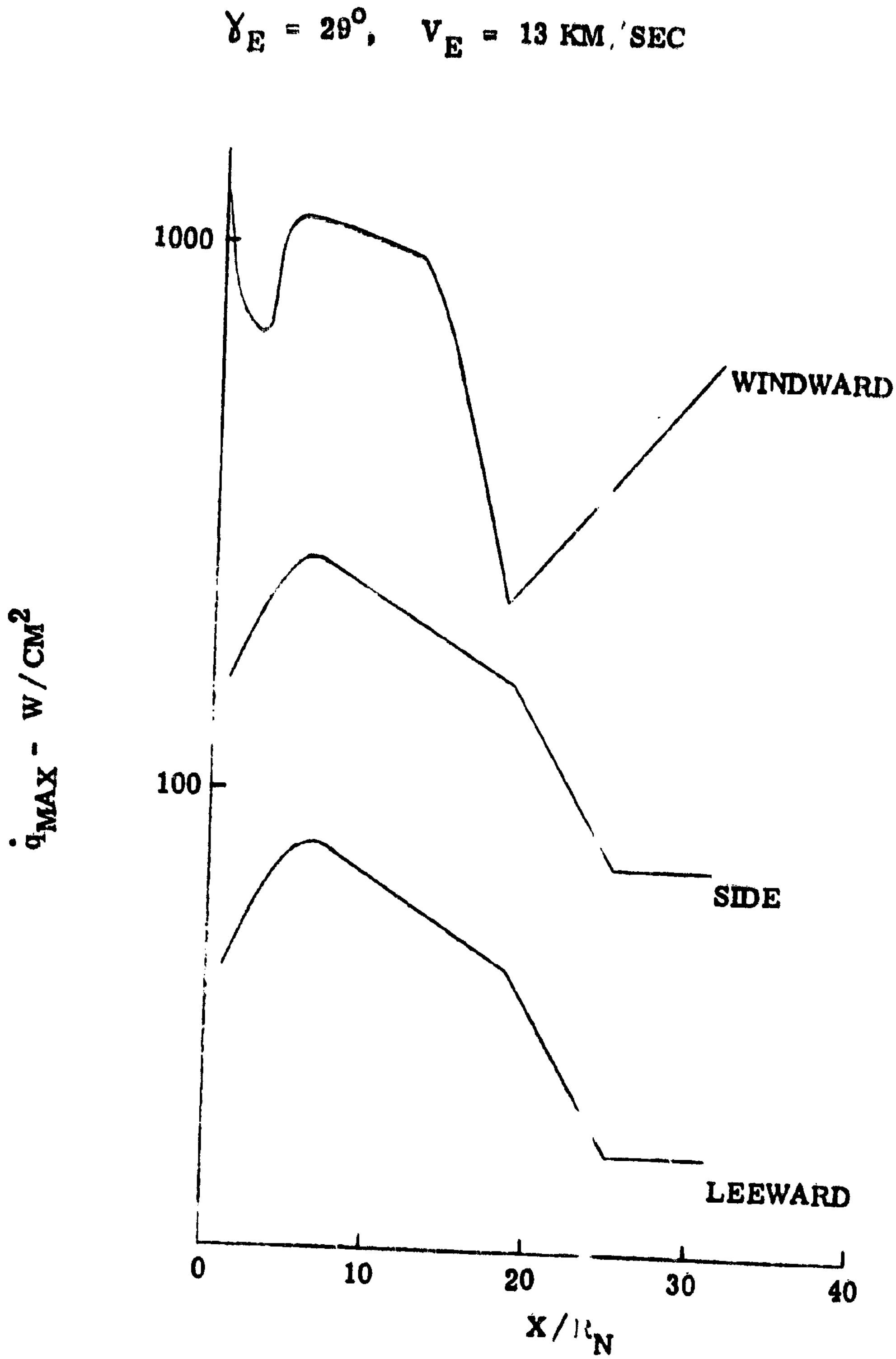

Figure IV-18 Peak Convective Heat Transfer Rates for S02P Vehicle

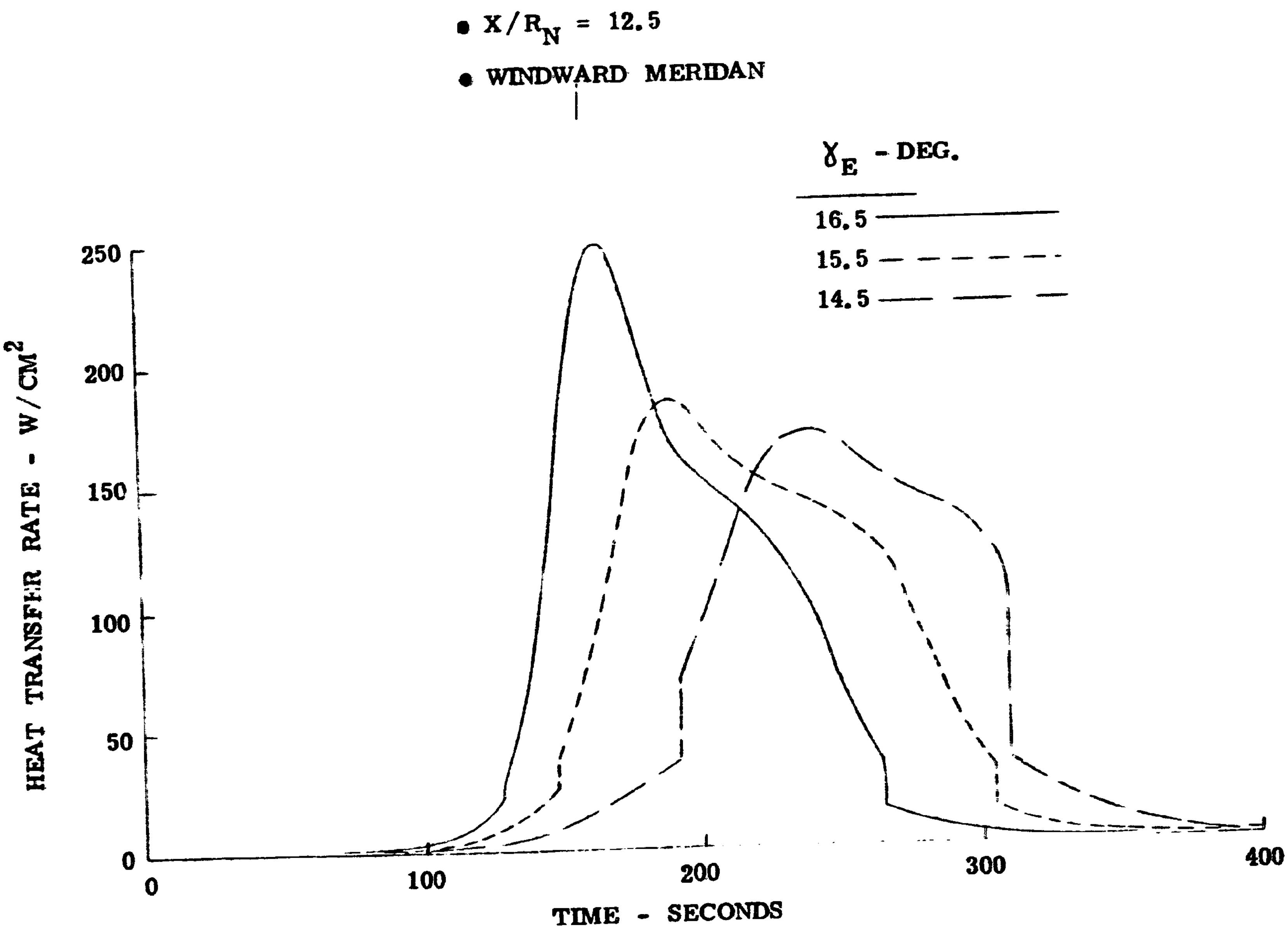

Figure IV-19 Heat Transfer Rate History for MSR Vehicle

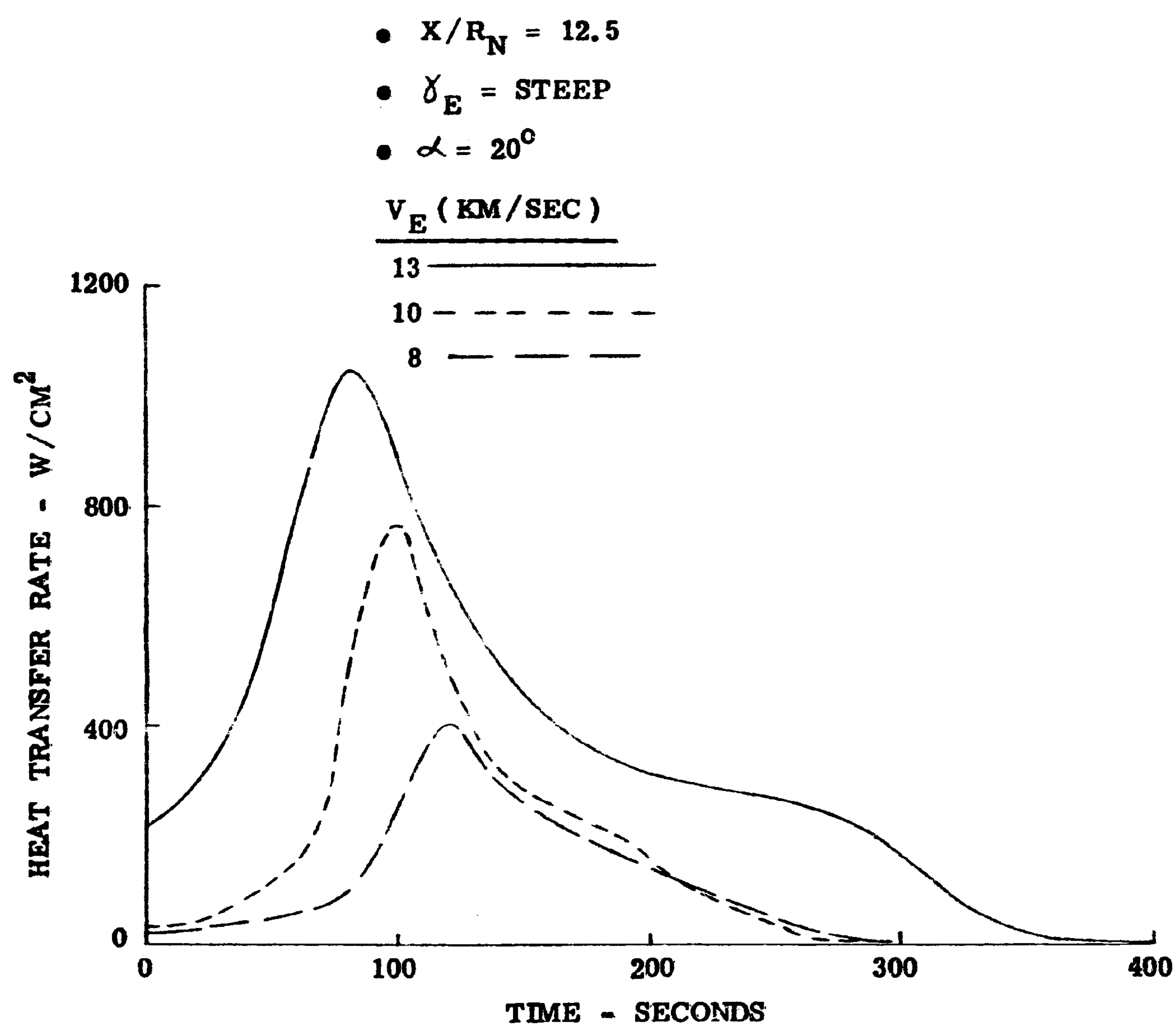

Figure IV-20 Convective Heat Transfer Rate History for S02P Vehicle Titan Entry

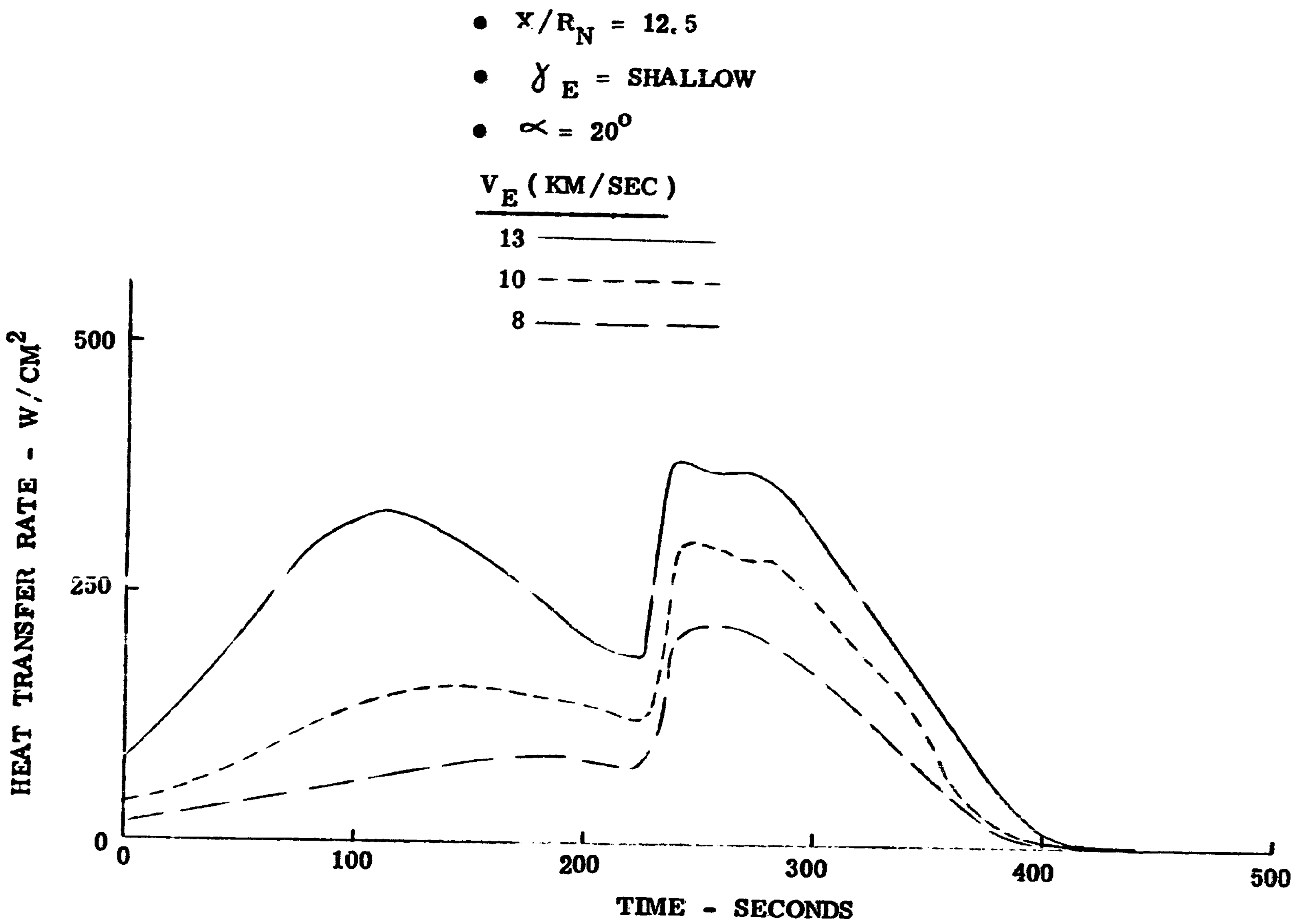

Figure IV-21 Convective Heat Transfer Rate History for S02P Vehicle Titan Entry

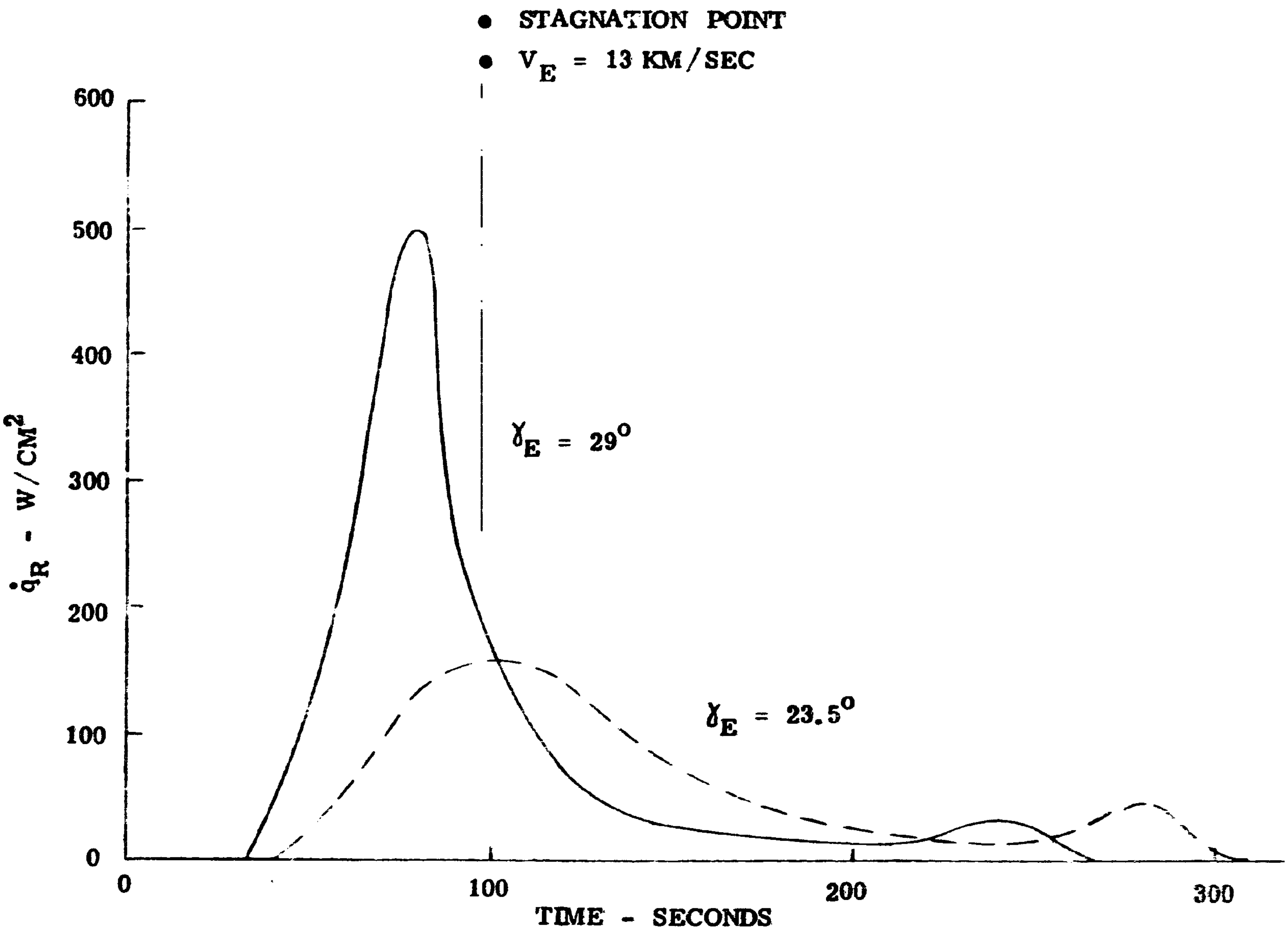

Figure IV-22 Radiative Heat Transfer Rate History for 502P Vehicle Titan Entry

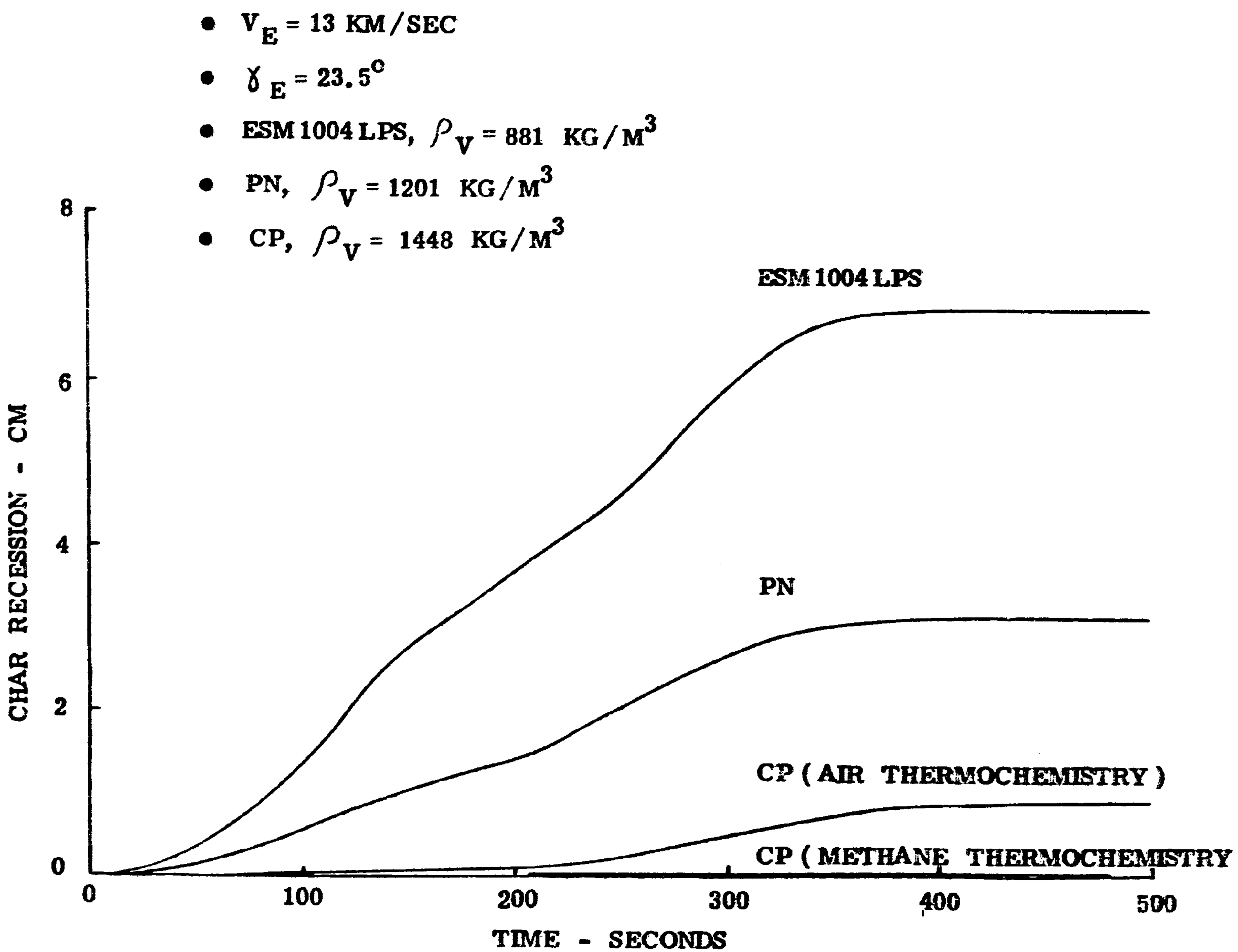

Figure IV-23 Ablator Char Recession for S02P Entry

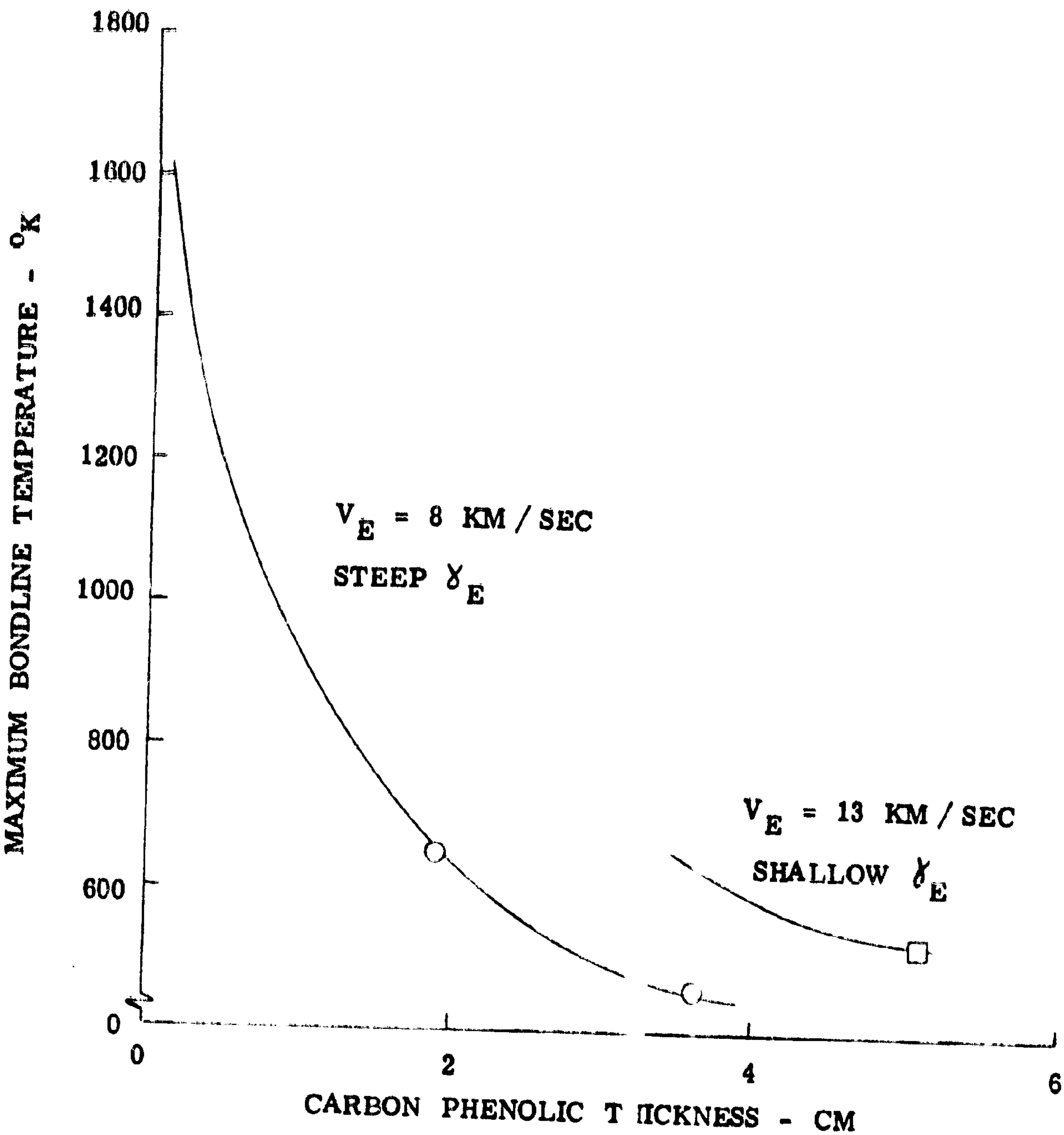

Figure IV-24 Carbon Phenolic Thick ess Requirements for SO2P Entry into a M thane Atmosphere

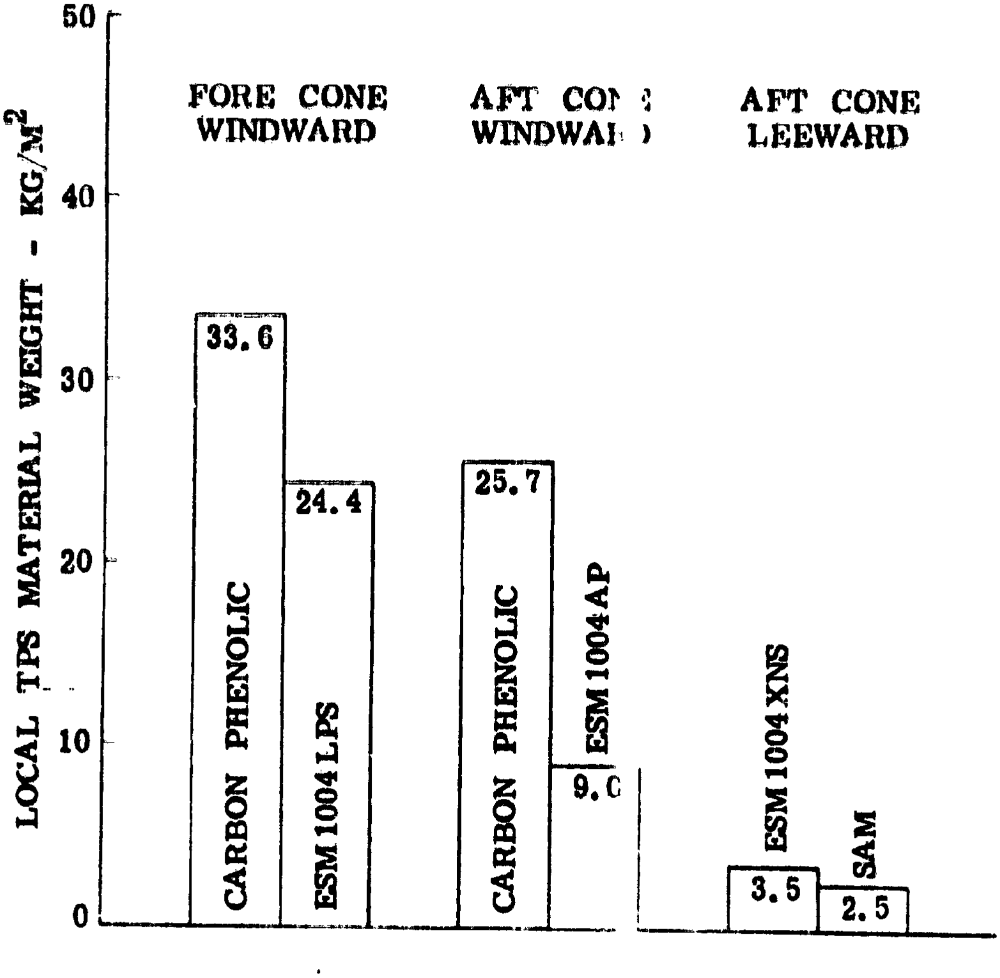

Figure IV-25 Comparison of Local TI Material Requirements for SO2F Entry, V = 8 km/sec

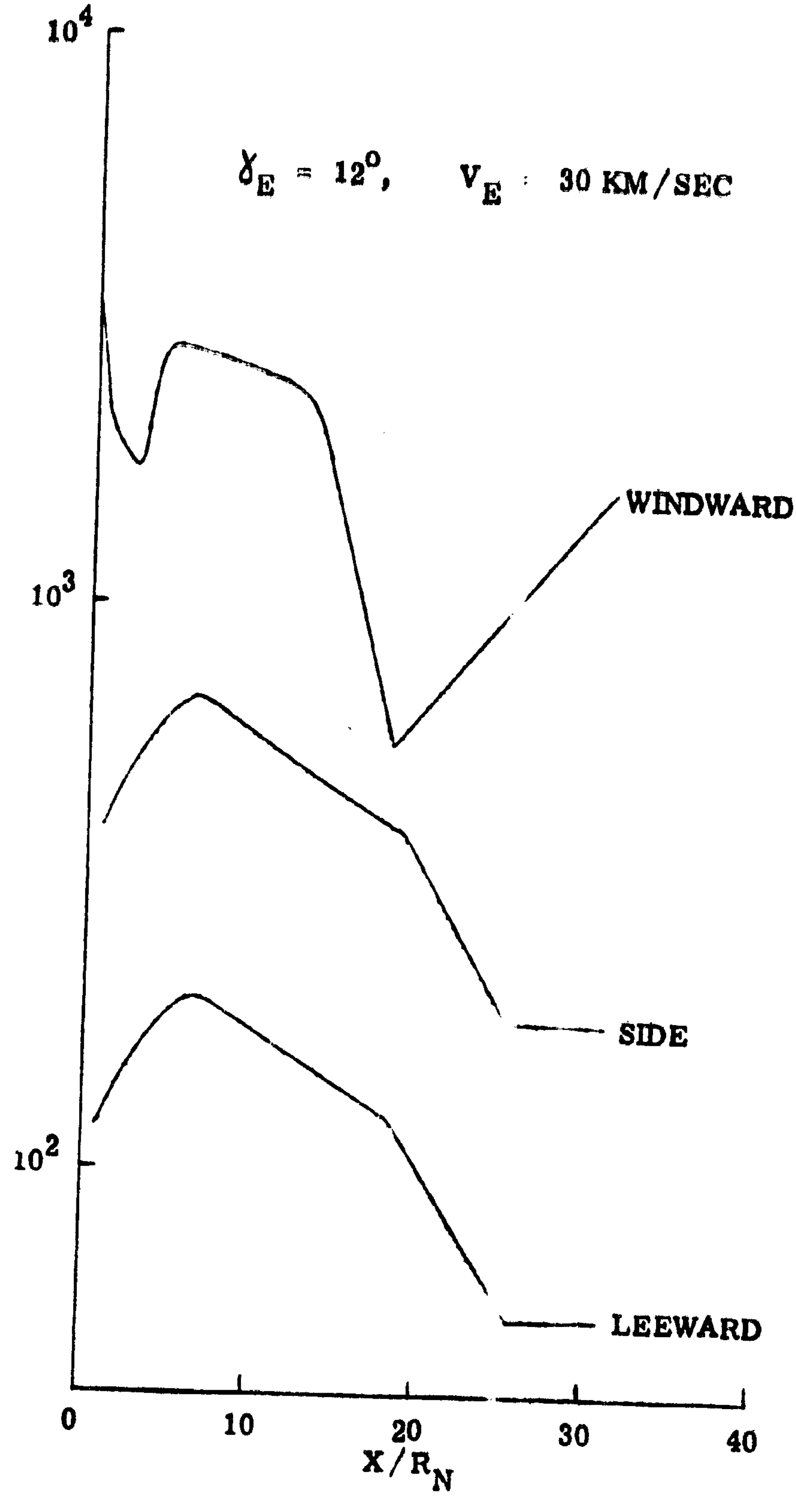

Figure IV-26 Peak Convective Heat Transfer Rates for Uranus Vehicle

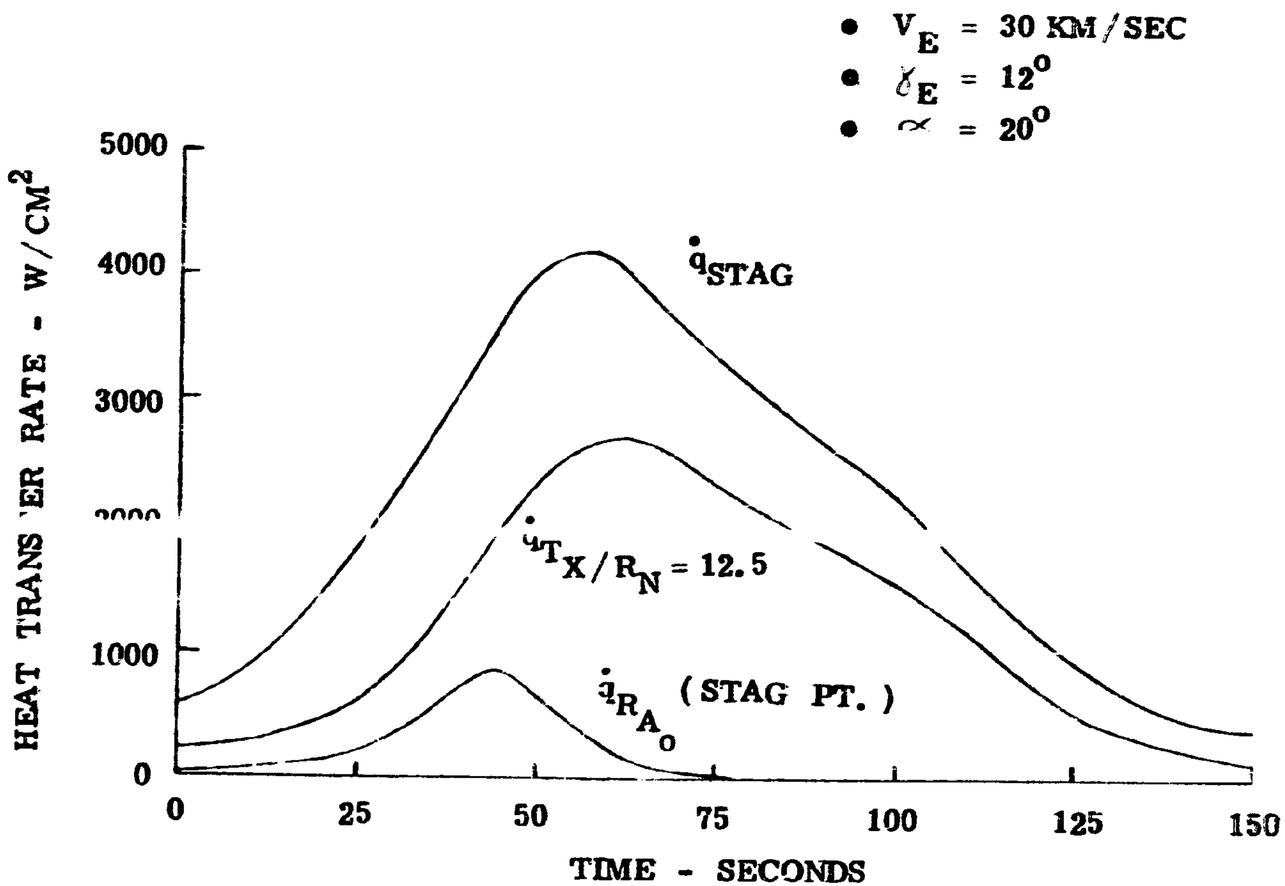

Figure IV-27 Heat Transfer Rate History for Uranus Vehicle

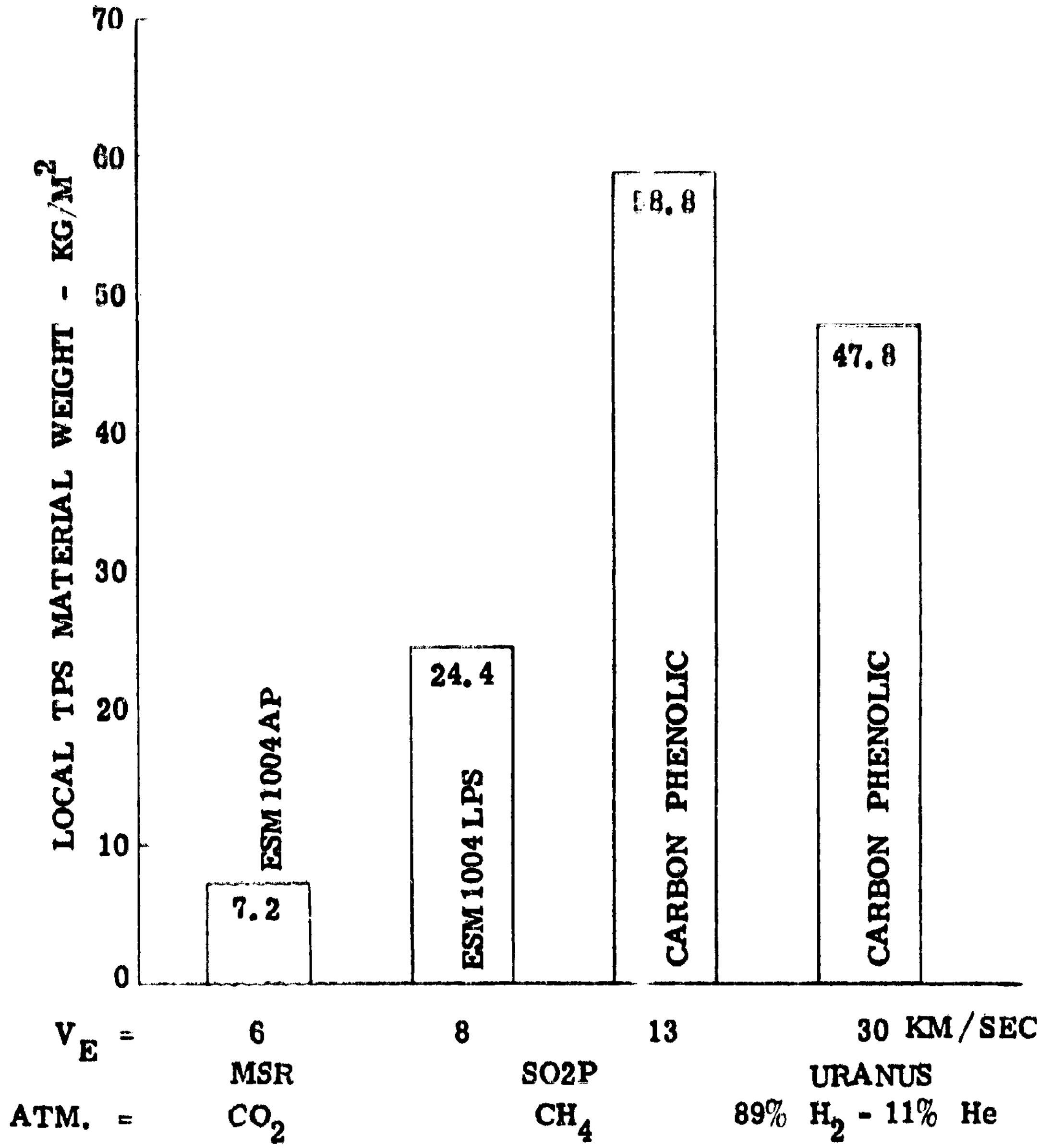

Figure IV-28 Comparison of Local Windward TPS Material Requirements on the orecone

V. CONTROL SYSTEMS

A. INTRODUCTION

Several concepts for control of the aerocapture vehicle during atmospheric flight have been evaluated during this study. Emphasis was placed onthe use of aerodynamic control techniques for countering the effects of roll disturbance torques. Performance of the several systems was demonstrated on a 3-1/2 DOF simulation using the atmospheric and planetary characteristics of Titan as a baseline (3-1/2 DOF indicates a simulation of a three degree of freedom controlled trajectory plus a one degree of freedom roll control loop). Weight estimates were made for each system along with atmospheric exit accuracies.

Six control approaches were studied:

1. Reaction Control System (RCS) Roll Control

   This is the simple on-off system with ± 5° deadband described in Ref. I-1. The control torque was set to provide [illegible] deg/sec^2 roll control acceleration with worst case roll asymmetry torques during the constant drag phase.

2. RCS with Pulse Width Modulation (PWM)

   In this case the duration of the jet pulse is made proportional to the roll error signal. Ignoring propulsion time delays this results in an RCS system whose performance is essentially linear and provides a significant increase in efficiency of fuel utilization.

3. Flap Trim Control

   With this scheme flaps are used to counter the effect of roll asymmetry torques but response to roll commands is accomplished by means of an RCS roll control system.

4. Flap Control

In this case flaps were used to provide response to roll commands as well as to counter roll disturbance torques. Experience indicates that the same flaps could be used to provide the required pitch/yaw damping. A full 6DOF simulation is required to include pitch/yaw damping and is recommended for investigation in further studies.

5. Moving Mass Roll Control (MMRC) Trim Control

In this mode, the MMRC is used only to counter the effect of roll disturbance torques and an RCS system provides response to roll commands. Performance on a 3-1/2 DOF simulation is essentially identical to that of the Flap Trim System.

6. MMRC Roll Control

In this case the MMRC is sized to provide response to roll commands as well as to counter the effect of roll disturbance torques. Roll control performance on a 3-1/2 DOF simulation is essentially identical to that of the Flap Control System. However, the MMRC system would not be capable of providing pitch/yaw damping.

The control system simulation trade-off studies used an SO2P Aerocapture vehicle and a Titan equatorial trajectory with the following parameters:

Entry Conditions

$H = 500$ km

$V = 10$ km/s

$\gamma = -29°$

Exit Conditions

$V_{EXIT} = 2400$ m/s

$AXBR = D_{REF} = -39.23\ m/s^2$ (4G)

Vehicle Characteristics

$M = 2606$ kg

$A = 5.47\ m^2$

$L_A = 10.75$ m

$I_R = 1324\ kg - m^2$

$I_P = I_Y = 5511\ kg - m^2$

$\alpha_T = 25°$

$C_A = .317$

$C_N = .939$

$C_D = .684$

$C_L = .717$

$\frac{L}{D} = 1.048$

$\frac{M}{C_D A} = 696.5$

$\frac{M}{C_L A} = 664.5$

Although these conditions were selected early in the study for the control simulations, they are representative of the SO2P aerocapture vehicle (baseline mission for generic aerocapture). The results obtained can be applied to a specific SO2P mission or other planetary missions.

B. RESULTS AND CONCLUSIONS OF THE CONTROL SYSTEM EVALUATIONS

Results of the control trade-off study are summarized in Table V-1 which lists estimated weights and effect of disturbance torque on exit velocity for the six control approaches.

a) The roll disturbance torques, as defined in Ref. I-1, are primarily due to c.g.-c.p. offset (C_2). For the control studies that were performed, a C_2 of 1.56 cm was used. This value is derived from the offset used in Ref. I-1, 2.5 cm, using a ratio of vehicle base diameters. The control system performance results presented in this section are based on the 1.56 cm offset. However, an updated analysis of vehicle design indicates that the value of C_2 can be held to 0 $\pm$0.6 cm. As a result, the control system performance requirements were extrapolated and the values of control system mass in Table V-1 were calculated for the 0.6 cm offset.

b) The exit velocity accuracy in this table is the total spread in exit velocity with C_{DIST} (disturbance torque coefficient) = 0 and $\pm 2.815 \times 10^{-5}$.

c) The RCS system mass has been estimated by extrapolating the results detailed in Ref. I-1.

d) The mass estimate for the PWM RCS system represents the theoretical minimum that could be achieved with an RCS system. Propulsion time delays were not included in the simulation. The effect of these delays can be partially compensated by control logic design. Therefore, the calculated system mass represents a somewhat optimistic solution.

e) Control simulation studies of flap systems utilized linear approximations of flap aerodynamics and limited roll flap deflection to δ_1 = = $\pm 10°$. The control moments (i.e. product of $C_{1\delta}$ and deflection angle) derived from this simulation were used to determine the flap performance requirements. The mass calculated for the flap system in Table V-1 is based on a deflection of δ_1 = 4.8 $\pm$ 4.8 degrees (see Section III). Further optimization of flap size and deflection as a function of aerodynamic performance and mass is recommended for further studies.

f) In Ref. I-1 flaps for a Flap Control System were used to counter maximum roll asymmetry torques and still provide twice the required control response for the dynamic pressure of the constant drag phase. Applying this philosophy to the simulation of the Titan vehicle with C_2 = 1.56 cm led to a requirement for 7° flap deflection to counter the disturbance torque leaving only 3° for control. This led to an error in exit velocity for one polarity of CDIST. To minimize this effect flaps were sized so that disturbance torques could be countered by 5° flap deflection, which of course leads to somewhat larger flaps. Thus with the Flap Control approach there is a potential trade-off between flap size and exit velocity error. The weight estimate in Table V-1, Column 4, is based on flaps which can provide twice the worst case roll disturbance torques.

The following conclusions can be drawn from the results of this study:

a) For the Titan mission, flaps do not offer a minimum weight solution for aerodynamic control. This is due primarily to the TPS mass requirements. Another factor is the need to minimize flap deflections with the large angles of attack postulated. However, it should be recognized that flaps do add flexibility to the system in that they can provide α_T adjustments to compensate for vehicle tolerances such as longitudinal c.g. - c.p. locations. Flaps also can handle larger lateral c.g. - c.p. offsets with minimum mass increase relative to the RCS system. For example, if C_2 increases from 0.6 to 1.56 cm, the RCS and MMRC weights in Table V-1 will increase to more than double their value while the flap weight can be compensated by additional deflection. Also for a generic vehicle, packaging a moving mass or moving part of the payload becomes impractical.

b) The Flap Control approach in which flaps are used both to counter roll disturbance torques and to provide response to roll commands requires larger flaps than the trim only control. However, further design trade-offs could reduce flap size.

c) The on-off reaction control approach does not appear attractive even with reduced value of C_2. An RCS scheme with more sophisticated control logic such as pulse width modulation provides increased fuel efficiency and should be investigated further prior to implementing a decision on roll control technique. The RCS system masses in Table V-1 are optimistic since the RCS system was not sized for worst case trajectory conditions. A significant advantage of the aerodynamic control approaches, flaps or MMRC, is that they are not too sensitive to trajectory conditions since control and disturbance torques are both proportional to dynamic pressure.

d) Reduction in the estimated lateral c.g. - c.p. uncertainty has considerable effect on selection of the best control approach. This emphasizes more exact estimates of vehicle mass properties and investigation of possible ways of minimizing them or compensating for them through vehicle design and payload integration; and through manufacturing and testing techniques. Also note that studies to date have assumed these disturbances constant. Disturbances which vary with time due to ablation and structural deformation, may impose further requirements on the roll control system. Prediction of roll disturbance torques are the major factor in the design of the roll control system.

C. ANALYSIS AND SIMULATION RESULTS

The nominal Titan aerocapture trajectory used in this study is illustrated in Figures V-1 through 7 which show trajectory variables for the case of Flap Trim Control and CDIST = 0. However, these curves for other cases do not differ significantly.

1. Roll Disturbance Torques - Calculation of roll asymmetry torques assumed in the analysis of the several roll control schemes is summarized below. The approach is the same as that discussed in Ref. I-1.

a) $\beta_T = 0.5°$

$C_{l\beta}$ was assumed to be 2.4×10^{-4}/deg.

$$\frac{C_{l\beta} A L_A \beta_T}{I_R} = \frac{(2.4 \times 10^{-4})\ (5.47)\ (10.75)\ (.5)}{1324}$$

$$= \underline{5.330 \times 10^{-6}}$$

b) Lateral c.g. - c.p. Uncertainty

For control studies this uncertainty was assumed to be 2.5 cm times the ratio of the base radius of the present vehicle to that of the Single Mission Vehicle of Ref. I-1. Thus, $C_2 = 1.56$ cm.

$$\frac{AC_2 \left(C_N + C_{l\beta} \frac{C_A}{C_{n\beta}}\right)}{I_R} = \frac{(5.47)\ (.0156)}{1324} \quad .939 - \left(\frac{(2.4 \times 10^{-4})\ (.317)}{8.86 \times 10^{-4}}\right)$$

$$= \underline{5.498 \times 10^{-5}}$$

Subsequent investigation of the problem of lateral c.g. - c.p. tolerance indicates that a better assumption is approximately 0.635 cm. Using this value the above number becomes 2.238×10^{-5}.

c) $C_{l_o} = 10^{-5}$

$$\frac{C_{l_o} A L_A}{I_R} = \frac{(10^{-5})\ (5.47)\ (10.75)}{1324}$$

$$= \underline{4.441 \times 10^{-7}}$$

d) Total Roll Disturbance

Adding the above three contributor with C_2 = 1.56 cm

CDIST = $\underline{6.075 \times 10^{-5}}$

with C_2 = .635 cm

CDIST = $\underline{2.815 \times 10^{-5}}$

The total roll disturbance acceler tion is then

DIST = CDIST * QB rad/sec^2

where QB is dynamic pressure in Ne tons/m^2

2. Pitch/Yaw Damping - The study results resented in Ref. I-1 indicated the necessity of providing pitch/yaw damping. One approach to doing this is to use RCS nozzles normal to the roll axis. Previous DOF studies showed the required torque to inertia ratio for the Single Mission ehicle to be 0.05 rad/sec. Using this number along with a lever arm of .32 L_A = 3.4 m the required nozzle thrust is

$$T_C = \frac{(.05)\ (5511)}{3.4} = 81 \text{ Newtons}$$

Assuming a total on time of 135 sec. the total mpulse required is

IMP = 81 x 135 = 10935

Using the approach to RCS design discussed in Ref. I-1, we arrive at the following RCS weight summary:

Fuel	1.5 kg
Oxidizer	2.4
Tanks	0.1
He System	0.2
Valves, Nozzles, etc.	1.8
	6.0 kg

Thus, the total weight for both pitch and yaw i 12 kg.

3. RCS Roll Control - For this case the RC roll control described in Ref. I-1 was used with thrust levels high enough to count r the roll disturbance torque.

Dynamic pressure during the constant drag p ase is

$$QB_N = \frac{D_{REF}M}{C_D A} = \frac{(39.23)\ (2606)}{(.684)\ \ (5.47)}$$

$$= 27325 \text{ N/m}^2$$

$$\text{For } C_2 = .635 \text{ cm}$$

$$\text{DIST} = (2.815 \times 10^{-5})\ (27325)$$

$$= .769 \text{ rad/sec}^2$$

Thus the RCS control acceleration must be .769 + .349 = 1.118 rad/sec. The required high thrust level is

$$T_C = \frac{(1.118)\ (1324)}{(2)\ \ \ \ (1.32)} = 560.7 \text{ New ons}$$

The control acceleration required here is a out the same as that for the Single Mission Vehicle in Ref. I-1 with C_L = 2.5 cm. For that case the maximum RCIMP = 192.4 rad/sec. Multiplying by the ratio of the time in the atmosphere we can estimate requirements for the Titan vehic e as 480 rad/sec. This correspond to a total impulse of 63550 N-m-sec. The estima ed RCS system weight to provide these characteristics is as follows:

Fuel	65.1 kg
Oxidizer	104.2
Tanks	3.9
He System	6.7
Valves, Nozzles, etc.	2.3
	182.2 kg.

The value of ΔV (exit) in Table V-1 is also base on studies in Ref. I-1.

4. PWM RCS Control - The large weight and poor performance of the previously discussed RCS system is due in part to the ineffective control of impulse resulting from the simple on-off logic. Thus it appears that considerable improvement could be made by using more sophisticated control logic. One possibility is the pulse width modulation (PWM) technique. This technique has been employed to drive electric motors in an MMRC control system. A potential problem is the propulsion system time delays which are much larger than the electrical time constants in a motor drive. In fact, propulsion delays represent a basic limitation on the performance of any RCS system. Although this problem was not addressed in this study, it appears that the effect of the time delays could be at least partially compensated in the control logic.

A block diagram of this system is shown in Figure V-8. The roll control computation is done at .1 sec intervals. At each step the pulse width command is stored as a count proportional to the error signal in an 8-bit counter such that 255 counts correspond to .1 sec. The propulsion system is activated at the beginning of the interval and turned off when the counter counts down to zero. When the count is 255 the thruster is on continuously.

To simulate this system, the flap control simulation was modified to agree with Figure V-8 and the pulse width command was simulated by 8-bit quantization of the PWC signal. The thrust level was assumed to be twice the value necessary to counter the roll disturbance torque at the dynamic pressure of the constant drag phase. Thus the thruster acceleration was .32 rad/sec^2.

Performance of the PWM RCS roll control is presented in Figures V-9 through 13. Figure V-9 shows TDIST, the average thrust acceleration in rad/sec^2, for CDIST = 0. The pulses are response to roll commands. Figure V-10 shows the response of the autopilot integrator for the same run. Figure V-11 shows TDIST for the case where CDIST = 6.075×10^{-5}. The average curve follows the magnitude of the roll disturbance torque which is proportional to dynamic pressure. The pulses are again responses to roll commands. Figure V-12 shows the autopilot integrator response for the same run. Figure V-3 shows the proportional part of the signal for the same run. The excursions t about 100 and 250 sec indicate control errors resulting from the fact that the ntegrator does not exactly track the rapid change in roll torque occurring at the e times.

Exit velocity for the three cases were

CDIST	VMEX
6.075×10^{-5}	2397 m/s
0	2400
-6.075×10^{-5}	2400

Worst case integrated acceleration was 320 rad/s c. Integrating dynamic pressure;

$$\int QB * dt = 5.26 \times 10^{6} \frac{n\text{-sec}}{m^2}$$

then multiplying by CDIST = 6.075×10^{-5} yields 319.5 rad/sec. Thus from a weight standpoint this idealized PWM system represents the theoretical optimum that can be achieved with an RCS system.

The weight estimate for this system is bas d on CDIST = 2.815×10^{-5}. Required thrust acceleration is 1.538 rad/sec an the propulsion thrust level is then

$$T_C = \frac{(1.538)\ (1324)}{2\ (1.32)} = 771 \text{ Newton}$$

Multiplying this value of CDIST by the integral f dynamic pressure gives a required angular impulse of 148.1 rad/sec which orresponds to a total impulse of 196100 n-m-sec. An estimate of the weight of an RCS system to achieve these requirements is as follows:

Fuel	20.1 kg
Oxidizer	32.1
Tanks	1.2
He System	2.1
Valves, Nozzles, etc.	2.3
	57.8 kg.

5. Flap Trim Control System - With this scheme flaps are used to counter the effect of roll asymmetry torques but the response to roll commands is accomplished by means of an RCS roll control system. One of the problems is to design the two systems to minimize interactions (i.e., disturbance torques have little effect on propellant requirements and roll commands produce relatively little flap motion). In order to minimize interactions at high altitudes the flap control was not activated until axial acceleration reached .05 earth g's.

A block diagram of the flap control portion of this system is shown in Figure V-14. For large roll commands, signals will be saturated and under these conditions it is desirable to have ER1R = 0, i.e.

$$K1 * LIM1 = LIM2$$

Since for large commands control is by means of the RCS system

$$ERG1 = 1.5\ RG1R$$

Thus for the signals to hit limits simultaneously

$$LIM1 = 1.5\ LIM2$$

which leads to K1 = .667. Setting LIM1 = .075 rad and LIM2 = .05 rad/sec is a matter of judgment. The deadband in the RCS system was also set at .075 rad. K2 was selected to give a rate loop crossover frequency of a little over 1 rad/sec.

For this case the flaps were designed so th maximum value of CDIST results in 9° flap deflection. Flap roll torque is proport onal to CDELR * DELR so

$$CDELR = \frac{6.075 \times 10^{-5}}{9} = 6.75 \times 1^{-6}$$

Response to roll commands is provided by an RCS system with control acceleration of 20 deg/sec or .3491 rad/sec^2. Operation of t is system is the same as that described in Ref. I-1 except that the deadband w s set at .075 rad and the low thrust actuation was eliminated. The required t rust level is

$$T_C = \frac{(.3491)\ (1324)}{(2)\ \ (1.32)} = 175 \text{ Newto s}$$

Integrated angular impulse for the three cases w re

CDIST	RCIMP
6.075×10^{-5}	6.1 rad/ ec
0	5.2
-6.075×10^{-5}	6.1

Using 7 rad/sec the total impulse required is 70 0 N-s. Estimated weight of the RCS system to provide these requirements is summ rized below.

Fuel	1.0 kg
Oxidizer	1.5
Tanks	0.1
He System	0.1
Valves, Nozzles, etc.	1.8
	4.5 kg

The maximum difference in exit velocity for the hree cases was 1 m/s.

Performance of this roll control system is illustrated in Figure V-15 thru 22. Figure 15 shows the flap motion with CDIST = 0 indicating the relatively small response to roll commands. Figure V-16 shows the even smaller response of the integrator which stores the flap command necessary to counter the roll disturbance torque. Figures V-17 through 19 show the flap motion and the proportional and integral components of the command for CDIST = 6.075×10^{-5}. With CDIST = -6.075×10^{-5} the response is essentially the mirror image. Figures V-20 through 22 show the first 100 seconds of these same curves illustrating the initial response in greater detail.

6. Flap Control System - In this approach flaps are used for total roll control. A low thrust RCS system was included to provide exospheric stabilization. This system had a control acceleration of .01 rad/sec^2 and was allowed to operate throughout the atmospheric flight. In this case the flap system was activated at the start of the entry trajectory. In the actual system, since the RCS system cannot provide significant atmospheric control, the flap system would probably be activated shortly before entry.

a) Design

Using the philosophy of flap system design outlined in Ref. I-1

$$CDELR * QB_N * DELC_{MAX} =$$

$$CDIST * QB_N + 2\ (.3616)$$

$$QB_N = 27325\ N/m^2$$

$$DELC_{MAX} = 10°$$

$$CDIST = 6.075 \times 10^{-5}$$

thus

$$CDELR = \frac{1.660 + 2\ (.3616)}{(27325)\quad (10)} = 8.72 \times 10^{-6}/deg$$

A block diagram of this system is shown in Figure V-23. The gain K2 was set at 450 to make the rate loop crossover frequency about 2 rad/sec.

For this system the flap deflection required to counter the disturbance torque is

$$\frac{CDIST}{CDELR} = \frac{6.075 \times 10^{-5}}{8.72 \times 10^{-6}} = 6.97°$$

With this large a value the additional flap motion due to roll commands causes the flaps to hit the 10° limit, particularly for negative CDIST. This is illustrated in Figures V-24 through 26, which show flap motion for CDIST = 0 and $\pm$ 6.075 x 10^{-5}. The net result is that the exit velocity is somewhat sensitive to disturbance torques as shown by the results below.

CDIST	V_{EXIT}
6.075 x 10^{-5}	2402 m/s
0	2400
-6.075 x 10^{-5}	2392

b) Redesign for Lower ΔV (exit)

In order to minimize the variation in exit velocity the flap size was increased so that worst case disturbance torques could be countered by 5° of flap delfection. Then

$$CDELR = \frac{6.075 \times 10^{-5}}{5} = 1.215 \times 10^{-5}/deg$$

No RCS roll control is needed since the flaps provide all roll control. Also it is assumed that flaps can provide pitch/yaw damping. This can be confirmed only by 6 DOF simulations which are recommended for future studies. Estimates of flap and actuation requirements are given in Section 9.

Performance of this system is illustrated in Figures 27 through 31 which show flap deflection for CDIST = 0 and $\pm$ 6.075 x 10^{-5}. It is seen that there is less tendency to hit the 10° flap limits than in the previous case. Maximum variation in exit velocity for the three cases was 1 m/s. The only change in the block diagram of Figure V-23 is that K2 was set at 325 to keep the rate loop crossover frequency the same.

7. MMRC Roll Trim System - The MMRC system was not actually simulated. However, with a design as shown in the block diagram of Figure V-32 its performance is similar to that of the flap trim system. Assuming that 90% of the travel must counter the worst case disturbance torque, with C_2 = .635 cm;

$$\dot{P}_{MAX} = CDIST * QB_N = 0.769 \text{ rad/sec}^2$$

$$= .9 \frac{C_N * QB_N * A}{M * I_R} M_m Y_m (MAX)$$

Substituting parameters from above

$$M_m Y_m (MAX) = 21.0 \text{ kg-m}$$

Assuming Y_m(MAX) = .45 m the weight of the movable mass is 46.7 kg. Assuming the weight of the support structure is 30% of this, the total MMRC weight is 61 kg. This system requires RCS control to provide response to roll commands and for pitch/yaw damping. The effect on exit velocity is assumed to be the same as that for the flap trim system.

8. MMRC Roll Control System - With this approach the MMRC is sized to provide response to roll commands as well as to counter roll disturbance torques. Although this system was not simulated, with a design as shown in Figure V-33 its performance is similar to that of the flap roll control system.

Using the techniques of Ref. I-1

$$\dot{P}_{MAX} = CDIST * QB_N + 2\ (.3616)$$
$$= .769 + 2\ (.3616) = 1.492\ \text{rad/sec}^2$$
$$= \frac{C_N * QB_N * A}{M * I_R} M_m Y_m\ (MAX)$$

Then $M_m Y_m$ (MAX) = 36.7 kg-m. Again assuming Y_m MAX) = .45m, M_m = 81.5 kg. Adding 30% for support structure the total MMRC weight is 106 kg. For a rate loop cross over frequency of W_{RL} = 2 rad/sec

K2 = 20 4

To counter the worst case roll disturbance torque about 52% of the mass travel capability is required. Thus we would expect to encounter only small errors in exit velocity. RCS roll control is not required since all roll control is provided by the MMRC. However, an RCS system for pitch/yaw damping is required. The effect on exit velocity was assumed to be the same as for the Flap Control System.

9. Estimate of Flap and Actuation Requirements

a) Simulation Studies

The time required for a flight tested MMRC to travel from zero to maximum excursion under no load conditions is about 0.2 sec. Assuming that the no load slew rate required is proportional to rate loop bandwidth. The requirements for flap trim and flap control are 5 deg/sec, and 10 deg/sec respectively. However, this no load speed must be maintained to some value of M_H which would be determined from control stability studies. Furthermore, the actuation must be capable of some lower slew rate at maximum hinge moment. This value would also be determined from control stability studies. Based on these considerations linear speed-torque requirements are estimated as shown in Figures V-34 and V-35.

Flap actuation response was approximated on the 3-1/2 DOF simulation by a first order actuator as illustrated in Figure V-36. For the entry velocity of 10 km/s, maximum dynamic pressure of 34500 N/m^2 occurred with entry $\gamma = -33°$. For this dynamic pressure A_{ZB} = -68 m/s^2. The slew rate limit was defined by

$$\begin{aligned} FLRL &= 1.0 - \frac{.6}{68} AZBM \\ &= 1.0 - 8.824 \times 10^{-3} AZBM \end{aligned}$$

where AZBM = $-A_{ZB}$. K_A was set at 0 deg/sec/deg for flap trim and 20 deg/sec/deg for flap control. Runs were made on the trajectory defined above. Performance was not significantly affected by the addition of the actuation response characteristics. Flap overshoots in response to roll commands increased somewhat as illustrated in Figures V-37 through 39 for flap trim and Figures V-40 through 42 for flap control. These can be compared to Figures V-15 and 17 for flap trim and V-27 through 29 for flap control to see the difference in overshoot.

b) Requirements for Flap Trim

Preliminary control studies on the 3-1/2 DOF simulation were based on linearized aerodynamics. However, the aerodynamic characteristics of flapped vehicles are actually quite non-linear. Thus, the characteristics of a realistic flap system will differ somewhat from those previously assumed. The following estimates of flap size and loading are based on a more realistic analysis of flap aerodynamics.

Maximum flap control torque must be at least sufficient to overcome the worst case predicted roll asymmetry torques. Thus

$$\frac{C_L(\delta_{MAX})\ AL_A}{I_R} = 2.815 \times 10^{-5}$$

where C_L (δ_{MAX}) is the roll torque due to the flaps with maximum roll deflection. Then C_L $(\delta_{MAX}) = 6.338 \times 10^{-4}$. As discussed in Section VI, this can be achieved with 18% flaps at 4.8° with ±4.8° of roll deflection, i.e., each flap varies from 0° to 9.6° with respect to the vehicle. Maximum flap hinge moment was found to be 4000 N-m for the following conditions.

$QB = 34500\ N/m^2$

$\alpha = 20°$

$\delta = 9.6°$

The 9.6° flap angle results from ~~a 4.8°~~ roll deflection from its neutral angle of 4.8°. Then if we assume a speed torque characteristic as shown in Figure V-43 the required actuator output power is:

$$P_A = \frac{1}{4}\ (5)\ (6680) = 8335 \text{ N-m-deg/sec}$$

or about 0.2 HP. To this must be added the power required to overcome friction.

Flap and actuator design is discussed in Section VI. Results are summarized below:

Flaps	68 kg
Support Structure	20
Actuation (Electric)	16
	104 kg

c) Requirements for Flap Control

Assuming the same flap deflection as for Flap Trim the required flap area is twice as great, i.e. 6% of the base area or $A_F = 1.97\ m^2$. Assuming hinge moment is proportional to the 3/2 power of the flap area, the maximum hinge moment is 11310 N-m. Using the speed-torque characteristic of Figure V-44 the required actuator output power is

$$P_A = \frac{1}{4}(10)(18860) = 47150 \text{ N m-deg/sec}$$

or about 1.1 HP. Again friction losses must be added. An estimate of the flap system weight is as follows:

Flaps	136 kg
Support Structure	30
Actuation (Electric)	20
	186 kg

10. Application to Mars Aerocapture - A brief investigation was made of the application of the above flap systems to Mars aerocapture. The trajectory used here was the same as that used in Ref. I-1 with entry conditions:

$$H = 200 \text{ km}$$

$$V = 5359 \text{ m/s}$$

$$\gamma = -15.5°$$

$$\psi = 89.61°$$

and

$$V_{EXIT} = 3650 \text{ m/s}$$

$$AXBR = -D_{REF} = -14.71 \text{ m/s } (1.5\text{ }) $$

Assumed characteristics of the MSR vehicle were

$$M = 4420 \text{ kg}$$

$$R_B = 1.72 \text{ m}$$

$$A = 9.294 \text{ m}^2$$

$$L_A = 14.01 \text{ m}$$

$$I_R = 184.5 \text{ kg-m}^2$$

$$I_P = I_Y = 13800 \text{ kg-m}^2$$

$$\alpha_T = 20°$$

$$C_A = .246$$

$$C_N = .746$$

$$C_D = .487$$

$$C_L = .617$$

then

$$\frac{L}{D} = 1.267$$

$$\frac{M}{C_D A} = 977$$

$$\frac{M}{C_L A} = 771$$

a) Pitch/Yaw Damping

Assuming a torque to inertia ratio of .05 rad/sec^2 and

$$L_C = .32\, L_A = 4.5 \text{ m}$$

The required nozzle thrust is

$$T_C = \frac{(.05)\ (13800)}{4.5} = 153.3$$

Assuming a total on time of 50 sec the required impulse is 7670 N-sec.

The weight summary for the RCS system is as follows:

Fuel	1.04 kg
Oxidizer	1.66
Tanks	0.1
He System	0.2
Valves, Nozzles, etc.	1.8
	4.8 kg

Thus the total weight for both pit h and yaw is 9.6 kg.

b) Roll Disturbance Torques

For control simulation studies rol disturbance effects are calculated as in Section 1 except that the as umed lateral c.g.-c.p. uncertainty C_2 = 2.04 cm. Results are summari ed below

τ = .5°		8.469×10^{-6}
C_2 = 2.04 cm		6.913×10^{-5}
$C_{LO} = 10^{-5}$		7.023×10^{-7}
	CDIST	7.83×10^{-5}

with C_2 = .635 cm this becomes CDI T = 3.069×10^{-5}

c) Flap Trim Control

For purposes of 6 DOF simulation s udies flaps were again sized o that the maximum value of CDIST r sults in 9° of flap deflectio.. Then

$$\text{CDELR} = \frac{7.83 \times 10^{-5}}{9} = 8.7 \times 10^{-6}$$

To keep ω_{RL} the same as in Figure 4, K2 was first set at 191. However, due to the fact that norm l acceleration builds up more rapidly than on the Titan traject y the flaps did not come out ast enough and performance was quite p or. The gains were then changed to K2 = 270, K3 = 0.2 With these ains satisfactory performance was achieved as indicated in Figure V- 5 through 61. Figures V-45 through 52 show trajectory parameters for DIST = 0. These are not significantly affected by other values of CDIST. Control response for CDIST i illustrated in Figures V-53 throug 55. It is seen that flap re ponse to roll commands is somewhat highe than before due to the higher control gains. Figures V-56 throu h 58 illustrate control perfo manc with CDIST = 7.83×10^{-5}. Figures V-59 through 61 show the init al response in greater detail. Response with CDIST = -7.83×10^{-5} s essentially the mirror image.

Exit velocity for three cases were

CDIST	V_{EXIT}
7.83×10^{-3}	3652
0	3653
-7.83×10^{-3}	3653

Thus ΔV_{EXIT} is 1 meter/sec.

To size the flap, CDIST = 3.069×10^{-5}. Then

$$\frac{C_L\ (\delta_{MAX})\ AL_A}{I_R} = \frac{3.069 \times 10^{-5}}{.9}$$

Then $C_L\ (\delta_{MAX}) = 4.832 \times 10^{-4}$. Using the same flap configuration as the Titan vehicle this requires flaps qual to 13.7% of the base are or $A_F = 1.27\ m^2$. Maximum $\overline{Q}$ on the Ma s trajectories was 22000 N/m^2.

Assuming

$$M_H \quad Q * A_F^{3/2}$$

and comparing to requirements for lap Trim on the Titan vehicle, the maximum hinge moment is

$$M_H = 4000 \left(\frac{22000}{34500}\right) (1.295)^{3/2} = 3670 \text{ N-m}$$

Then from Figure V-43

$$P_A = 7835 \text{ N-m-deg/sec}$$

or about .2 HP.

Assuming TPS requirements of 7.2 kg/sq meter the weight of the flap system is estimated as follows:

Flaps	28 kg
Support Structure	15
Actuation (Electric)	16
	59 kg

The required thrust level for the RCS system is

$$T_C = \frac{(.3491)}{(2)} \frac{(1845)}{(1.72)} = 187 \text{ Newtons}$$

Worst case integrated impulse was less than 4 rad/sec. Using 5 rad/sec the total impulse required is 5360 N-sec. Estimated weight of the RCS system is as follows:

Fuel	0.75 kg
Oxidizer	1.15
Tanks	0.1
He System	0.1
Valves, Nozzles, etc.	1.8
	3.9 kg

d) Flap Control - Sizing the flaps for simulation so that the maximum value of CDIST results in 5° flap deflection we have

$$\text{CDELR} = \frac{7.83 \times 10^{-5}}{5} = 1.566 \times 10^{-5}$$

To keep ω_{RL} the same as in Figure '3, K2 was set at 200. The trajectory parameters for this case did not differ significantly from

Figures 45-52. Control performance is illustrated in Figures V-62 through 66. Figures V-62 through 64 show flap motion for CDIST = 0 and $\pm$ 7.83 x 10^{-5}. Figures V-65 and V-66 show the initial response in more detail for CDIST = $\pm$ 7.83 x 10^{-5}. Comparing these to Figures 27 and 28 it is seen that the flaps come out considerably slower than for the Titan mission since initial dynamic pressure is lower (.05 Earth g's axial acceleration occurs at about 140 sec. as opposed to about 18 sec. after the start of the Titan trajectory). Also the flap motion is somewhat oscillatory due to the fact that this transient occurs before the point where rate loop gain variation is started. Control stability improves at higher dynamic pressure. In any case system performance is satisfactory.

Exit velocities for the three cases were:

CDIST	V_{EXIT}
7.83 x 10^{-5}	3652 m/sec
0	3652
-7.83 x 10^{-5}	3651

Thus ΔV_{EXIT} = 1 m/sec

Required flap area is twice that for Flap Trim. Using the same approach as for the Titan vehicle we find maximum hinge moment to be 10380 N-m and required actuator output power about 1.0 HP. Estimated weight of the flap system is as follows:

Flaps	55 kg
Support Structure	30
Actuation (Electric)	16
	101 kg

D. TRAJECTORY STUDIES

Entry trajectory studies were made on the 3-1/2 DOF simulation using Flap Trim roll control for Titan, Mars and Uranus. The purpose of these studies was to define sensitivity of trajectory and guidance performance to entry velocity and path angle and their effects on vehicle heating. Heating results derived from these trajectories are discussed in Section IV.

1. SO2P Trajectories - Titan aerocapture trajectories were run for several combinations of entry velocities and path angles in an attempt to define a set of nominal entry conditions for which satisfactory performance could be achieved with a tolerance of ± 5° on entry path angle. Vehicle characteristics were the same as those used in control studies except that α_T = 30°. Aerodynamic characteristics were

$$C_A = 0.367$$

$$C_N = 1.220$$

$$C_D = .928$$

$$C_L = .873$$

then

$$\frac{L}{D} = .94$$

$$\frac{M}{C_D A} = 513.4$$

$$\frac{M}{C_L A} = 545.7$$

Desired exit velocity was 2400 m/sec and values of AXBR ($-D_{REF}$) used were as follows:

V (m/s)	AXBR (m/s^2)	
6000	-14.71	(1.5 G_E)
8000	-29.42	(3.0 G_E)
10000	-39.23	(4.0 G_E)
13000	-39.23	(4.0 G_E)

The S02P trajectories are presented in Appendix A, included in Volume II of this final report. Table V-2 gives a summary of exit velocities for the various entry conditions. It is seen that a tolerance of ± 5° on entry γ can be accommodated only for V = 8 and 10 Km/s and even for these cases the error in exit velocities exceeded the desired 25 m/sec at the edge of the entry path angle band.

2. Mars Trajectories - Mars trajectory studies were conducted only for the aerocapture trajectory used in Ref. I-1. Characteristics are discussed therein and in Part C of this section. Desired exit velocity was 3650 m/s and AXBR = -14.71 m/s^2 (1.5 G_E).

Trajectory results, presented in Appendix B, Volume II, are illustrated in Figures B1 through B9 for γ = -14.5°, Figures B10 through B18 for γ = -15.5° and Figures B19 through B27 for γ = -16.5°. Exit velocities (H = 250 km) were as follows:

γ	V_{EXIT}	ΔV_{EXIT}
-14.5°	3649 m/s	-4 m/s
-15.5°	3653	-
-16.5°	3658	+5

No further studies were made on Mars Aeromaneuver trajectories. However, with Flap Trim control system performance will be quite similar to that illustrated in Figure V-16 of Ref. I-1. In this case the disturbance torque CDIST = 0 and control acceleration of the RCS system was 20 deg/sec^2.

3. Uranus Trajectories - Uranus trajectory studies were conducted for the following entry conditions:

$$H = 500 \text{ km}$$

$$VA = 30 \text{ km/sec}$$

$$FPA = -8°, -10°, -12°$$

Desired exit velocity was 21288 m/sec and values of AXBR of -196.13 m/sec^2 (20 G_E) and -147.10 m/sec^2 (15 G_E) were used. Vehicle characteristics are summarized below:

$$M = 1600 \text{ kg}$$

$$R_B = 1.32 \text{ m}$$

$$A = 5.47 \text{ m}^2$$

$$\alpha_T = 20°$$

$$C_A = .272$$

$$C_N = .689$$

$$C_D = .491$$

$$C_L = .555$$

then

$$\frac{L}{D} = 1.13$$

$$\frac{M}{C_D A} = 595.7$$

$$\frac{M}{C_L A} = 527.0$$

Trajectory results, presented in Appendix C, Volume II, are illustrated in Figures C1 through C24 for D_{REF} = 20 G_E and in Figures C25 through C48 for D_{REF} = 15 G_E. Variations in entry path angle resulted in sizeable variations in exit velocity as indicated in Table V-3. One factor in these variations is the roll-over maneuver to correct cross-range errors. With high lift acceleration, occurrence of a roll-over near the point where the vehicle starts its exit results in the exit velocity being very sensitive to perturbations. This factor should be investigated thoroughly in future studies. However, the simulations do demonstrate feasibility of aerocapture using the above defined vehicle and provide estimates of heating for TPS design. However from Table V-4 it is seen that changing cross-range deadband from 5000 m (value used for results in Figures C1 through C24) to 7500 m did not change the variation in V_{EXIT} significantly for D_{REF} = 20 G_E. Variations with D_{REF} = 15 G_E were considerably smaller. The only conclusion to be drawn from this brief study is that there is a potential sensitivity of exit velocity to control response timing and variations in trajectory parameters.

Table V-1 Control System Summary

	Control System	Roll RCS Mass (kg)	P/Y RCS Mass (kg)	Flap Mass (kg)	MMRC Mass (kg)	Total Mass m/s	Exit Velocity Accuracy m/s
1.	RCS	182.2	12.0	-	-	194.2	40
2.	PWM RCS	57.8	12.0	-	-	69.8	3
3.	Flap Trim	4.5	12.0	104	-	120.5	1
4.	Flap Control	-	-	186	-	186.0	1
5.	MMRC Trim	4.5	12.0	-	61	77.5	1
6.	MMRC Control	-	12.0	-	106	118.0	1

Table V-2 Exit Velocities, 502P Trajectory

V m/s	α deg.	V_{EXIT} m/s	ΔV_{EXIT} m/s
6000	-22.5	2396	- 4
↓	-26.5	2400	-
	-30.5	2378	-22
8000	-23.0	2443	+41
↓	-28.0	2402	-
	-33.0	2406	+ 4
10000	-23.0	2394	- 7
↓	-28.0	2401	-
	-32.5	2377	-24
	-33.0	2350	-51
13000	-23.5	2407	+ 7
↓	-26.0	2400	-
	-29.0	2387	-13

Table V-3 Exit Velocities, anus Trajectory

D_{REF} G_E	CRDB Meters	α(°) Deg.	V_{EXIT} m/s	ΔV_{EXIT} m/s
20	5000	- 8	21660	+380
		-10	21280	-
		-12	21450	+170
	7500	- 8	21130	-150
		-10	21280	-
		-12	21580	+300
15		- 8	21280	0
		-10	21280	-
		-12	21320	+ 40

Figures, Section V

The figures of Section V present the following relationships:

QB vs. VA	Dynamic Pressure (N/m^2) vs. Air Relative Velocity (m/sec)
H vs. DRNG	Altitude (m) vs. Downrange Distance (km)
H vs. T	Altitude (m) vs. Time (seconds)
VA vs. T	Air Relative Velocity (m/sec) vs. Time (seconds)
FPA vs. T	Air Relative Flight Path Angle (deg) vs. Time (seconds)
AXW vs. T	Drag (m/sec^2) vs. Time (seconds)
RGCD vs. T	Bank Angle Command (deg) vs. Time (sec)
TDIST vs. T	Average Thruster Acceleration (rad/sec^2) vs. Time (sec)
API vs. T	Autopilot Integrator Signal vs. Time (sec)
PROP vs. T	Autopilot Proportional Signal vs. Time (sec)
DELRC vs. T	Roll Flap Deflection Command vs. Time (sec)

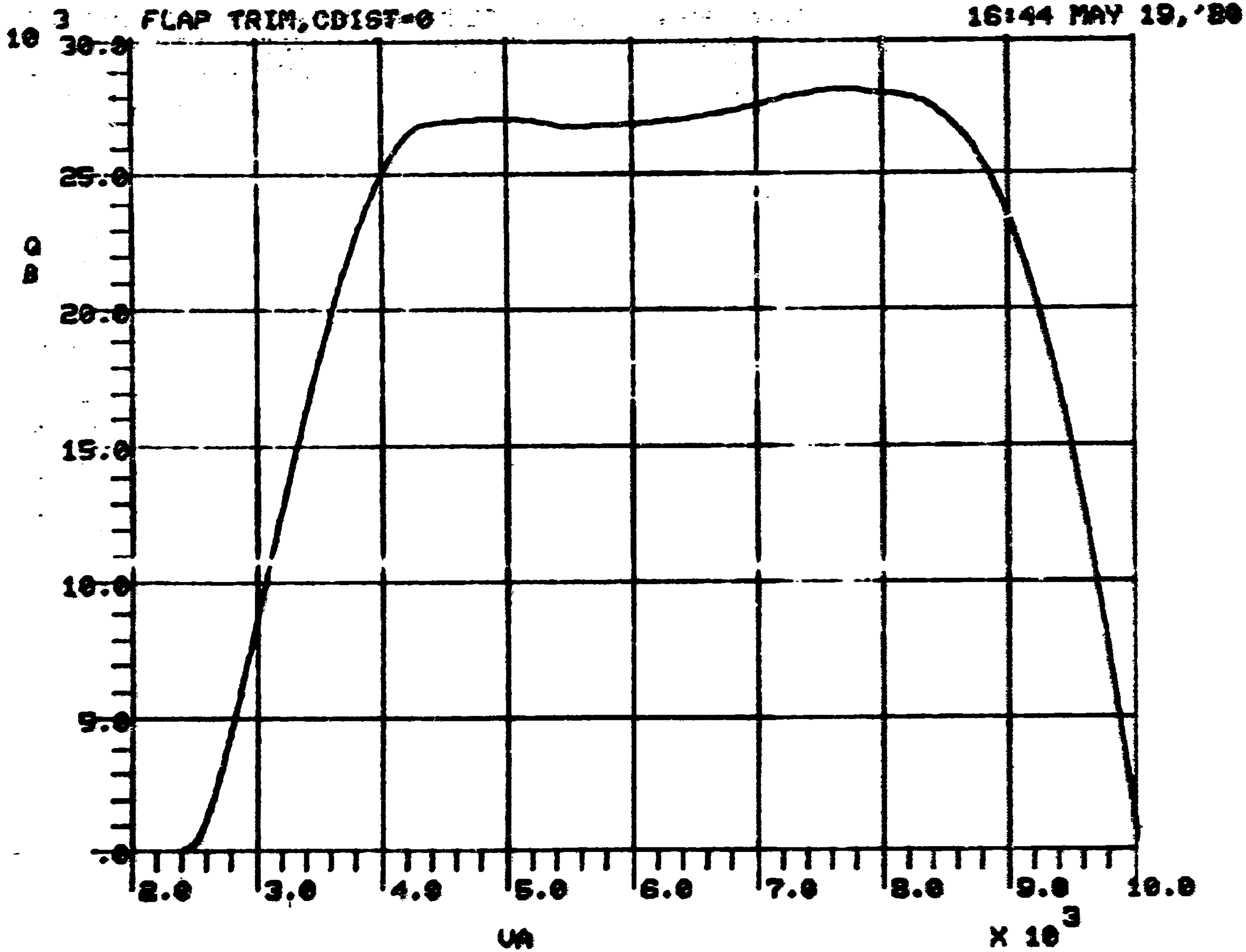

Figure V-1 Dynamic Pressure, Titan Trajectory

V-2

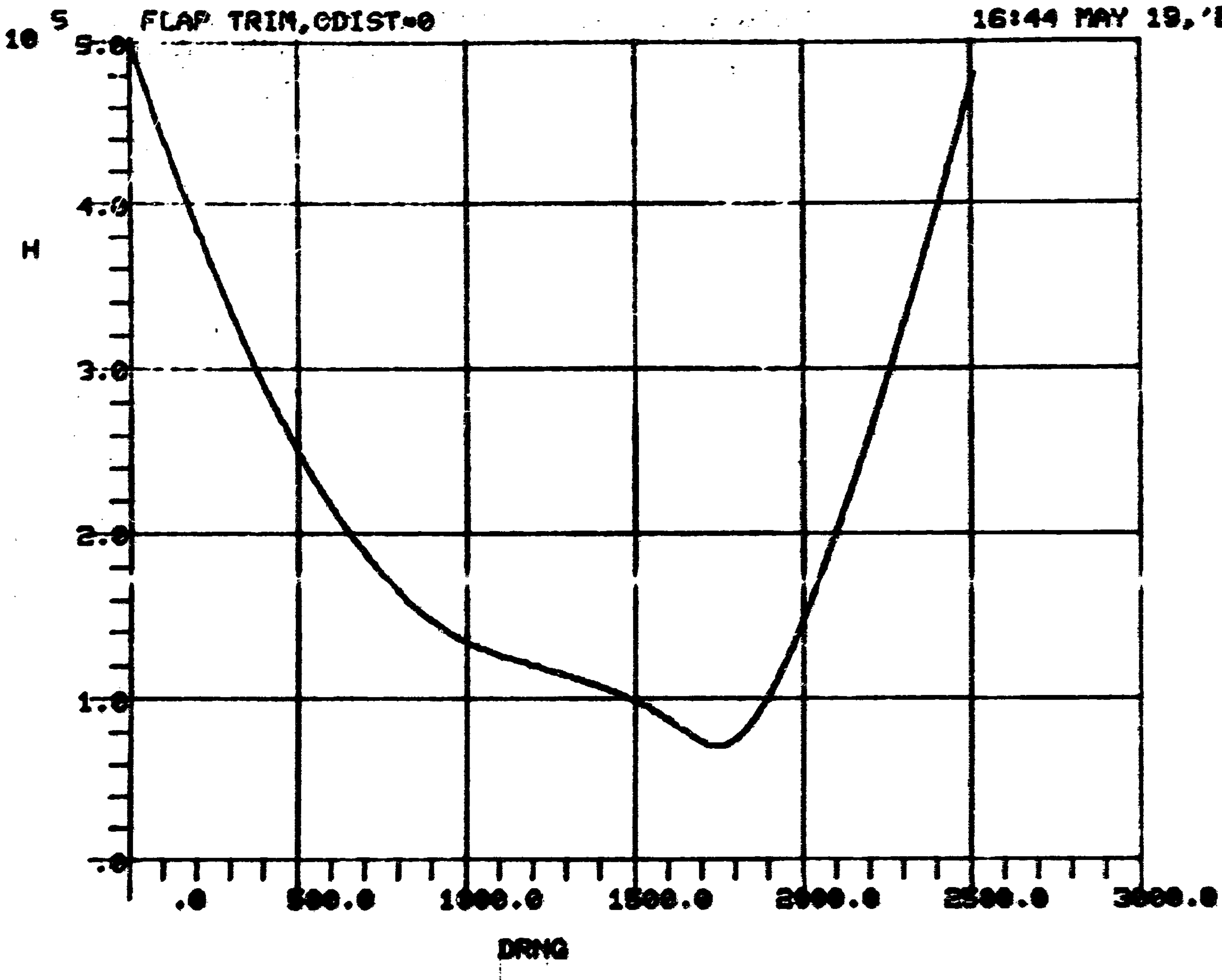

Figure V-7 Altitude, Titan Trajectory

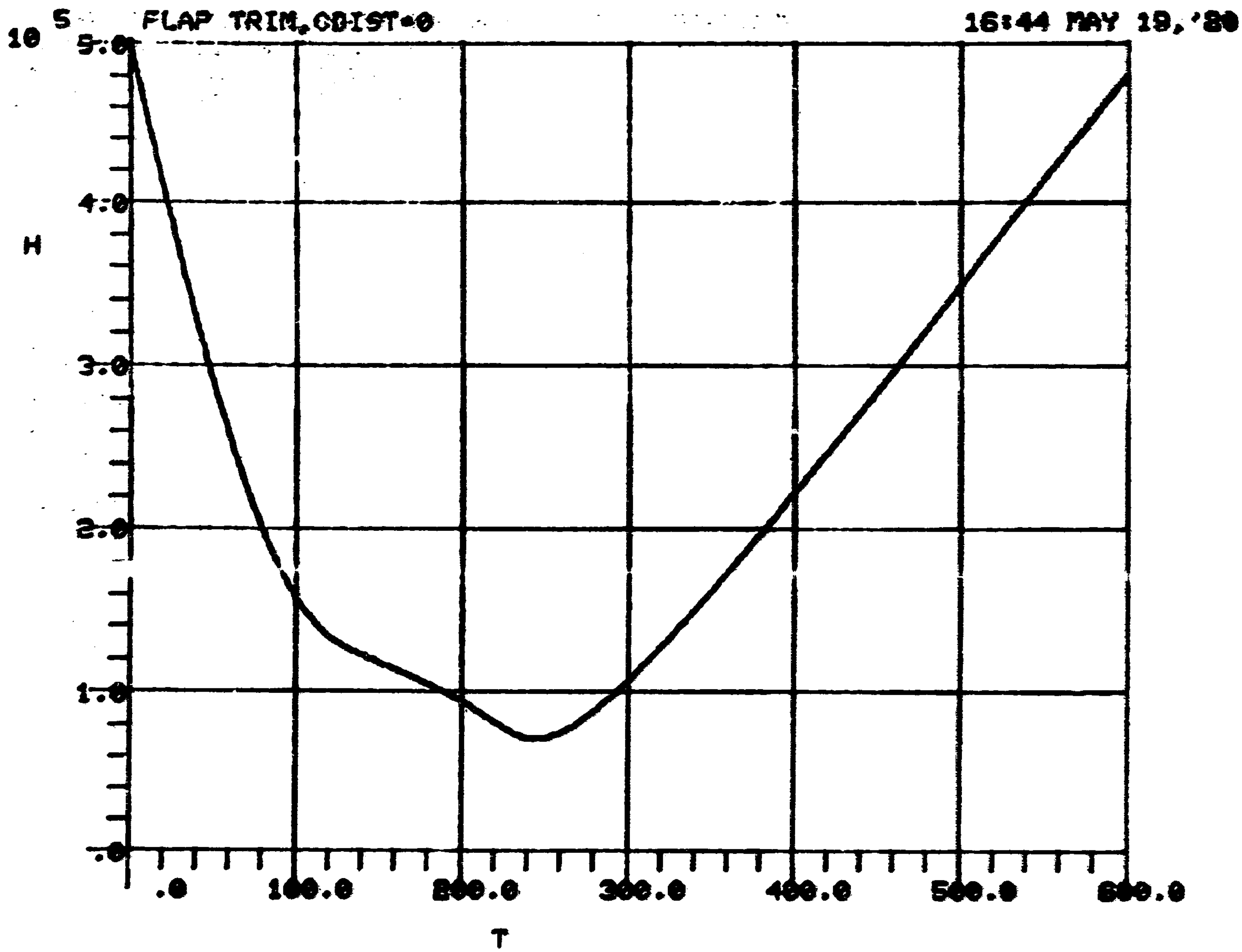

Figure V-3 Altitude, Titan Trajectory

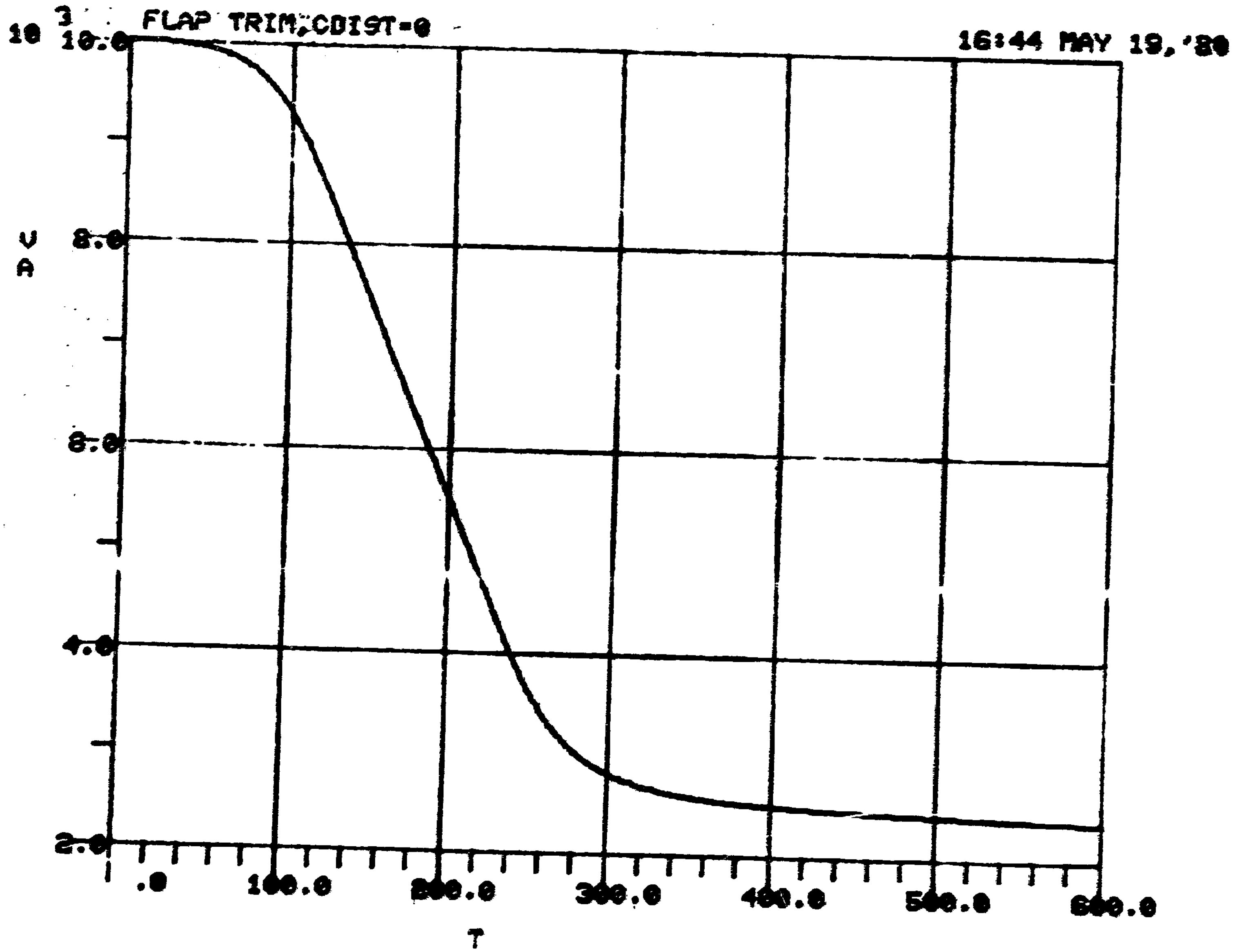

Figure V-4 Velocity, Titan Trajectory

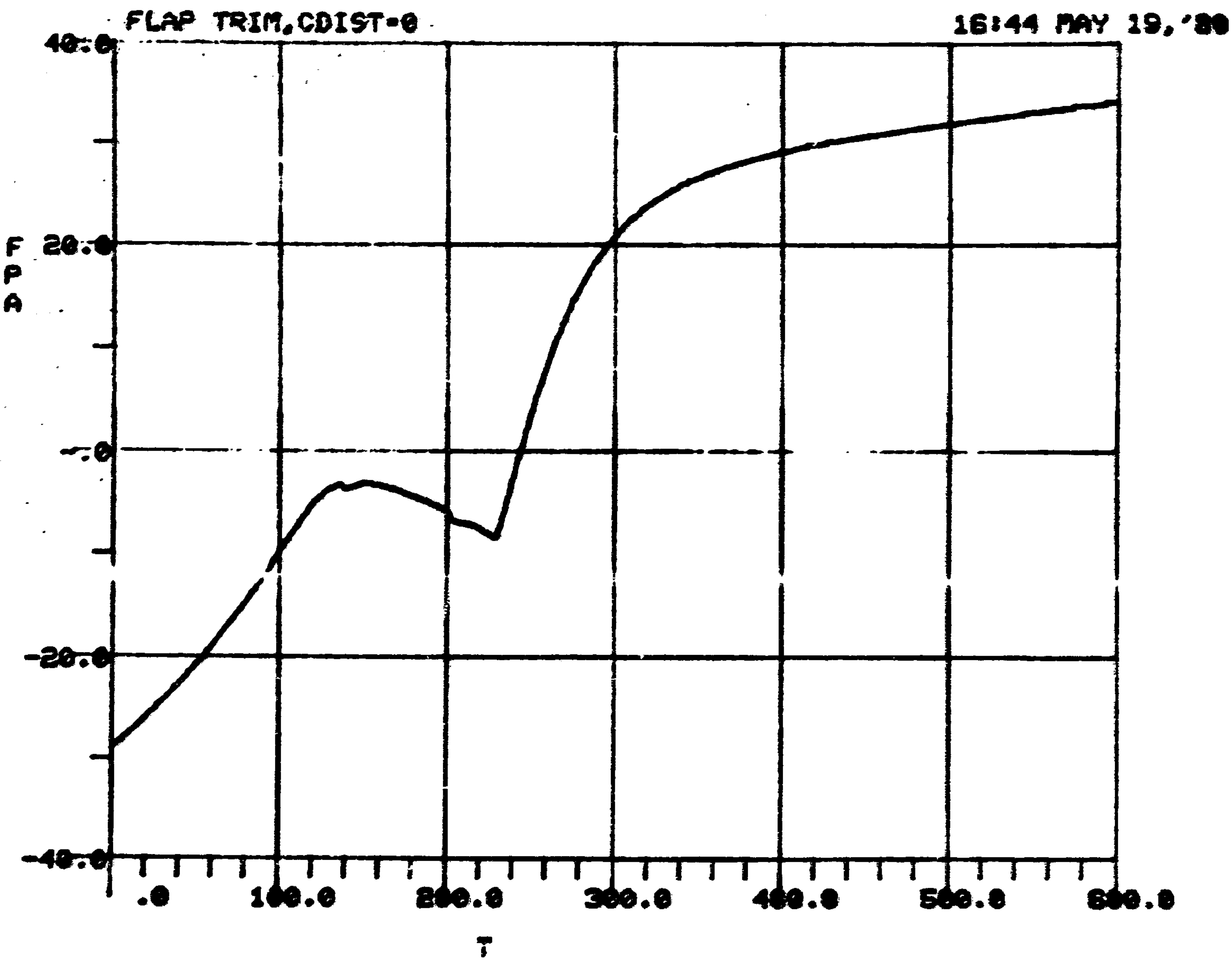

Figure [illegible]-5 Flight Path Angle, Titan Trajectory

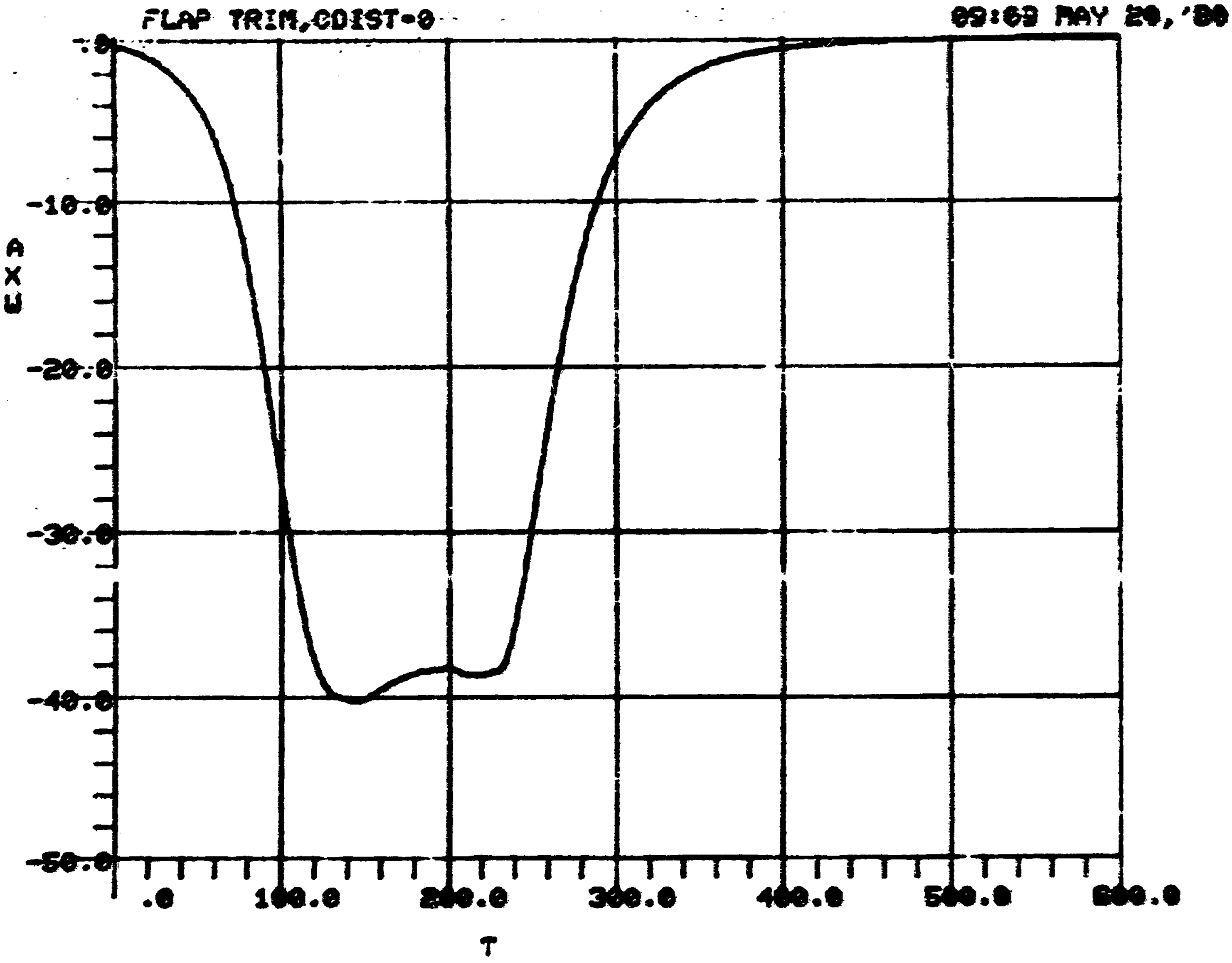

Figure V-6 Drag, Titan Trajectory

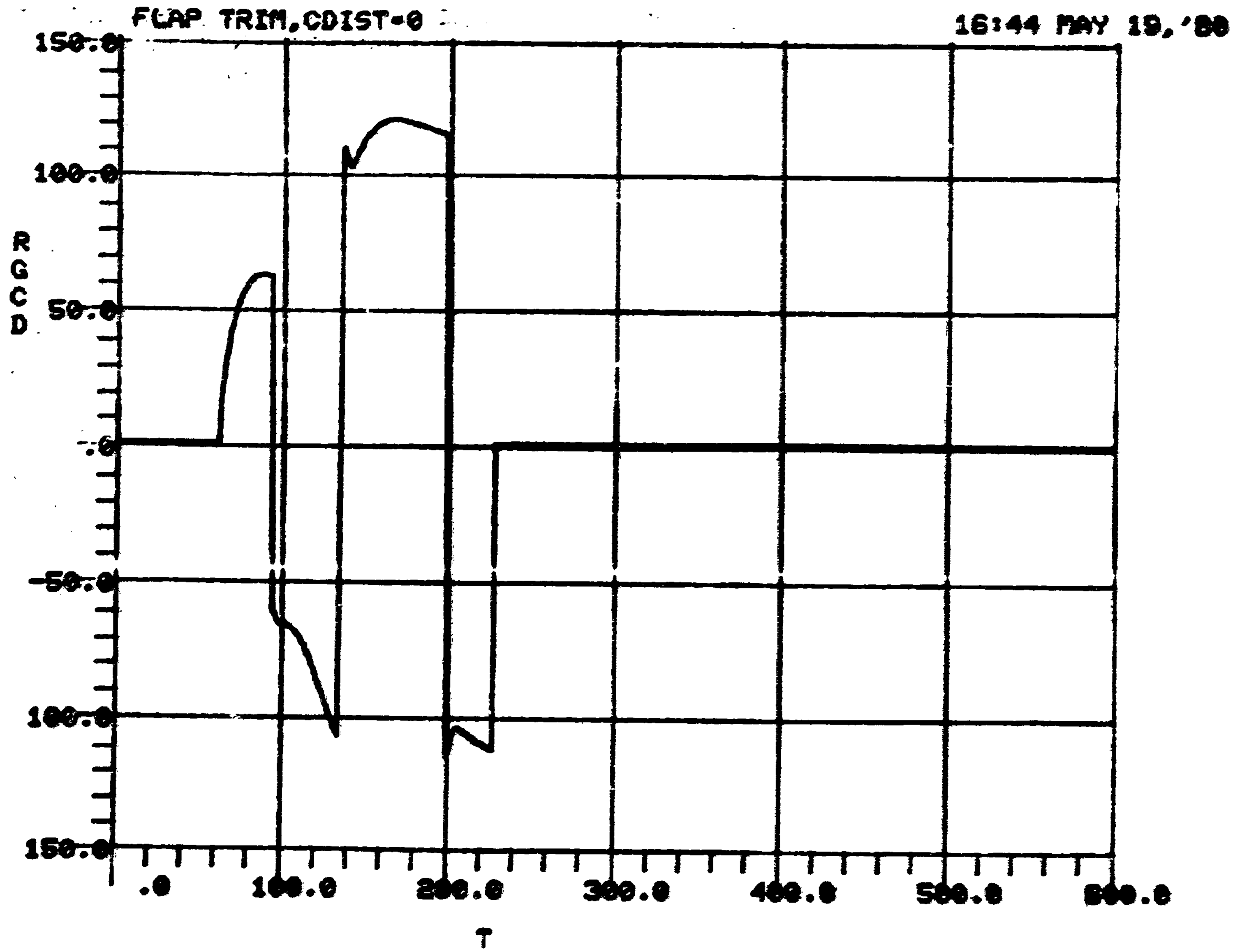

Figure V-7 Bank Angle Command, Titan Trajectory

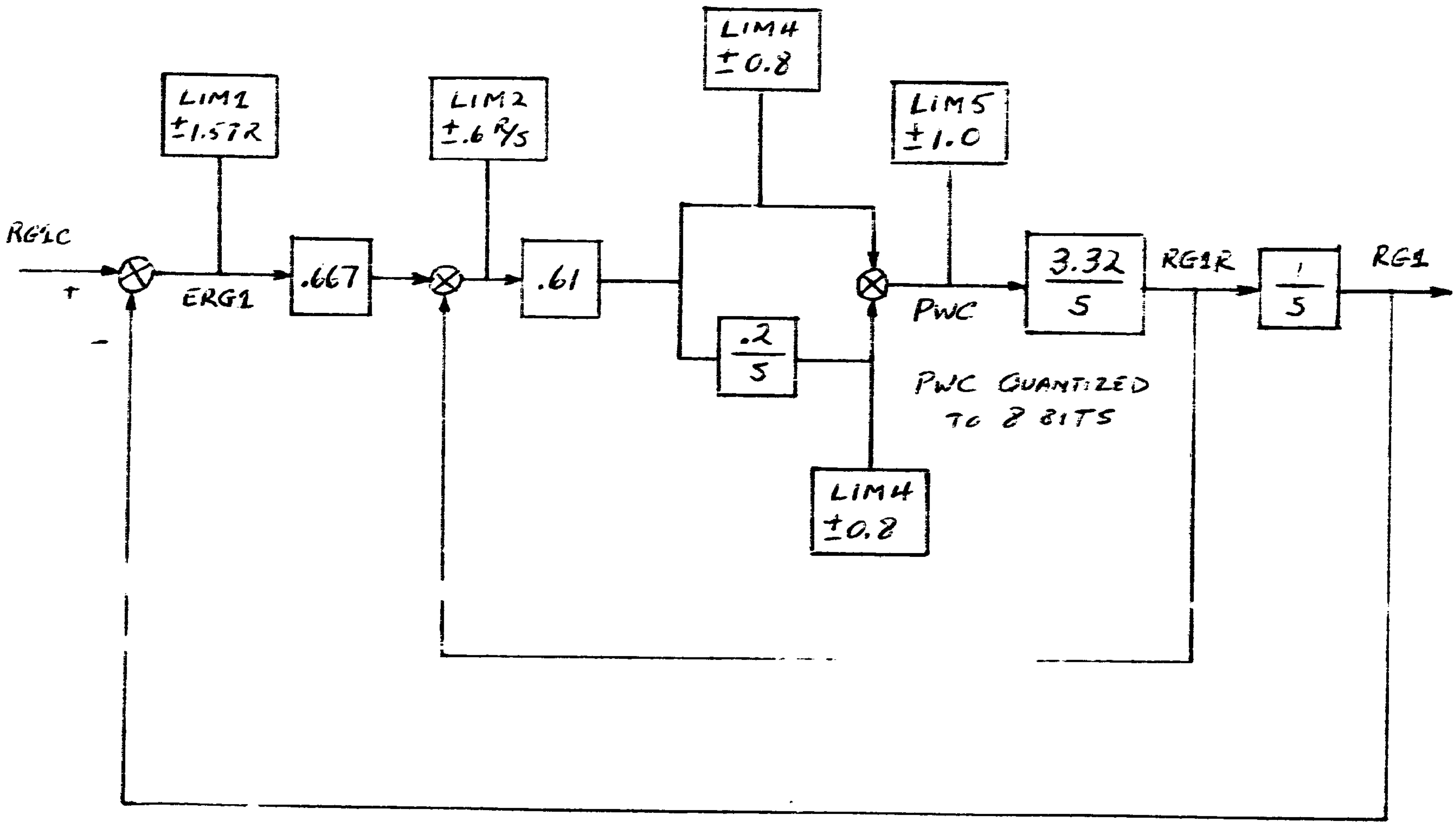

Figure V-8 PWM PCS Roll Control

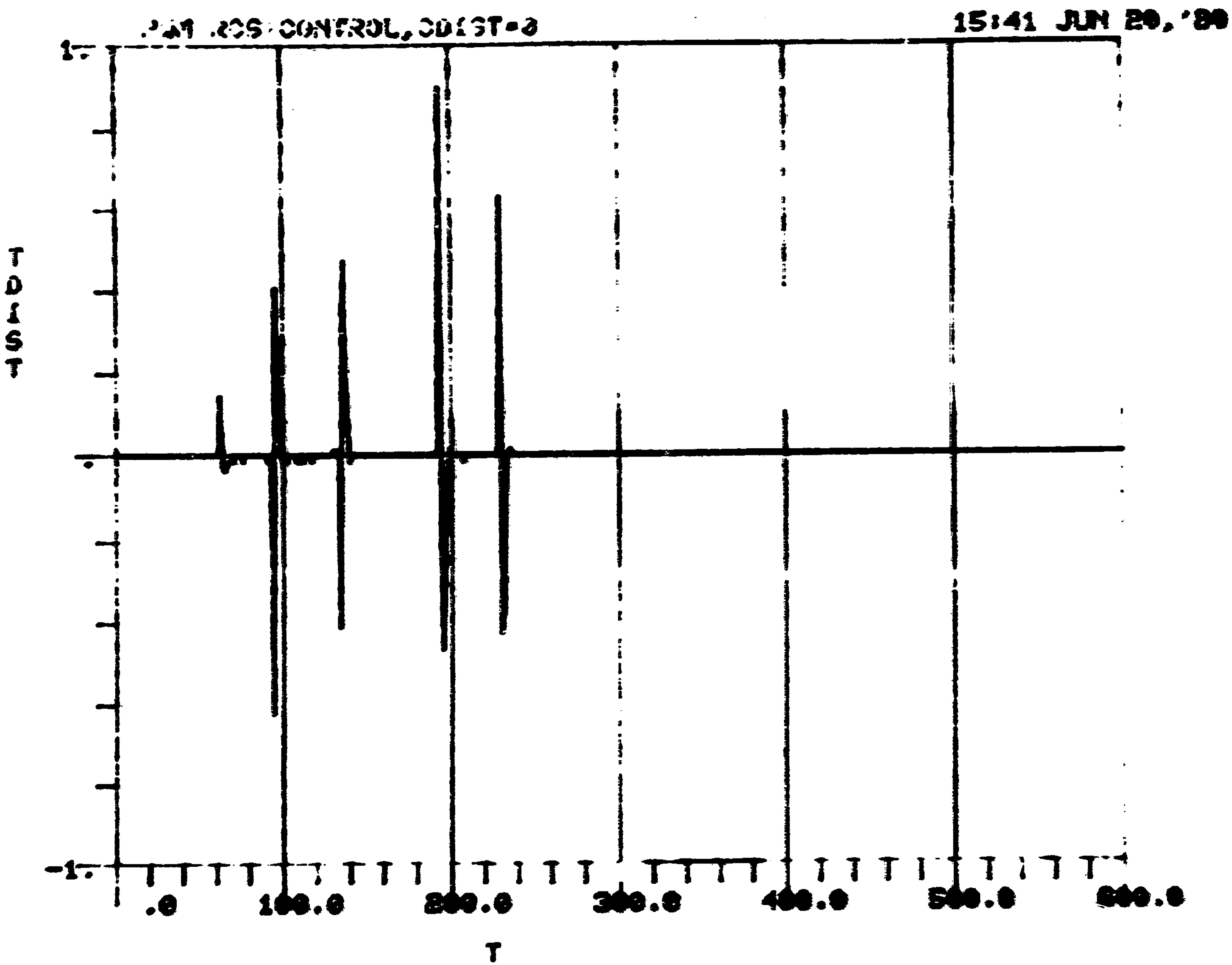

Figure V-9 Average Thruster Acceleration, PWM Roll Control

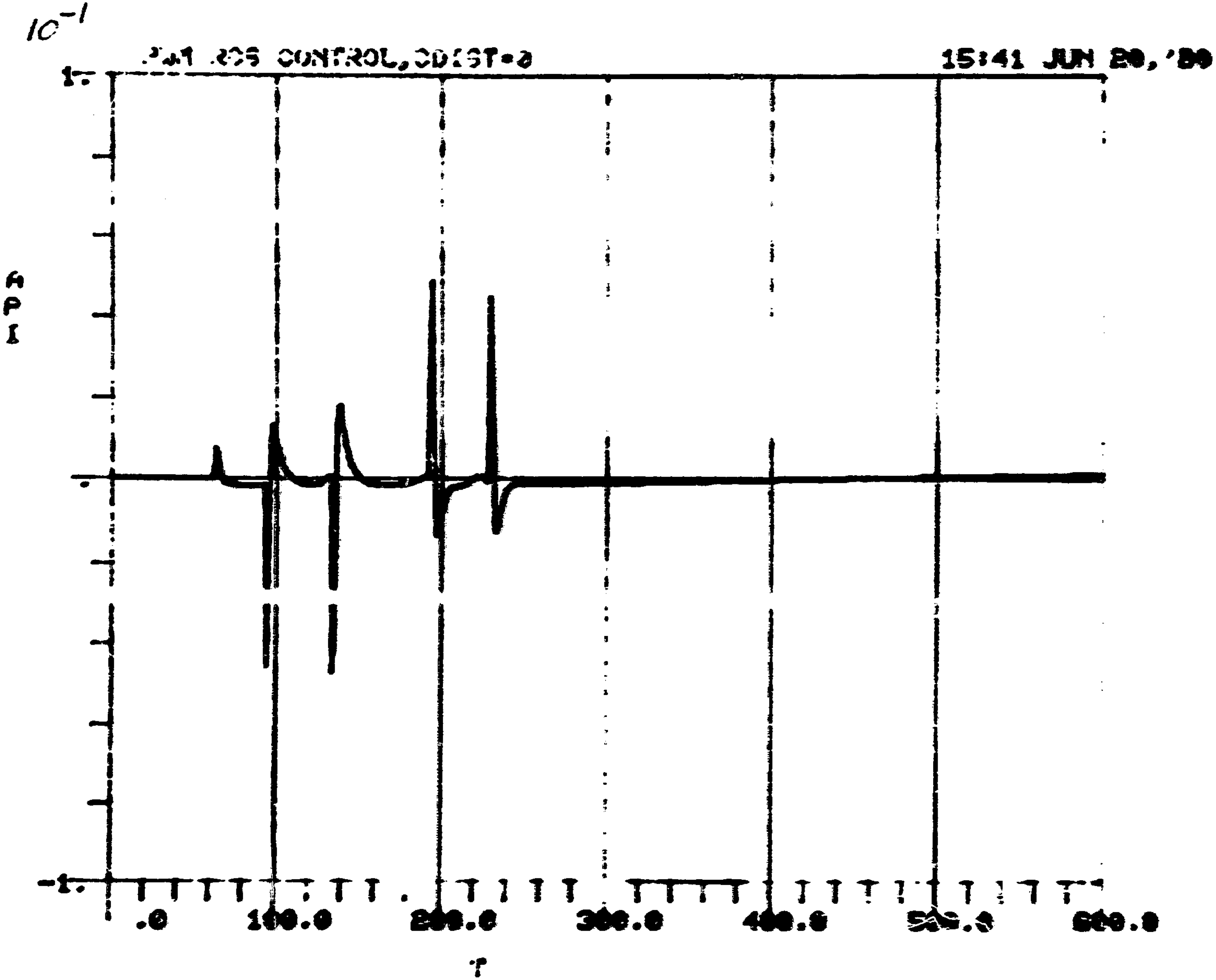

Figure V-10 Autopilot Integrator Signal, YAW Roll Control

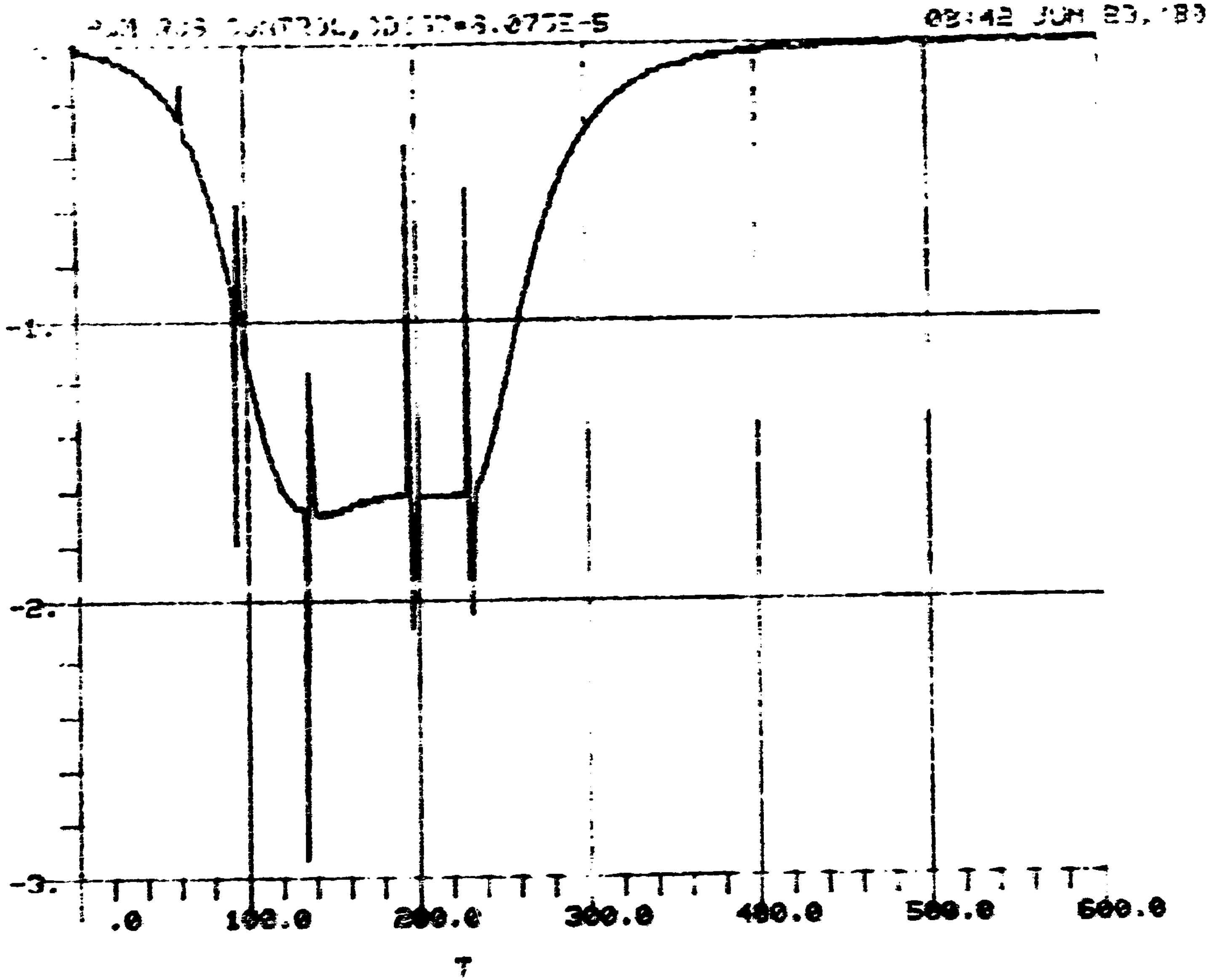

Figure V-11 Average [illegible] Acceleration, [illegible]

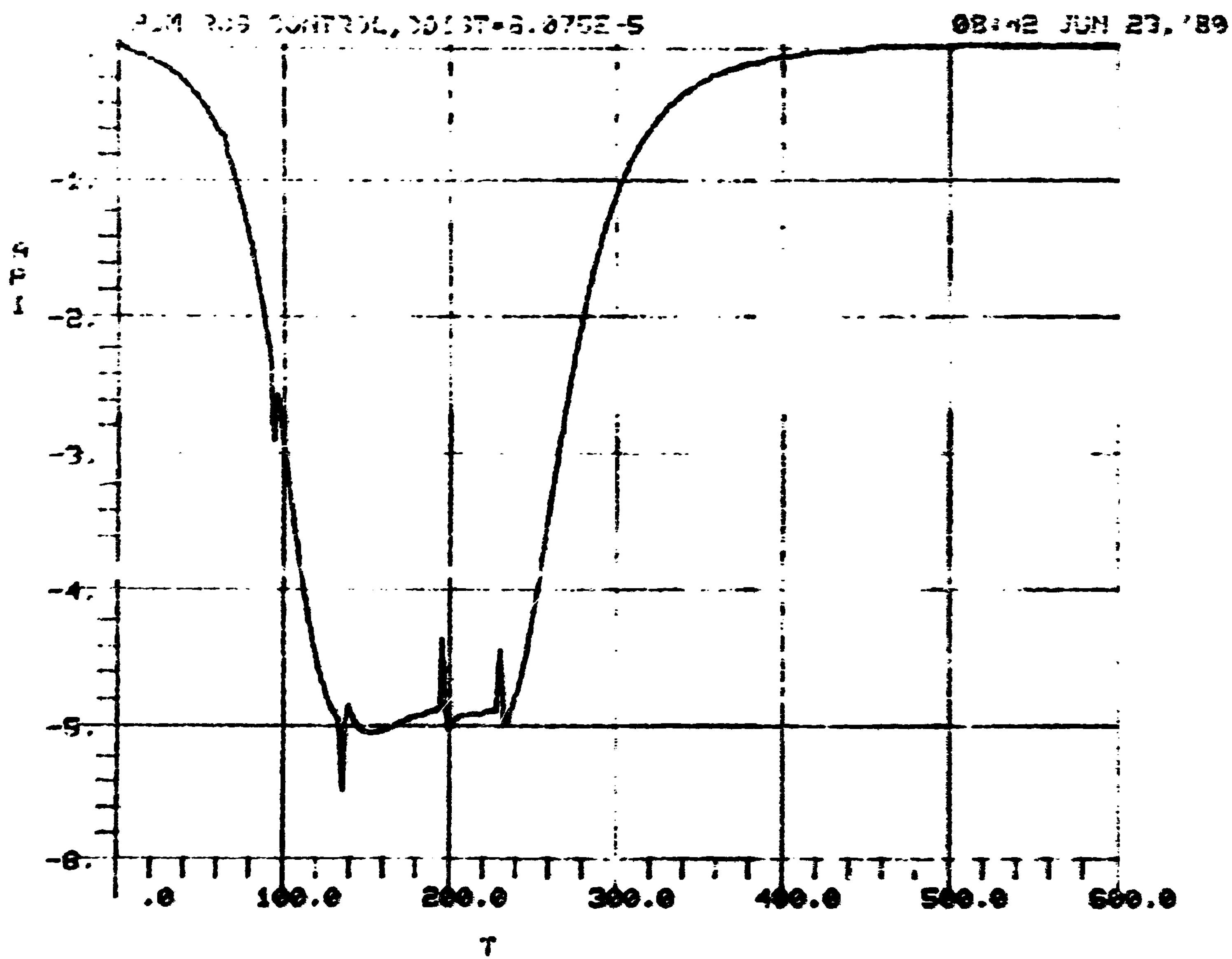

Figure V-12 Autopilot Integrator Signal, PWM Roll Control

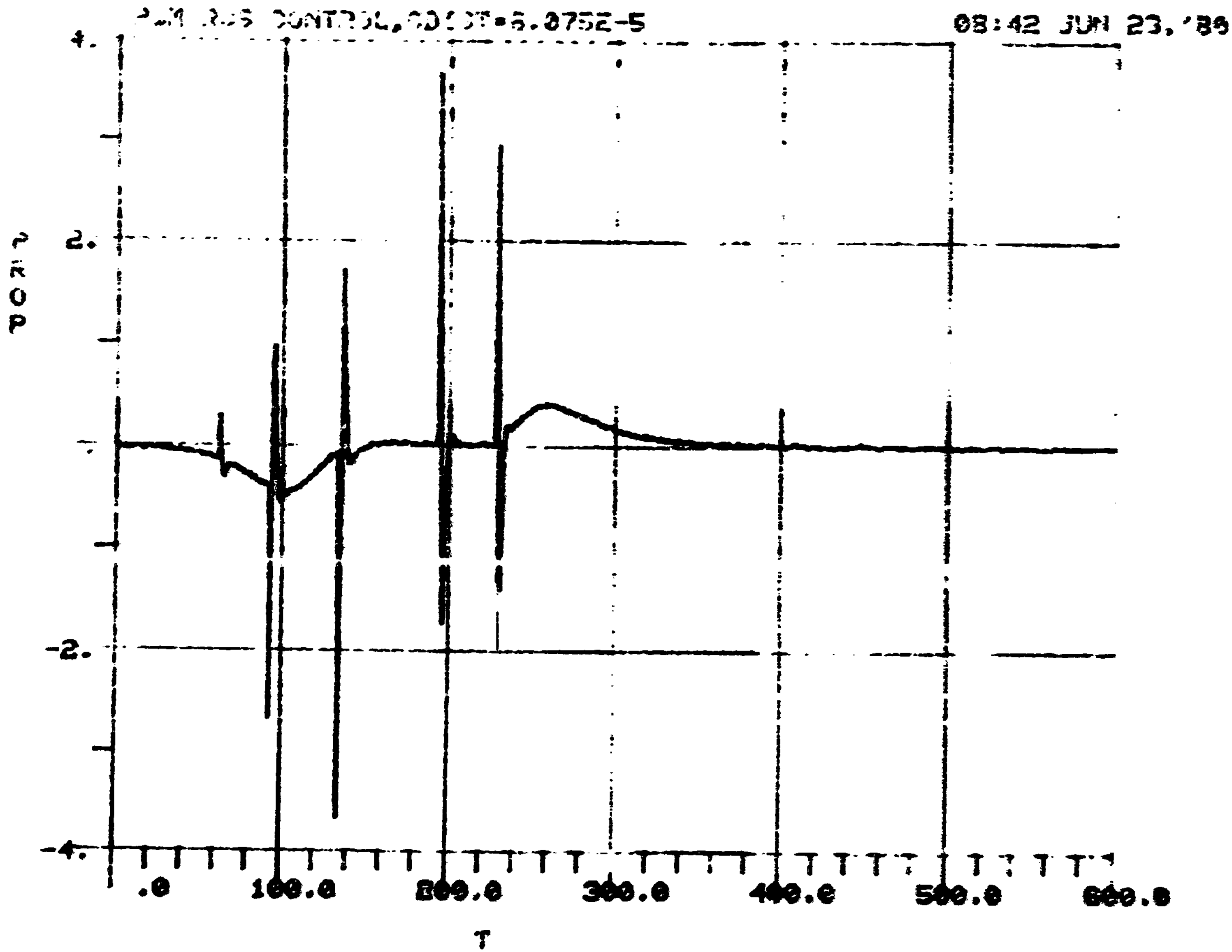

Figure V-15 Autopilot Proportional Signal, PWM Roll Control

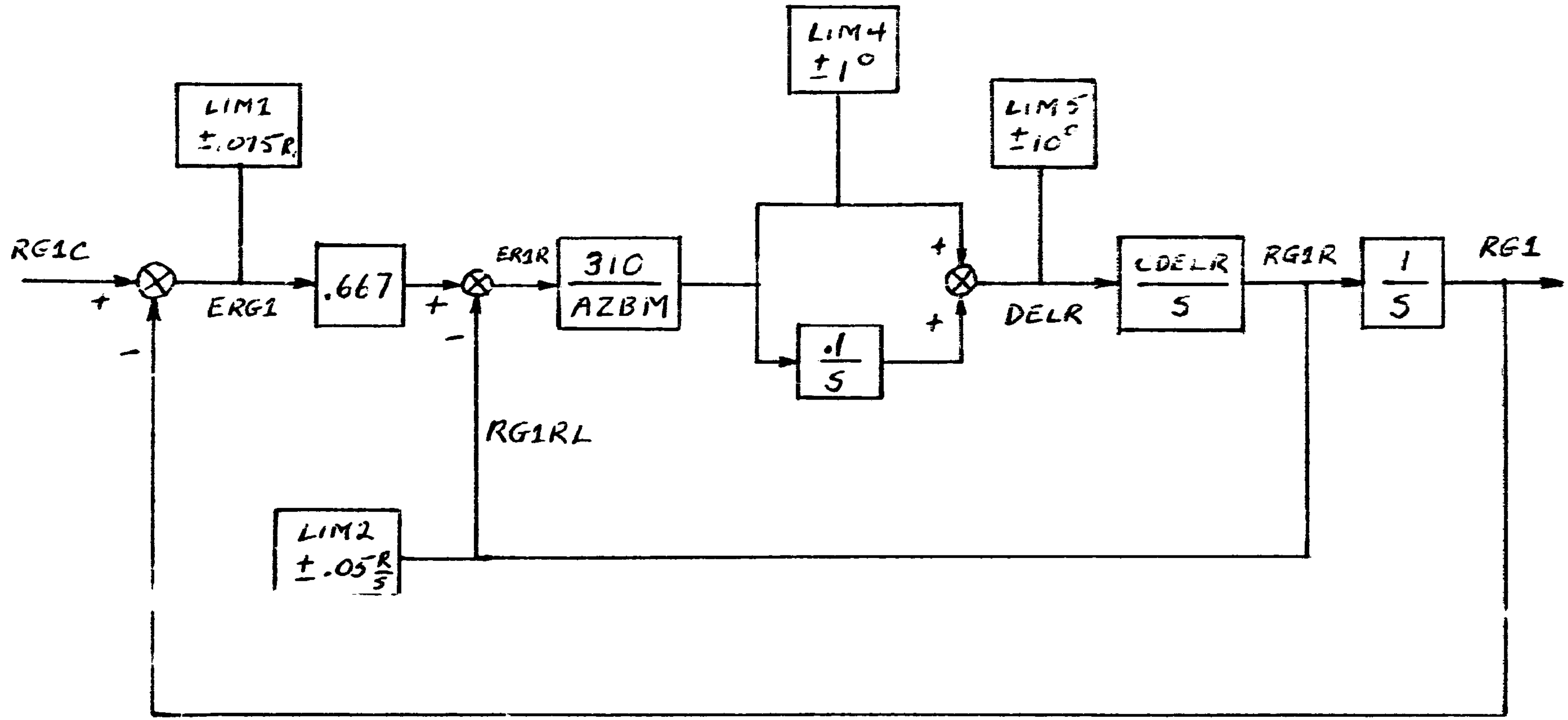

$$AZBM = -AZB \text{ WITH MINIMUM VALUE } 1.24\ m/s^2$$

$$\omega_{RL} = \frac{K2 * M * CDELR}{C_N * A} = 1.06\ RAD/SEC$$

Figure V-14 Flap Trim Control

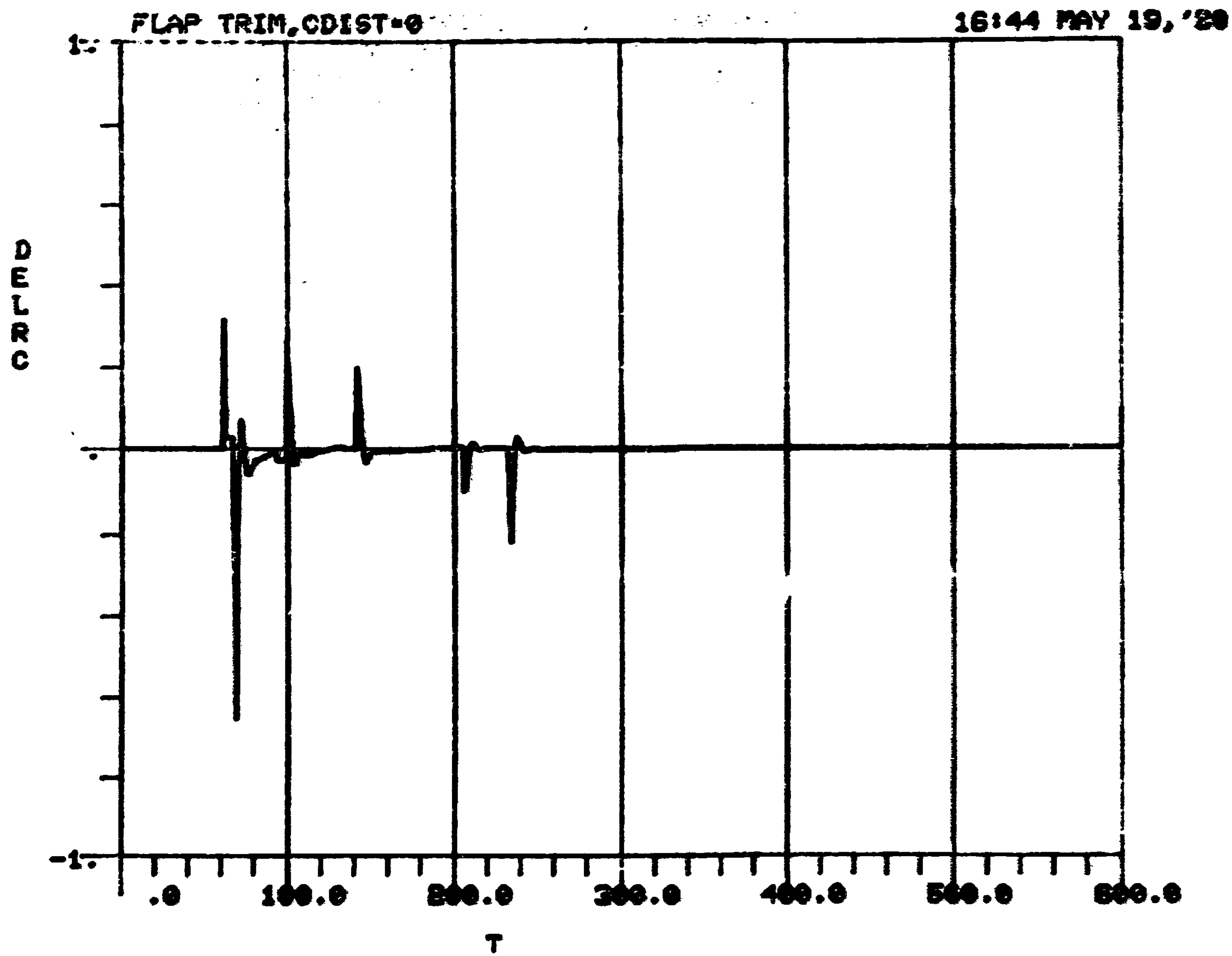

Figure V-15 Roll Flap Deflection Command, Flap Trim Control

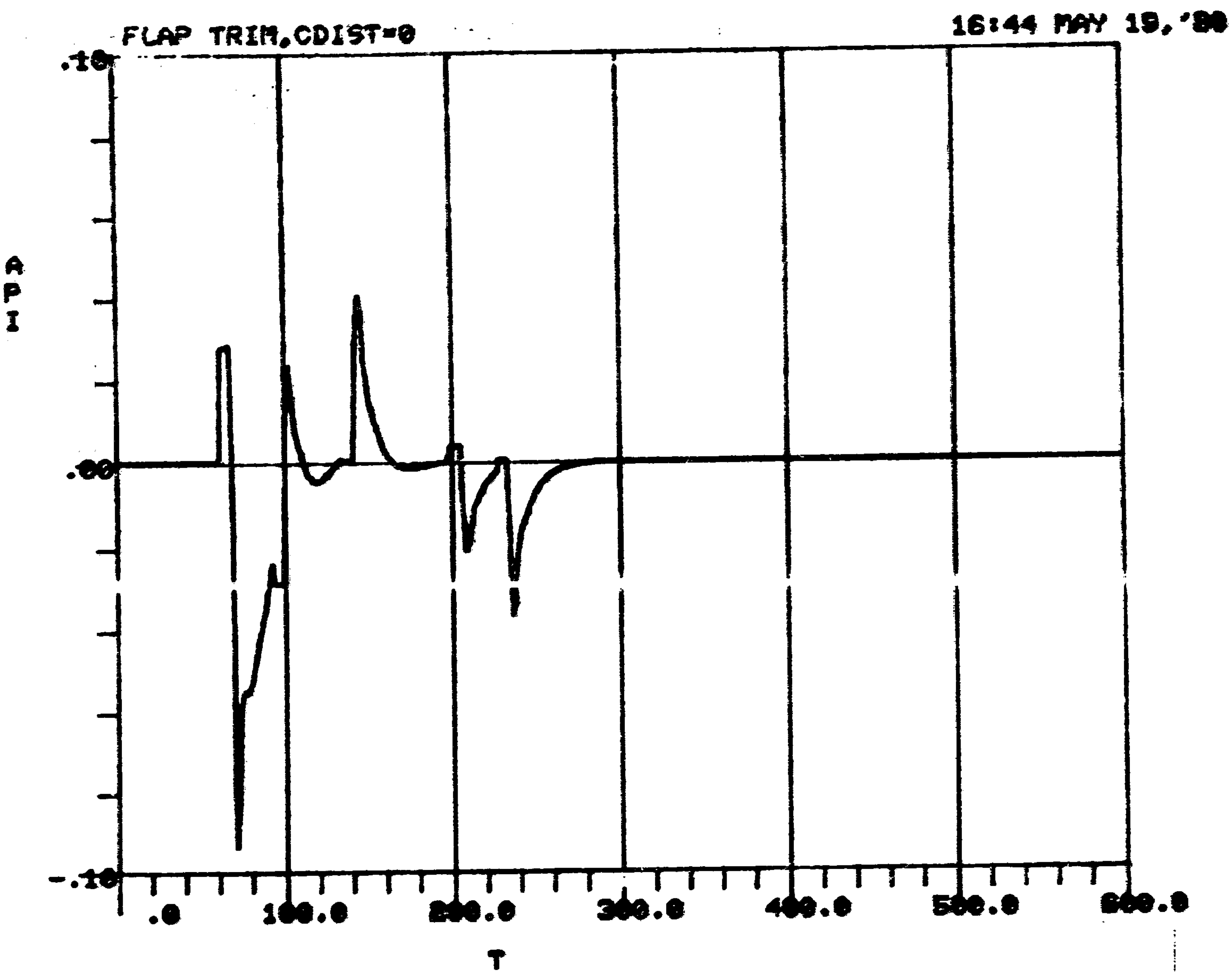

Figure V-16 Autopilot Integrator Signal, Flap Trim Control

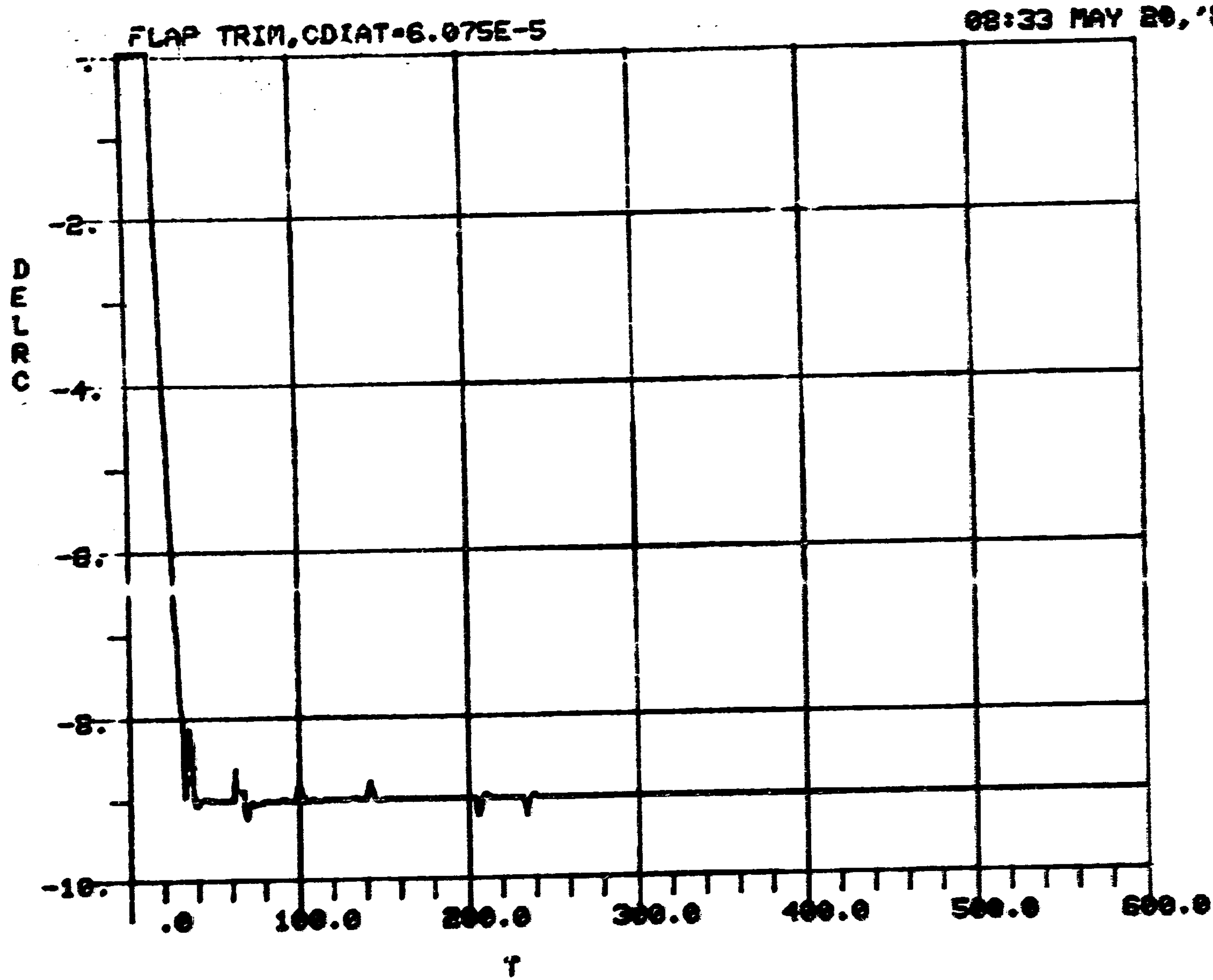

Figure V-17 Roll Flap Deflection Command, Flap Trim Control

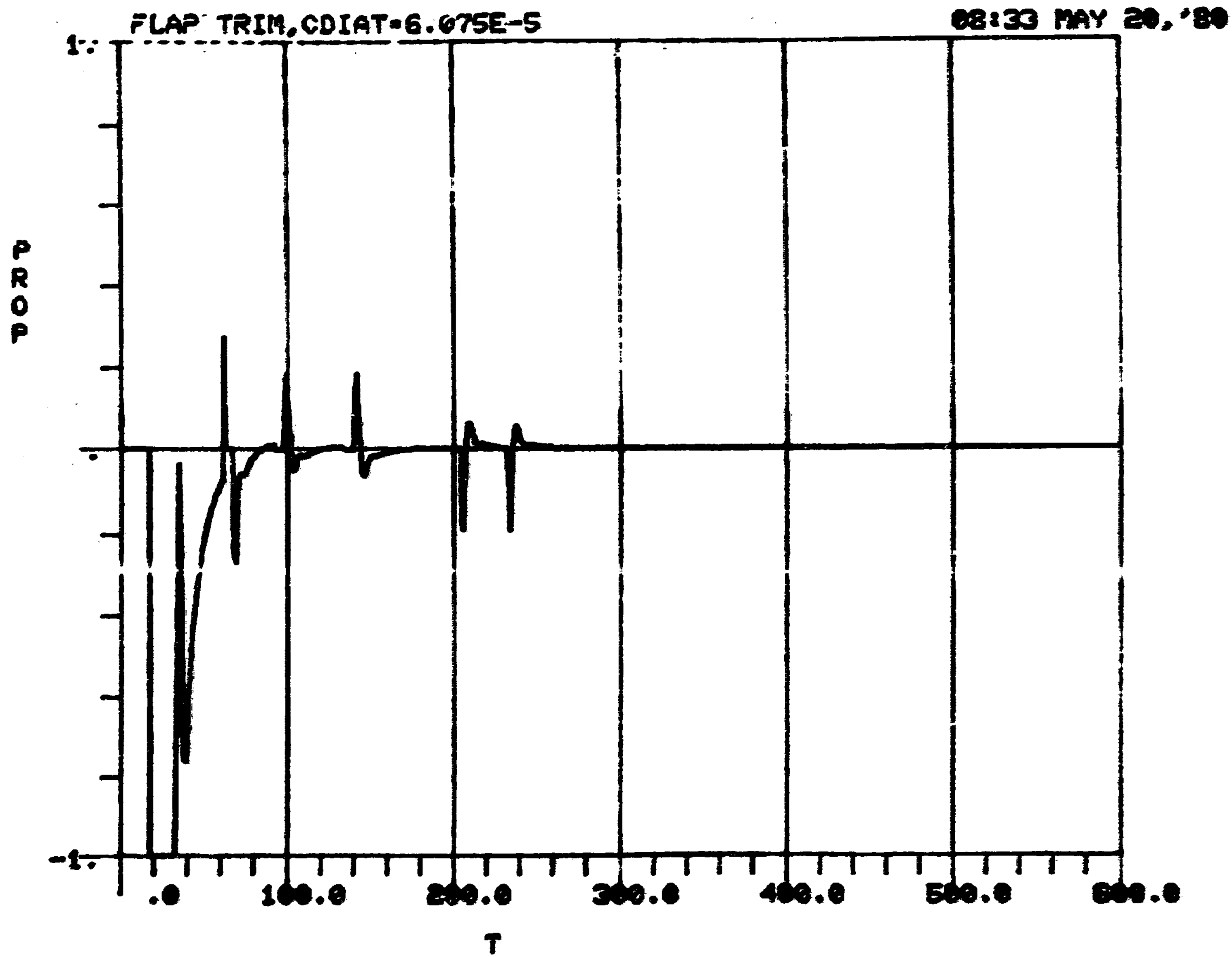

Figure V-18 Autopilot Proportional Signal, Flap Trim Control

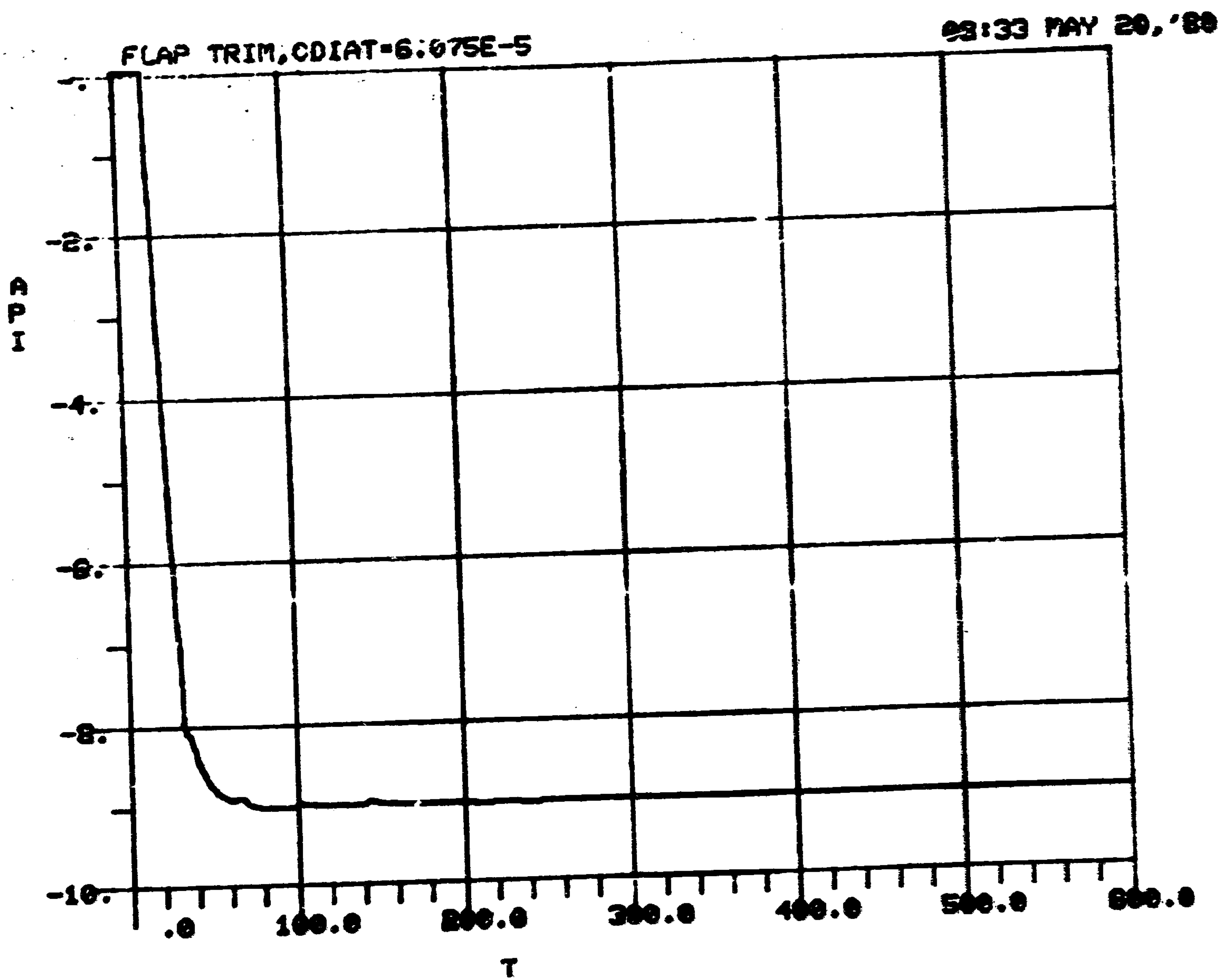

Figure V-19 Autopilot Integrator Signal, Flap Trim Control

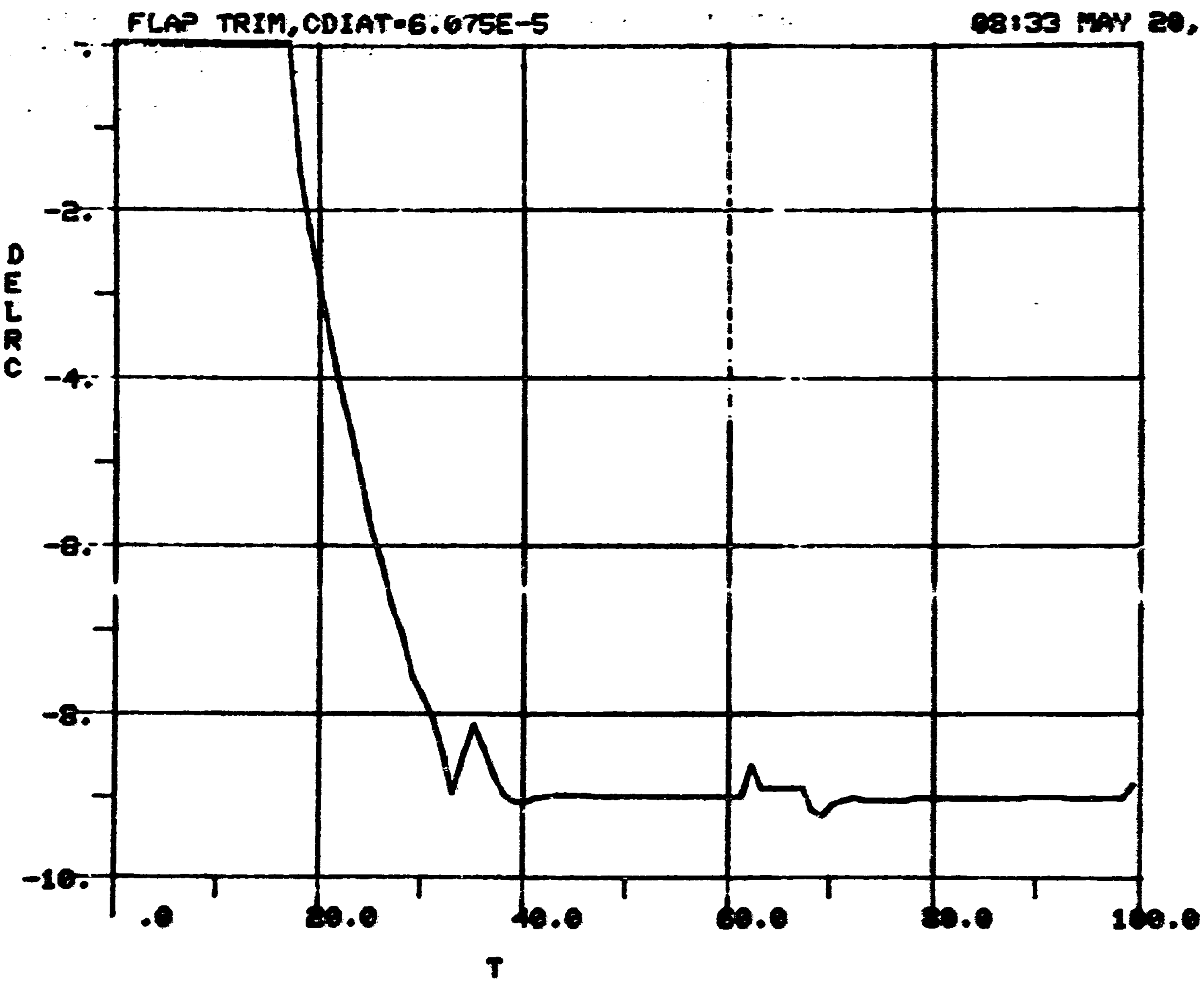

Figure V-20 Roll Flap Deflection Command, Flap Trim Control

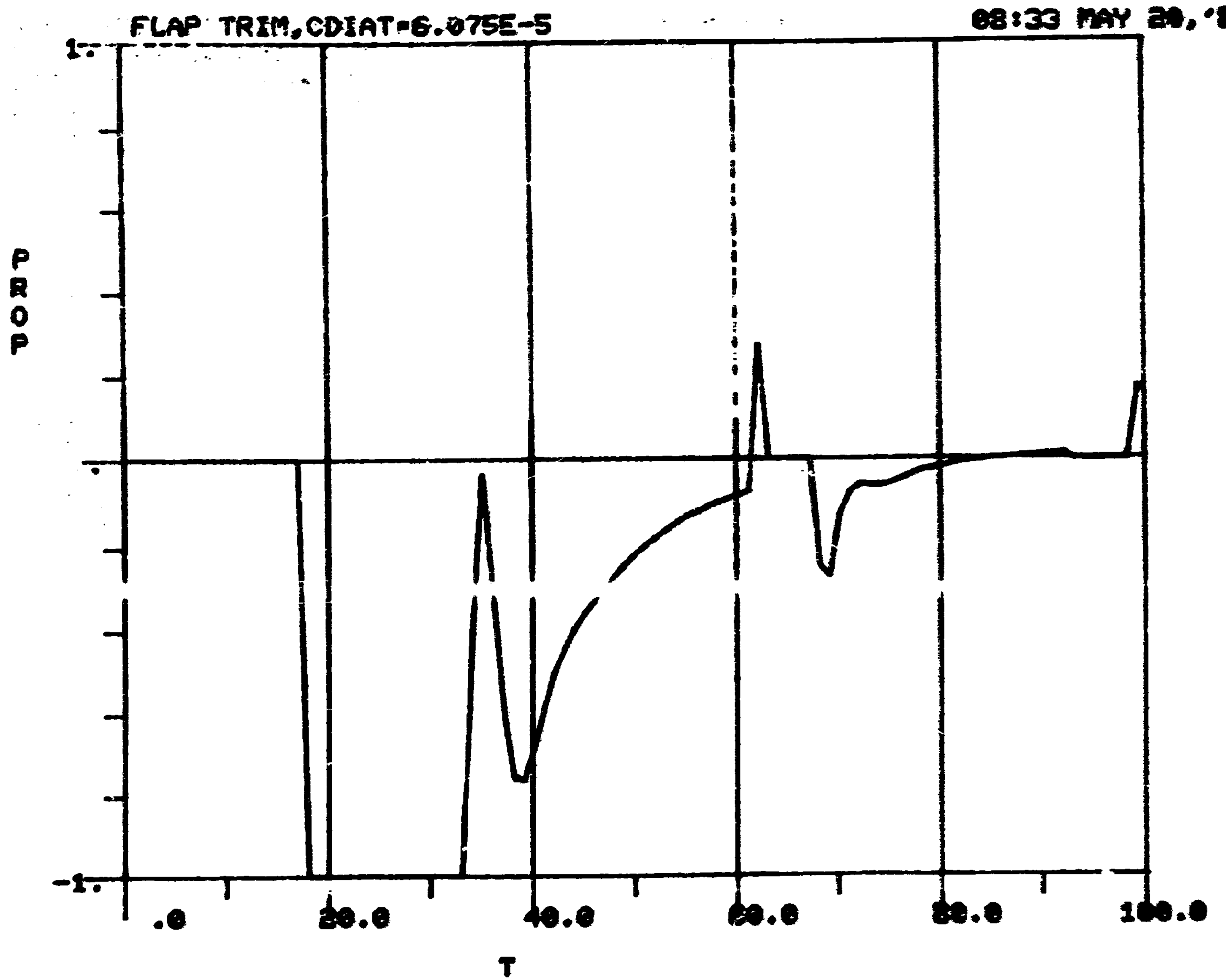

Figure V-21 Autopilot Proportional Signal, Flap Trim Control

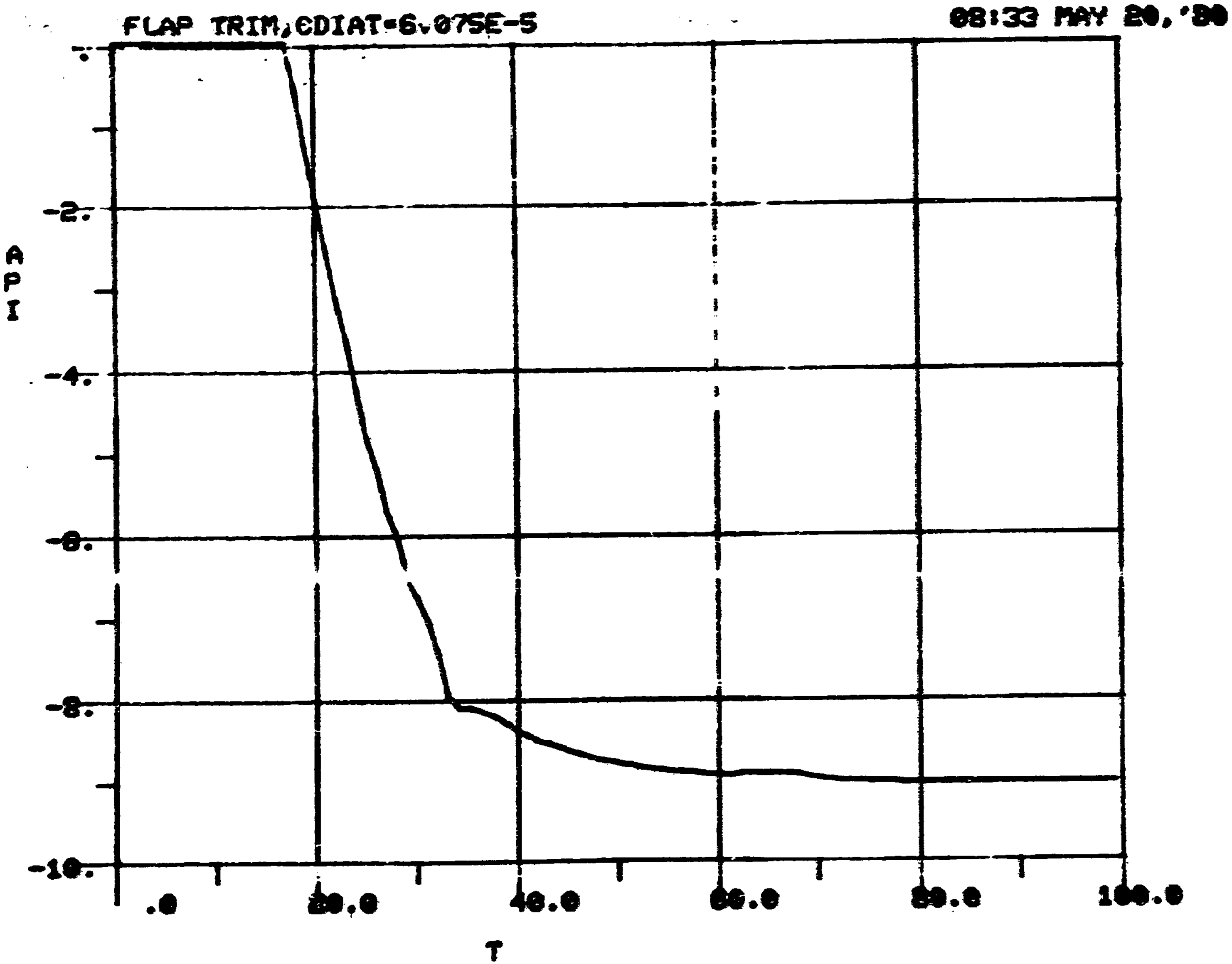

Figure V-22 Autopilot Integrator Signal, Flap Trim Control

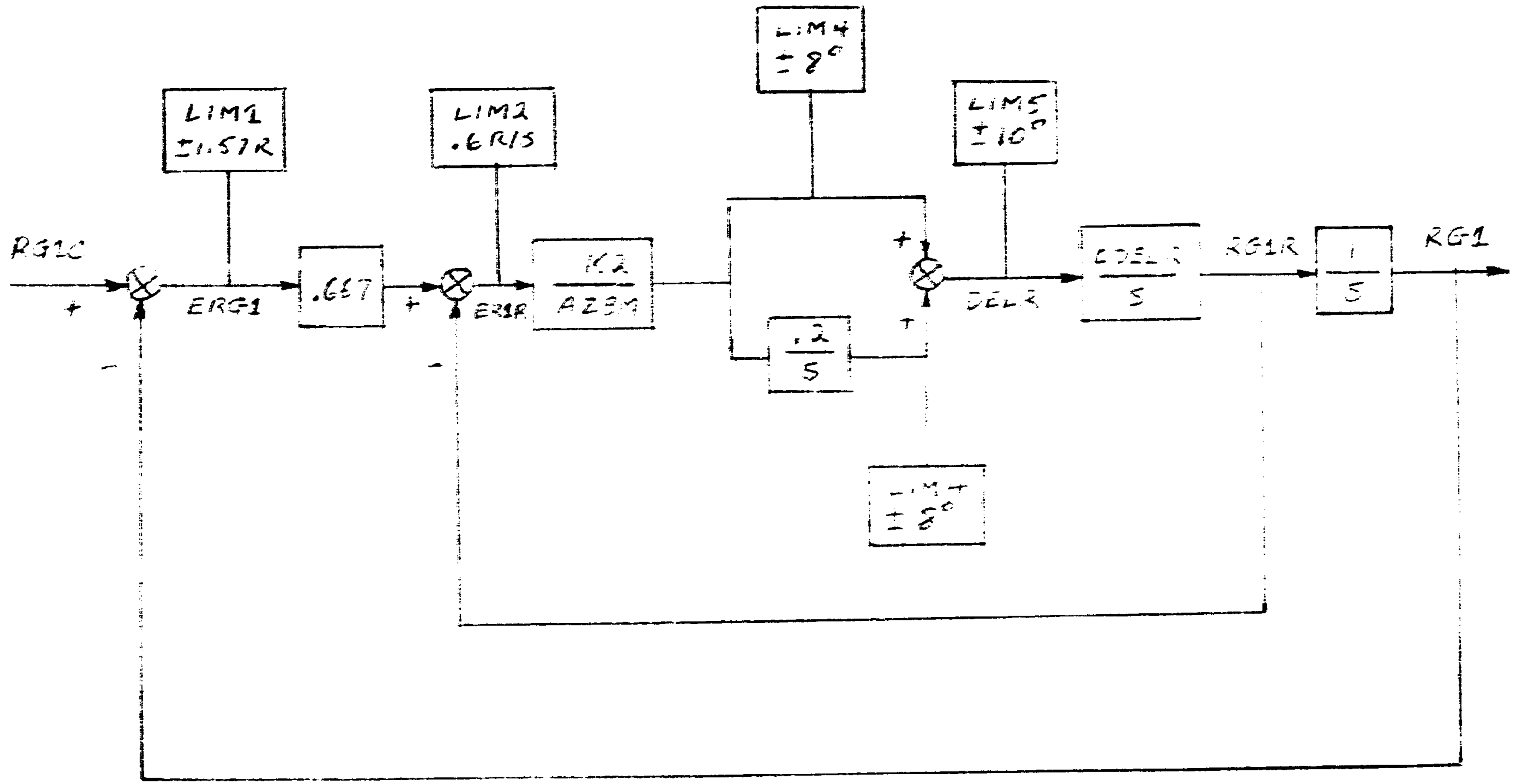

AZBM = − AZB WITH MINIMUM VALUE $1.24\ m/s^2$

Figure V-23 Flap Control System

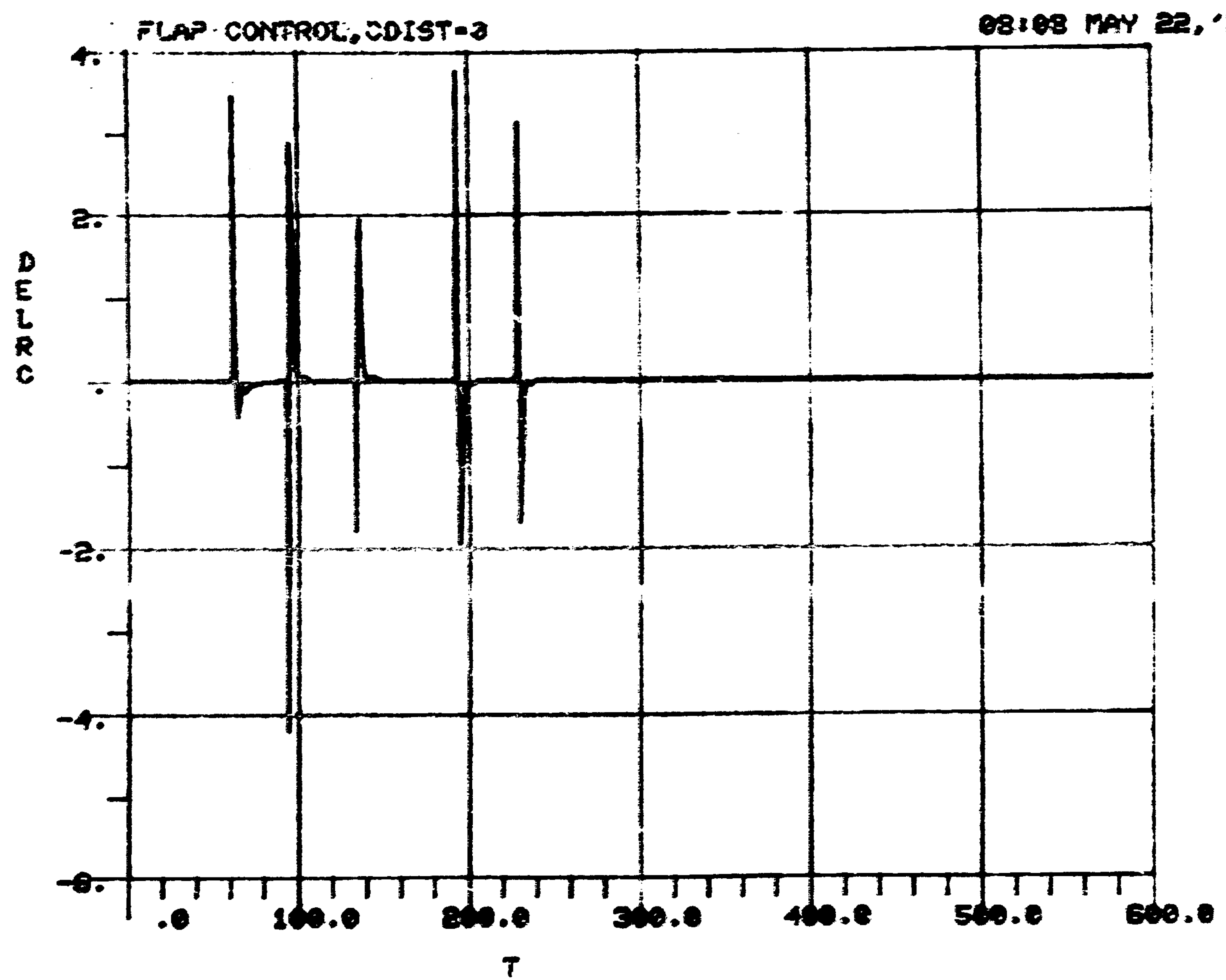

Figure V-2? Roll Flap Deflection Command, Flap Control

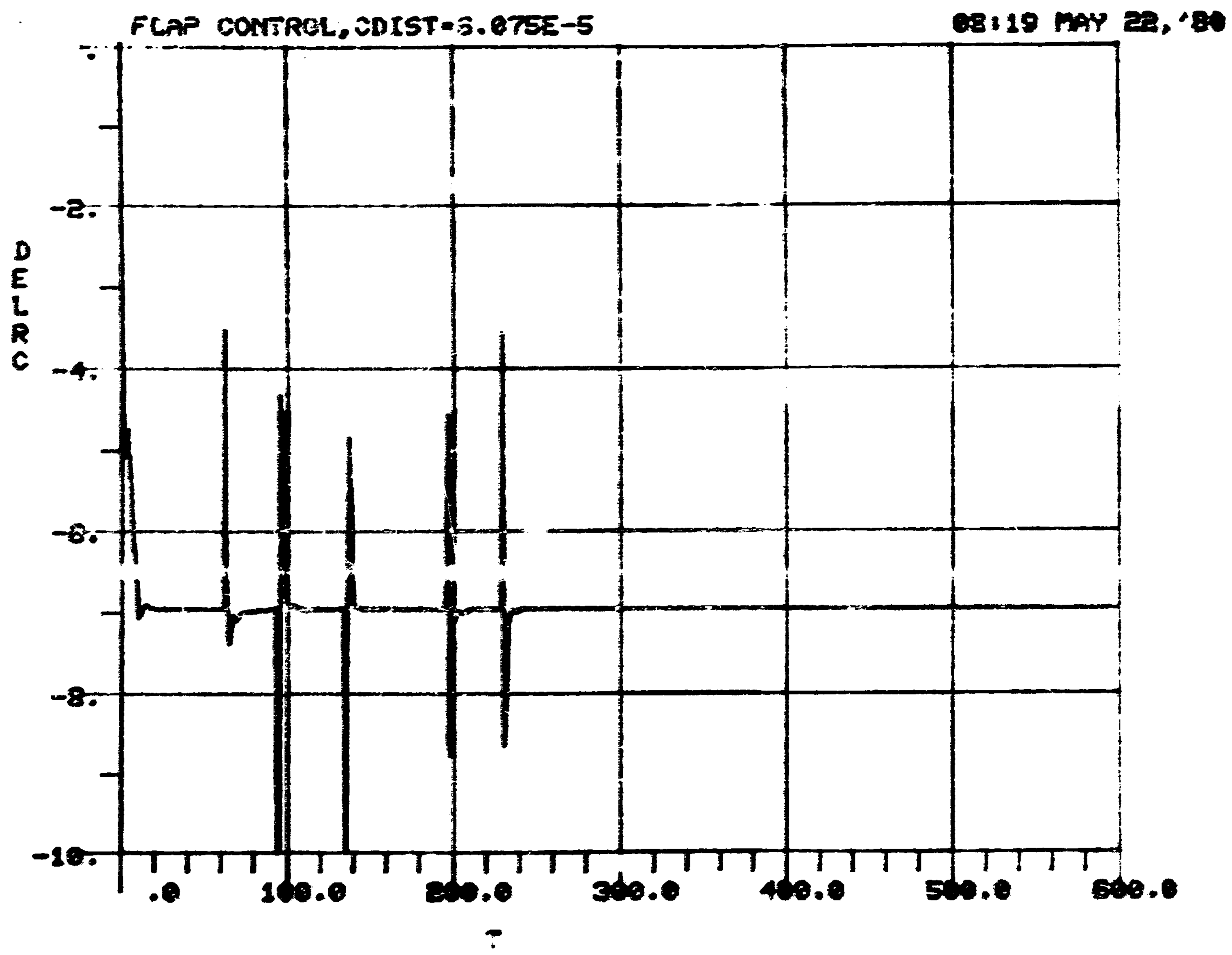

Figure V-25 Roll Flap Deflection Command, Flap Control

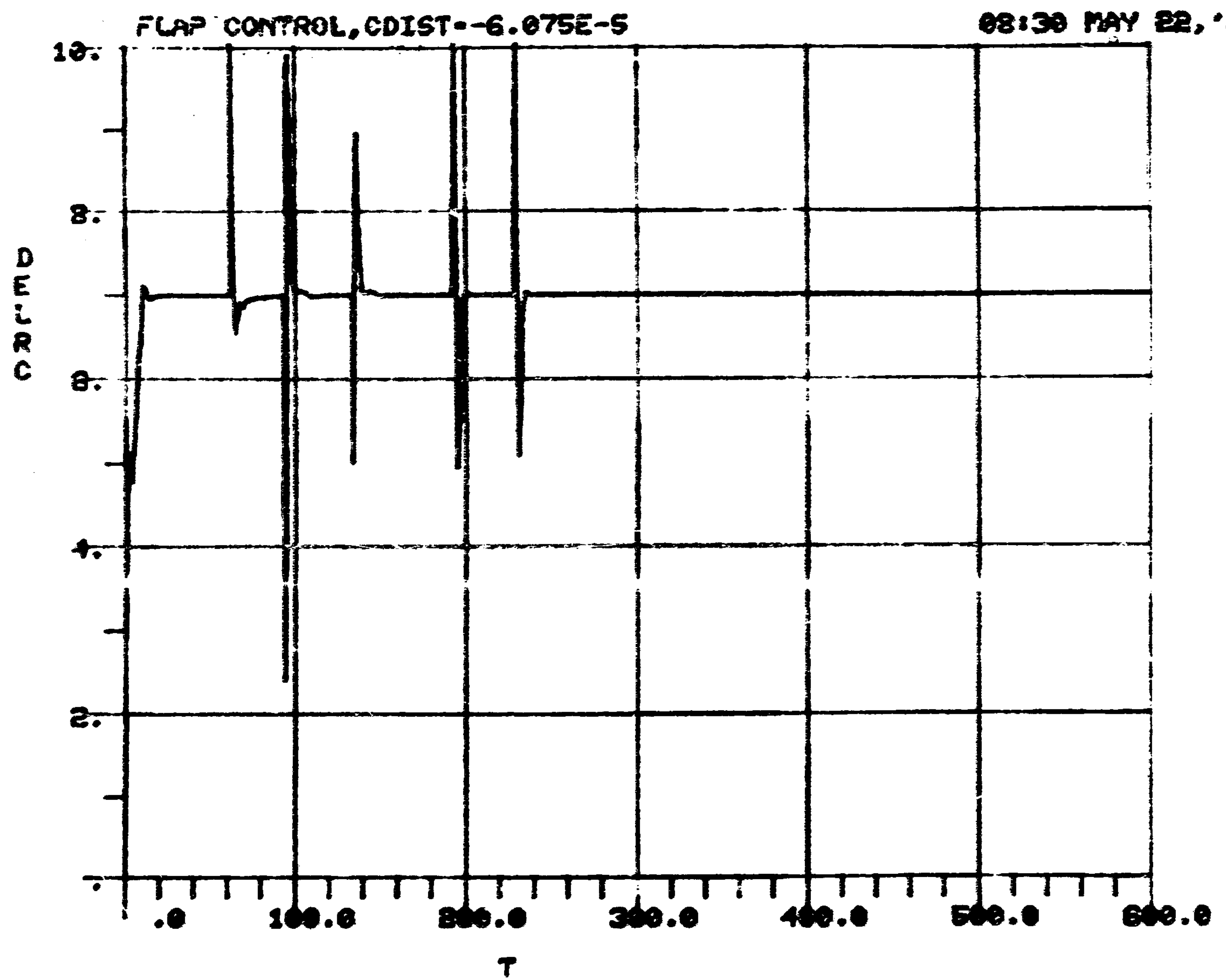

Figure V-26 Roll Flap Deflection Command, Flap Control

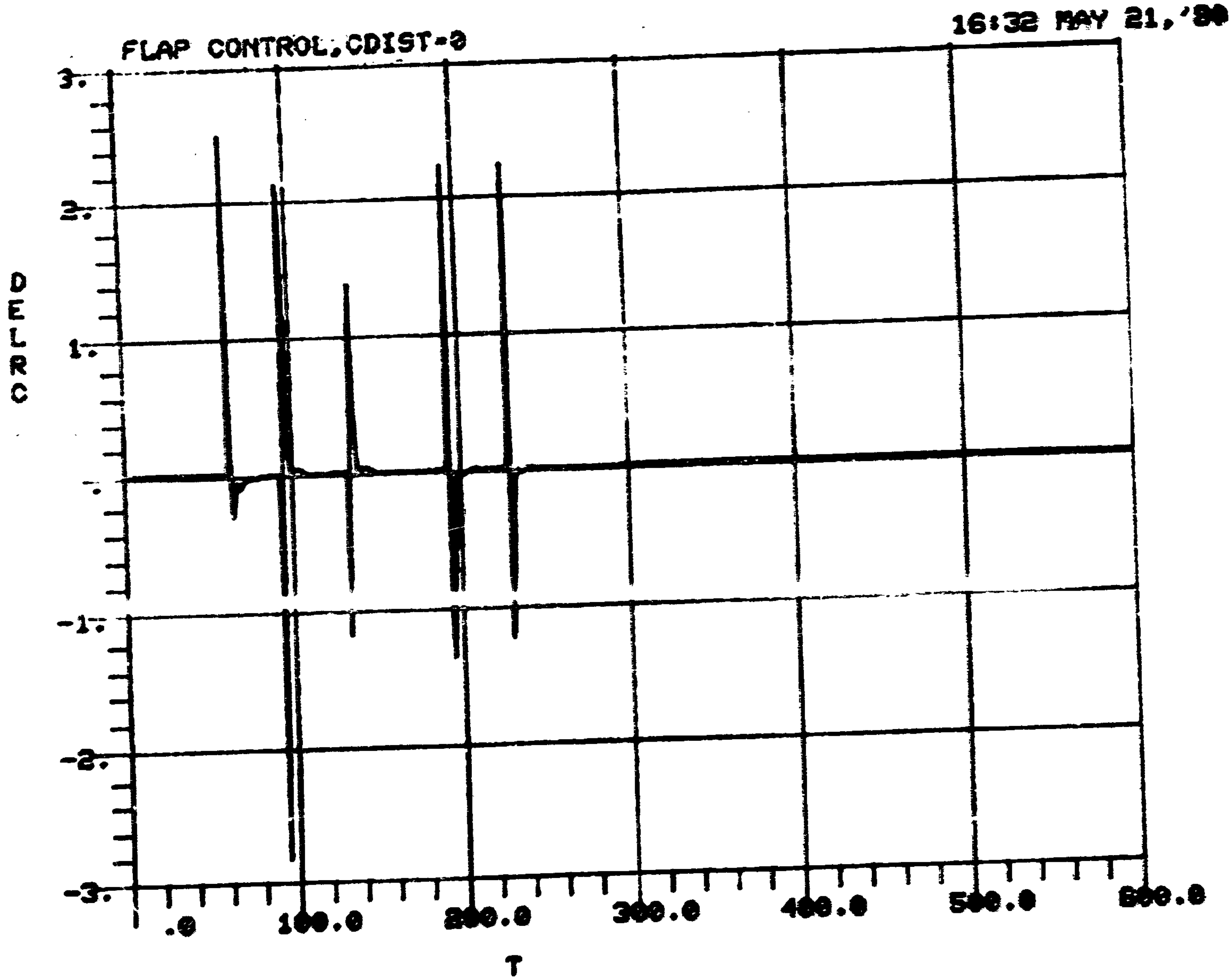

Figure V-27 Roll Flap Deflection Command, Flap Control

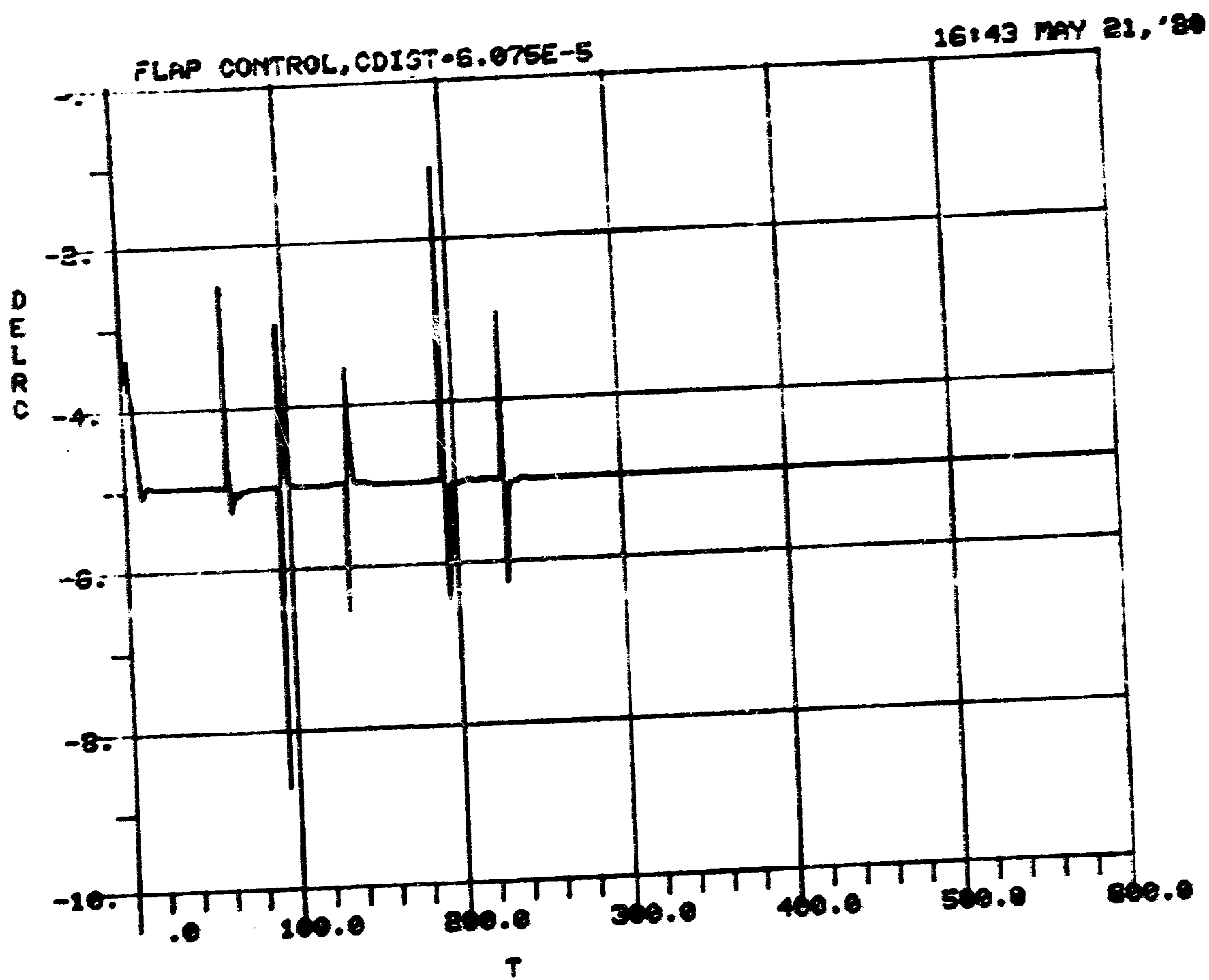

Figure V-28 Roll Flap Deflection Command, Flap Control

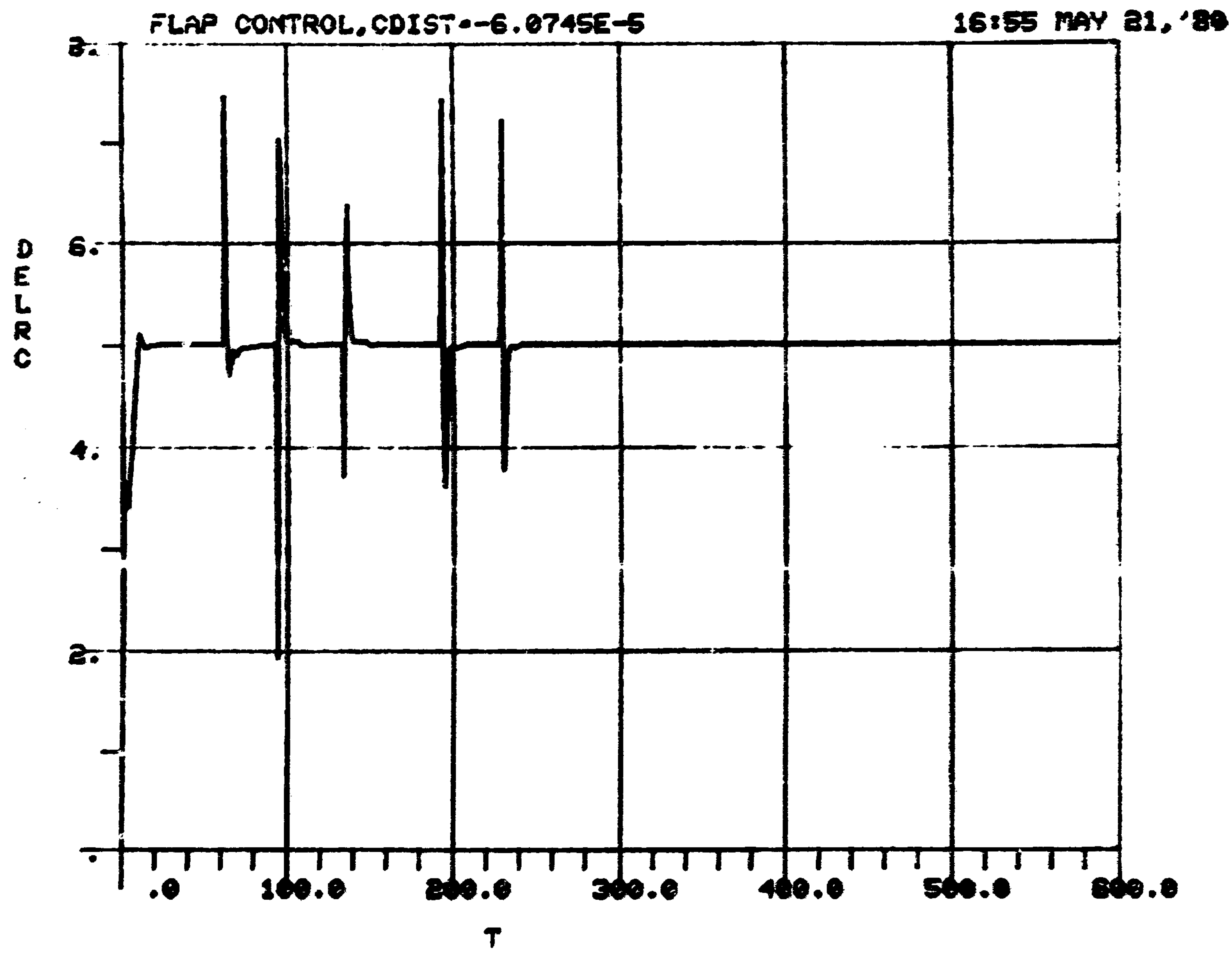

Figure V-29 Roll Flap Deflection Command, Flap Control

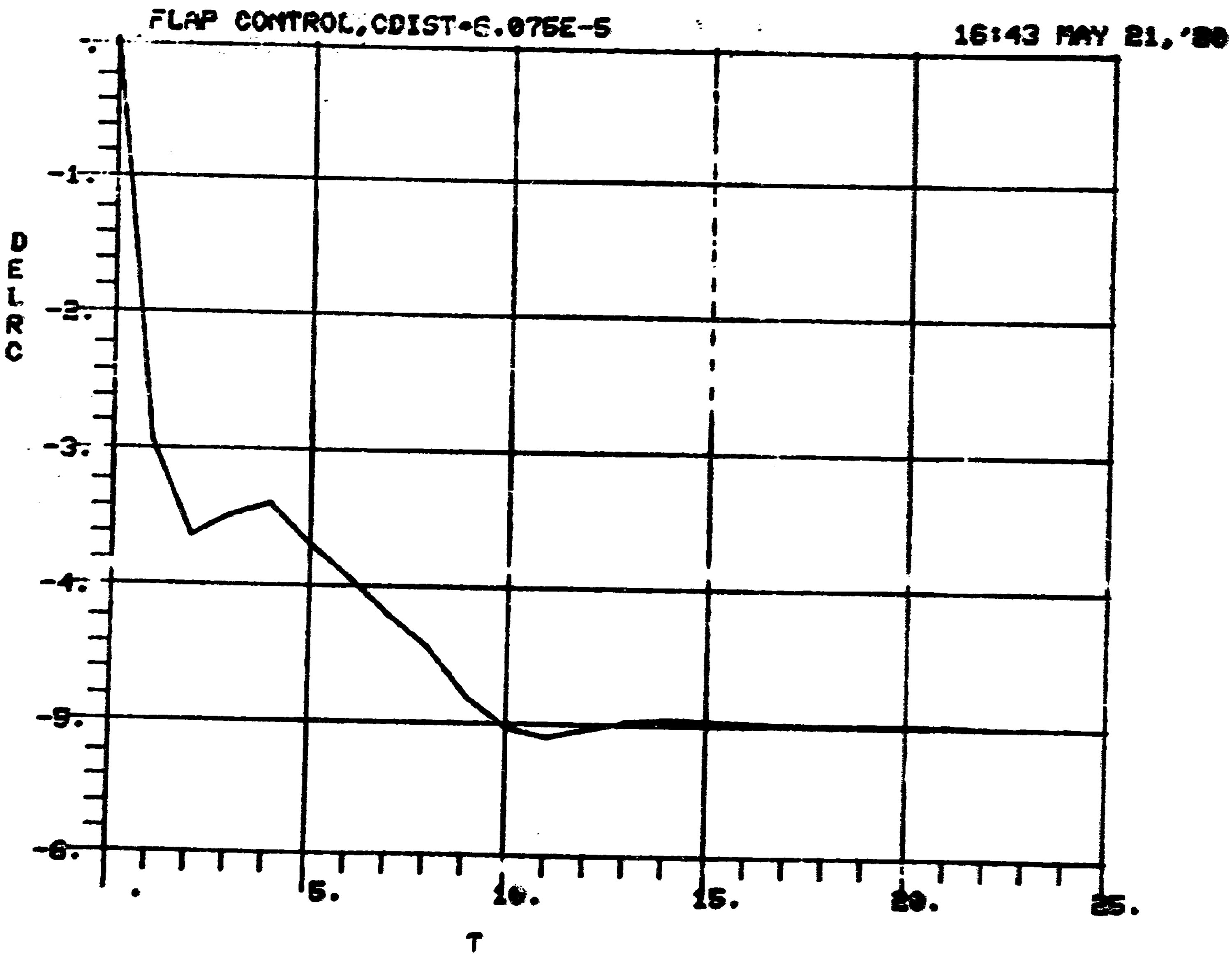

Figure V-30 Roll Flap Deflection Command, Flap Control

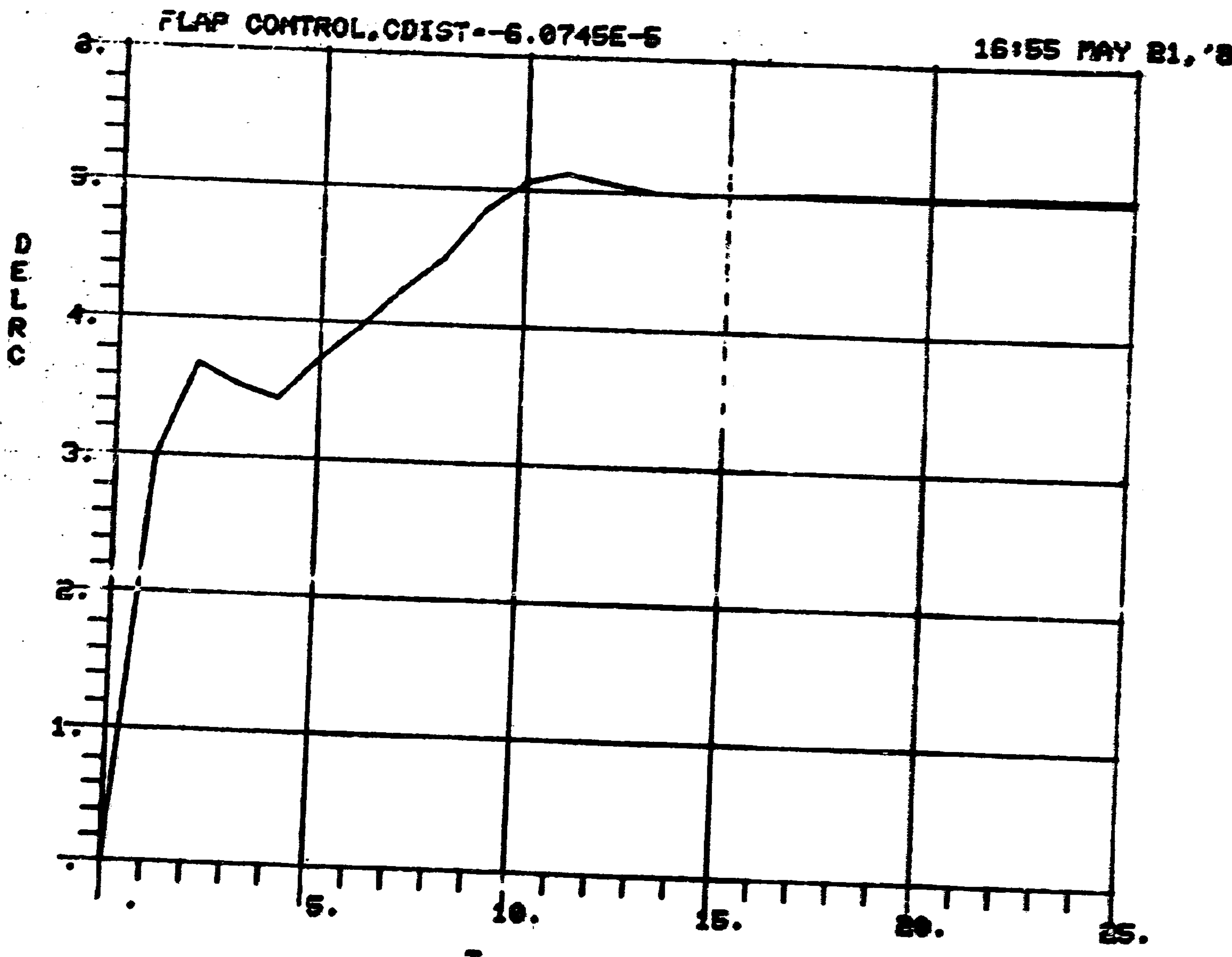

Figure V-31 Roll Flap Deflection Command, Flap Control

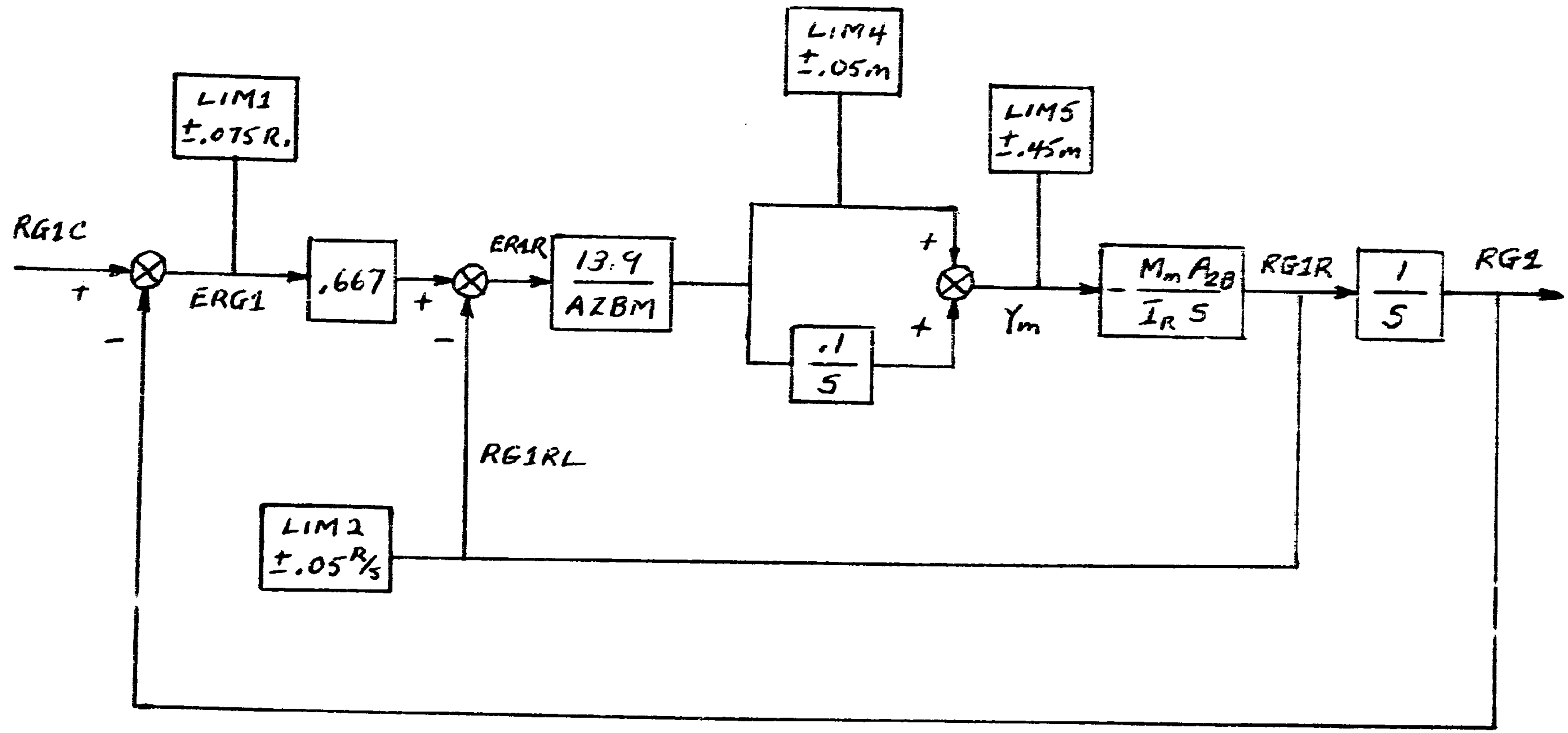

$$AZBM = -A_{ZB} \quad \text{WITH MINIMUM VALUE } 1.24\ m/s^2$$

$$\omega_{RL} = \frac{K2 * M_m}{I_R} = 1.06\ \text{RAD/SEC}$$

Figure V-32 MMRC Trim Control

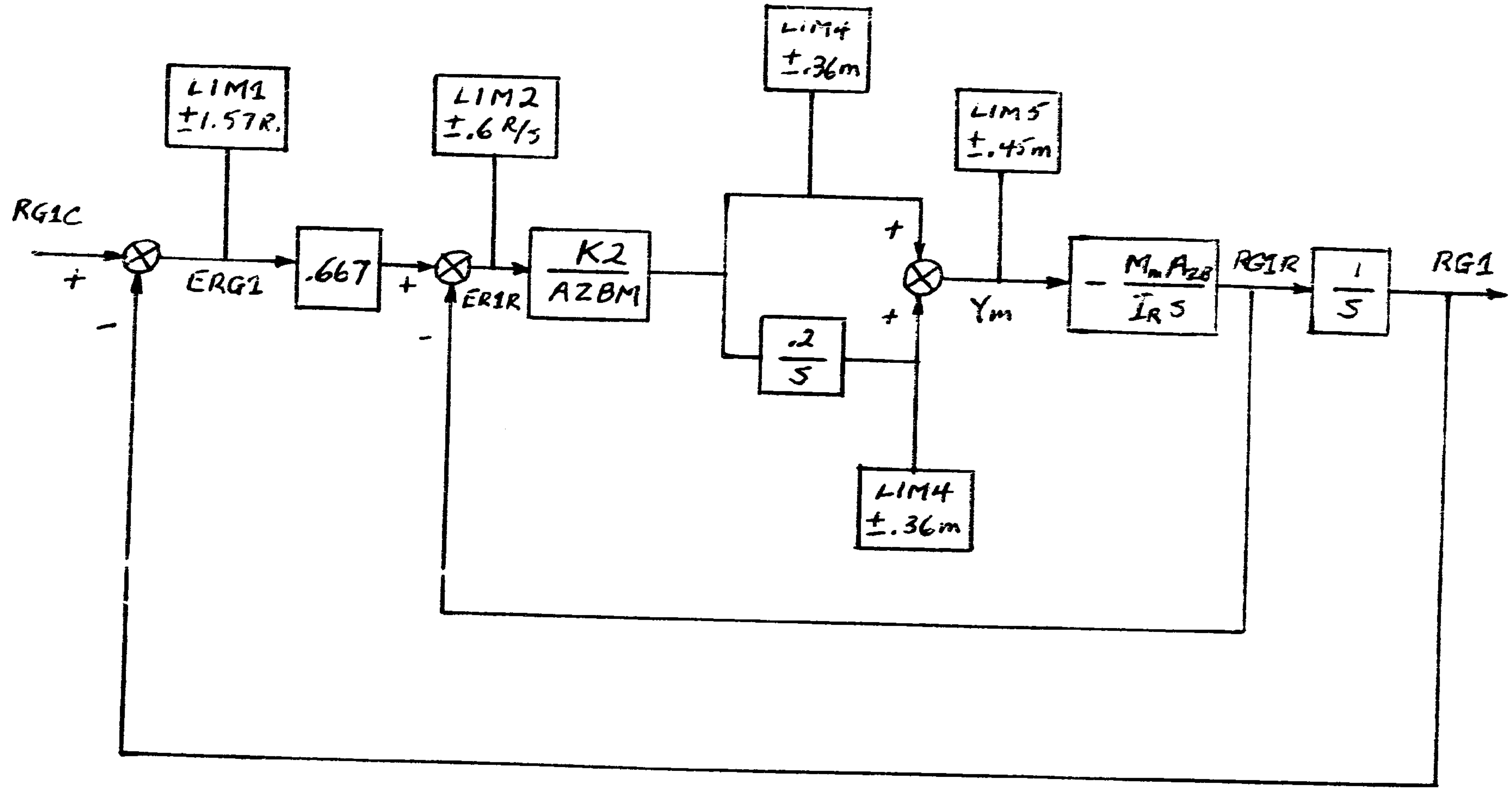

AZBM = −AZB WITH MINIMUM VALUE 1.24 m/s^2

Figure V-33 MMRC Roll Control System

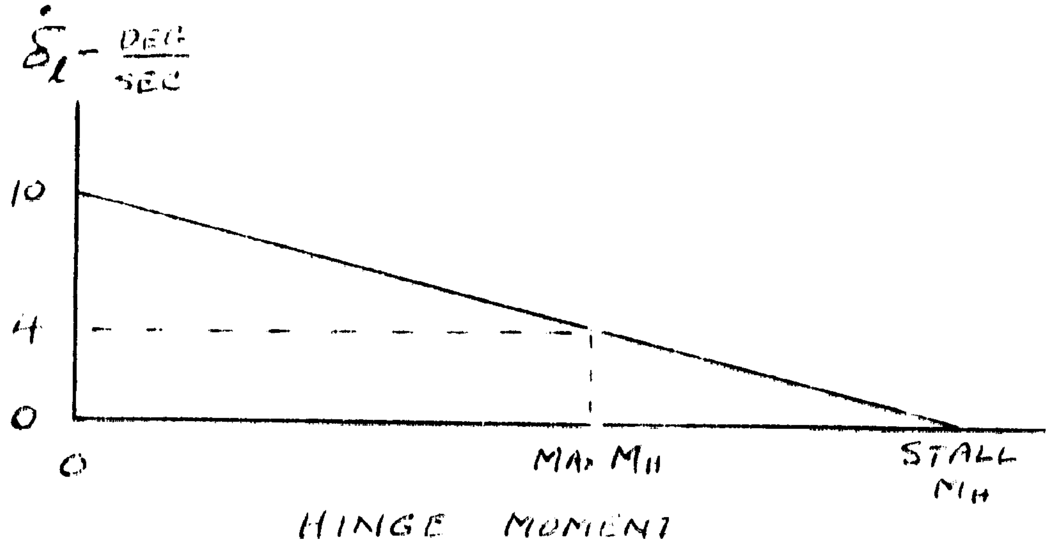

Figure V-34 Flap Actuation Requirements - Flap Trim Linear Simulation

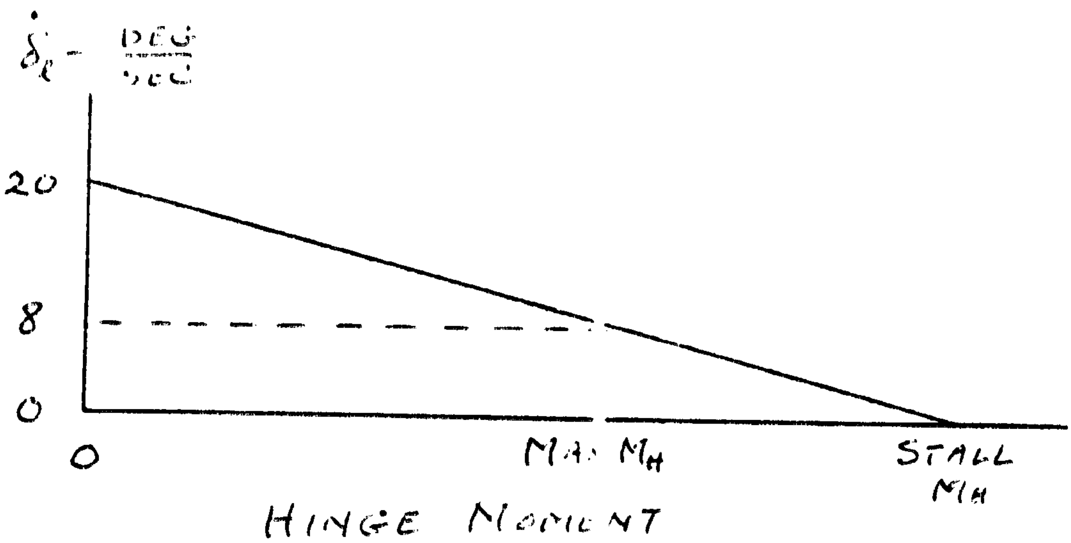

Figure V-35 Flap Actuation Requirements - Flap Control Linear Simulation

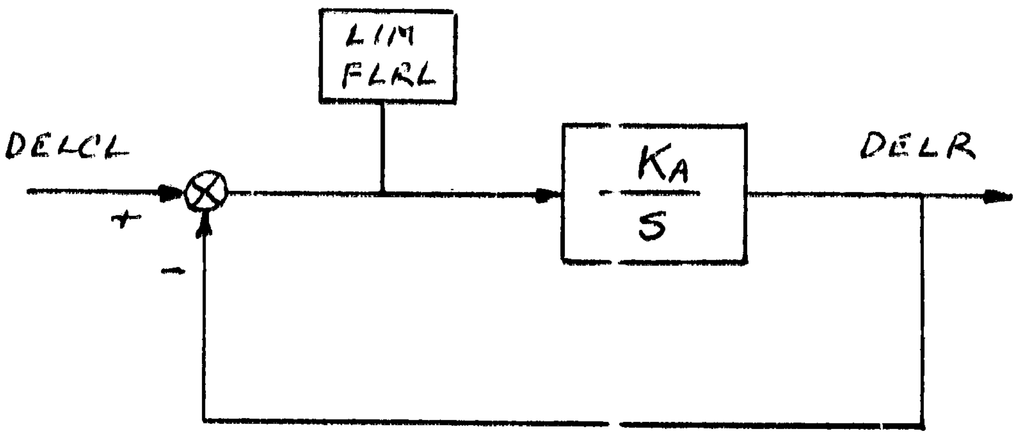

Figure V-36 First Order Actuation Simulation

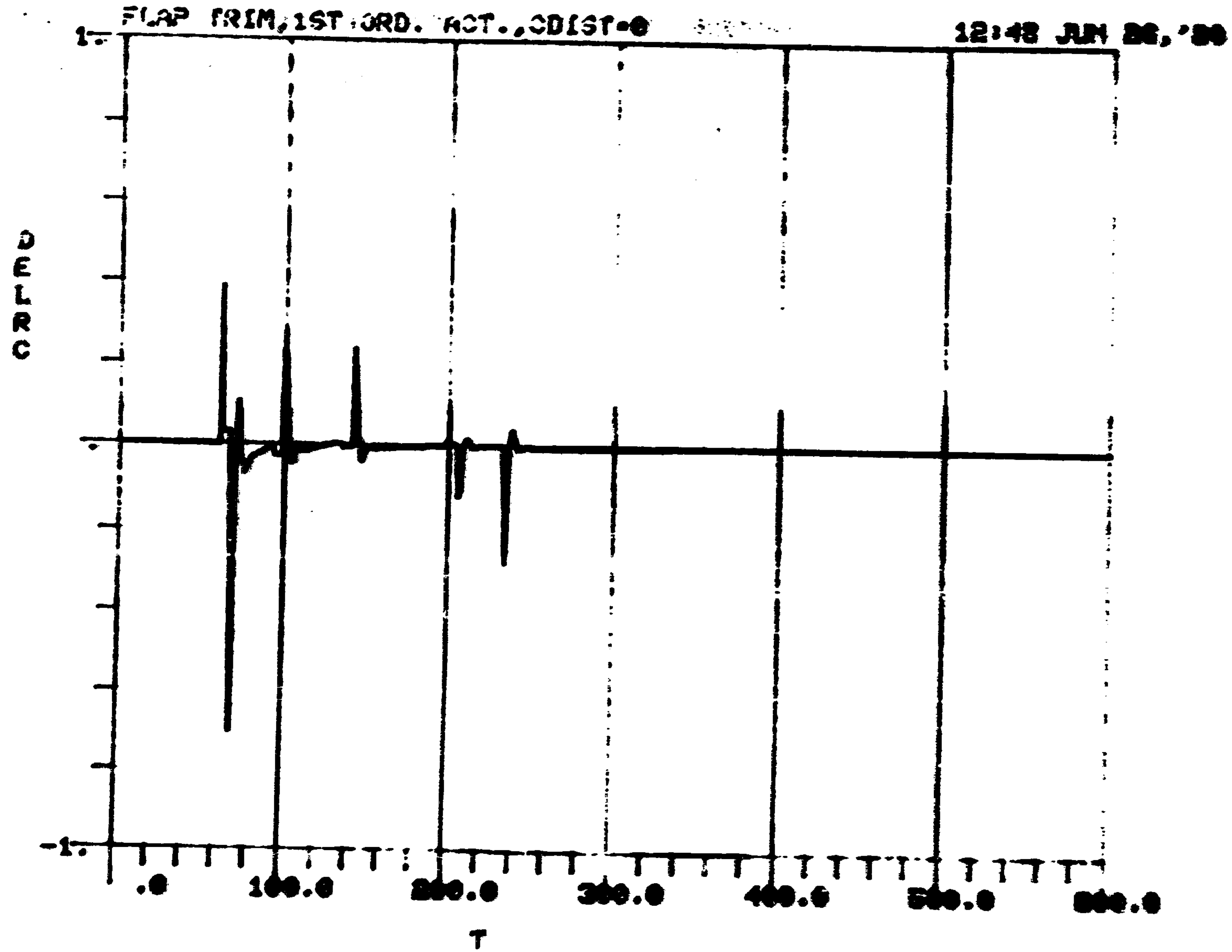

Figure V-37 Roll Flap Deflections Command, Flap Trim Control

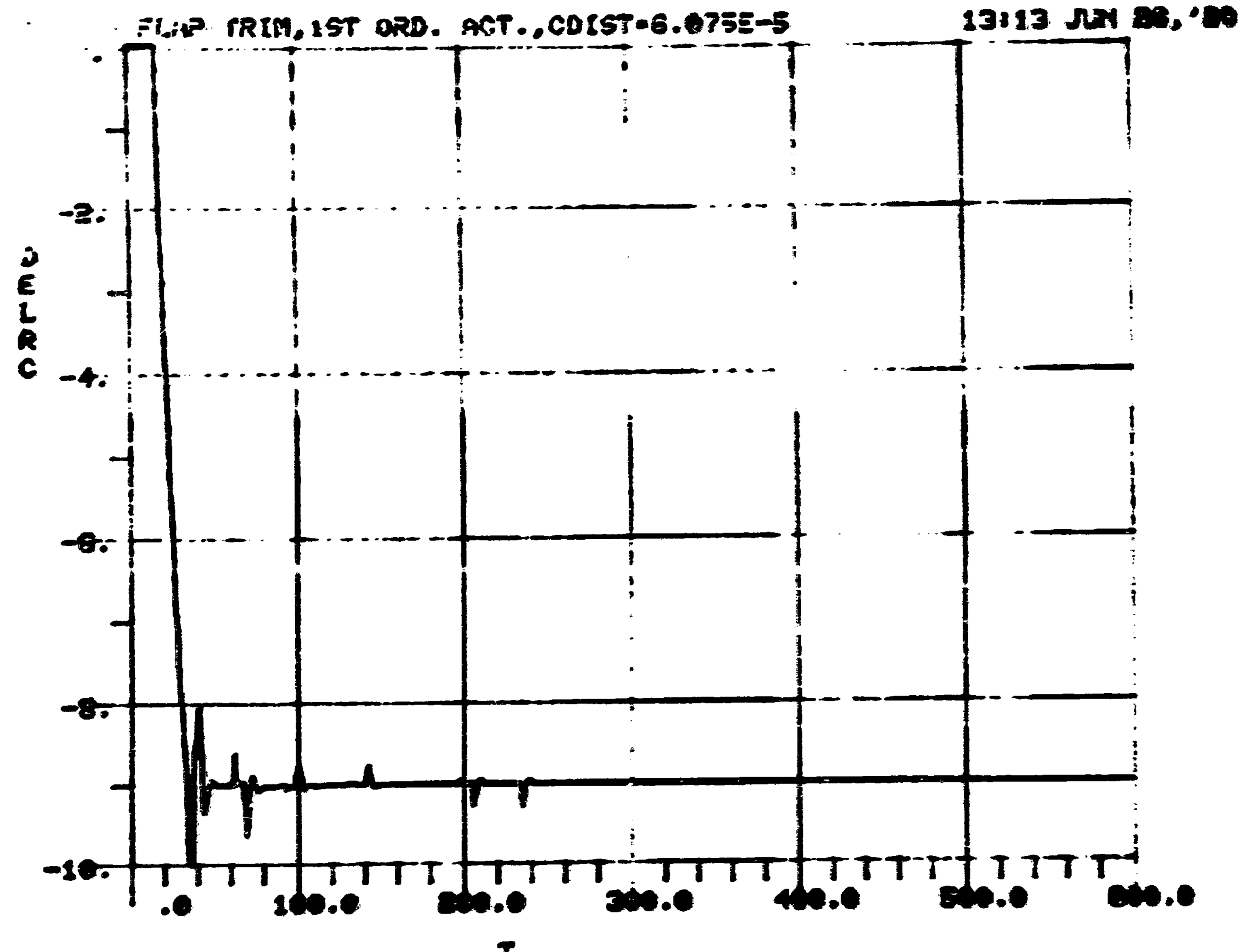

Figure V-38 Roll Flap Deflection Command, Flap Trim Control

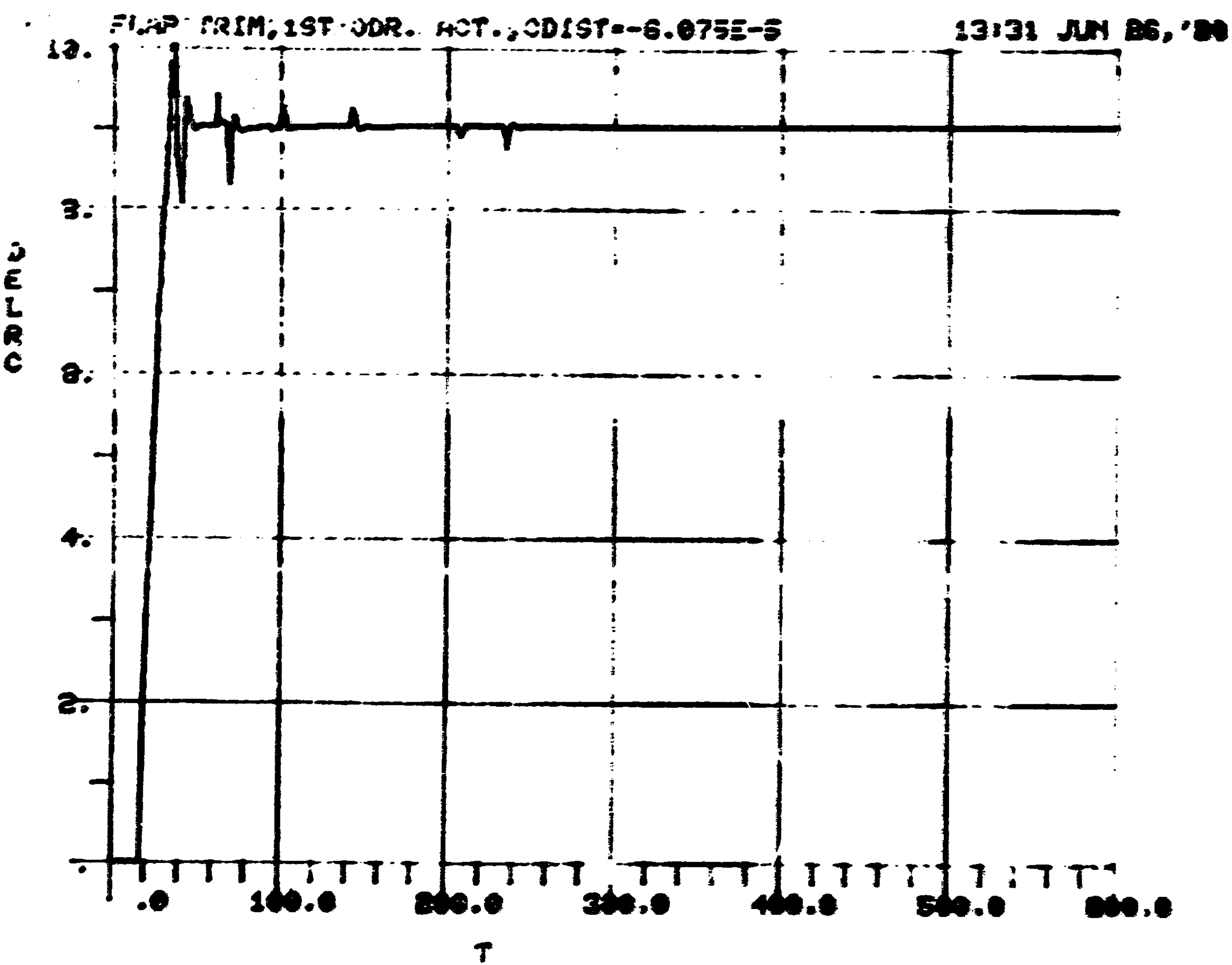

Figure V-39 Roll Flap Deflection Command, Flap Trim Control

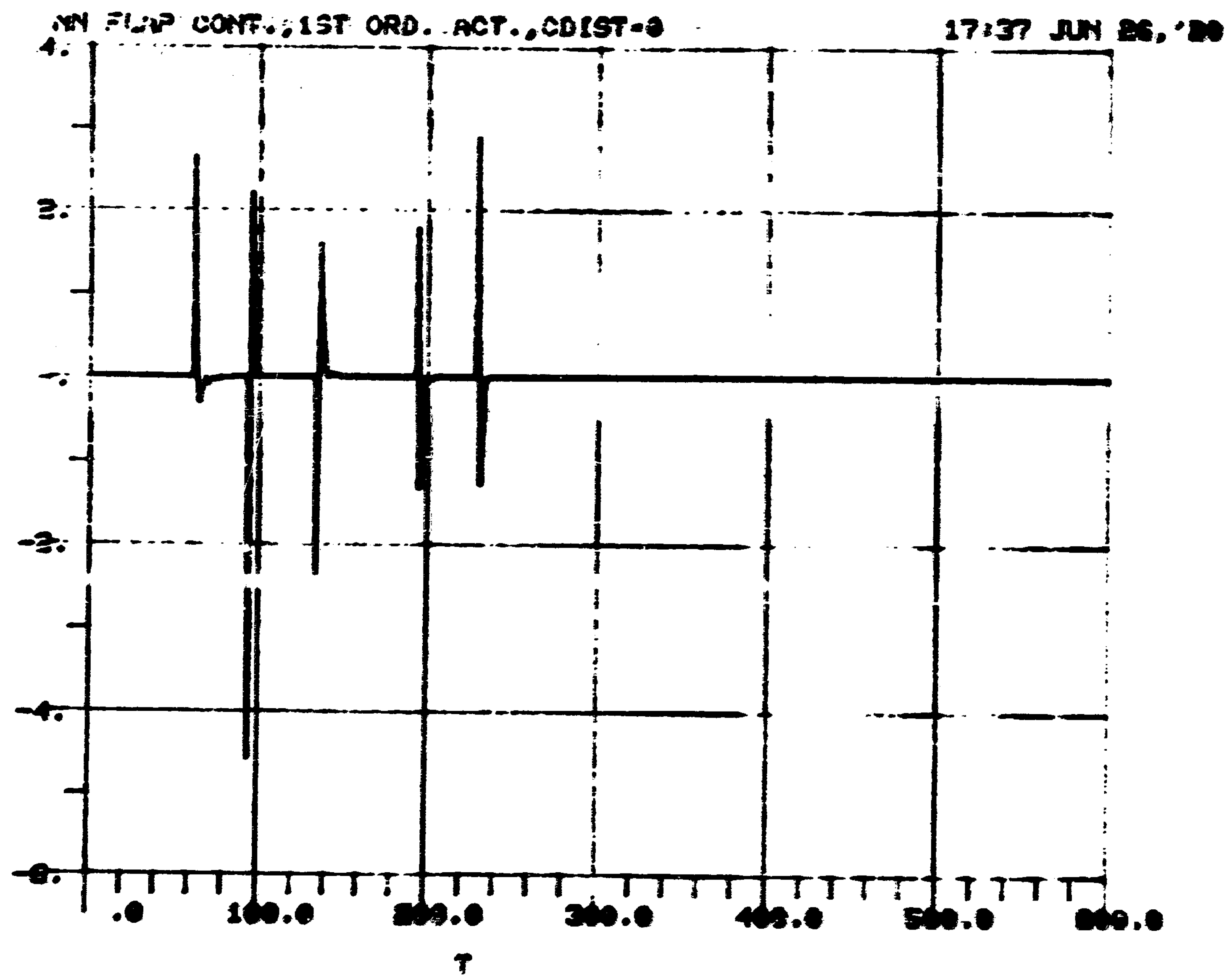

Figure V-40 Roll Flap Deflection Command, Flap Control

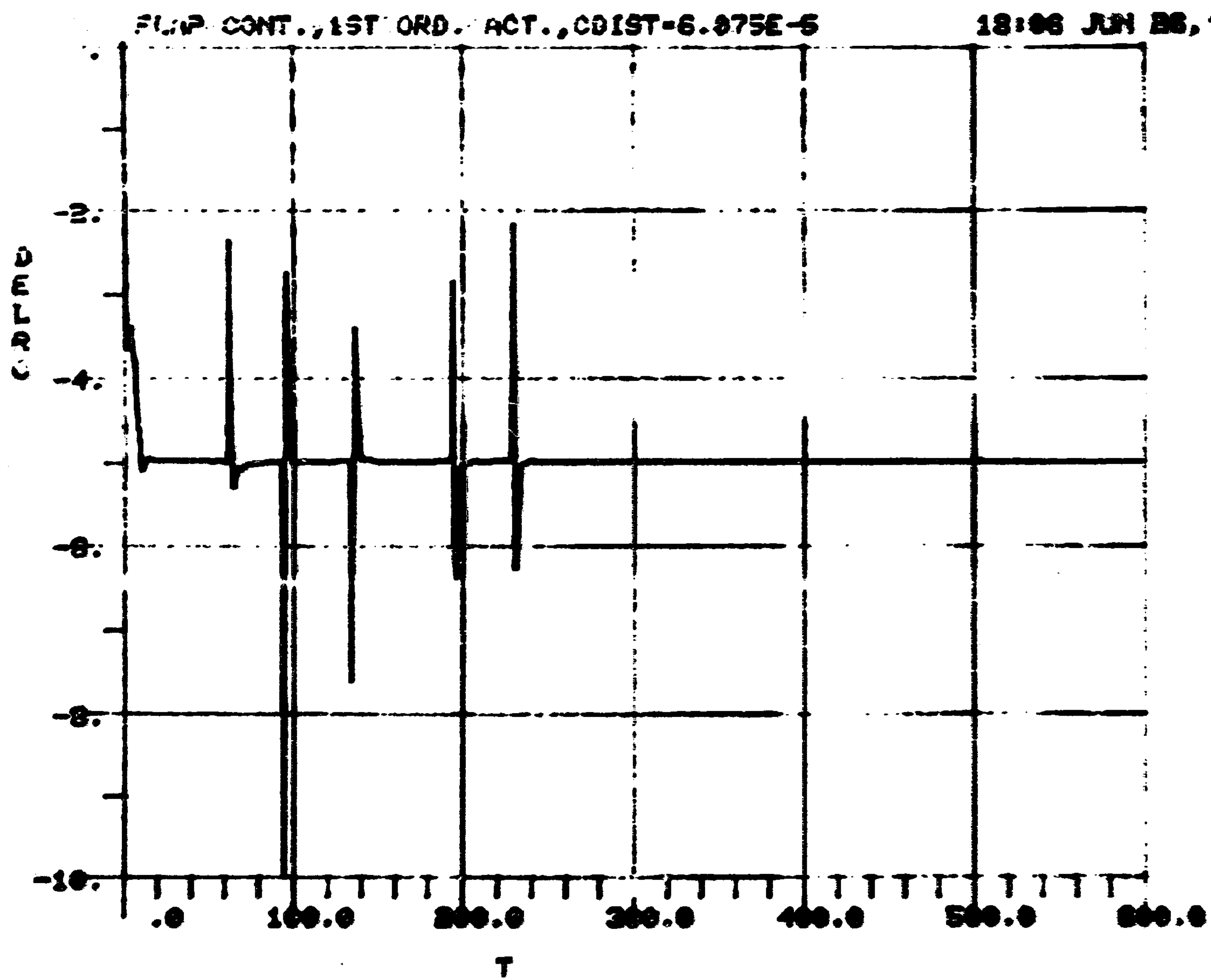

Figure V-41 Roll Flap Deflection Command, Flap Control

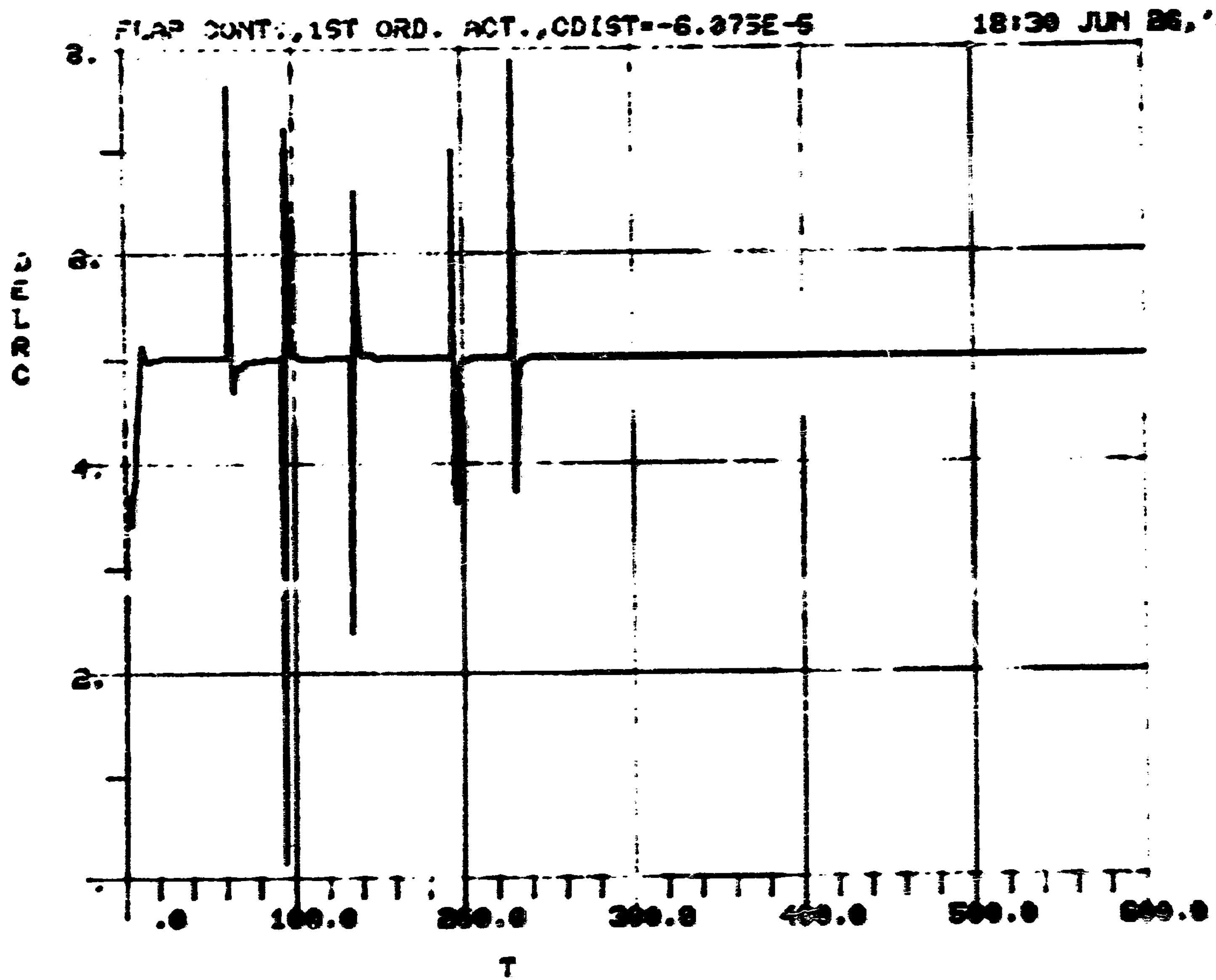

Figure .-42 Roll Flap Deflection Command, Flap Control

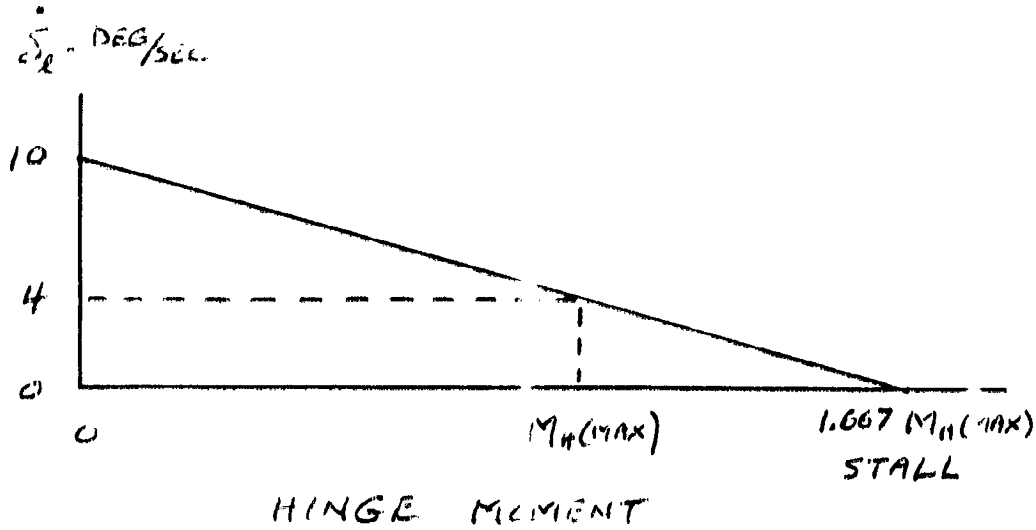

Figure V-43 Flap Trim

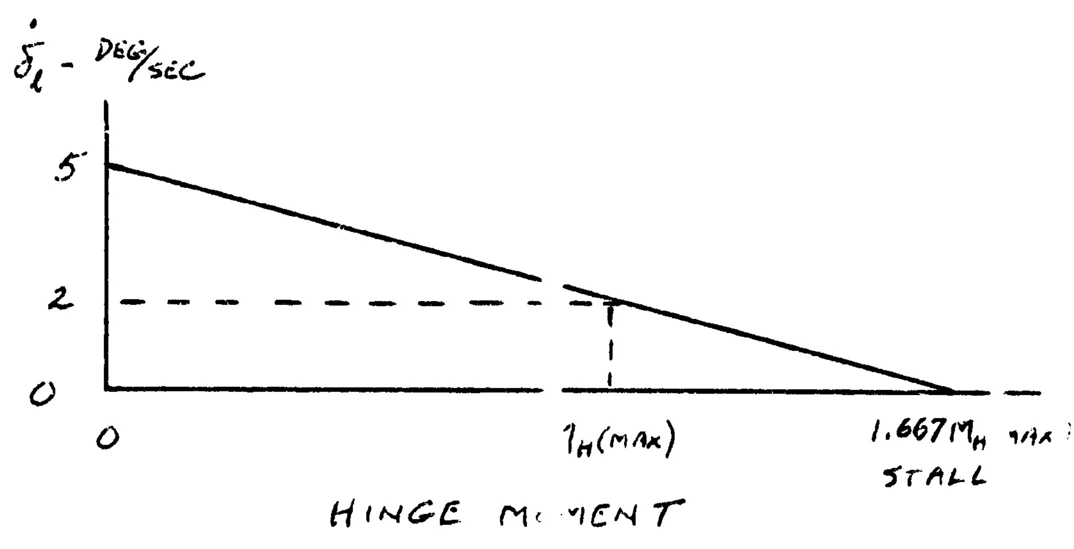

Figure V-44 Flap Control

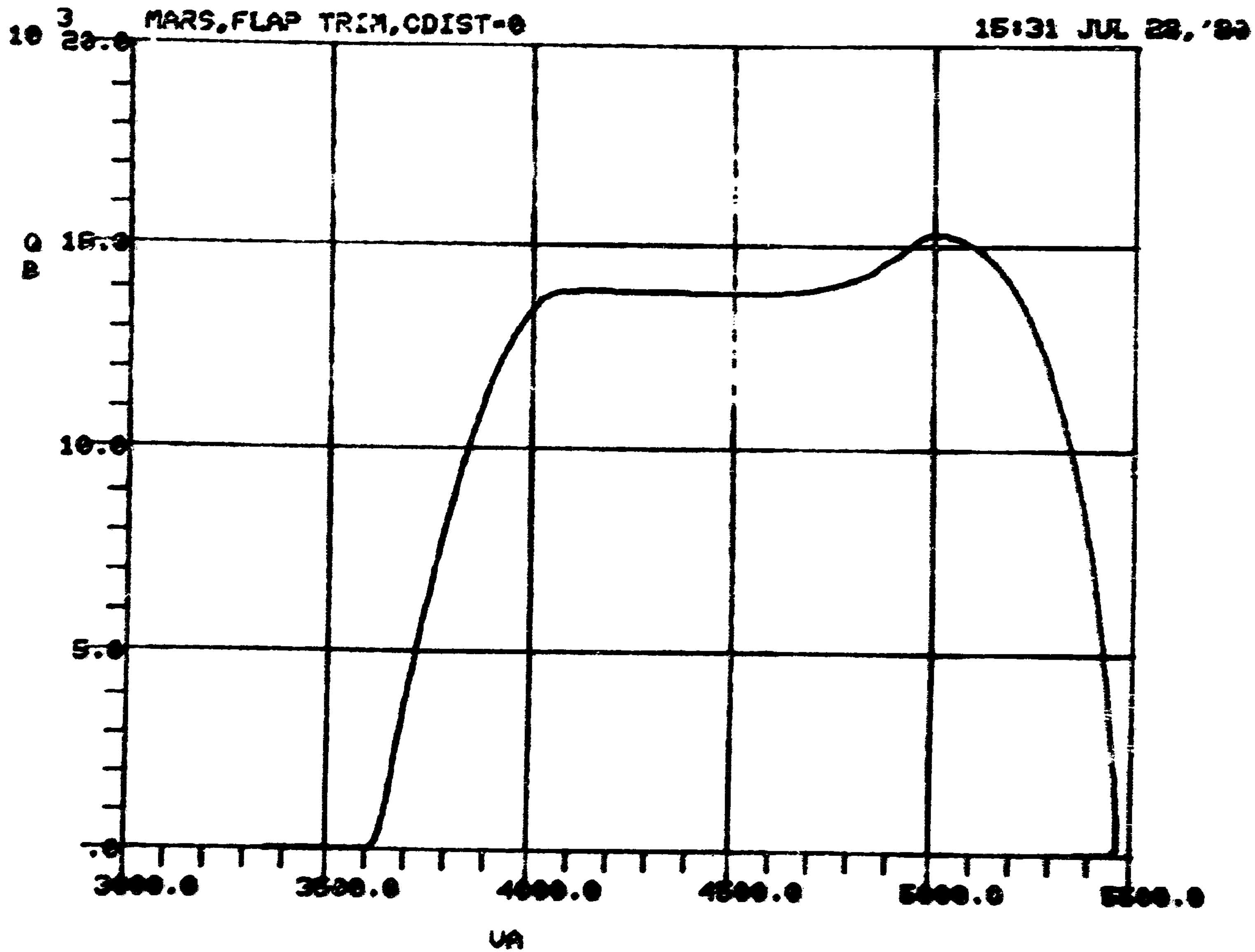

Figure V-45 Dynamic Pressure, Mars Trajectory

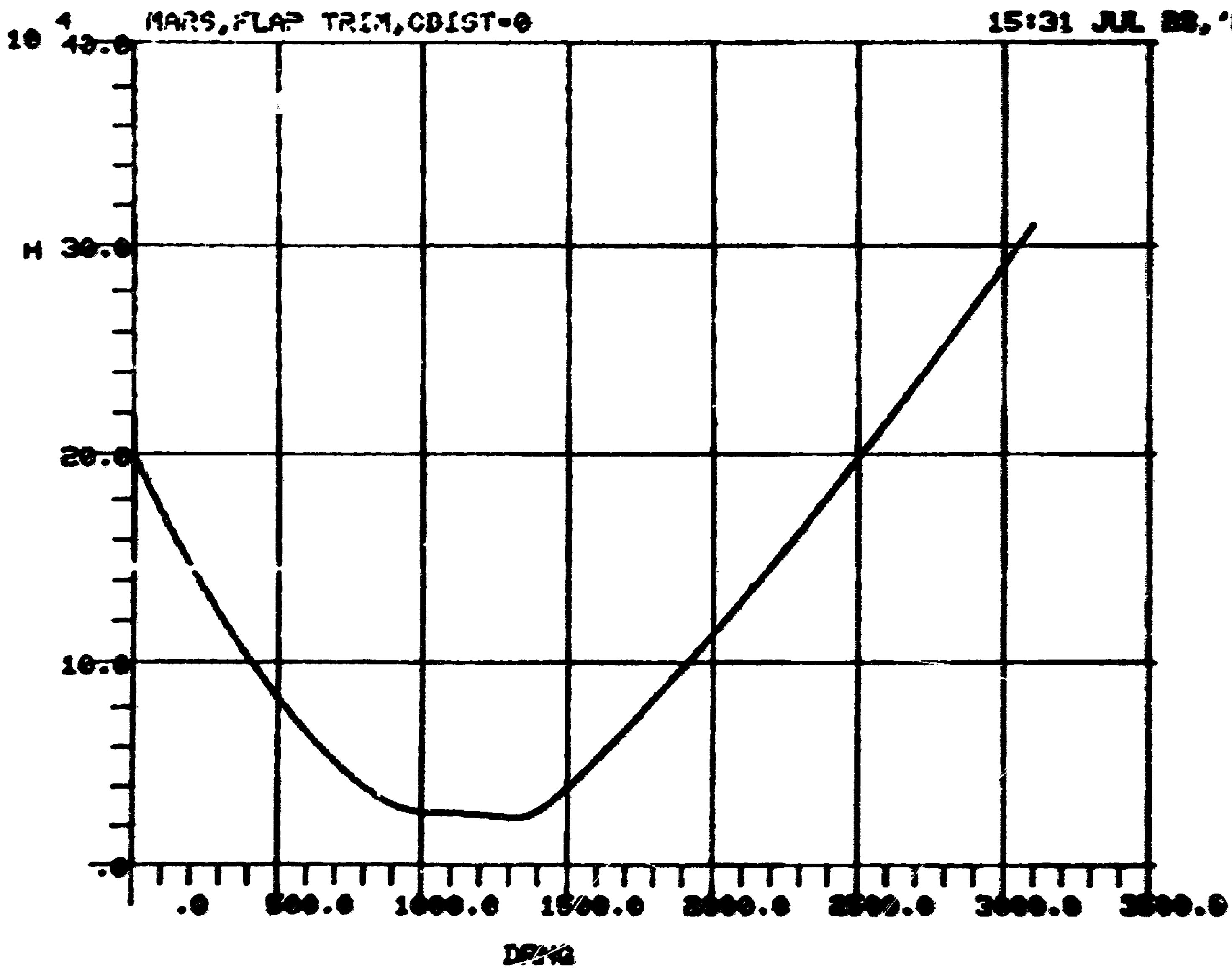

Figure V-45 Altitude, Mars Trajectory

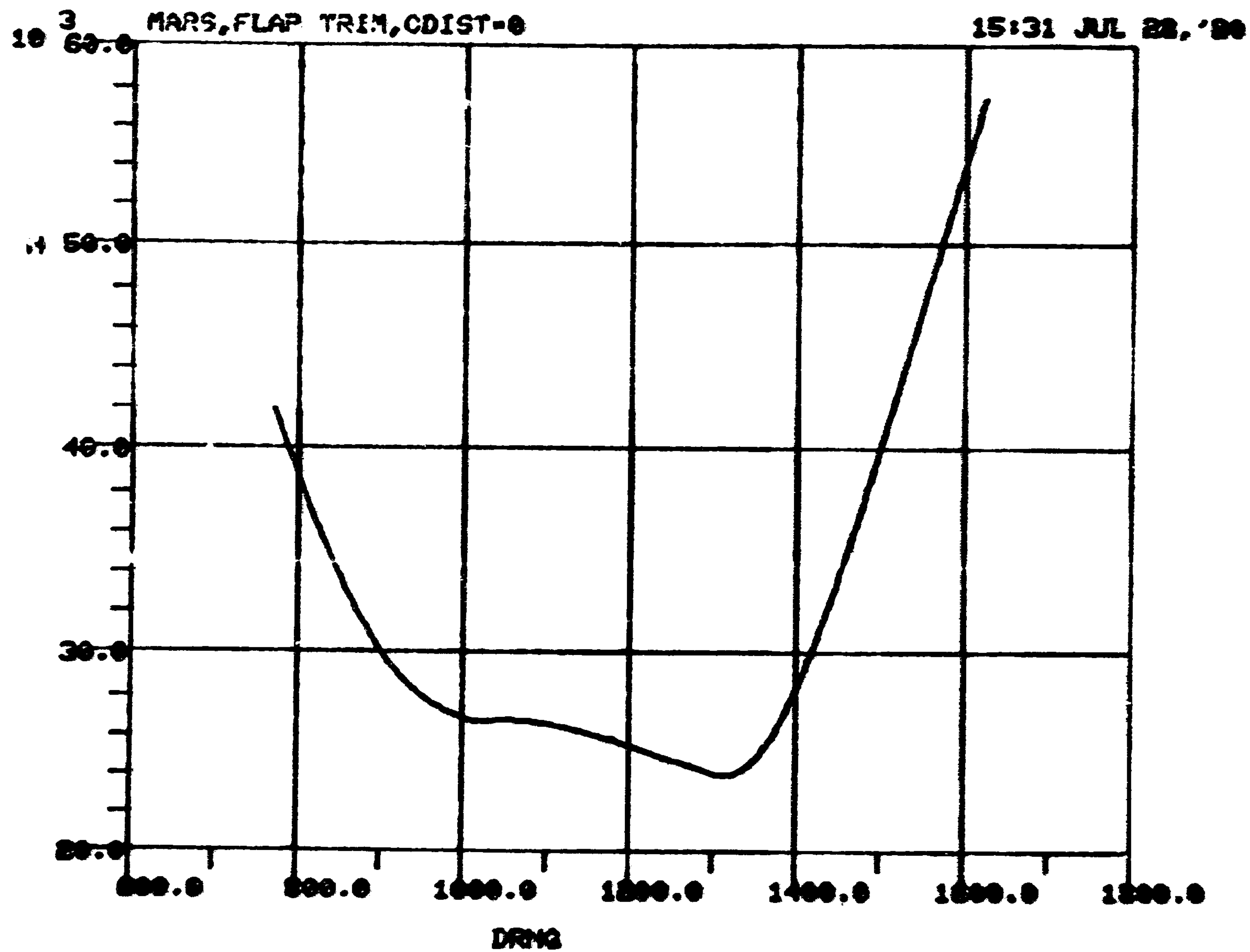

Figure V-47 Altitude, Mars Trajectory

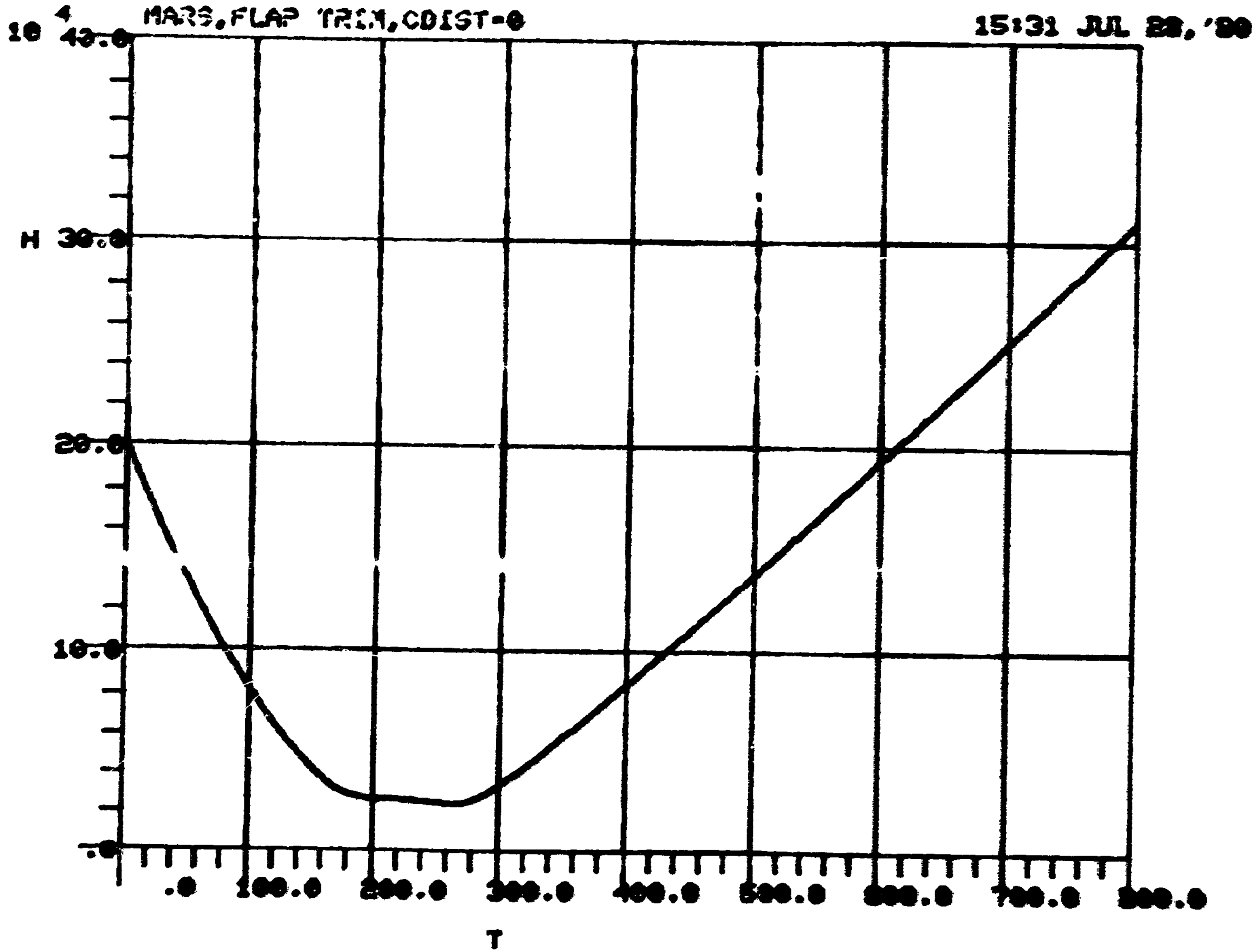

Figure V-48 Altitude, Mars Trajectory

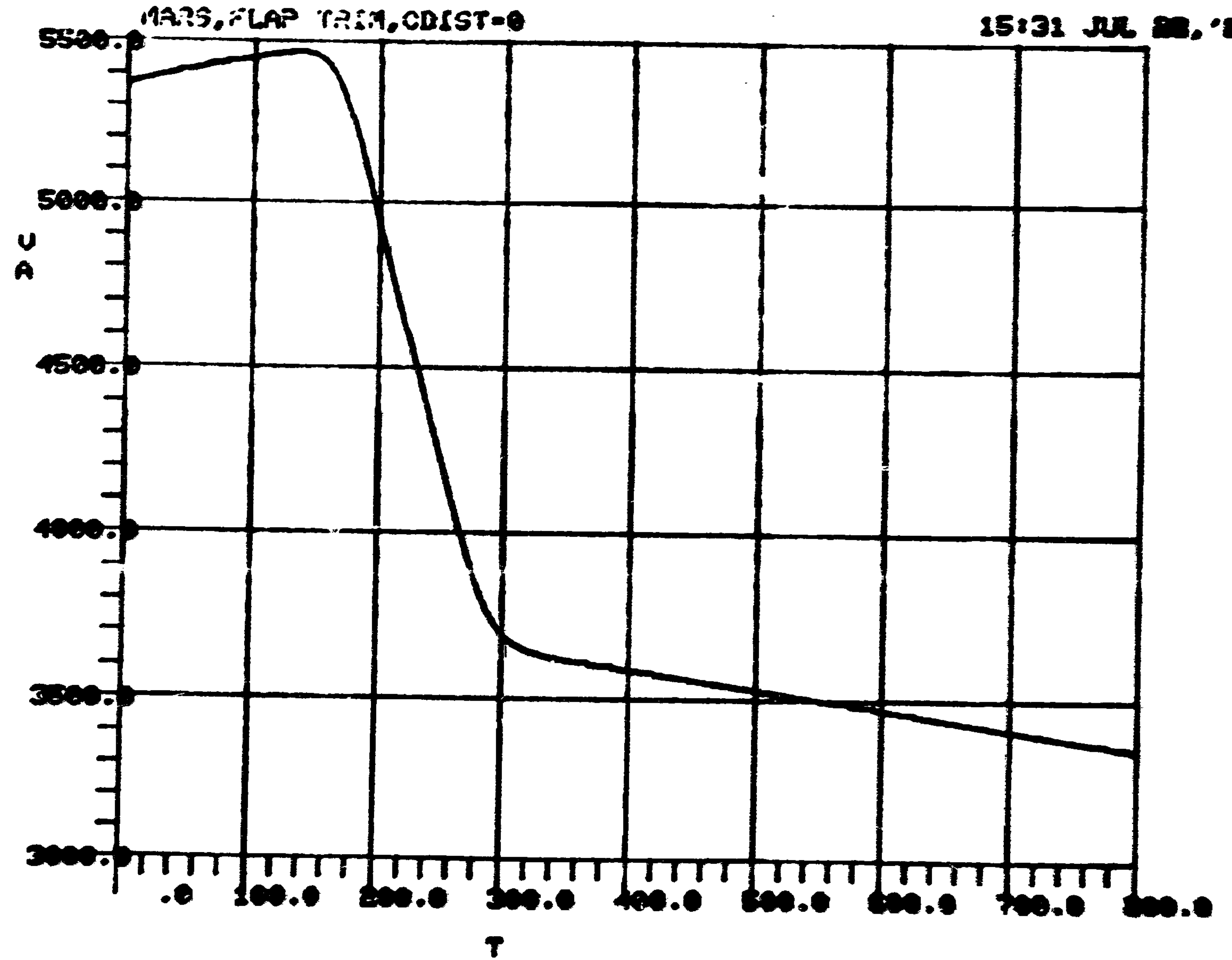

Figure V-49 Air Relative Velocity, Mars Trajectory

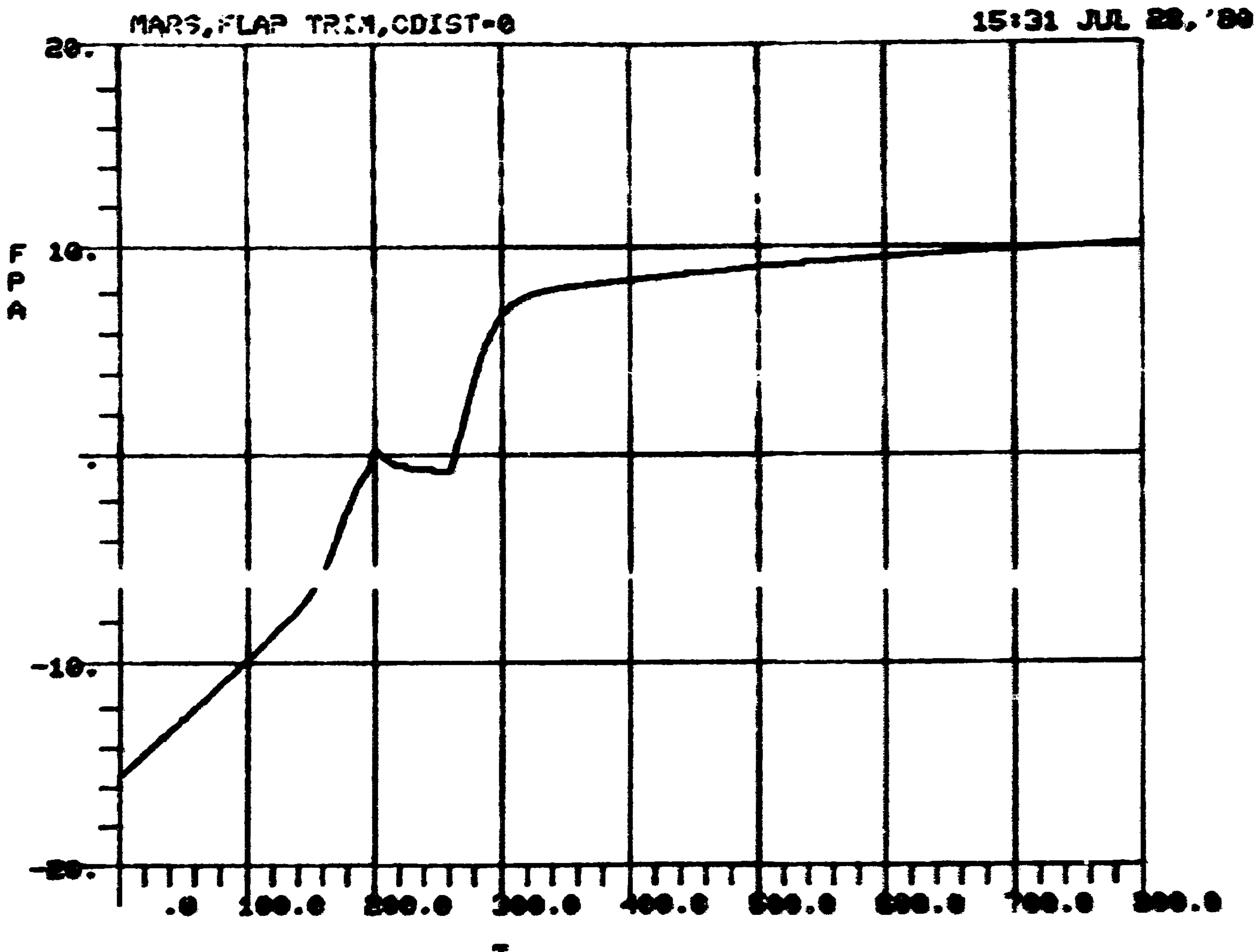

Figure V-50 Air Relative Flight Path Angle, Mars Trajectory

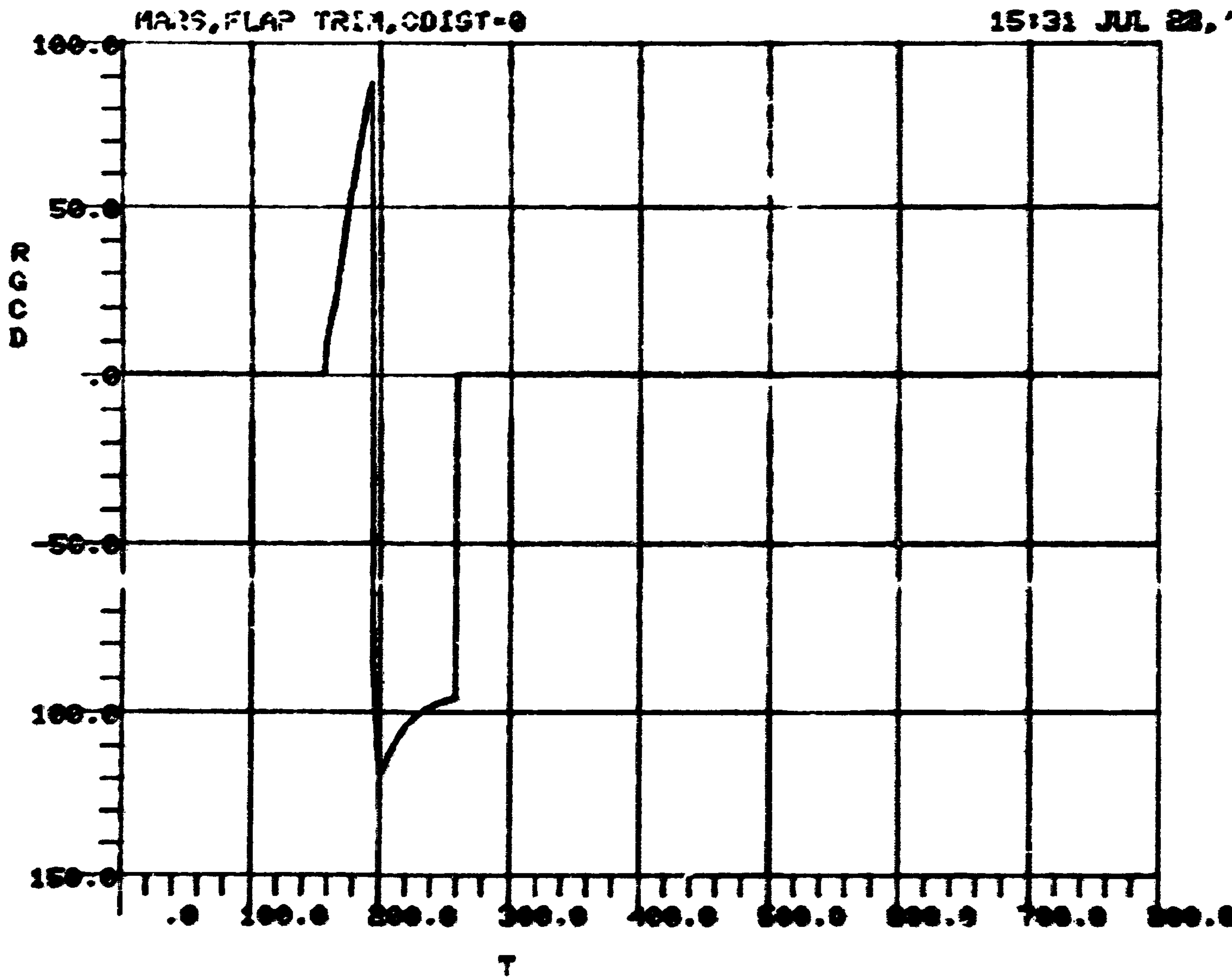

Figure V-51 Bank Angle Command, Mars Trajectory

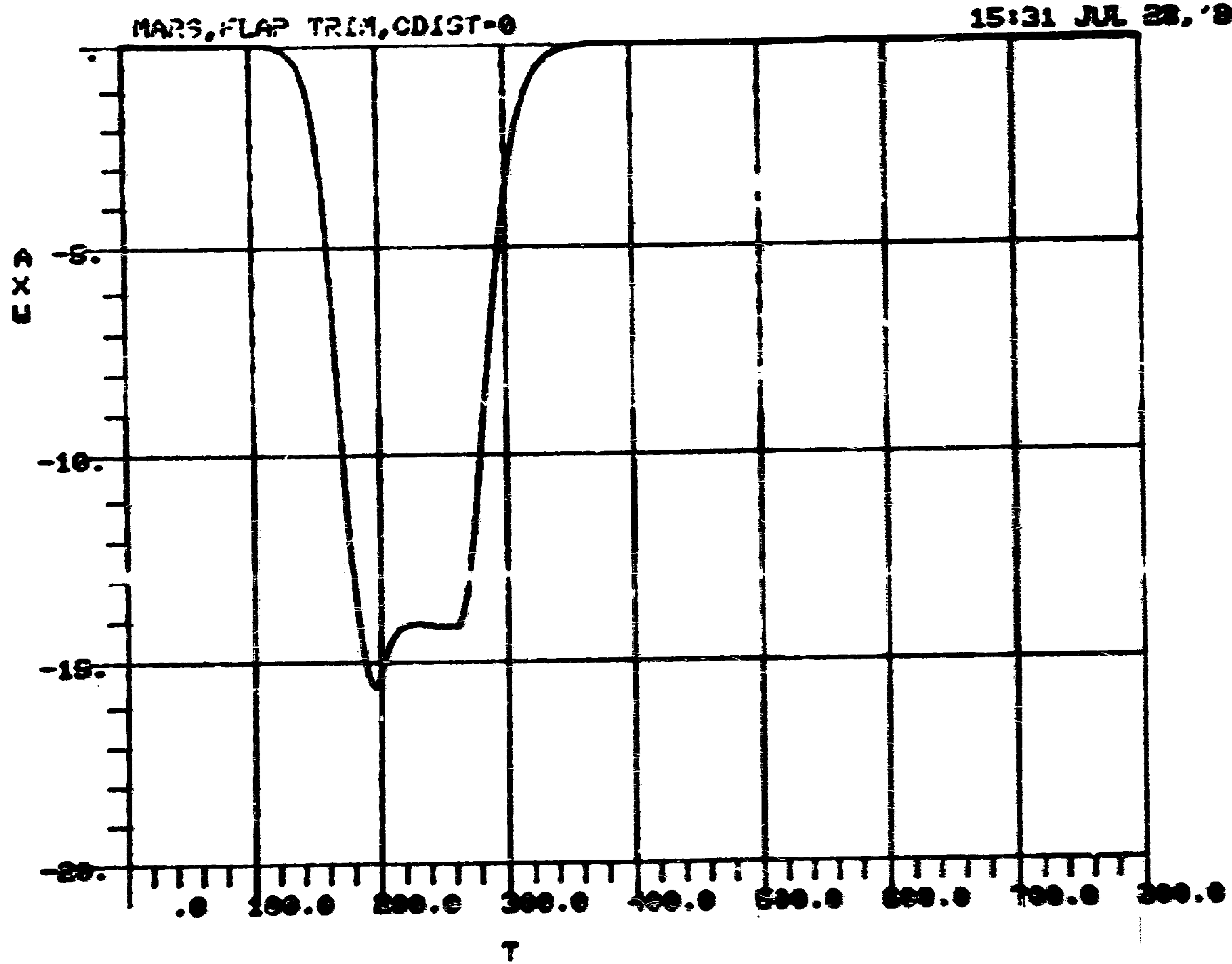

Figure V-52 Drag, Mars Trajectory

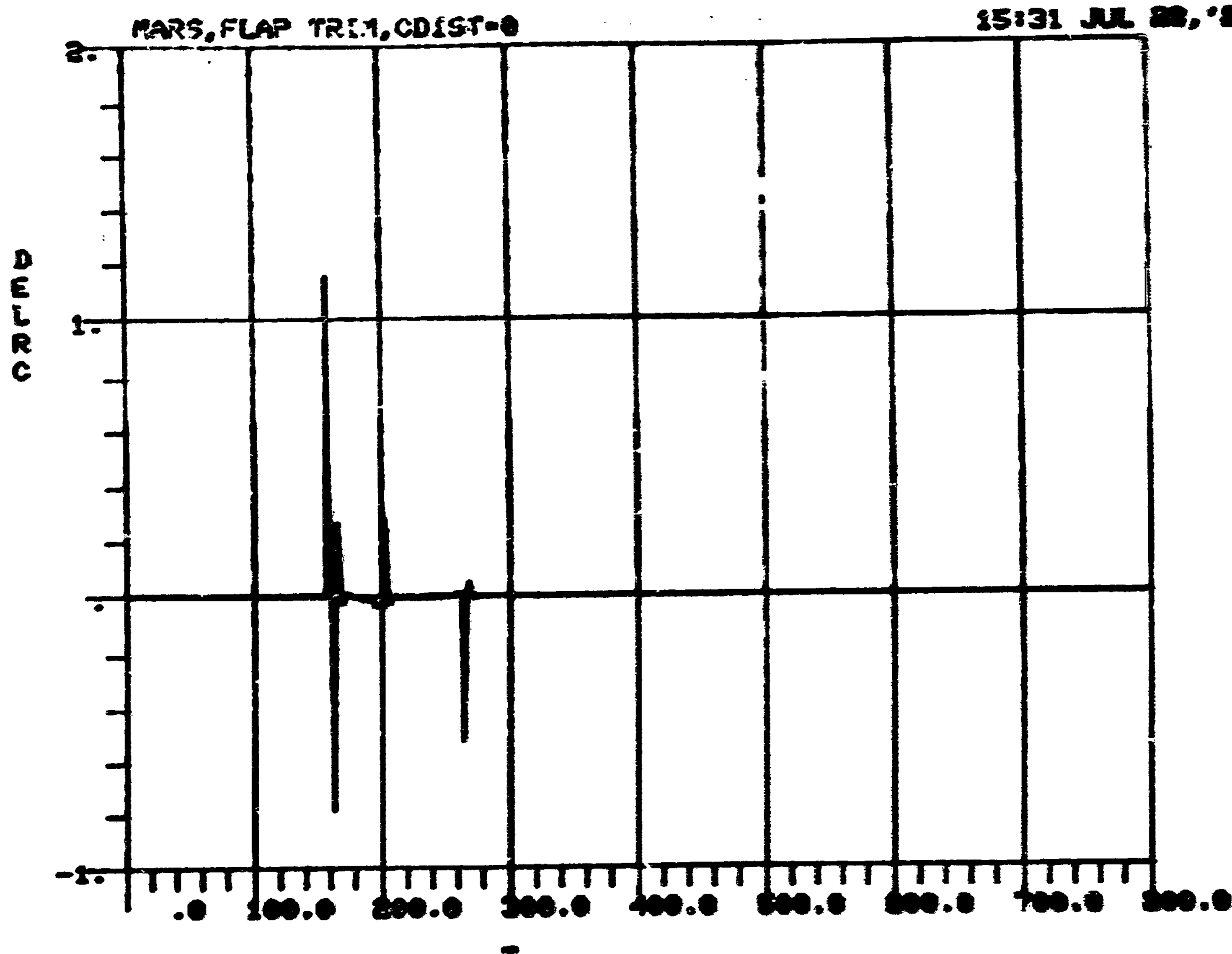

Figure V-53 Roll Flap Deflection Command, Flap Trim Control

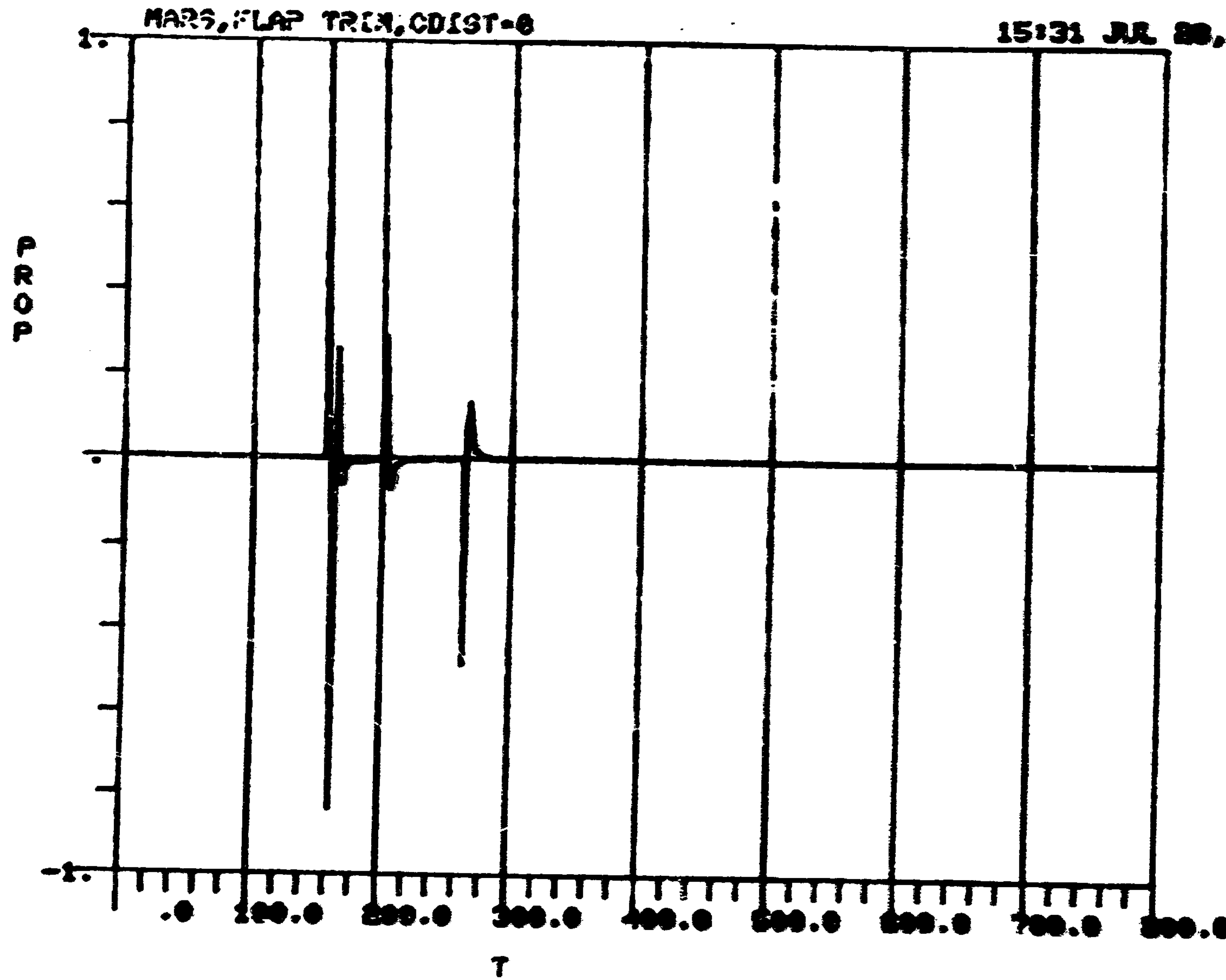

Figure V-54 Autopilot Proportional Signal, Flap Trim Control

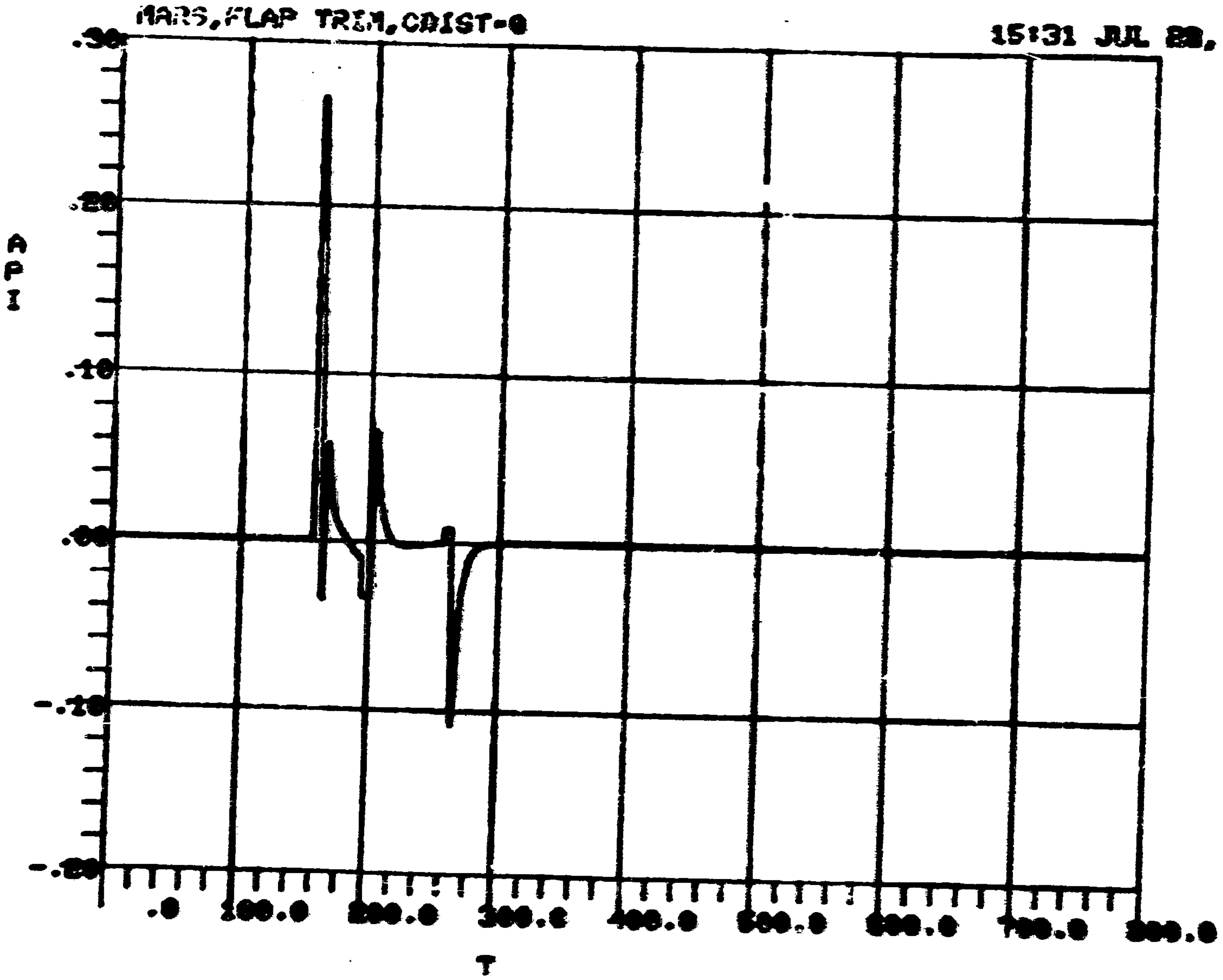

Figure V-55 Autopilot Integrator Signal, Flap Trim Control

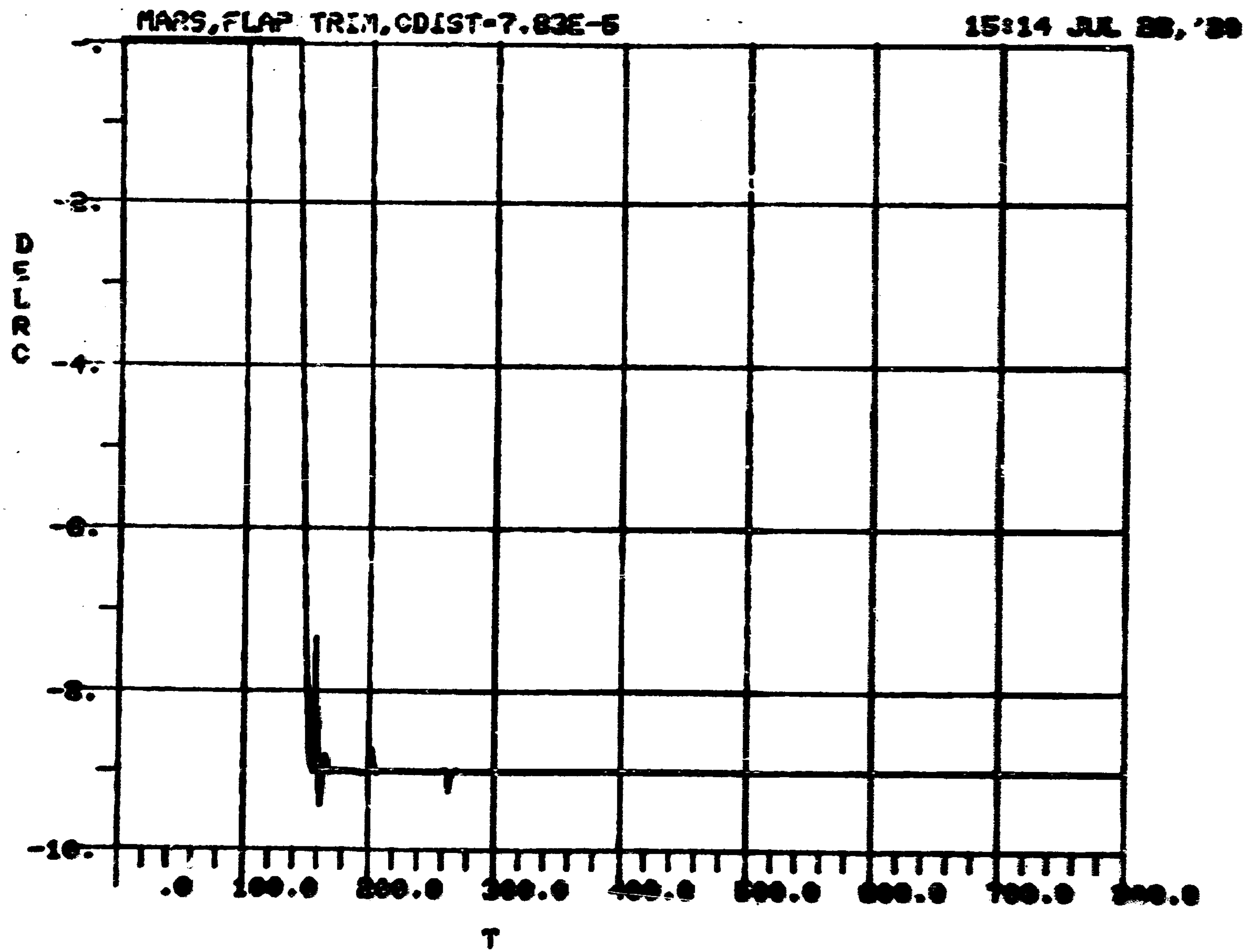

Figure V-56 Roll Flap Deflection Command, Flap Trim Control

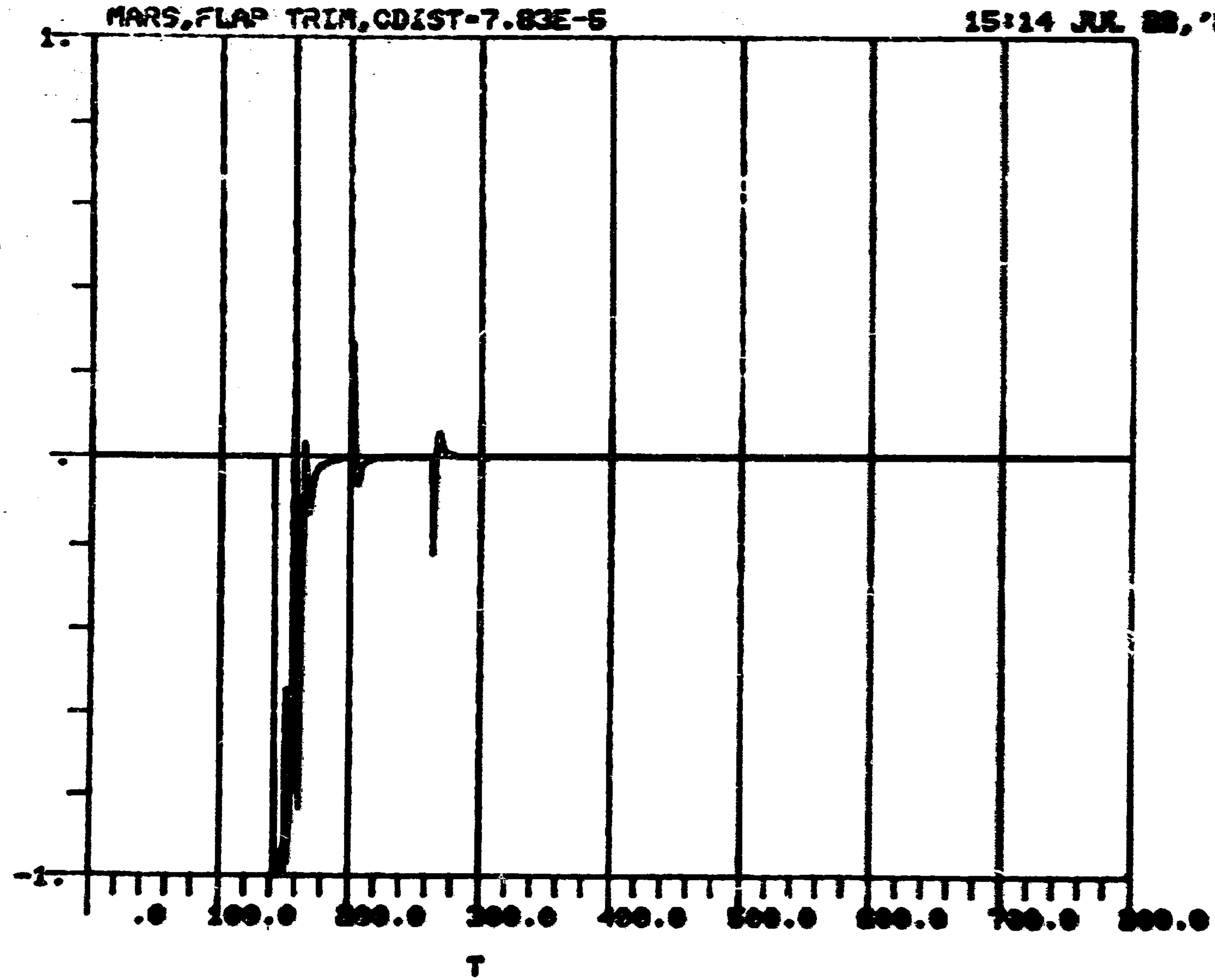

Figure V-57 Autopilot Proportional Signal, Flap Trim Control

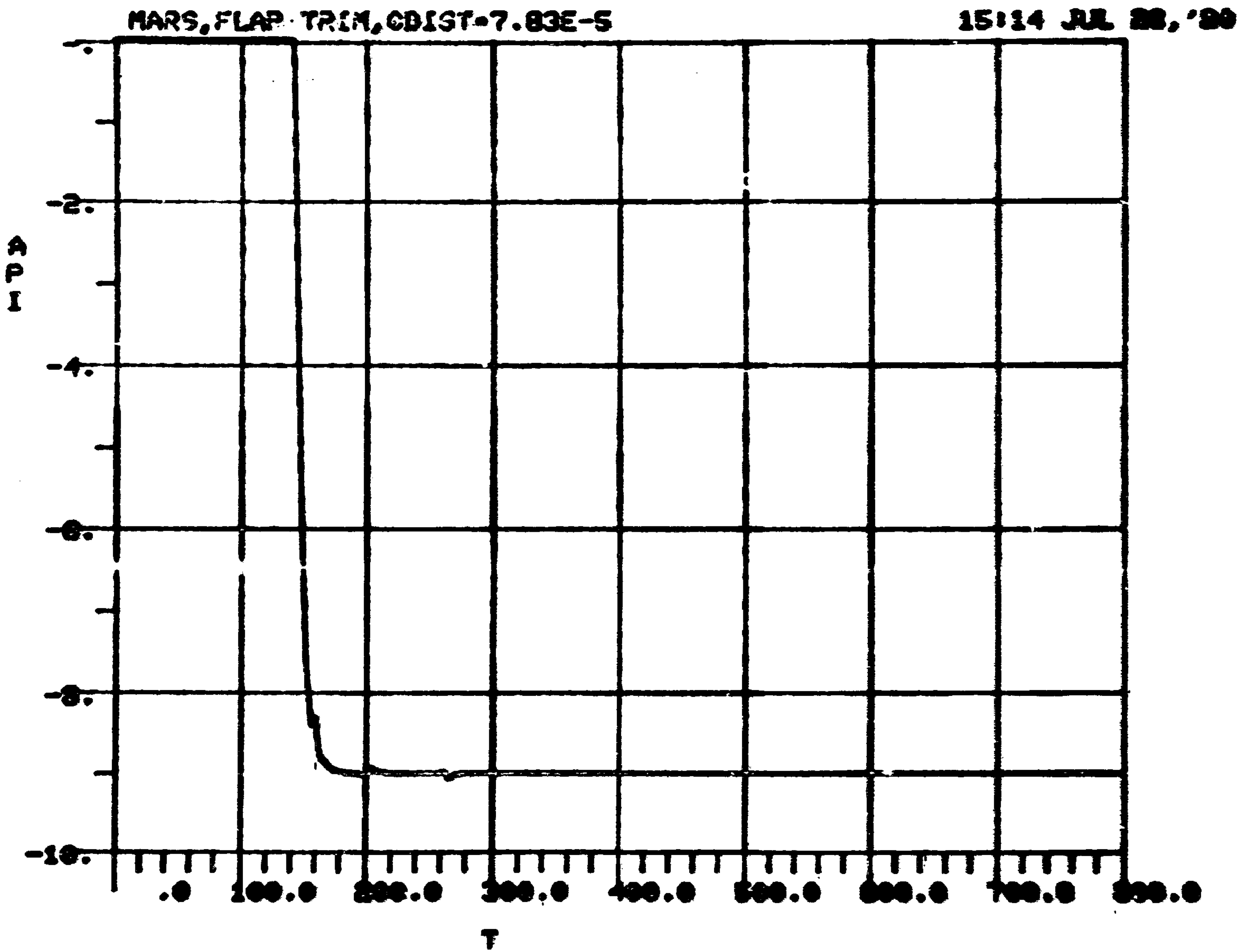

Figure V-58 Autopilot Integrator Signal, Flap Trim Control

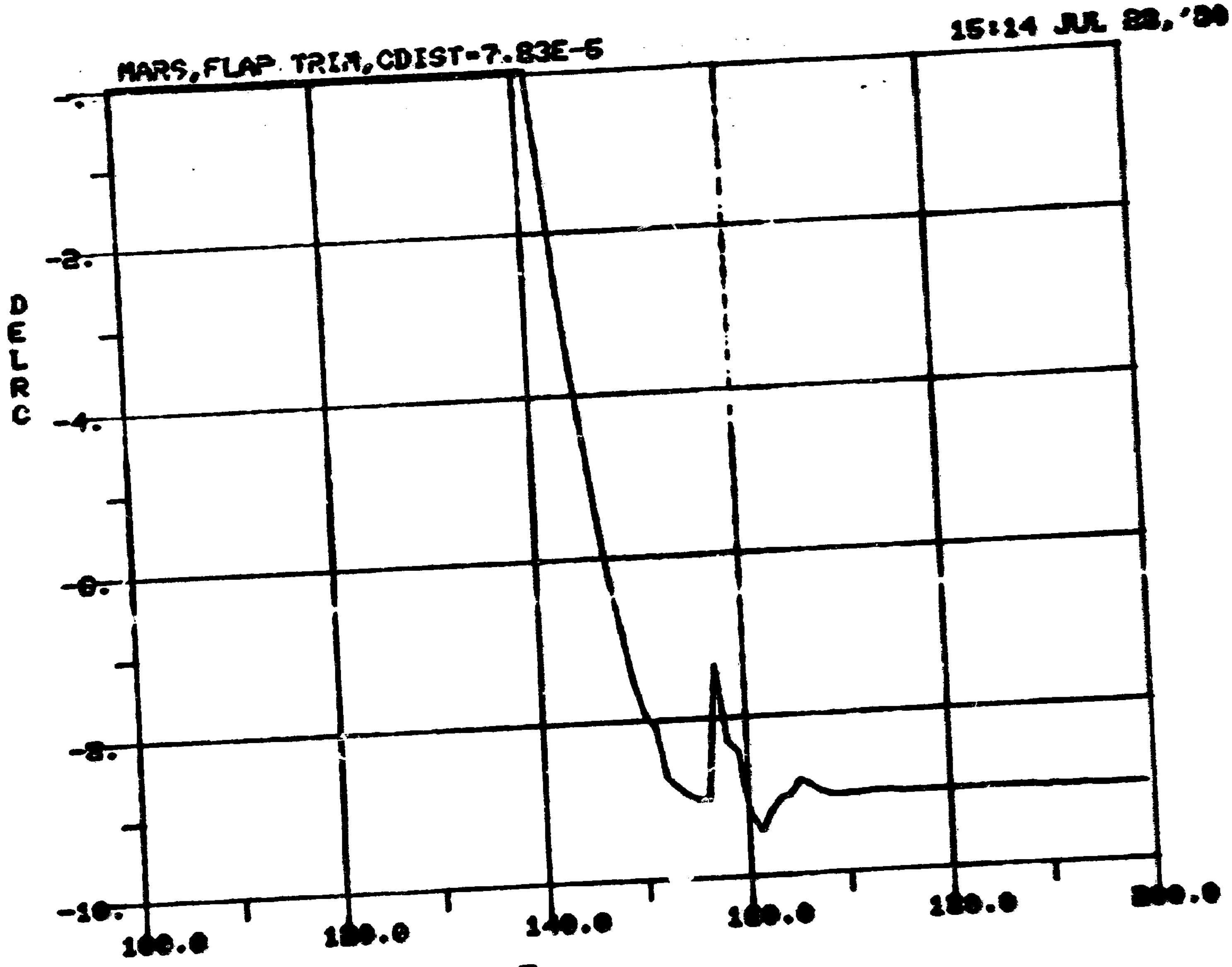

Figure V-59 Roll Flap Deflection Command, Flap Trim Control

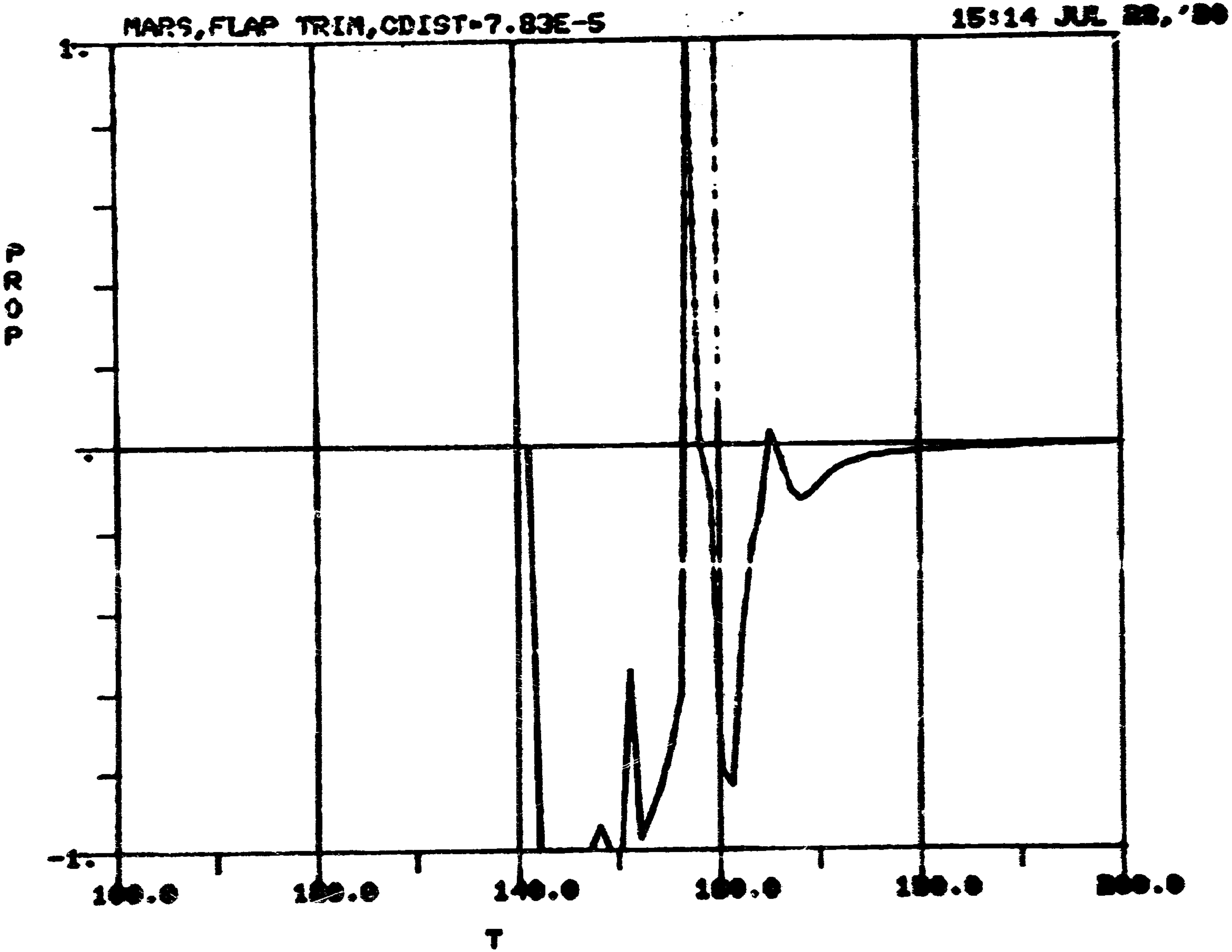

Figure V-60 Autopilot Proportional Signal, Flap Trim Control

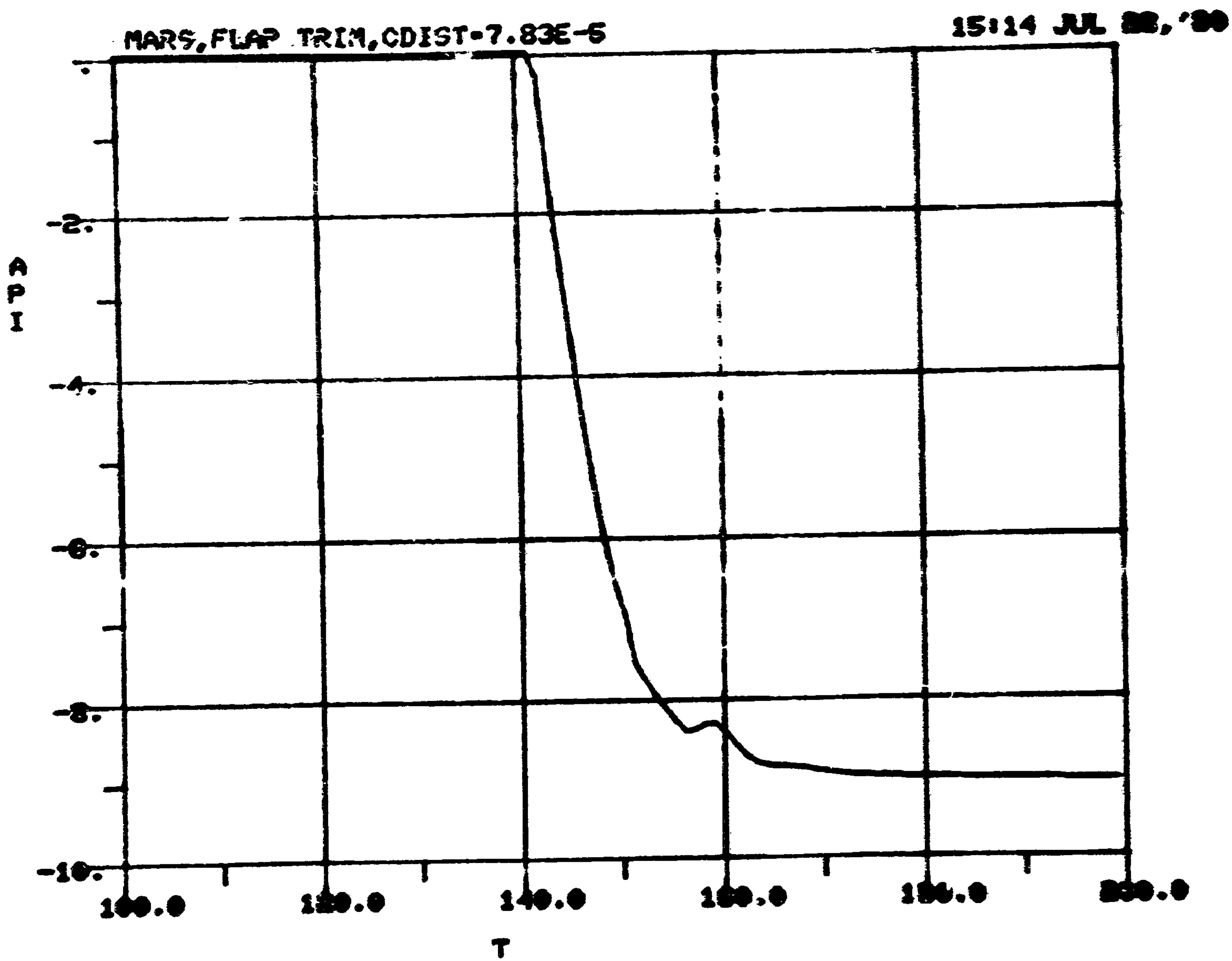

Figure V-61 Autopilot Integrator Signal, Flap Trim Control

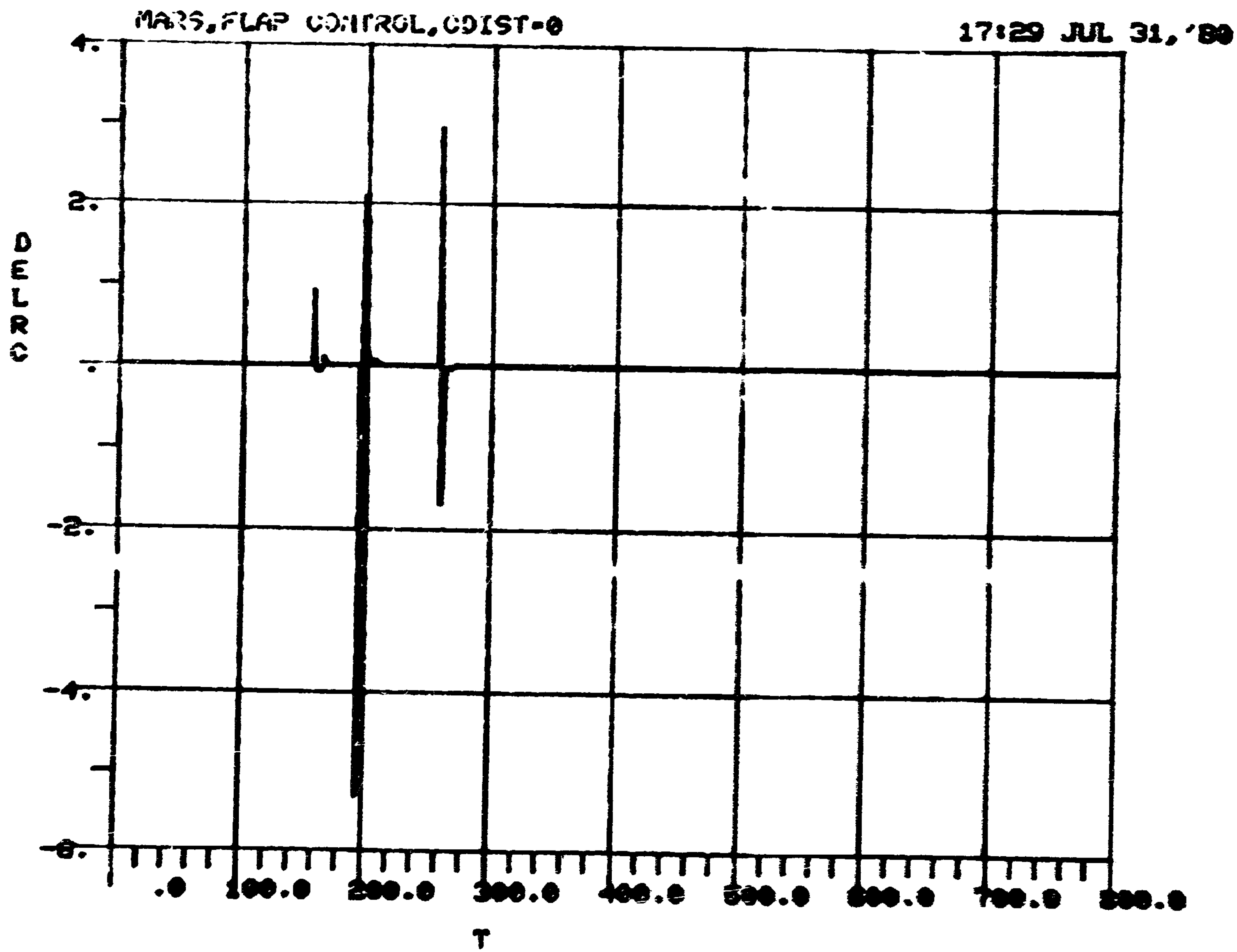

Figure V-62 Roll Flap Deflection Command, Flap Control

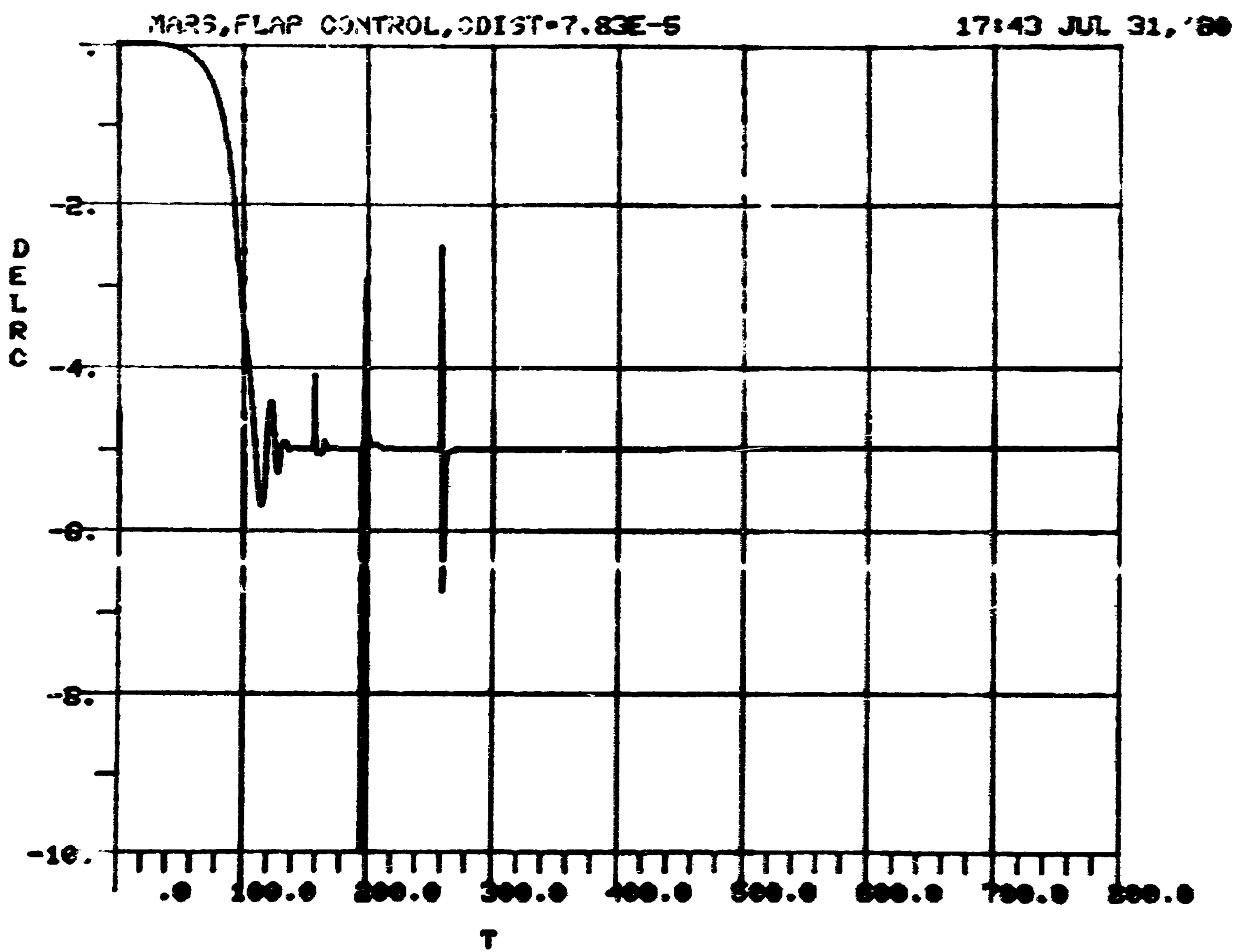

Figure V-63 Roll Flap Deflection Command, Flap Control

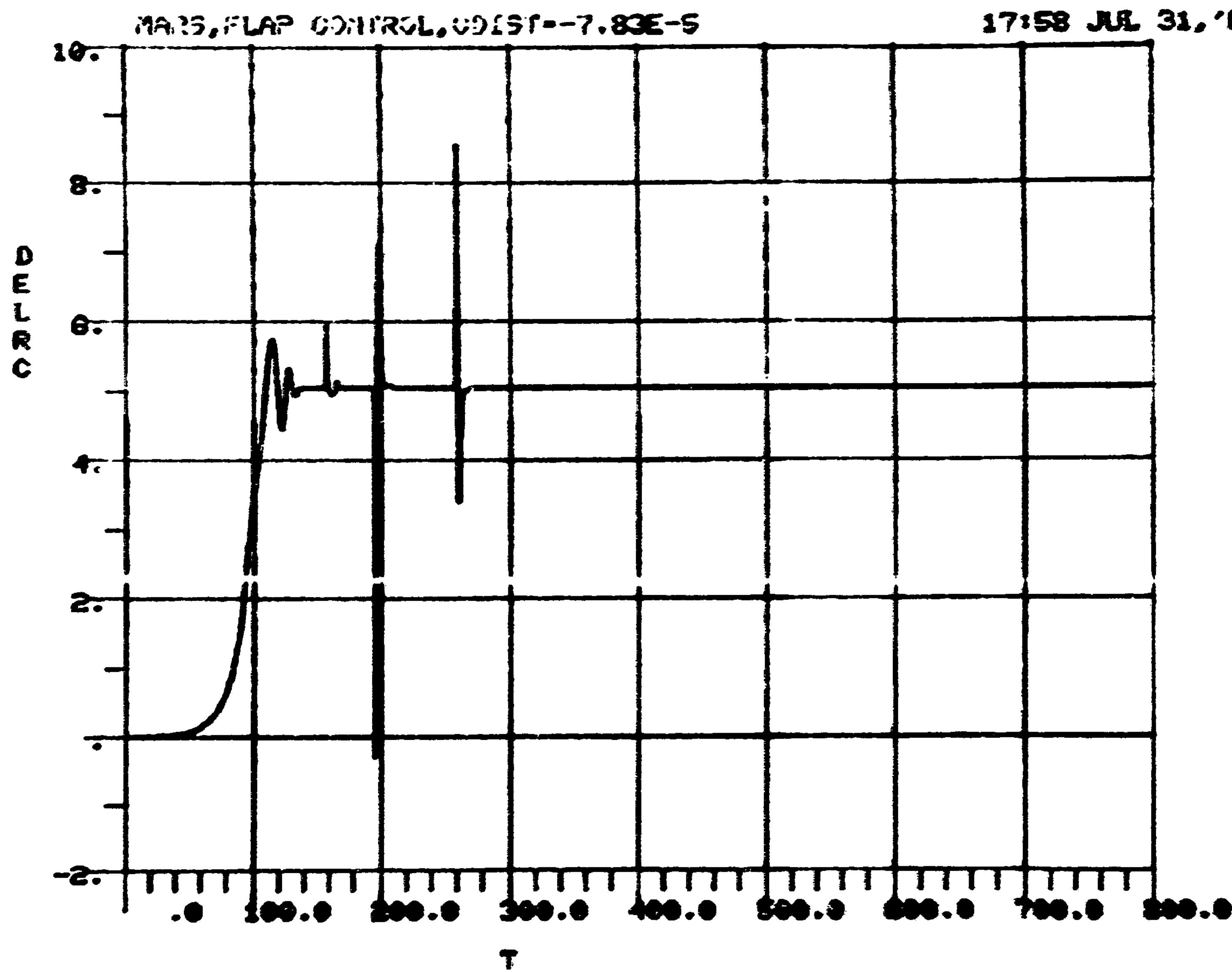

Figure V-64 Roll Flap Deflection Command, Flap Control

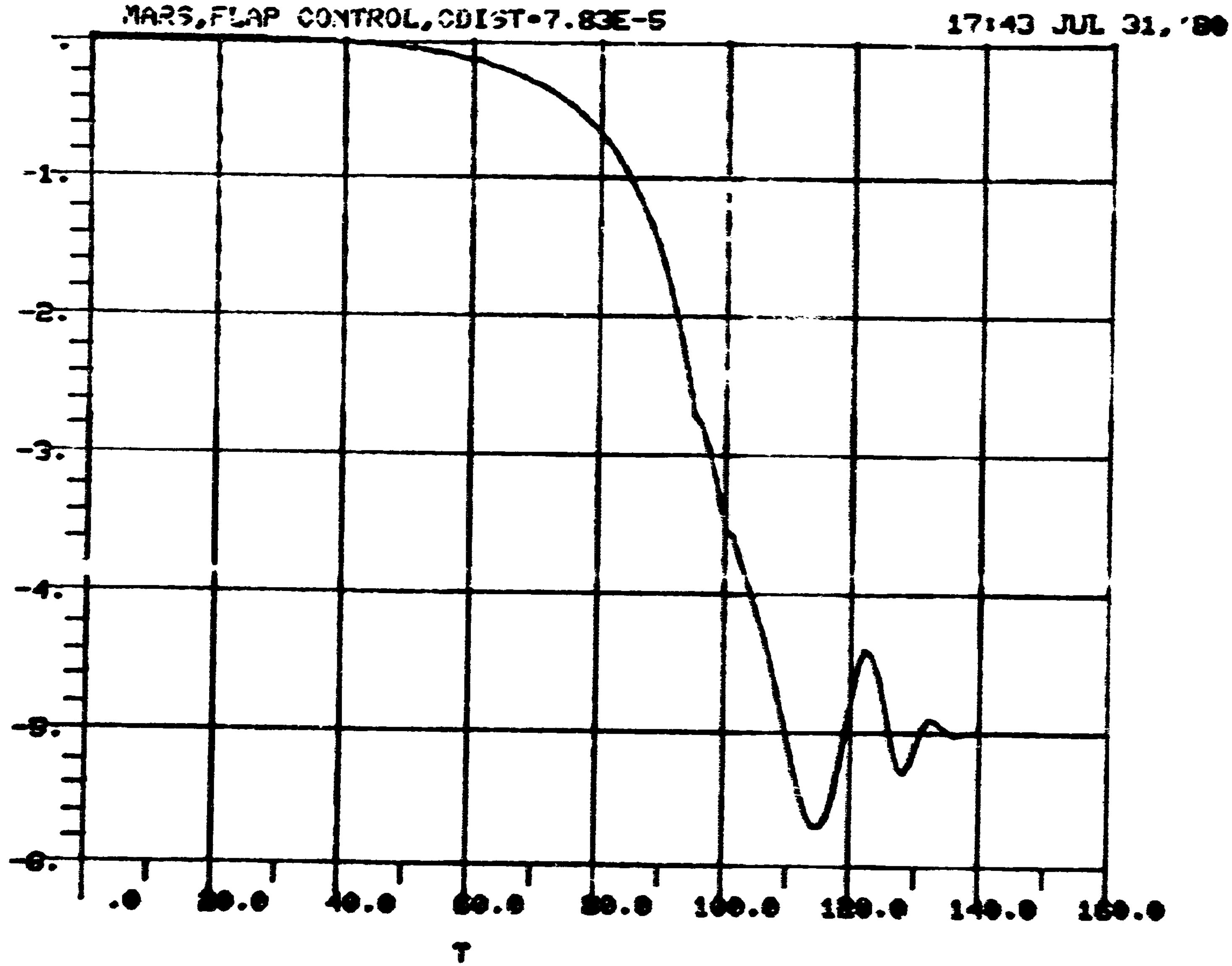

Figure V-65 Roll Flap Deflection Command, Flap Control

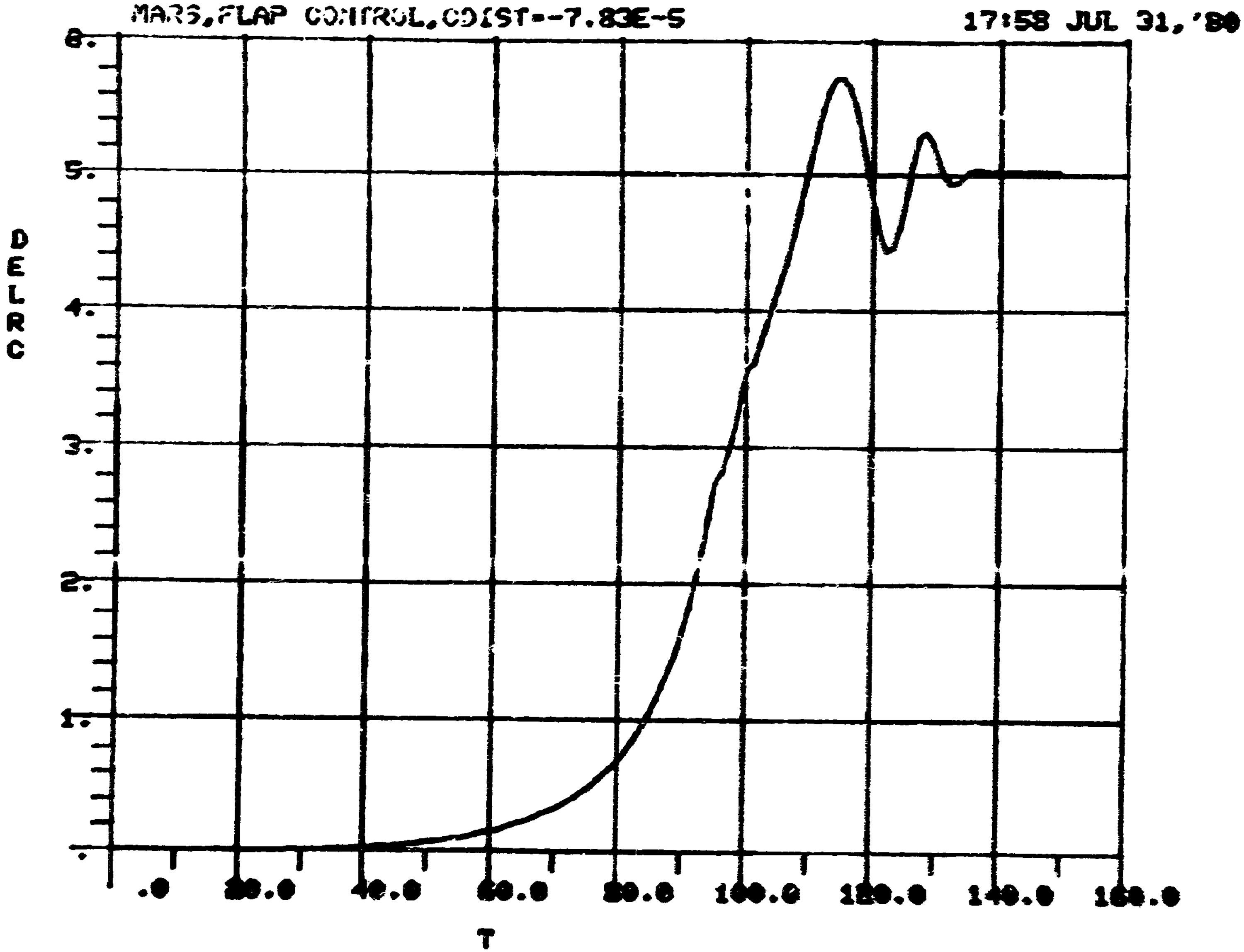

Figure V-66 Roll Flap Deflection Command, Flap Control

VI. VEHICLE DESIGN

A. APPROACH

The design approach for this study was to evolve a single generic spacecraft concept for several aerocapture planetary missions. The goal was to develop a structural design such that either skirts, panels or sections can be added so that the basic design can meet length constraints and still package the mission payload.

A generic spacecraft aeroshell configuration was developed that met performance and packaging requirements for the SO2P, and Uranus missions. The STS IUS/SEPS launch limited the length to 6.3 m for these missions. For the MSR mission the basic configuration is lengthened by a 3.3m long skirt added to the basic shape (allowed because the SEPS stage is not planned for the MSR mission). The output of this vehicle design effort consists of a definition of the aeroshell design concept, including geometry and mass properties required for Titan, Mars and Uranus aerocapture.

The section is partitioned into a Generic Design discussion that presents data common to aeroshells for all missions and characteristics of specific design concepts for the SO2P, MSR and Uranus missions. The spacecraft configuration selection is based on aerodynamic, thermodynamic, control, interface and packaging constraints. The first three parameters are discussed in Sections III, IV, and V. Interface and packaging constraints are listed in Table VI-1 along with their effects on aeroshell design.

A comparison of configurations evaluated in Section III vs. vehicle design parameters is shown in Figure VI-1. A geometric visual comparison of the studied shapes is shown in Figure VI-2. Shape 7-6 was selected for study analysis based on the packaging volume, the results of JPL's packaging studies and the data available on its characteristics as the SM configuration used in the Mars Aerocapture Vehicle Definition Study, Ref. 1-1.

B. GENERIC VEHICLE DESIGN

This section contains data and analyses that are applicable to the generic aerocapture vehicle as studied for various planetary missions. It contains geometry, unit mass properties and structural analyses that are applicable to the basic 6.3m long SM configuration and its extension to a 9.6m long design.

Geometric and aerodynamic data are presented in Figure VI-3. A geometric solution for the intersection of the two frustums is shown in Figure VI-4. Achieving a smooth intersection is not straightforward since the frustum cuts end up as different ellipses unless the cut angle is compromised and a step is formed. Three solutions were studied: a) A wedge inserted between the two sections with each cut at right angles to its centerline; b) Use of an elliptical forebody or afterbody; and c) Use of an offset centerline, a slanted cut giving a matched intersection with coincident ellipse.

The last method was chosen based on minimum perturbation to aerodynamic characteristics and manufacturing simplicity. This results in slightly modified geometry when holding basic shape dimensions as inputs.

Surface areas, centroids, enclosed volumes and unit inertias are given in Table VI-2 for the shell parts. These are used to develop the properties for a specific mission condition after the structure and thermal protection requirements are set.

The shell structure sizing analysis is done parametrically by analyzing for a range of atmospheric pressures that might be sustained during aerocapture. A range of dynamic pressures from 13 to 150 kPa was used for sizing the aluminum honeycomb sandwich used as the shell design. Inertia relief is based on preliminary center-of-mass locations for the aeroshell and payload. The pressure distributions used are shown in Figures VI-5 and 6. A basic sandwich design using aluminum face sheets and honeycomb core was used. The depth is varied to provide the required strength. Figure VI-7 gives the unit mass versus depth.

C. SATURN ORBITER DUAL PROBE AEROSHELL DESIGN

The SO2P mission spacecraft is designed for a Titan atmosphere aerocapture. It will be transferred by the STS shuttle to a low earth orbit and propelled in the trans-Saturn phase by a IUS-SEPS combination.

The spacecraft will consist of an aeroshell supporting and packaging a Titan probe, a Saturn probe and a Galileo type Saturn orbiter. Study configuration (Figure VI-9) supplied by JPL placed the Titan probe at the nose and would be deployed after the aerocapture maneuver; the Saturn re-entry probe is next in line and is ultimately deployed into the Saturn atmosphere.

The SO2P estimated payload mass as defined by JPL for this mission is:

Orbiter		1072 kg
Titan Probe and Support		228
Saturn Probe and Support		250
	Total =	1550 kg

Using the mission performance curves of Figure VI-10 the net allowable spacecraft mass depending on mission time is as follows:

Entry Velocity	Spacecraft Mass
8 km/s	2660 kg
10	2600
13	2400

Hence the mass goal for the Aerocapture system varies between (2400 - 1550 =) 850 and (2660 - 1550 =) 1110 kg. As the aeroshell mass increases with increasing entry velocity, the greatest allowable Aerocapture mass occurs at V_∞ = 8 km/sec.

The design and mass properties for the SO2P aeroshell are obtained by combining those for the structure and thermal protection subsystems that are required for typical Titan capture missions at entry velocities of 8 and 13 km/s. An aeroshell mass summary is presented in Table VI-3 for an ISM solution at 8 km/sec and carbon phenolic solutions at 8 and 13 km/sec.

1. Aeroshell Design - The shell structure sizing has been performed at the high and low extremes of likely entry velocities. It is based on the maximum pressure attained during control system runs of Section V and on the accelerations during IUS boost. The pressures correlate with the following TPS solutions:

V	α	Q
8 km/S	-23°	15 kPa
13	-23.5	20.5

An aluminum sandwich was assumed as the shell configuration for the monocoque aluminum structure. The aluminum structure is protected to room temperature during peak pressures even though it soaks out to 590K after aerocapture loading has subsided.

The sandwich shell used is defined in Figure VI-7 as to geometry and unit weights. Figure VI-8 gives parametric data on the honeycomb thickness required for a range of static pressures for the three frustums of the vehicle.

The structural shell requirements and ring masses for the aeroshell are given in Figures VI-11 and 12. Mass and center-of-mass analyses for the structure are included in Table VI-3.

The thermal protection materials as defined in Section IV and unit masses are shown in Figures VI-13 and 14. Tables VI-4 and 5 contain the detail mass and CM analyses for the TPS, and Table VI-6 for the structure.

A summary of the structure and TPS masses required for the SO2P aeroshell at the Titan entry conditions are given in Table VI-3.

An alternate TPS consisting of carbon phenolic material in the high heat areas of the vehicle was examined for the 8 km/s entry velocity mission. The required protection map is shown in Figure VI-15, and the analysis in Table VI-7. This TPS solution would impose 2 145 kg mass penalty.

2. Mass Properties - The structure, TPS and aeroshell (structure plus TPS) masses have been presented in Tables VI-3 through 7 for the three parametric design concepts evolved in this study. In addition, the aeroshell inertia properties are presented in Tables VI-8 and 9.

3. Flap Implementation Analysis - SO2P - This section contains the results of analyses performed to determine the design impact of using flaps to achieve roll trim for an aerocapture vehicle. This analysis was performed in support of Section V - Attitude Control where six control configurations are examined:

1. RCS Roll Control
2. RCS with Pulse Width Modulation
3. Flap Trim Control
4. Flap Control
5. MMRC Trim Control
6. MMRC Roll Control

The results presented provide a weight est mate in support of 3 (Flap Trim Control) for a specific SO2P mission and config ration.

The assumed design is a trailing, split-wi dward flap concept on the 6.[illegible] long vehicle as shown in Figure VI-16. The tr ling flap has a lesser impact on the aerodynamic and structural characteristi s of the vehicle than would cur with a larger slice for body mounted flaps. However, the trailing flaps can complicate the interface with the propulsion module or a jettisonable skirt arrangement like the one evaluated for the MSR mission.

The following design requirements and assumptions are derived from the simulations discussed in Section V.

Roll for Titan A/C (QB = 34.5 kPa; α = 20° δ = 9.6°)

Trim for 6.3 mm center-of-mass offset

Area - 18% of base area (0.98m^2)

Span - 1.15m

Chord - 0.86m

Operating Angle - 4.8° $\pm$4.8°

Pitch Rate - 5 ^{o}/s

Pitch Freq. - 3 Hz

Operating Time 200s

Hinge Moment - 4000 Nm

The flap structure and thermal protection details are defined in Table VI-10. The required aeroshell supporting structure is given in Table VI-11. The total masss of the flap installation using the lightest weight actuation subsystem is given in Table VI-12 as 100 kg.

The dynamic requirements for flap actuation can be met by hydraulic, pneumatic, or electric actuation systems. Hydraulic actuation was rejected as unsuitable for space application, so a trade-off was made between electric and pneumatic designs.

The electric system allows the easiest maintenance and check-out procedures. The system comprises a drive electronics package, and two actuators, each consisting of a 1/2 HP samarium cobalt permanent magnet DC servo motor driving an acme worm through a gearbox. The system weights are:

2 Actuators	8.3 kg
2 Motors	4.5
Drive Electronics	1.8
Cable	.7
Battery Delta	.5
Total	15.9 kg

The pneumatic system comprises a 69000 kPa helium storage bottle with a fill and squib valve, a 5500 kPa regulation, two actuators and a control electronics package. Each actuator employs a differential area piston with system pressure on the smaller area (rod end). Pressure in the large end is controlled by a torque motor operated three way low leakage poppet valve. The actuators are 9.6 cm in diameter and 33 cm long plus devices. System weights are:

Filter Tank	4.5 kg
Regulator	.7
2 Actuators w/Control Valves	5.5
Lines	.7
Control Electronics	.2
Total	11.6 kg

The pneumatic system is lighter and has the potential for better dynamic performance. The electrical system simplifies servicing and check-out procedures and has an inherently longer storage life. Final selection must be based on interplanetary cruise time, overall system mass and potential integration with payload power sources.

D. MARS SAMPLE RETURN AEROSHELL DESIGN

The Mars Sample Return Aerocapture aeroshell is designed for a Mars atmosphere entry as defined in Sections IV and V of this report. The payload will be the Orbiter, Lander, and the trans-Mars flight components. The spacecraft and IUS are to be launched to a low Earth orbit where the spacecraft/IUS assembly is deployed. The IUS then provides the velocity increment for transit to Mars.

This spacecraft mission was studied extensively as reported in Ref. I-1. The current study was directed toward using a generic configuration for the MSR mission that can also be used at other planets.

The allowable vehicle length for the SO2P and Uranus missions is 6.3m. This is based on packaging of the spacecraft and their propulsion stages in the shuttle. However, the MSR mission propulsion allows a vehicle length of 9.6m. The MSR spacecraft as defined in this section consists of a 6.3m long vehicle as generic to Saturn and Uranus with a 3.3m skirt added to the base to provide a 9.6m aeroshell to house the MSR Orbiter and Lander. This presents a challenge to packaging the MSR payload. A potential inboard view was developed by JPL and shown in Figure VI-17.

1. Aeroshell Design - The structural shell sandwich is defined in Figure VI-7 and the unit masses are given in Figure VI-18. Table VI-13 contains the analyses for the mass and CM of both the AC and AM configurations.

The thermal protection required materials and unit masses are shown in Figure VI-19. TPS mass and center-of-mass analysis is summarized in Table VI-14.

The combined mass properties for both the aerocapture and aeromaneuver aeroshells are given in Figure VI-20 and Table VI-15.

E. URANUS MISSION AEROSHELL DESIGN

The generic spacecraft configuration was adapted to the Uranus mission by designing a thermal protection and structural system to meet the requirements for an entry at V - 30 km/s and α = -12°.

The basic honeycomb sandwich structure of Figure VI-7 was sized for depth Figure VI-21, by using Figure VI-8. Table VI-15 contains the data on structure mass and center-of-mass location.

The thermal protection map is given in Figure VI-22. TPS mass and CM numbers are contained in Table VI-17.

F. VEHICLE DESIGN SUMMARY

The Vehicle Design Study results support the feasibility of a design solution for a structure and thermal protection system of a generic aeroshell to accomplish the proposed missions to Saturn, Mars and Uranus.

A 6.3m long aeroshell has been defined for use on the SO2P and Uranus missions and a 9.6m long aeroshell defined for the MSR mission by adding a "skirt" to the basic configuration. The MSR "skirt" can be jettisoned after Mars aerocapture so that the forward section will perform the aeromaneuver to a specified landing site.

Table VI-18 summarizes the mass properties of the aeroshells for the SO2P, MSR and Uranus missions.

Table VI-1 Configuration Selection Criteria

PARAMETER	DESCRIPTION/DISCUSSION
SURFACE AREA	Minimum surface area of the vehicle results in minimum structure and thermal protection mass.
INTERNAL VOLUME	The internal packaging volume is to be maximum to accommodate the payload vehicles and equipment. Since the center-of-mass of the packaged equipment must be near the nose of the shape where the space is least, a packaging evaluation criterion is used which compares the maximum diameter of spheres with centers at the vehicle c.p.
CM/CP LOCATION	The configuration that has the most aft center-of-pressure is the easiest to package with the need to maintain the center-of-mass at the center-of-pressure.
MASS INERTIAS	Minimizing roll, pitch and yaw inertias reduce the attitude control energy needed to maneuver the spacecraft during the complete mission.
SHUTTLE SPACE	Vehicle length is critical due to the shuttle bay space required for the propulsion modules required for the deep space missions. A maximum length of 6.3m is allowed for the SO2P and Uranus missions; 9.6m for the MSR mission. The 4.5m bay diameter was not found restrictive for the biconic shapes considered.
INTERFACES	The spacecraft base attaches to the propulsion module. The propulsion module may be a SEPS, IUS or other developed propulsion unit. The interface to the payload orbiter or probe shall provide for structural support, thermal protection, separation and deployment. External interface accommodations provide for antennae, radiators, attitude control and guidance components and science sensors.

Table VI-2 Aeroshell Unit Data

Part	L (m)	r (m)	R (m)	Surface Area (m^2)	$\bar{X}_{fb}$ (m)	Volume (m^3)	I_R (kgm^2)	$I_{P\&Y}$ (kgm^2)
Nose	(0.2)	-	0.2	0.25	0.1	0.02	0.0267M	0.0167M
13° Frustum	3.37	0.2	0.98	12.82	1.31	4.22	0.50M	0.15M
7° Frustum	2.74	0.98	1.32	19.95	1.30	11.47	1.35M	1.30M
Base @ R = 1.32	-	-	1.32	5.47	0	0	0.871M	0.136M
7° Skirt	3.3	1.32	1.72	31.75	1.58	24.09	2.35M	2.08M
Base @ R = 1.72	-	-	1.72	9.29	0	0	1.48M	0.74M

NOTES: Basic - SM Shape 6.3m long

Extended - 3.3m long skirt added

Table VI-3 SO2P Aeroshell Mass and Center of Mass

Entry Condition V(km/s)	α	TPS Matl.	TPS Mass (kg)	TPS $M\bar{X}$ (kgm)	Structure Mass (kg)	Structure $M\bar{X}$ (kgm)	Aeroshell Mass (kg)	Aeroshell $M\bar{X}$ (kgm)	Aeroshell $\bar{X}_{fb}$ (m)
8	-23°	ESM/SAM	343	1101	129	288	472	1389	2.94
13	-23.5°	CP/ESM	781	2264	138	288	919	2552	2.80
8	-23°	CP/ESM	488	1412	129	308	617	1720	2.7[illegible]

Table VI-4 S02P - TPS Mass and Center of Mass, V = 8 km/s

Part	A (m^2)	M/A (kg/m^2)	M (kg)	$\overline{X}_{fb}$ (m)	$M\overline{X}$ (kgm)
Nose	.25	92.8	23	6.2	144
Fwd. Cone Upper 160°	5.70	4.9	28	4.05	113
Fwd. Cone Lower 200°	7.12	24.4	174	4.05	704
Aft Cone Upper 160°	8.87	2.5	22	1.30	29
Aft Cone Lower 200°	11.08	7.7	85	1.30	111
Base	5.47	2	11	0	0
			343	3.21	1101

Table VI-5 S02P - TPS Mass and Center of Mass, V = 13 m/s

Part	A (m^2)	M/A (kg/m^2)	M (kg)	$\overline{X}_{fb}$ (m)	MX (kgm)
Nose	0.25	210	53	6.2	326
Upper 13° Cone	6.41	9.05	58	4.05	235
Lower 13° Cone	6.11	47.2	303	4.05	1226
Δ 7° Cone	2.9	8.12	24	2.30	54
Upper 7° Cone	7.1	4.74	34	1.30	43
Lower 7° Cone	10.0	29.28	293	1.30	380
Base	5.47	3	16	0	0
			781	2.90	2264

Table VI-6 SO2P Structure Mass and Center of Mass

Part	A (m^2)	X_{fb} (m)	V = 8 km/s M/A (kg/m^2)	M (kg)	MX (kgm)	V = 13 km/s M/A (kg/m^2)	M (kg)	MX (kgm)
Nose	0.25	6.2	2.8	1	4	2.9	1	4
Fwd. Fru.	2.8	5.3	2.8	8	42	2.9	8	43
Fwd. Ring	-	4.7	-	5	23	-	6	28
Mid Fru.	10.0	3.6	3.0	30	108	3.1	31	112
Brk. Ring	-	2.74	-	6	16	-	7	19
Aft Fru.	20.0	1.3	3.1	62	81	3.3	66	86
Base Ring	-	0	-	10	0	-	11	0
Sep. S/S	-	2.0	-	7	14	-	8	16
				129	288		138	308
		$\bar{X}_8 = 2.23$				$\bar{X}_{13} = 2.23$		

Table VI-7 SO2P - TPS Mass and Center of Mass (CP Alt.)

Part	A (m^2)	M/A (kg/m^2)	M (kg)	$\bar{X}_{fb}$ (m)	$M\bar{X}$ (kgm)
Nose	.25	132	33	6.2	205
Upper 13° Fru.	6.41	7.48	48	4.05	194
Lower 13° Fru.	6.41	27.4	176	4.05	711
A7° Fru.	2.9	7.33	21	2.30	49
Upper 7° Fru.	7.1	3.42	24	1.30	32
Lower 7° Fru.	10.0	17.0	170	1.30	221
Base	5.47	3	16	0	0
			488	2.89	1412

Table VI-8 SO2P Aeroshell Inertias, V = 8 km/s

Part	M (kg)	I_{R_2} (kgm^2)	$I^0_{P\&Y}$ (kgm^2)	$\bar{X}_{CM}$* (m)	$\bar{X}^2 M$ (kgm^2)	$I_{P\&Y}$ (kgm^2)
Nose	25	1	Negl.	3.26	265	265
13° Frustum	240	120	276	1.11	296	572
7° Frustum	169	228	220	1.64	455	675
Base	11	10	5	2.94	95	100
Fwd. Ring	5	2	1	1.76	15	16
Brk. Ring	6	6	3	0.20	-	3
Base Ring	10	19	10	2.94	86	96
SEP S/S	7	7	4	0.94	6	10
		338				1737

* CM 2.94m from Base

Table VI-9 SO2P Aeroshell Inertias, V = 13 km/s

Part	M (kg)	I_{R_2} (kgm^2)	$I^0_{P\&Y}$ (kgm^2)	$\bar{X}_{CM}$* (m)	$\bar{X}^2 M$ (kgm^2)	$I_{P\&Y_2}$ (kgm^2)
Nose	54	1	[illegible]	3.4	624	6[illegible]5
13° Frustum	400	200	46[illegible]	1.25	625	1[illegible]5
7° Frustum	417	563	54[illegible]	1.50	938	1[illegible]0
Base	16	14	[illegible]	2.80	125	[illegible]32
Fwd. Ring	6	2	1	1.9	22	[illegible]3
Brk. Ring	7	7	4	0.34	1	5
Base Ring	11	21	1[illegible]	2.80	86	[illegible]6
Sep. S/S	8	8	[illegible]	0.80	5	13
		816				3[illegible]9

* CM @ 2.80m

Table VI-10 Flap Structure and TPS Characteristics

Structure

H/C Core - .19m thick at 83.5 kg/m^3	1.48 kg
Skins (2) 1.02mm thick aluminum alloy	5.55
Torsion Bar leading edge - aluminum alloy	2.68
Horn Assembly (2)	0.5
Hinge Assembly (4)	0.6
	10.81
+ 10% Allowance for bond and hardware	1.08
Flap Structure Weight =	12.0 kg

TPS

Windward Surface and Edges

30mm thick carbon phenolic at 500 kg/m^3 =	48.0 kg

Leeward Surface

14mm thick ESM at 550 kg/m^3 =	8.0 kg

Table VI-11 <u>Aeroshell Support Structure Characteristics</u>

<u>Circular Rings (2)</u>

React Flap Hinge Moments

1.07m Spacing

P = 7500 N.; BM = 1390 N-m

75mm Deep Alum. Alloy Channel

Weight = 0.077 gm/Linear mm

<u>Longitudinal Intercostals (4)</u>

React Actuator Loading

P = 1350 N (tension)

L = 1.07 M

75mm Deep Alum. Alloy Channels (0.08 gm/mm)

Table VI-12 Flap Weight

Flaps			
	Structure + FTG	12 kg	
	Carbon Phenolic H/S	48	
	ESM H/S	8	
			68 kg
Support Structure			
	Intercostals (4)	4 kg	
	Rings (2)	13	
	FTG + Contingencies	3	
			20 kg
Actuation S/S			
	Tank & Gas	4.5 kg	
	Regulars	.7	
	Actuators (2)	5.5	
	Lines	.7	
	Control Electronics	.2	
			11.6 kg

Total Weight of Flap System - ~100 kg

Table VI-13 MSR Structure Mass and Center of Mass

Part	A (m^2)	M/A (kg/m^2)	M (kg)	A/C Config. $\overline{X}_{fb}$ (m)	A/C Config. MX (kgm)	A/M Config. X_{fb} (m)	A/M Config. MX (kgm)
Nose	0.25	3.0	.8	9.5	8	6.2	5
Fwd. Cone	12.82	3.0	38.5	7.35	283	4.05	156
Center Cone	19.95	3.3	65.8	4.60	303	1.30	85
Aft Cone	31.75	3.4	107.9	1.58	171		
Break Ring			6	6.03	36	2.74	16
Sep. Ring			10	3.3	33	0	0
Base Ring			16	0	0		
Sep. Parts			10	1.65	17		
ACΣ	74		255	3.34	851		
AMΣ	33		121.1			2.16	262

Table VI-14 MSR TPS Mass and Center of Mass

Part		A/C Configuration					A/M Configuration			
		A (m^2)	M/A (kg/m^2)	M (kg)	X_{fb} (m)	MX (kgm)	M/A (kg/m^2)	M (kg)	X_{fb} (m)	MX (kgm)
Nose		0.25	7.14	1.8	9.5	17		1.8	6.2	11
Forecone	100°	3.56	7.19	25.6	7.35	188		25.6	4.05	104
	260°	9.26	2.40	22.2	7.35	163		22.2	4.05	90
Aft Cone L - 2.7	100°	5.54	6.85	37.9	4.6	175		37.9	1.30	49
	260°	14.41	2.40	34.6	4.6	159		34.6	1.30	45
L - 3.3	100°	8.82	6.85	60.4	1.58	95				
	[illegible]	[illegible]	[illegible]	[illegible]	1.56	67				
Base		9.29	1.00	9.3	0	0				
		74.06		246.8	3.58	884		122.1	2.45	299

Table VI-15 MSR Aeroshell Inertias

	A/C Conf. (CM @ 3.46)						A/M Config. (CM @ 2.31)					
	M (kg)	I_R (kgm^2)	$I^o_{P\&Y}$ (kgm^2)	$\overline{X}$ (m)	$M\overline{X}^2$ (kgm^2)	$I_{P\&Y}$ (kgm^2)	M (kg)	I_R (kgm^2)	$I^o_{P\&Y}$ (kgm^2)	$\overline{X}$ (m)	$M\overline{X}^2$ (kgm^2)	$I_{P\&Y}$ (kgm^2)
Nose	2.6	-	-	6.04	94.9	94.9	2.6	Negl.	Negl.	3.89	39	42
Fwd. Cone	86.3	43.1	99.2	3.89	1305.9	1405.1	86.3	43.1	99.2	1.74	261	360
Center Cone	138.3	186.7	179.8	1.14	179.7	359.5	138.3	186.7	179.8	1.01	141	321
Aft Cone	223.3	524.8	464.5	1.88	789.2	1253.7						
Break Ring	6	5	1	2.57	39.6	40.6	6	5	[illegible]	.48	[illegible]	[illegible]
Sep. Ring	10	14	7	0.16	.3	7.3	10	14	7	2.31	53	60
Base Ring	16	46	23	3.46	191.5	214.5						
Sep. Parts	10	8	1.81	32.8	40.8							
Base Shield	9.3	13.8	6.9	3.49	113.3	120.2						
	502	839.4				3536.6	243	247				785

Table VI-16 Uranus Structure Mass and Center of Mass

Part	A (m^2)	M/A (kgm^2)	M (kg)	X_{fb} (m)	MX (kgm)
Nose	.25	3.2	1	6.2	144
Fwd. Frustum	2.8	3.2	9	5.3	47
Fwd. Ring	-		10	4.7	47
Mid Frustum	10.0	4.0	40	3.6	144
Brk. Ring	-		12	2.74	33
Aft. Frustum	20.0	4.5	90	1.30	117
Sep. S/S	-		10	2.0	20
Base Ring	-		20	0	0
			192	2.15	413

Table VI-17 Uranus TPS Mass and Center of Mass

Part	A (m^2)	M/A (kg/m^2)	M (kg)	X_{fb} (m)	MX (kgm)
Nose	0.25	55.05	13.76	6.2	85
Upper 13° Cone	6.41	17.25	110.57	4.05	448
Lower 13° Cone	6.41	37.25	238.77	4.05	967
Δ 7° Cone	2.9	22.02	63.86	2.30	147
Upper 7° Cone	7.1	14.68	104.23	1.30	135
Lower 7° Cone	10.0	24.77	247.7	1.30	322
Base	5.47	3	16	0	0
			795	2.65	2104

Table VI-18 Mass Property Summary

Mission	V(km/s)	α(°)	Structure Mass (kg)	TPS Mass (kg)	Aeroshell Mass (kg)	Aeroshell CM Loc. (m from base)	Aeroshell I_R (kgm^2)	Aeroshell $I_{P\&Y}$ (kgm^2)
S02P	8 (1)	-23	129	343 (1)	472	2.94	338	1737
S02P	8 (2)	-23	129	488 (2)	617	2.75	-	-
S02P	13	-23.5	138	781	919	2.80	816	3459
Uranus	30	-12	192	795	987	2.55		
MSR-AC			255	247	502	3.46	839	3537
MSR-AM			121	122	243	2.3[illegible]	247	785

(1) Minimum Mass Thermal Protection

(2) Carbon Phenolic Thermal Protection

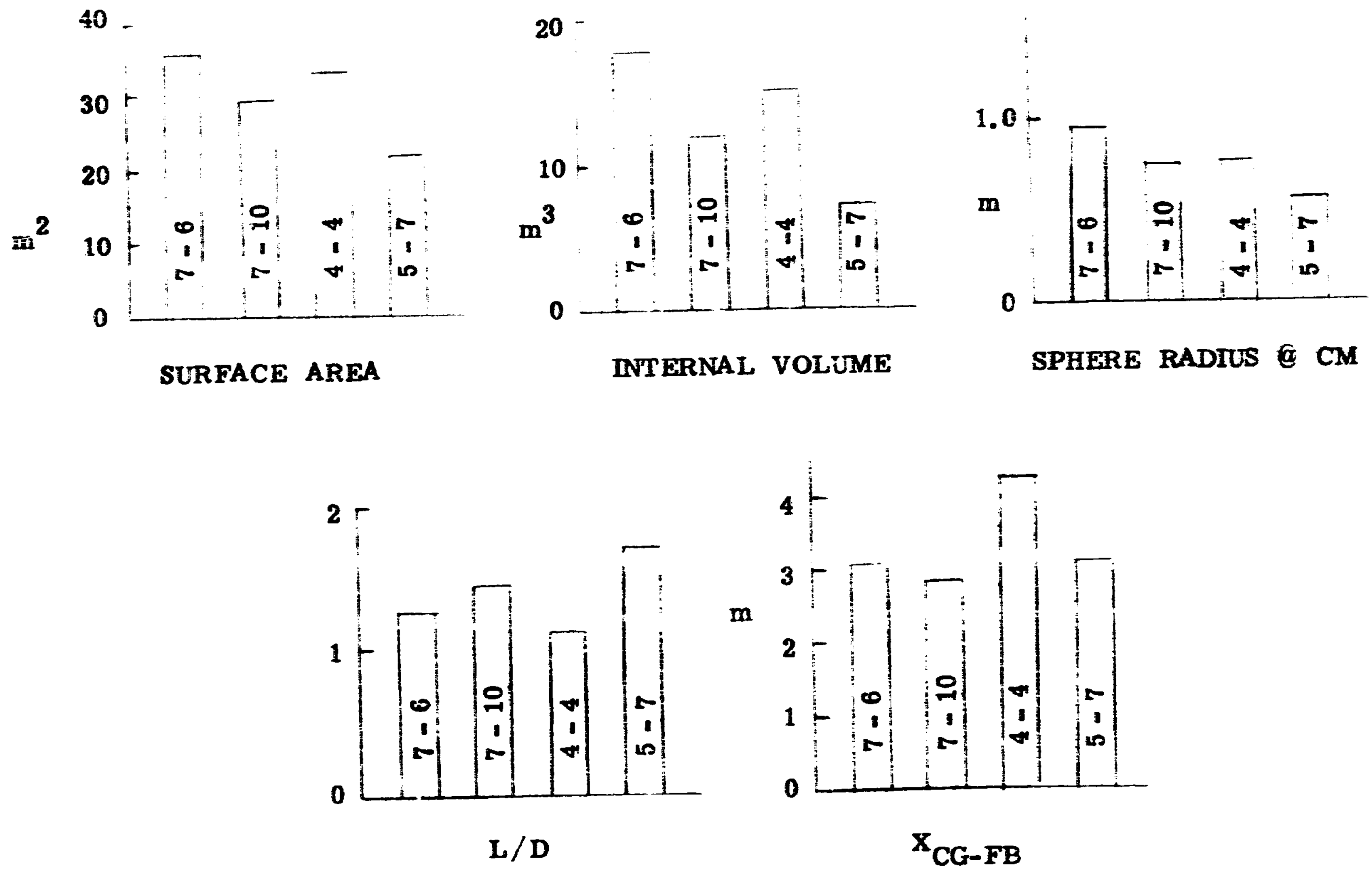

Figure VI-1 Configuration Geometric Data

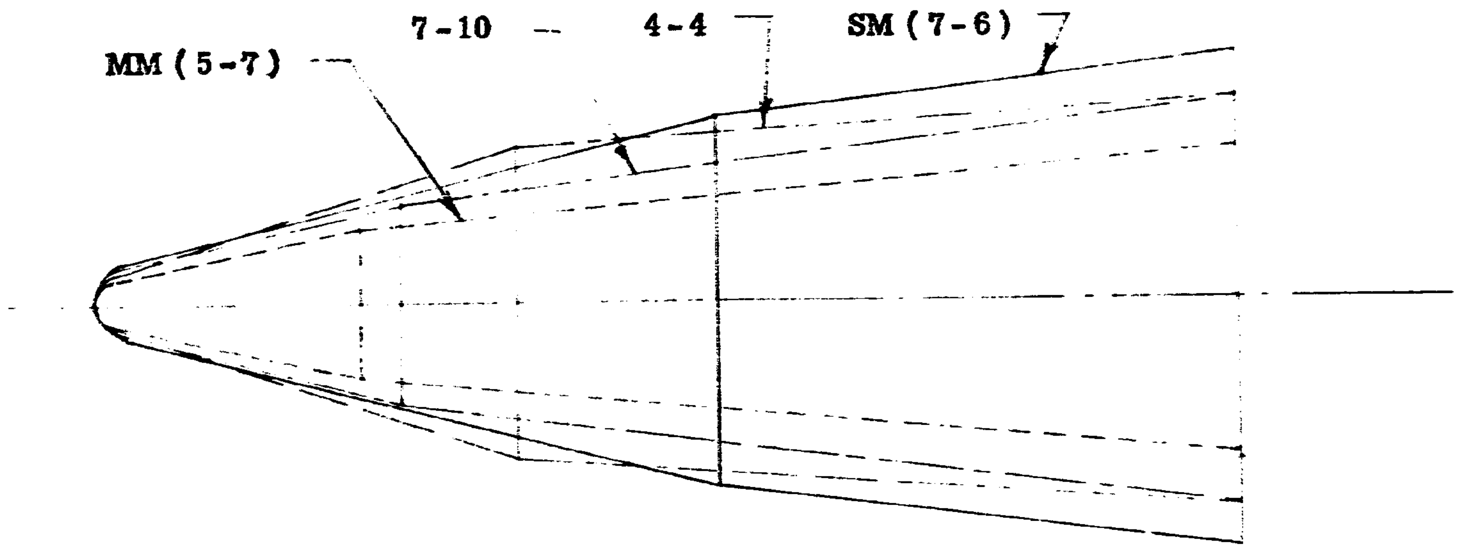

SHAPE	L	R_N	R_I	R_B	θ_F	θ_N	L_F
7-6 (SM)*	6.3	0.20	0.98	1.32	7°	13°	2.74
4-4	6.3	0.18	0.54	1.09	4°	16°	3.78
7-10	6.3	0.14	0.83	1.09	7°	12°	4.41
5-7 (MM)*	6.3	0.12	0.40	0.81	5°	10°	4.61

* Reference I-1

Figure VI-2 Candidate Configuration Geometry

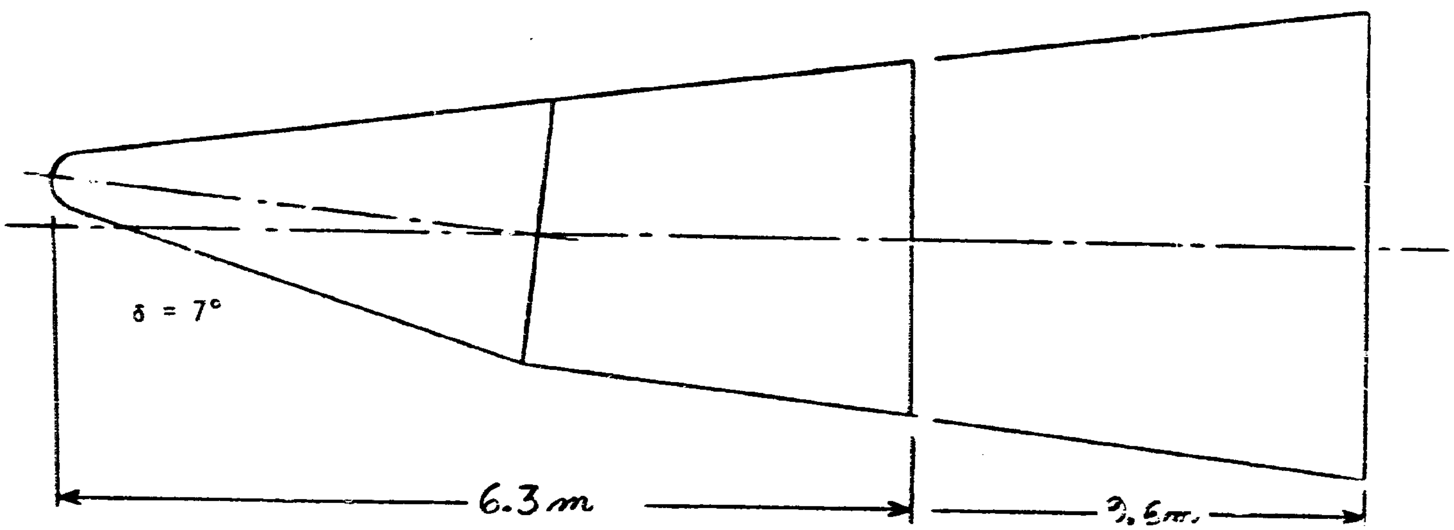

Figure VI-3 Generic Aeroshell Geometry

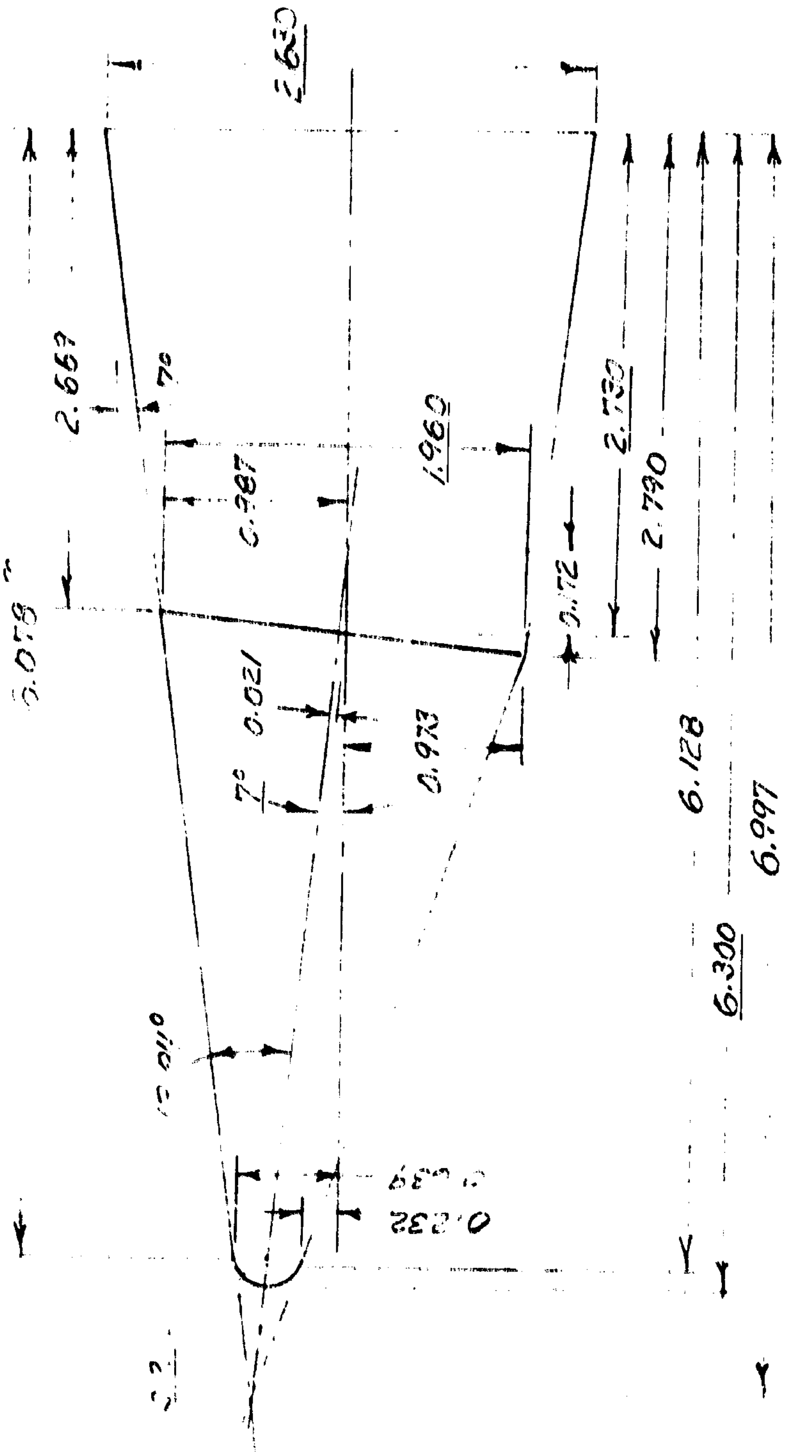

Figure VI-4 Frustum Insersection Geometry

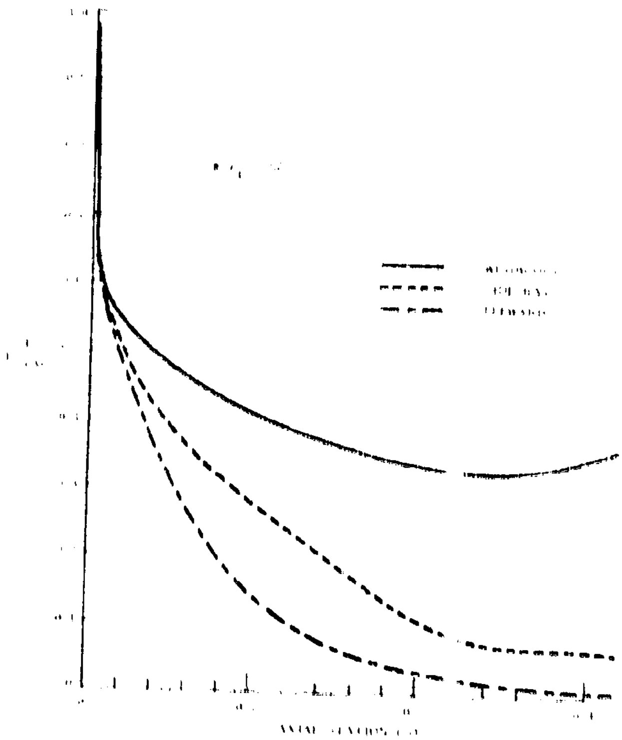

Figure VI-5 SO2P Nose Pres ure Distribution

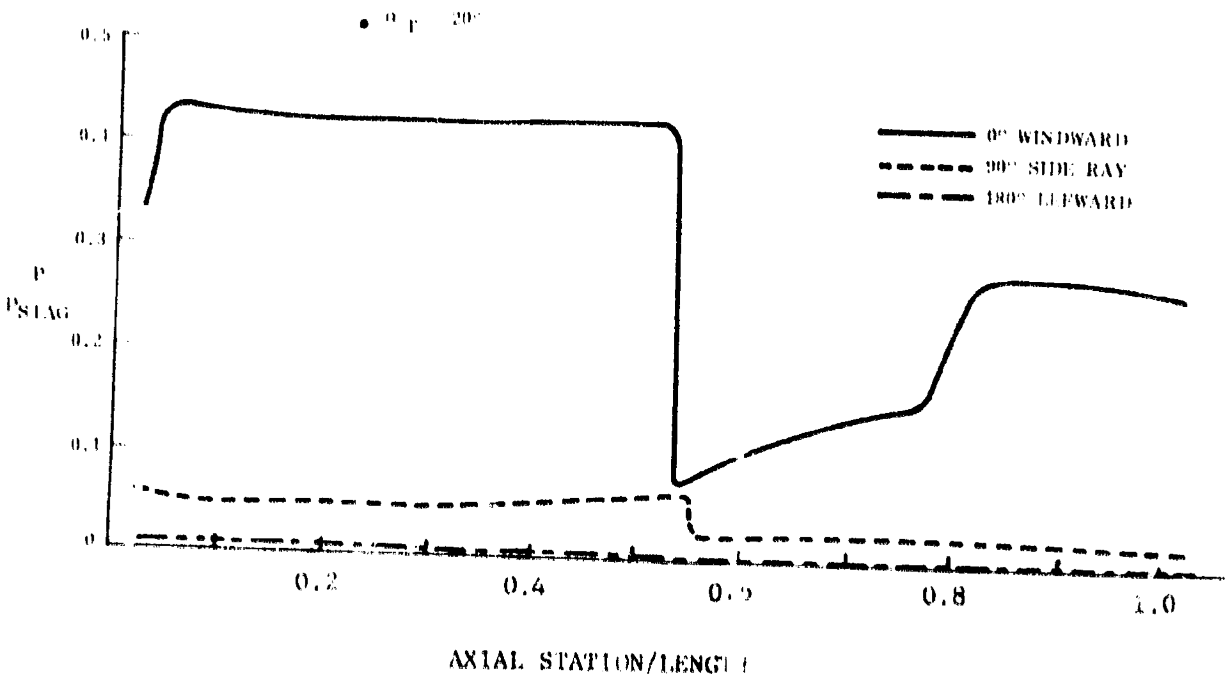

Figure VI-6 SO2P Vehicle Pres ure Distribution

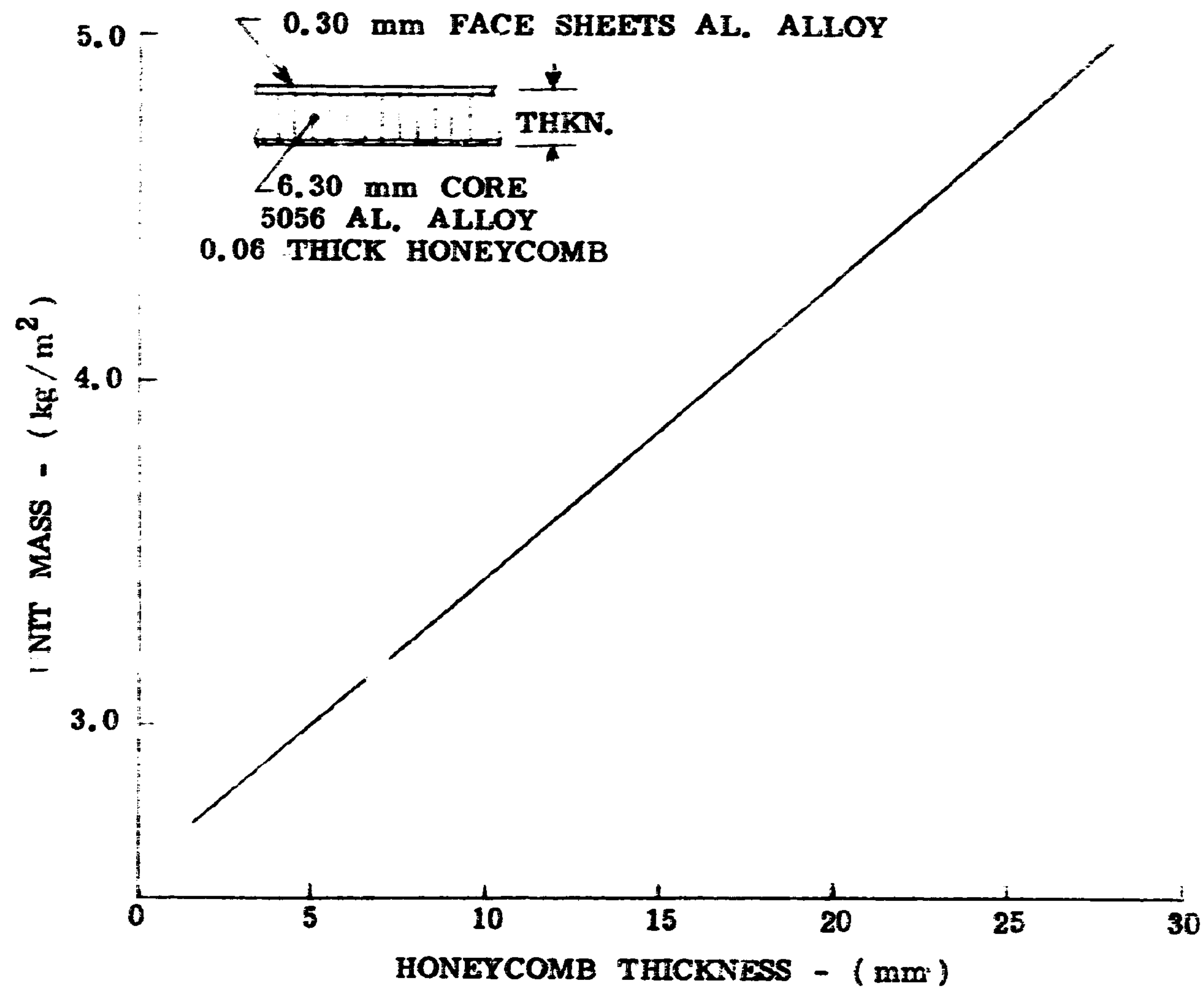

Figure VI-7 Shell Structure Unit Mass vs. Thickness

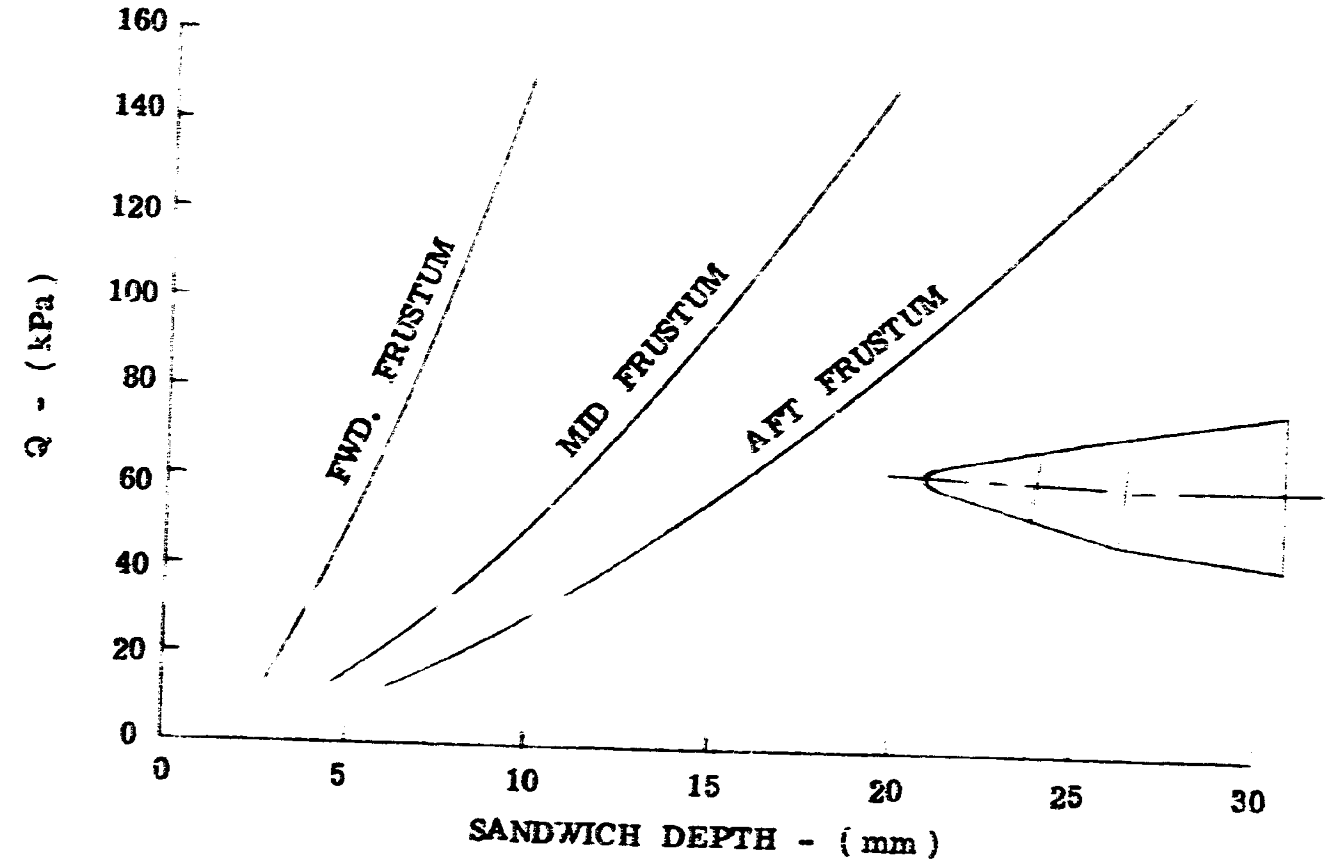

Figure VI-8 Structure Depth vs. Dynamic Pressure

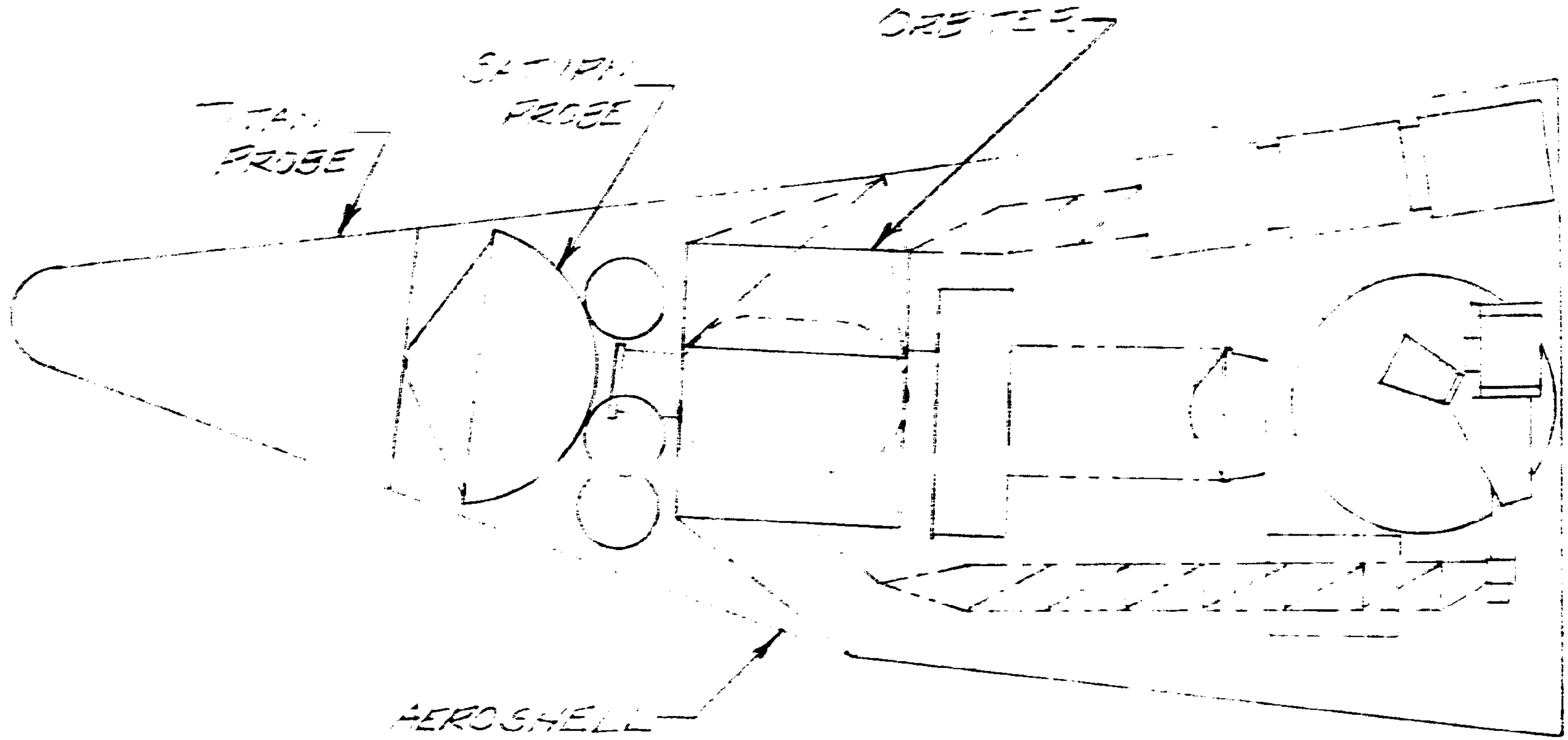

Figure VI-9 S02P Inboard Profile

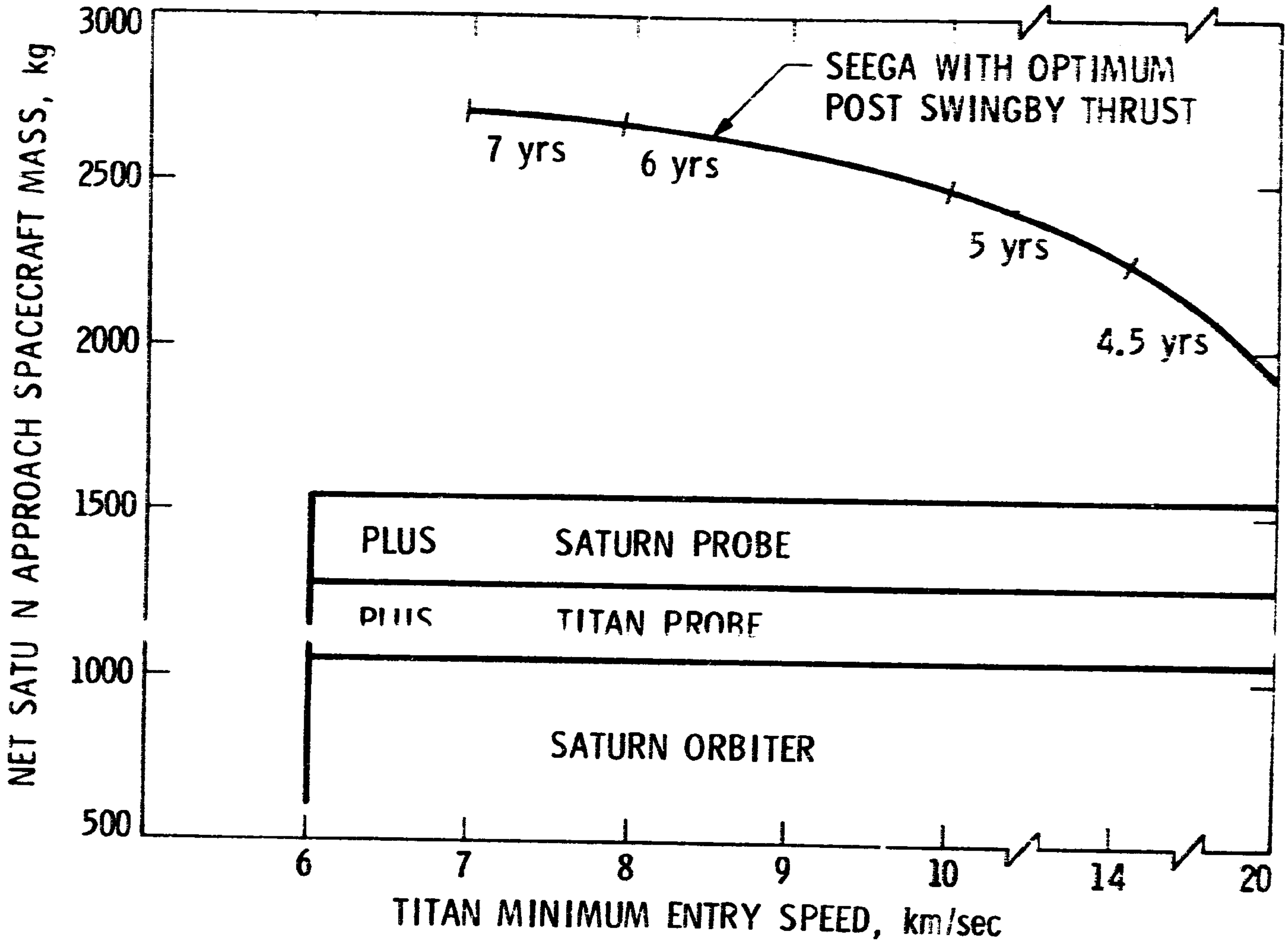

Figure 10 S02P Performance

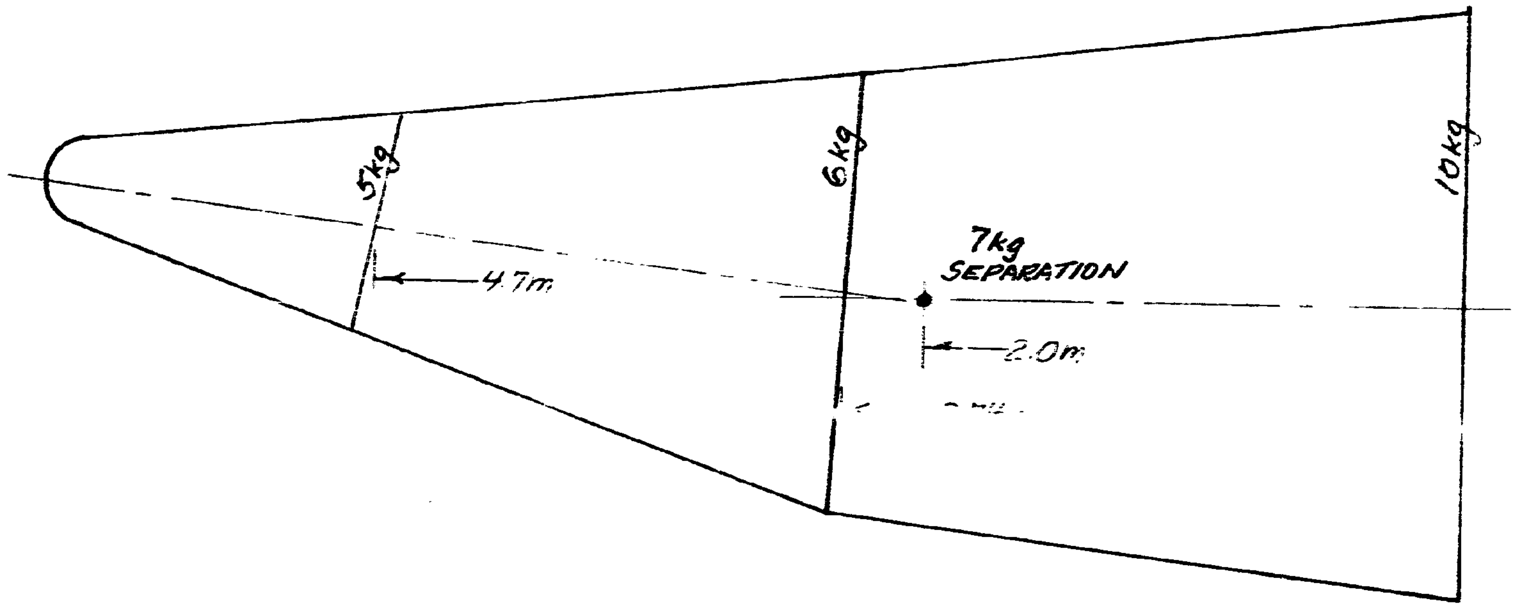

Figure VI-11 SO2P Structure, V = 8 km/sec

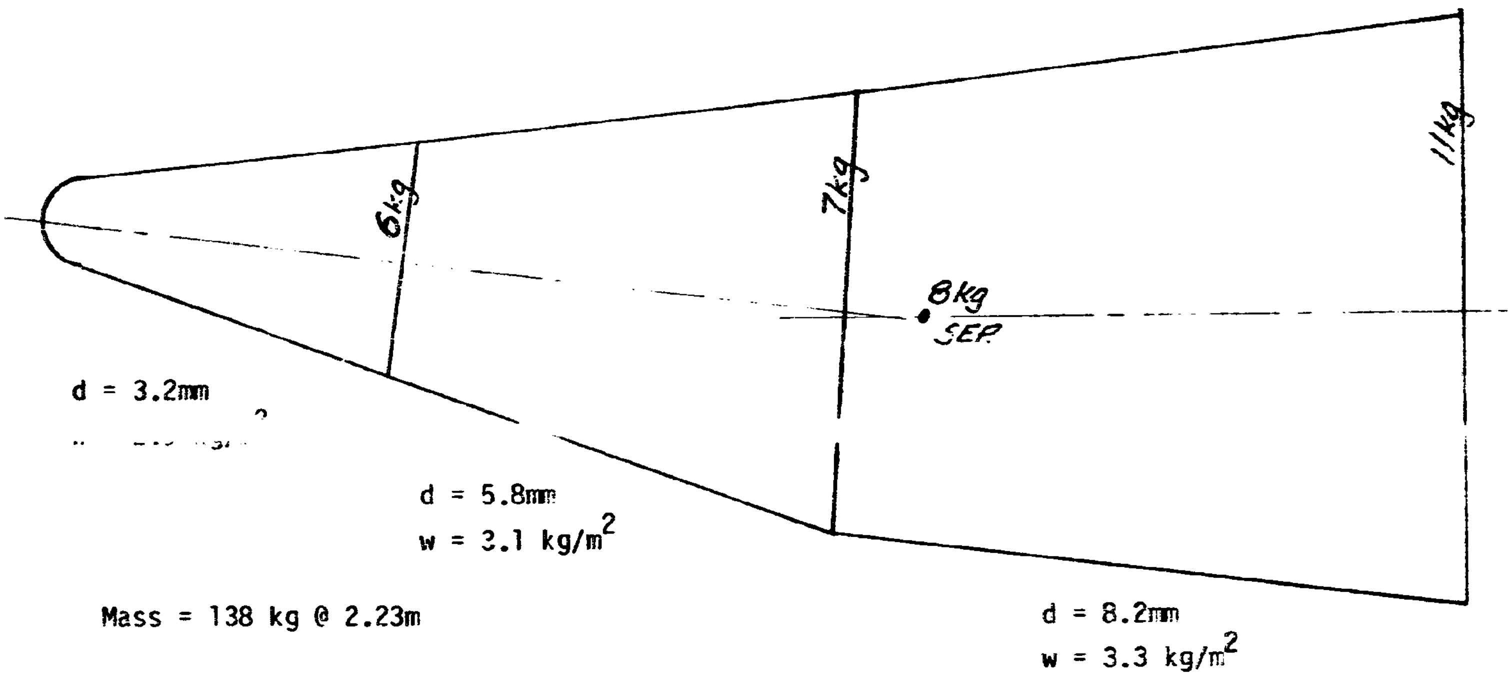

Figure VI-12 <u>SO2P Structure, V = 13 km/sec</u>

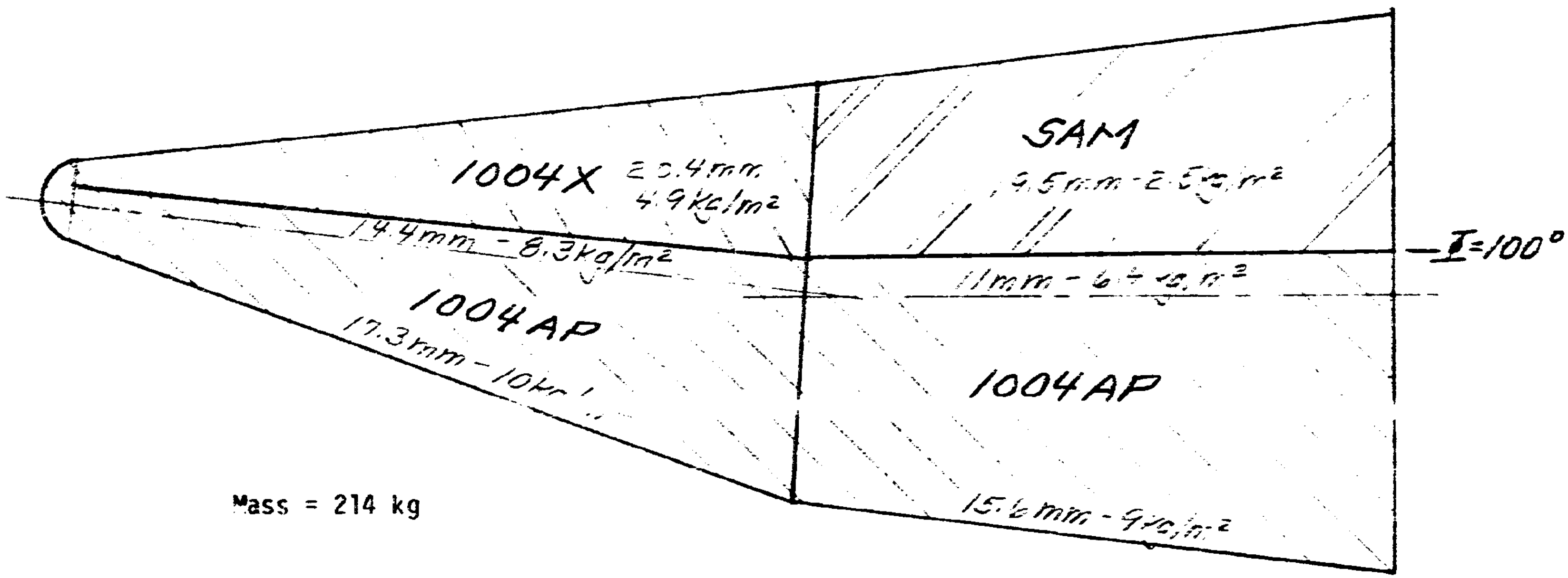

Mass = 214 kg

Figure VI-13 SO2P TPS, V = 8 km/sec

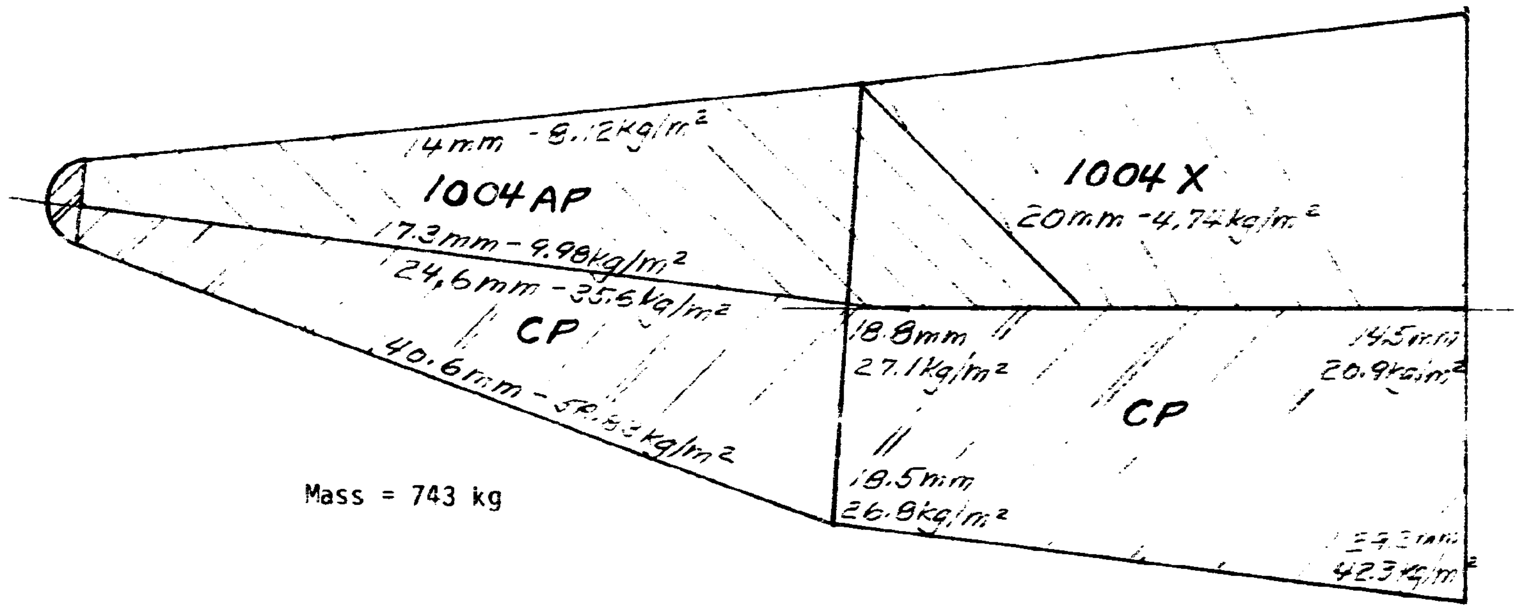

Mass = 743 kg

Figure VI-14 <u>SO2P TPS, V = 13 km/sec</u>

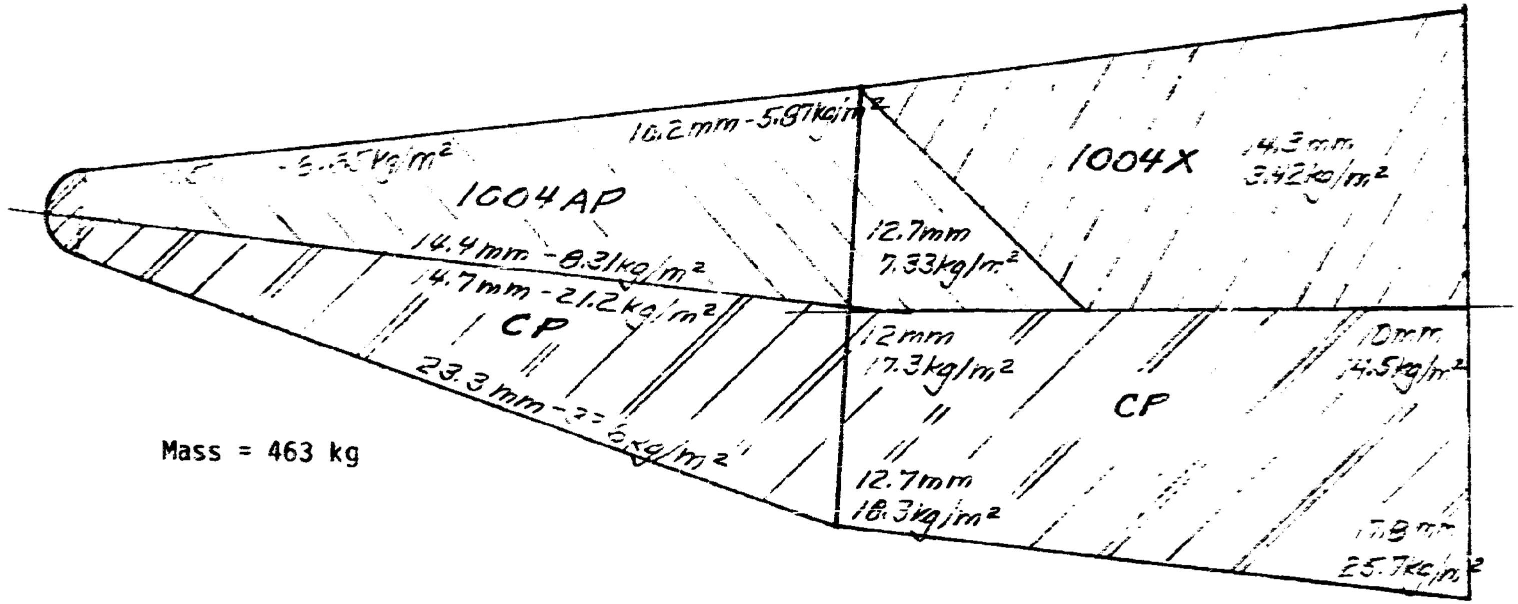

Figure VI-15 <u>S02P TPS, Carbon Phenolic Alternate, V = 8 km/sec</u>

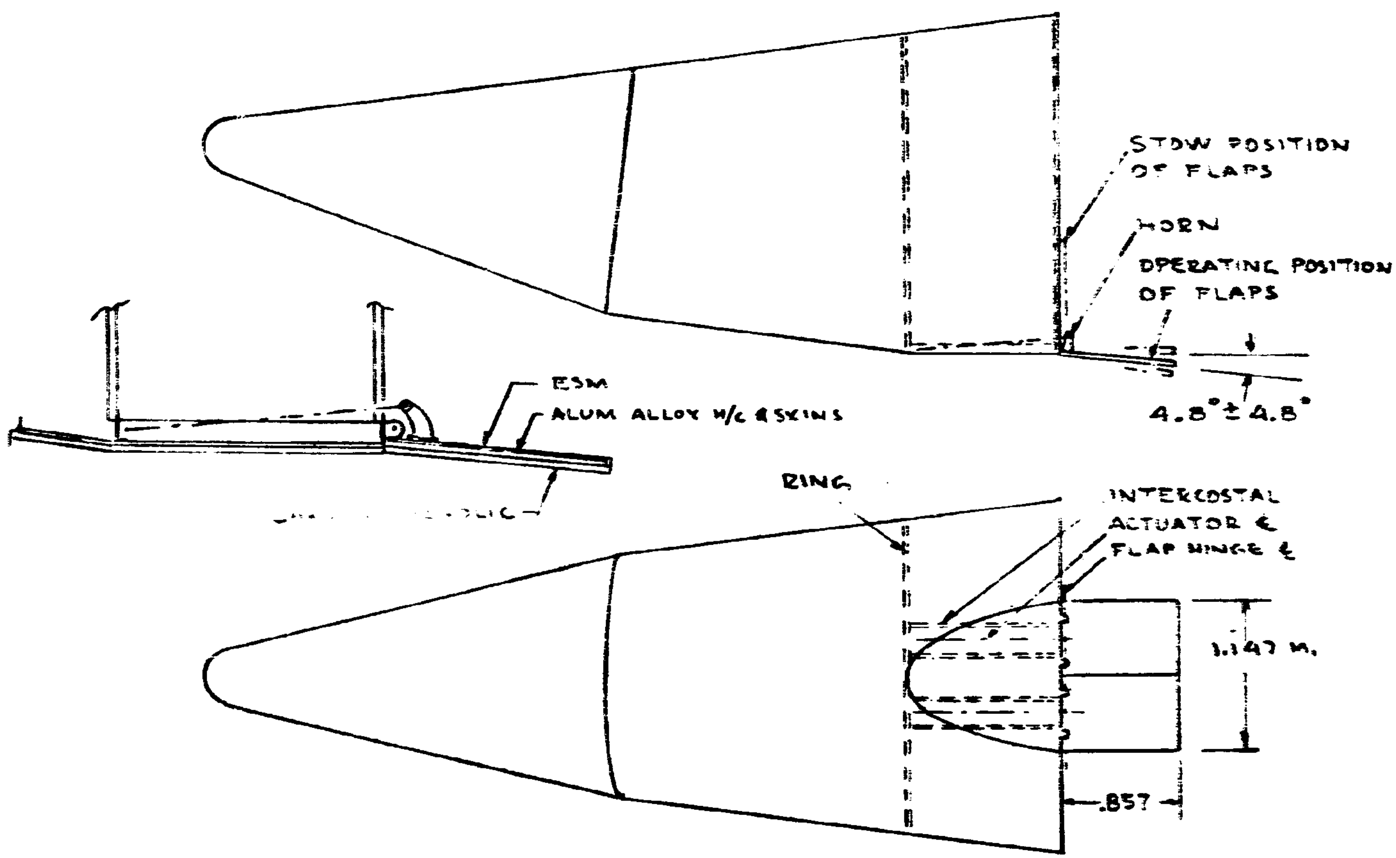

Figure VI-16 Flap Concept

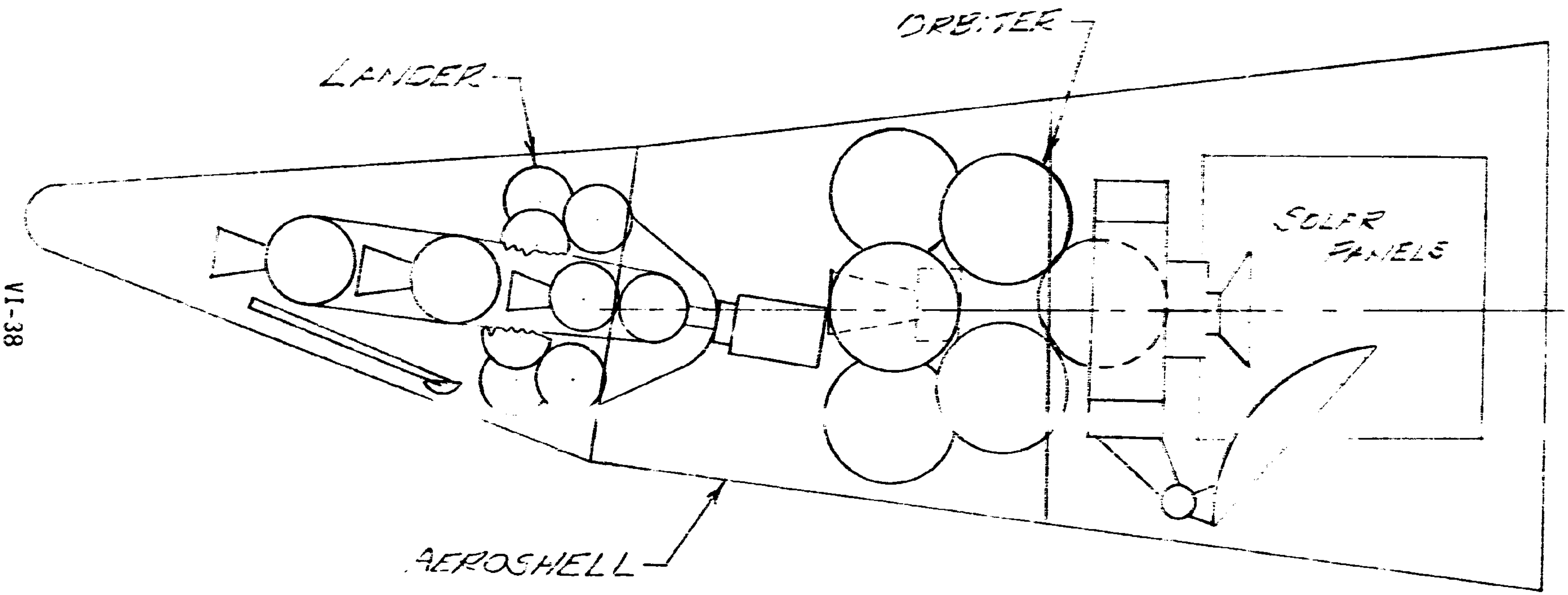

Figure VI-17 MSR Inboard Profile

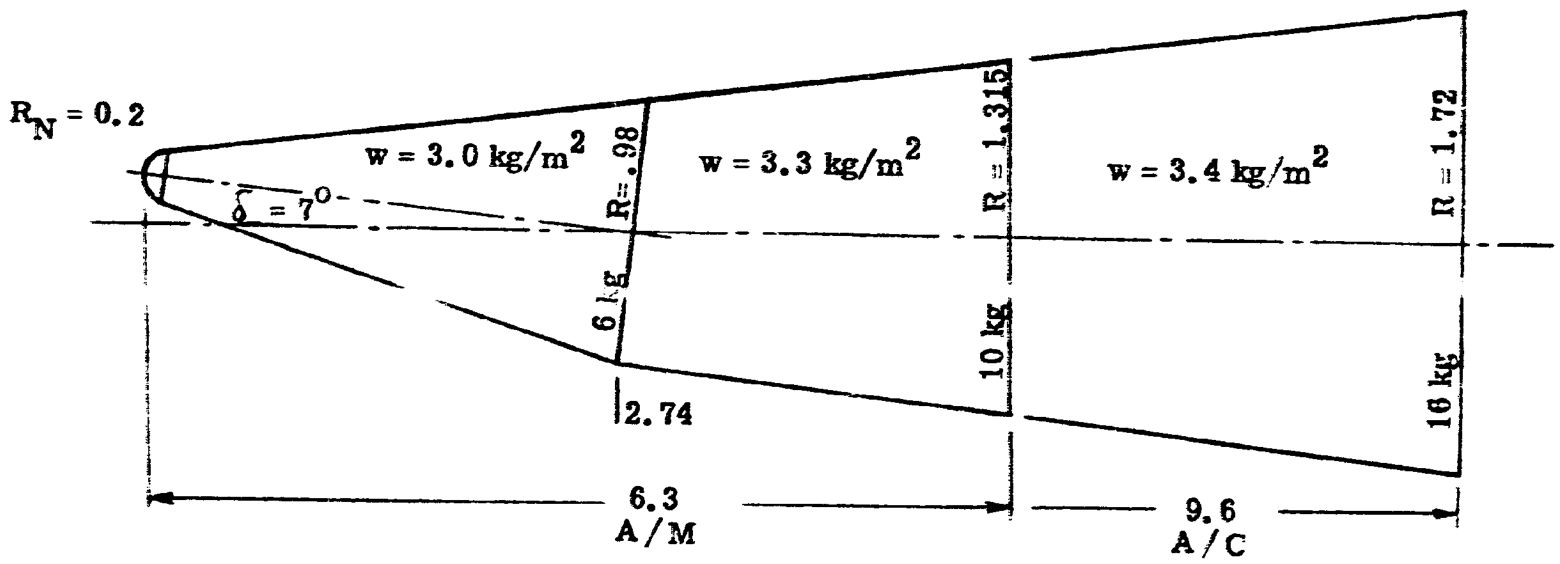

Figure VI-18 MSP Structure Unit Mass

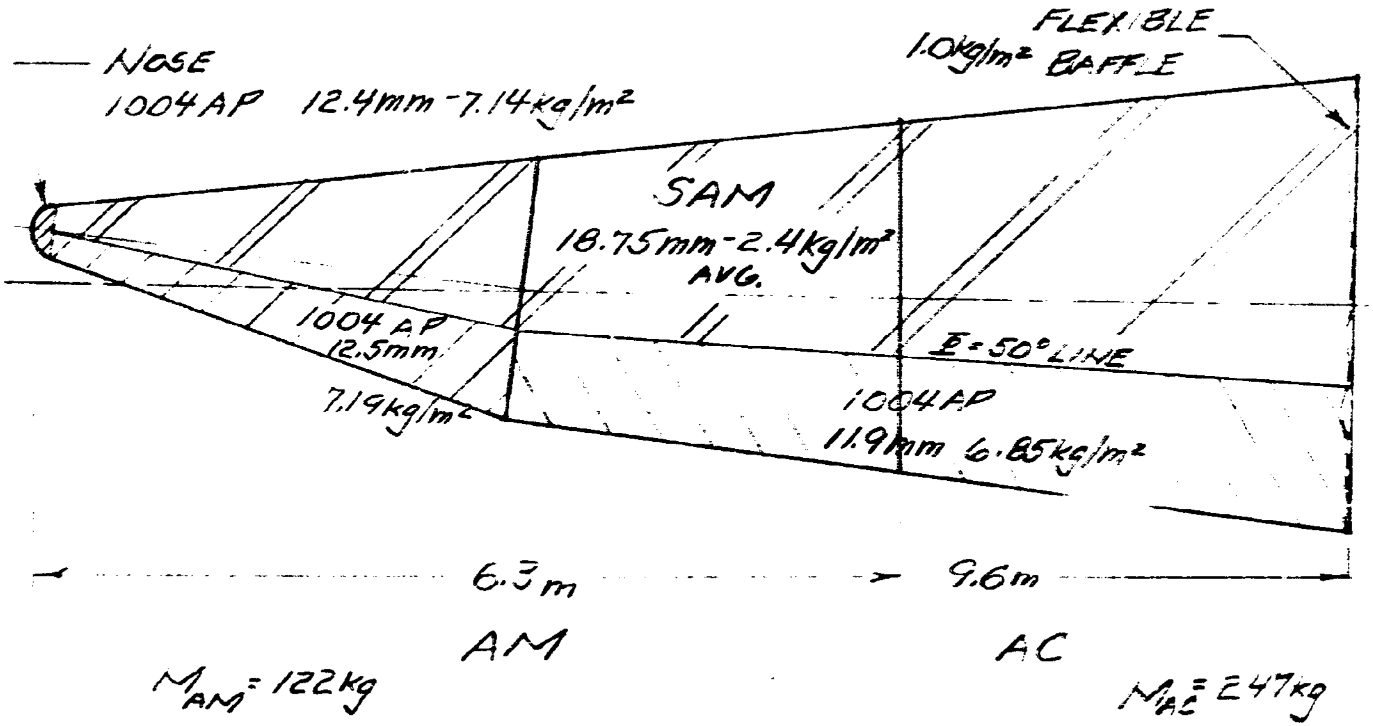

Figure VI-19 MSR TPS

MSR AEROSHELL MASS PARAMETERS

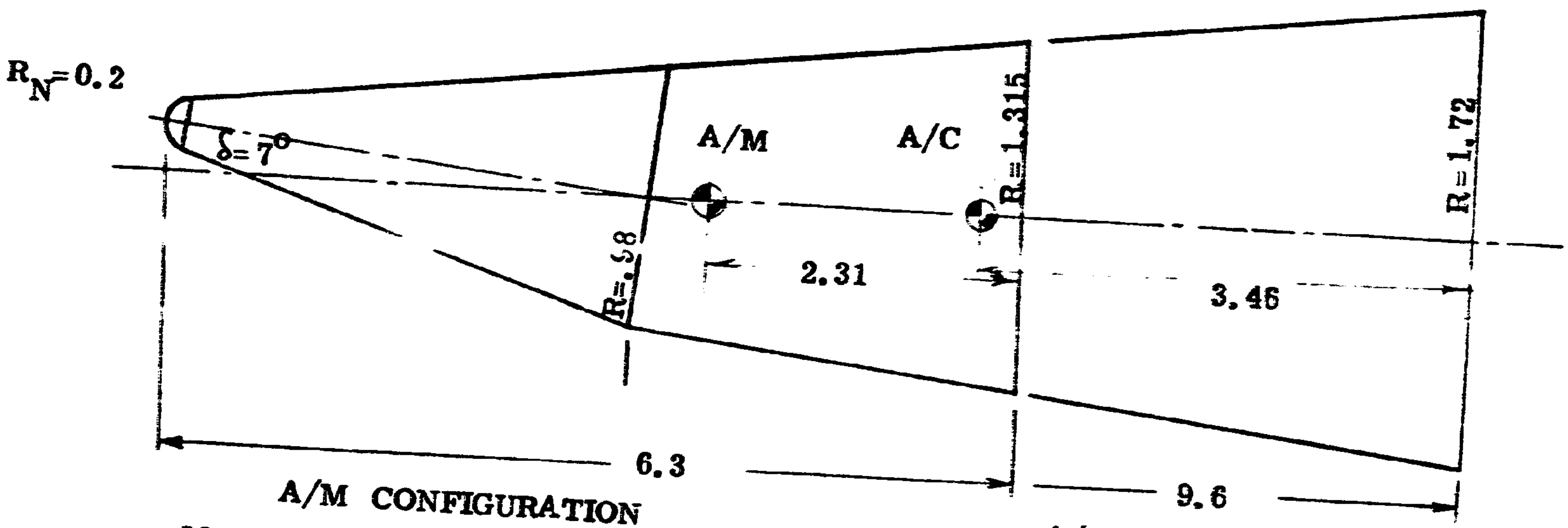

A/M CONFIGURATION

$M_{STR} = 121$ kg $I_R = 247\ kg\,m^2$

$M_{TPS} = 122$ $I_{P\&Y} = 785\ kg\,m^2$

$\epsilon = 243$

A/C CONFIGURATION

$M_{STR} = 255$ kg $I_R = 839\ kg\,m^2$

$M_{TPS} = 247$ $I_{P\&Y} = 3537\ kg\,m^2$

$\epsilon = 502$

Figure VI-20 MSR Aeroshell Mass Parameters

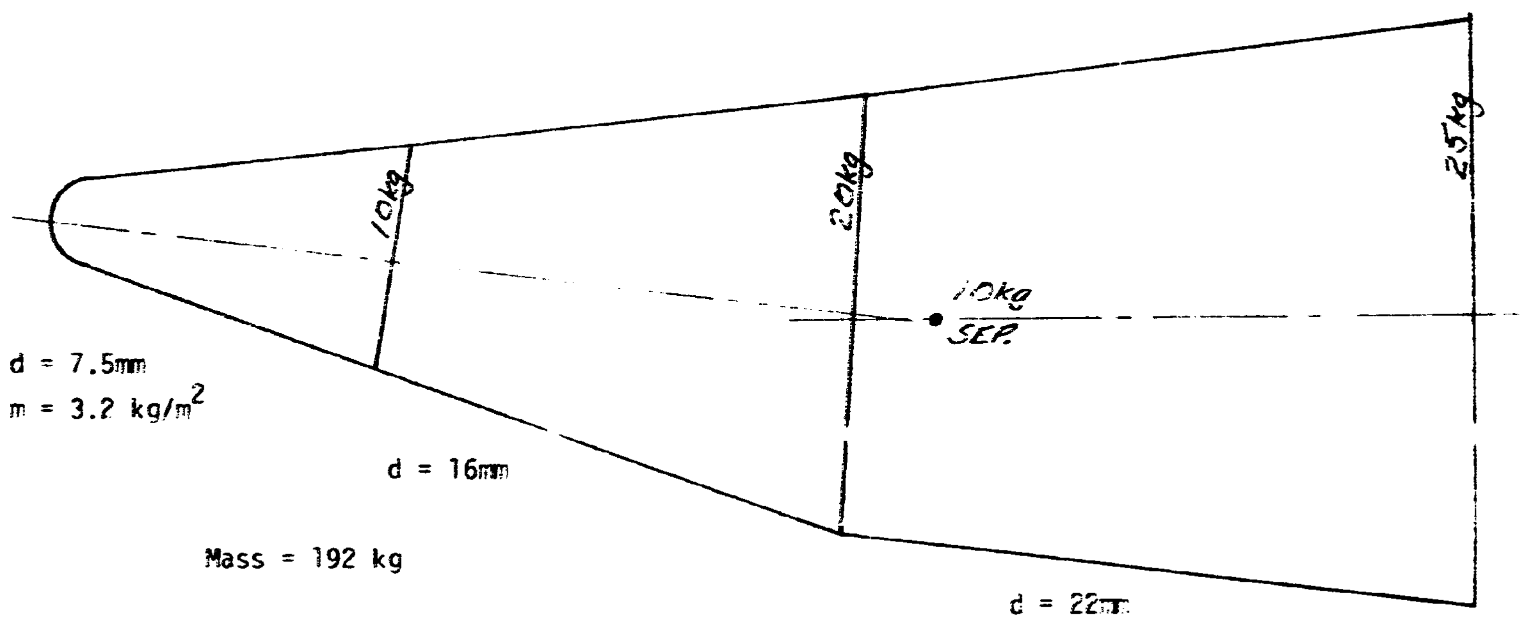

Figure VI-21 Uranus Structure

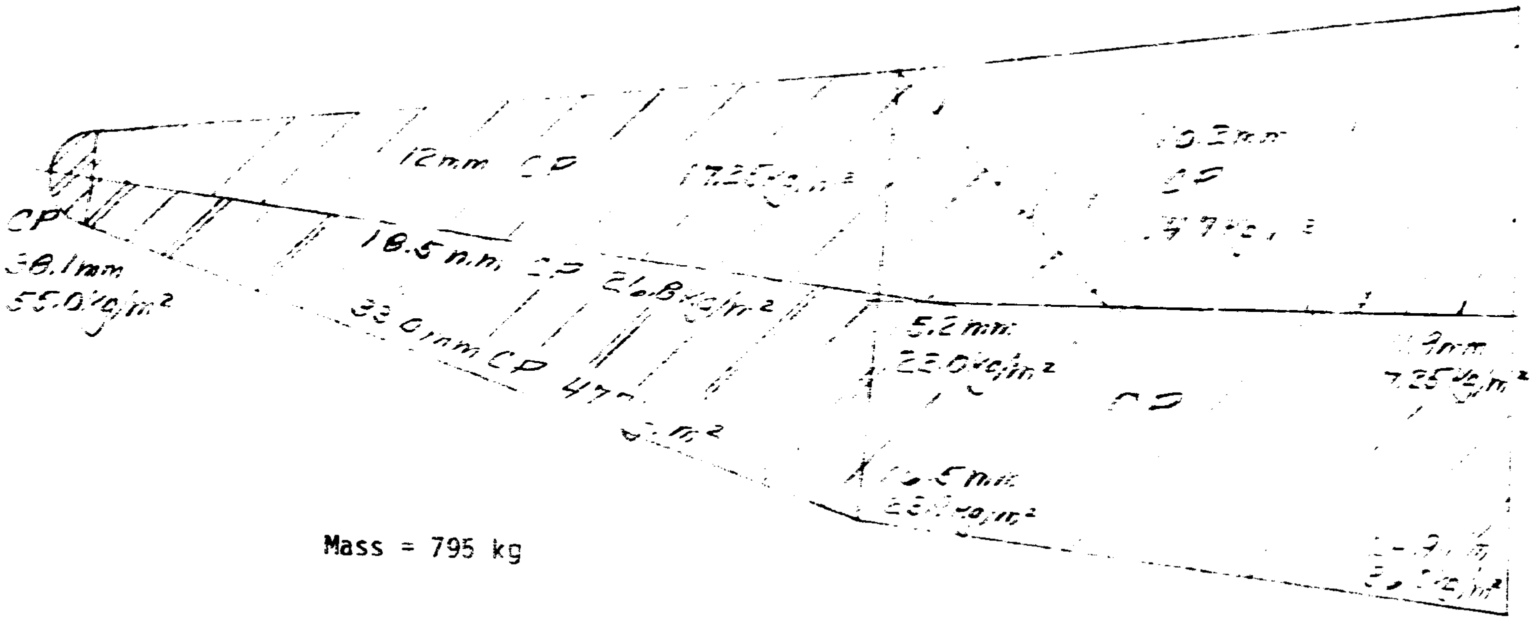

Mass = 795 kg

Figure VI-22 Uranus TPS

VII. CONCLUSIONS

This study has resulted in system design concepts for a generic Aerocapture configuration for the SO2P, MSR and Uranus missions. These concepts, along with the controlled entry simulations, support the feasibility of the generic Aerocapture concept. The design concepts consist of: aerodynamic configuration; control systems for atmospheric energy management; entry thermal protection; and structural definition.

The design concepts meet the requirements of Section II with the exception of SO2P payload mass at 13 km/sec. However, the 8 km/sec entry has a significant mass margin and it is estimated that entries up to 11 km/sec can accommodate the current payload mass estimate. Additional capability can become available as overall mission studies progress relative to SO2P payload and launch trajectory.

Based on the results of this study, the 6 3m configuration design concept for SO2P could also be used as the MSR aeromaneuver vehicle. It would be very inefficient from the mass standpoint but would allow not only a generic configuration but an identical design for both missions.

VIII. NEW TECHNOLOGY AND RECOMMENDATIONS

Based on the results of this study, it is strongly recommended that existing aerothermodynamic design technology be expanded to meet generic Aerocapture needs. Emphasis should be placed on thermal protection systems and associated vehicle interactions. Specific recommendations are as follows:

A. Thermal Protection Material Response in Aerocapture Environment

1. Contemporary thermal protection materials like carbon phenolic should be evaluated in plasma arc ground tests in air to assess their performance capabilities for the long heating time high heating rate environments
2. Reuse capability of the above contemporary ablators for subsequent entry in a more benign ballistic probe type environment should be evaluated in plasma arc ground tests.
3. New composite thermal protection materials, such as carbon/carbon over a carbon foam, which offer potential to significantly reduce TPS weight should be surveyed and several selected, fabricated, and tested for comparison to the contemporary material .
4. Full scale panel to panel ablator gaps should be tested in a plasma arc at angle of attack to determine ablative shape change effects on gap thermal performance.

B. Aerothermochemistry Effects in Dissociated Hypersonic Flows

1. Material surface - gas phase interactions between carbon and silica and CH_4 and N_2 should be evaluated.

2. In-depth thermal response of carbon phenolic, refrasil phenolic and elastomeric shield materials in dissociated H_2, He, CH_4, and N_2 should be evaluated analytically.

3. Facilities should be surveyed to determine where plasma arc tests can be conducted to validate the thermal response modeling of task 2 above.

4. Plan and conduct plasma arc tests where feasibility has been indicated in task 3 above.

C. Hypersonic Heat Transfer in Planetary Atmospheres

1. Thermodynamic and transport properties for CH_4 and N_2 should be generated.

2. Laminar and turbulent heat transfer to typical aerocapture configurations (with and without aerodynamic control surfaces) should be experimentally evaluated on the windward side, leeward and base areas. Predictions for the combination of gas composition and test conditions should be made utilizing the GE - 3DV code for windward and side areas and a semi-empirical separated flow heat transfer algorithm on the leeside and base areas. Predictions should also be made for typical aerocapture missions.

3. Uncoupled radiative heat transfer computations should be made for the SO2P and Uranus aerocapture missions.

D. Aerothermal Design of An Aerodynamic Control Surface

1. Ablative shape change of a split windward flap control surface should be evaluated laterally and axially by employing heat transfer distributions from task C-2 and the analytical ablative material models calibrated in task B-2 above.

2. Thermal design of the flap hinge line and actuator box seals should be investigated in sufficient detail to provide preliminary design type weight estimates. Design concepts should be derived from previous DOD flapped vehicle designs.

3. Aerocapture vehicle nose bend required vs. body slice size (to accommodate a split windward flap installation) should be generated.

4. Techniques to enhance the aerodynamic yaw stability like yaw tabs, bumps, or ears should be investigated.

5. Refined weight estimates of the split windward flap thermal protection and structural support system should be made.

E. Aerothermal - Material Interaction Effects on Aerocapture Performance

Six-degree-of-freedom aerodynamic characteristics should be generated, including the effects of:

1. Vehicle asymmetries

2. Ablative mass addition phase lag

3. Skewed laminar - turbulent boundary layer transition front

4. Ablator roughness

5. Split windward flap shape change

6. Free stream gas composition

F. Trajectory and control simulations should be performed to demonstrate the mission impact of items 1 through 6 above.

IX REFERENCES

I-1 Armento, R., "Mass Aerocapture Vehicle Definition Study Final Report," GE Report 79SDR2258, 17 August 1979

III-1 Dawitt, J. Brant, D. and Bosworth, F., "Computational Technique for Three Dimensional inviscid Flow Fields About Re-entry Vehicles," SAMSO-TR-79-5, April 1978.

III-2 Hecht, A. M., and Nestler, D. E., "A Three Dimensional Boundary Layer Computer Program for Sphere-Cone Type Re-entry Vehicles," AFFDL-TR-78-67, July 1978.

III-3 Gentry, A. E., Smyth, D. N., Oliver. W. R., "The Mark IV Supersonic-Hypersonic Arbitrary-Body Program," Vol. I, II and III, AFFDL-TR-73-159, November, 1973.

III-4 Marshall, L., "Hypersonic Dynamic Stability," GE-TIS-66SD333, Oct. 27, 1966

IV-1 Brewer, R. A., "A Comparison of Experimental Data and Theoretical Predictions for Laminar Stagnation Point Convective Heat Transfer in the Martian Entry Environment", GE-TDM-8151-107.

IV-2 Moss, J. N., Anderson, E. C., and Beiz, C. W., Jr., "Viscous-Shock Layer Solutions with Radiation and Ablation Injection for Jovian Entry", AIAA Paper 75-671, May 1975.

IV-3 Haviland, R., "Handbook of Satellites and Space Vehicles," D. Van Nostrand Co., Inc. New York, 1965, Pg. 354 - 374.

IV-4 Moss, J. N., Simmons, A. L. and Anderson, E. C., "The Impact of Turbulence on a Radiating Shock Layer with Coupled Ablation Injection", AIAA Paper 78-1186, July 10-12, 1978.

IV-5 Moss, J. N., "A Study of the Aerothermal Entry Environment for the Galileo Probe", AIAA Paper 79-1081, AIAA 14th Thermophysics Conference, June 4-6, 1979.

IV-6 Moss, J. N., "Flow Field Analysis for Future Planetary Entry", AIAA Paper 79-0918, Hampton, Va., May 8 - 11, 197[illegible].

IV-7 Nestler, D. E., Personal Communication June 1980

Feldhuhn, R. H. and Pasiuk, L., "An Experimental Investigation of the Aerodynamic Characteristics of Slender Hypersonic Vehicles at High Angles of Attack, "NOL Tech. Rept. [illegible]3-52, May 1968.

Moyer, R. E., "Skybolt Heat Transfer Data Analysis Angle of Attack," GE MSD TDM-8151-004, November 1962.

Widhopf, G. F., "Turbulent Heat Transfer Measurements on a Blunt Cone at Angle of Attack," Aerospace Rept. TR-0059 (S6816-60)-1, February 22, 1971.

Widhopf, G. F., "Transitional and Turbulent Heat Transfer Measurements on a Yawed Blunt Conical Nosetip," AIAA Paper No. 72-212.

IV-8 Sutton, K. "Fully Coupled Nongray Radiating Gas Flows with Ablation Product Effects about Planetary Entry Bodies", AIAA Paper 73-672, July 1973.

IV-9 Falanga, R. A., and Olstad, W. B., "An Approximate Inviscid Radiating Flow Field Analysis for Sphere-Cone Venusian Entry Vehicles", AIAA Paper 74-75, July, 1974.

IV-10 Brewer, R. A., D. N. Brant and R. P. Fezaroli, "Development of a Steady-State Shape Change Ablation Code for the Design of Outer Planet Probes" AIAA Paper 77-95, presented at AIAA 15 Aerospace Sciences Meeting, Los Angeles, January 1977.

IV-11 Brewer, R. A. and D. N. Brant, "Thermal Protection System for the Galileo Mission Atmospheric Entry Probe," AIAA paper 80-0358, presented at AIAA 18th Aerospace Sciences Meeting, Pasadena, Cal., Jan. 1980.

IV-12 Brewer, R. A., "Selection of a Heat Protection System for Venusian Entry," AIAA paper #75-731, presented at AIAA 10th Thermophysics Conference, Denver, Colorado, May 1975.

IV-13 Page, W. A., and Woodward, H. T., "Radiative and Convective Heating During Venus Entry", AIAA J., Vol. 10, October 1972, pp. 1379-1381.

IV-14 Page, W. A., Compton, D. L., Borucki, W. J., Ciffone, D. L., and Cooper, D. M., "Radiative Transport in Inviscid Nonadiabatic Stagnation Region Shock Layers", AIAA Paper 68-784, Los Angeles, California, 1968.

IV-15 Florence, D. A. Hecht, and E. Vogel, "Hypersonic Entry Heat Transfer" Pioneer Venus, GE RESD, Philadelphia, Pa. 1972

IV-16 Wolf, F., and Spiegel, JM, "Status of Basic Shock-Layer Radiation Information for Inner-Planet Atmospheric Entry", J. of Spacecraft and Rockets, 4 pp. 1166-1173, September 1967.

IV-17 Marvin, J. G. and Deiwert, C. S., "Convective Heat Transfer in Planetary Gases", NASA TR R-224, July 1965.

IV-18 Zoby, E. V., "Empirical Stagnation-Point Heat-Transfer Relaxation in Several Gas Mixtures at High Enthalpy Levels" NASA TND-4799, October 1968.

IV-19 Nicolet, W. E., Morse, H. L., Neuner, G. J., and Gomez, A. V., "Outer Planet Probe Entry Thermal Protection", Aerotherm Final Report 74-92, February 10, 1975.

IV-20 Nicolet, W. E., Private Communication, November 18, 1975.

IV-21 Stickford, G. H., and Menard, W. A., "Bow Shock Composition and Radiation Intensity Calculations for a Ballistic Entry into the Jovian Atmosphere", AIAA 3rd Thermophysics Conference, Paper No. 68-787 (1968).

IV-22 Berman, R. J., "Bow Shock Shape About a Spherical Nose", AIAA J., Vol. 3, No. 4 pp. 779, 780, April 1965.

IV-23 Serbin, H., "Supersonic Flow Around Blunt Bodies", J. Aerospace Sci. 25, 58-59 (1958).

IV-24 Li, T.-Y., and Geiger, R.E., "Stagnation Point of a Blunt Body in Hypersonic Flow", J. Aerospace Sci. 24, 25-32 (1957).

IV-25 Ridyard, H. W., and E. M. Storer, "Stagnation Point Shock Detachment of Blunt Bodies in Supersonic Flow", J. Aerospace Sciences, 29, 751-752 (1962).

IV-26 Storer, E. M., "A Simple Method for Calculating the Stagnation Point Shock Detachment of Spherical Bodies in Supersonic Flow", GE RESD Aerodynamics Fundamentals Memo 64-2, May 6, 1964.

IV-27 Florence, D., H. Thibault and A. Hiltz, "Selection, Development, Characterization and Flight Test of a Thermal Protection System for an Earth Entry Satellite Vehicle", AIAA paper #78-86 , presented at 2nd AIAA/ASME Thermophysics & Heat Transfer Conference, Palo Alto, Cal., May 1978.

IV-28 Kottock, S., "The Development of a Phenolic Nylon Model for a Reaction Kinetics Ablation Program", GE-TIS-65SD320, Sept. 1965.

IV-29 Cline, P. B., and Schultz, F. L., "Investigation of the Effect of Material Properties on Composite Ablative Material Behavior," NASA CR-72142, April 1967.

IV-30 Berkowitz, A. M., Kyriss, C. L., and Martellucci, A., "Boundary Layer Transition Flight Test Observations," AIAA Paper No. 77-125, January 24-25, 1977.

IV-31 Juneau, P. W., Jr., et J. Brazel, J. W. Metzger, C. Fehl, & R. M. Fenton, "Ablative Materials for High Heat Loads - Part III - Insulative Layers for Carbon/Phenolic Heatshields", AFML-TR-70-95, Part III, June 1973.

IV-32 Moss, J. M., personal communication, September 1980.